

Science and Technology of Nuclear Installations

# Uncertainty Analysis in Reactor Physics Modeling

Guest Editors: Kostadin Ivanov, Carlo Parisi,  
and Oscar Cabellos





---

# **Uncertainty Analysis in Reactor Physics Modeling**

Science and Technology of Nuclear Installations

---

# **Uncertainty Analysis in Reactor Physics Modeling**

Guest Editors: Kostadin Ivanov, Carlo Parisi,  
and Oscar Cabellos



---

Copyright © 2013 Hindawi Publishing Corporation. All rights reserved.

This is a special issue published in “Science and Technology of Nuclear Installations.” All articles are open access articles distributed under the Creative Commons Attribution License, which permits unrestricted use, distribution, and reproduction in any medium, provided the original work is properly cited.

## Editorial Board

Nusret Aksan, Switzerland  
Antonio C. M. Alvim, Brazil  
Won Pil Baek, Korea  
Stephen M. Bajorek, USA  
George Bakos, Greece  
Jozsef Banati, Sweden  
Ricardo Barros, Brazil  
Anis Bousbia Salah, Belgium  
Giovanni B. Bruna, France  
Nikola Čavlina, Croatia  
Xu Cheng, China  
Leon Cizelj, Slovenia  
Alejandro Clausse, Argentina  
Francesco D' Auria, Italy  
Marcos P. de Abreu, Brazil  
Giovanni Dell'Orco, France  
Juan Carlos Ferreri, Argentina  
Nikolay Fil, Russia  
Cesare Frepoli, USA  
Giorgio Galassi, Italy  
Regina Galetti, Brazil

Michel Giot, Belgium  
Valerio Giusti, Italy  
Horst Glaeser, Germany  
Satish Kumar Gupta, India  
Ali Hainoun, Syria  
Keith E. Holbert, USA  
Kostadin Ivanov, USA  
Yacine Kadi, Republic of Korea  
Ahmed Khedr, Egypt  
Tomasz Kozlowski, USA  
Tomoaki Kunugi, Japan  
Mike Kuznetsov, Germany  
H.-Y. Lee, Republic of Korea  
Bundit Limmeechokchai, Thailand  
Jiri Macek, Czech Republic  
Annalisa Manera, USA  
Borut Mavko, Slovenia  
Oleg Melikhov, Russia  
Rafael Miró, Spain  
Josef Misak, Czech Republic  
Rahim Nabbi, Germany

Manmohan Pandey, India  
Yuriy Parfenov, Russia  
Yves Pontillon, France  
Nik Popov, Canada  
Piero Ravetto, Italy  
Francesc Reventos, Spain  
Enrico Sartori, France  
Carlo Sborchia, France  
Massimo Sepielli, Italy  
Arkady Serikov, Germany  
James F. Stubbins, USA  
Iztok Tiselj, Slovenia  
Rizwan Uddin, USA  
Eugenijus Ušpuras, Lithuania  
Richard Wright, Norway  
Chao Xu, China  
X. George Xu, USA  
Yanko Yanev, Bulgaria  
Zhiwei Zhou, China  
Enrico Zio, Italy  
Massimo Zucchetti, Italy

# Contents

**Uncertainty Analysis in Reactor Physics Modeling**, Kostadin Ivanov, Carlo Parisi, and Oscar Cabellos  
Volume 2013, Article ID 697057, 2 pages

**Propagation of Cross-Section Uncertainties in Criticality Calculations in the Framework of UAM-Phase I Using MCNPX-2.7e and SCALE-6.1**, C. J. Díez, J. J. Herrero, O. Cabellos, and J. S. Martínez  
Volume 2013, Article ID 380284, 10 pages

**Uncertainty Analysis of Light Water Reactor Fuel Lattices**, C. Arenas, R. Bratton, F. Reventos, and K. Ivanov  
Volume 2013, Article ID 437409, 10 pages

**PSI Methodologies for Nuclear Data Uncertainty Propagation with CASMO-5M and MCNPX: Results for OECD/NEA UAM Benchmark Phase I**, W. Wieselquist, T. Zhu, A. Vasiliev, and H. Ferroukhi  
Volume 2013, Article ID 549793, 15 pages

**SCALE Modeling of Selected Neutronics Test Problems within the OECD UAM LWR's Benchmark**, Luigi Mercatali, Kostadin Ivanov, and Victor Hugo Sanchez  
Volume 2013, Article ID 573697, 11 pages

**Presentation and Discussion of the UAM/Exercise I-1b: "Pin-Cell Burn-Up Benchmark" with the Hybrid Method**, O. Cabellos  
Volume 2013, Article ID 790206, 12 pages

**Uncertainty and Sensitivity Analyses of a Pebble Bed HTGR Loss of Cooling Event**, Gerhard Strydom  
Volume 2013, Article ID 426356, 16 pages

**A Two-Step Approach to Uncertainty Quantification of Core Simulators**, Artem Yankov, Benjamin Collins, Markus Klein, Matthew A. Jessee, Winfried Zwermann, Kiril Velkov, Andreas Pautz, and Thomas Downar  
Volume 2012, Article ID 767096, 9 pages

**Computational Method for Global Sensitivity Analysis of Reactor Neutronic Parameters**, Bolade A. Adetula and Pavel M. Bokov  
Volume 2012, Article ID 109614, 11 pages

**Sensitivity Studies for the Exercise I-1 of the OECD/UAM Benchmark**, E. Canuti, A. Petruzzi, F. D'Auria, and T. Kozłowski  
Volume 2012, Article ID 817185, 10 pages

**Uncertainty and Sensitivity of Neutron Kinetic Parameters in the Dynamic Response of a PWR Rod Ejection Accident Coupled Simulation**, C. Mesado, A. Soler, T. Barrachina, R. Miró, J. C. García-Díaz, R. Macián-Juan, and G. Verdú  
Volume 2012, Article ID 625878, 10 pages

**Perturbation-Theory-Based Sensitivity and Uncertainty Analysis with CASMO-4**, Maria Pusa  
Volume 2012, Article ID 157029, 11 pages

**Uncertainty Propagation Analysis for PWR Burnup Pin-Cell Benchmark by Monte Carlo Code McCARD**, Ho Jin Park, Hyung Jin Shim, and Chang Hyo Kim  
Volume 2012, Article ID 616253, 6 pages

**Asymptotic Analysis for the Variance-Based Global Sensitivity Indices**, Pavel M. Bokov  
Volume 2012, Article ID 253045, 8 pages

## Editorial

# Uncertainty Analysis in Reactor Physics Modeling

**Kostadin Ivanov,<sup>1</sup> Carlo Parisi,<sup>2</sup> and Oscar Cabellos<sup>3</sup>**

<sup>1</sup> Pennsylvania State University, University Park, PA 16802, USA

<sup>2</sup> ENEA, Santa Maria di Galeria, 00123 Rome, Italy

<sup>3</sup> Universidad Politecnica de Madrid, 28006 Madrid, Spain

Correspondence should be addressed to Kostadin Ivanov; knil@psu.edu

Received 18 November 2013; Accepted 18 November 2013

Copyright © 2013 Kostadin Ivanov et al. This is an open access article distributed under the Creative Commons Attribution License, which permits unrestricted use, distribution, and reproduction in any medium, provided the original work is properly cited.

In recent years, there has been an increasing demand from nuclear research, industry, safety, and regulation for best estimate predictions to be provided with their confidence bounds. Consequently, Organization for Economic Cooperation and Development (OECD)/Nuclear Energy Agency (NEA) has initiated an international uncertainty analysis in modeling (UAM) benchmark focused on uncertainty analysis in best-estimate coupled code calculations for design, operation, and safety analysis of light water reactors (LWRs). The title of this benchmark is “OECD/NEA UAM-LWR benchmark”. Reference systems and scenarios for coupled code analysis are defined to study the uncertainty effects for all stages of the system calculations. Measured data from plant operation are available for the chosen scenarios.

The proposed technical approach is to establish a benchmark for uncertainty analysis in best-estimate modeling and coupled multiphysics and multiscale LWR analysis, using as bases a series of well-defined problems with complete sets of input specifications and reference experimental data. The objective is to determine the uncertainty in LWR system calculations at all stages of a coupled reactor physics/thermal hydraulics calculation. The full chain of uncertainty propagation from basic data, engineering uncertainties, across different scales (multi-scale), and physics phenomena (multiphysics) is tested on a number of benchmark exercises for which experimental data are available and for which the power plant details have been released. The principal idea is (a) to subdivide the complex system/scenario into several steps or exercises, each of which can contribute to the total uncertainty of the final coupled system calculation, (b) to identify input, output, and assumptions for each step, (c) to calculate the resulting uncertainty in each step and (d) to

propagate the uncertainties in an integral system simulation for which high quality plant experimental data exist for the total assessment of the overall computer code uncertainty. The main scope covers uncertainty (and sensitivity) analysis (SA/UA) in best estimate modeling for design and operation of LWRs, including methods that are used for safety evaluations. As part of this effort, the development and assessment of different methods or techniques to account for the uncertainties in the calculations are to be investigated and reported to the participants.

The general frame of the OECD/NEA UAM-LWR benchmark consists of three phases with different exercises for each phase: Phase I (neutronics phase), Phase II (core phase), and Phase III (system phase). The focus of Phase I is on propagating uncertainties in standalone neutronics calculations and consists of the following three exercises.

Exercise I-1: “Cell Physics” focused on the derivation of the multigroup microscopic cross-section libraries and associated uncertainties.

Exercise I-2: “Lattice Physics” focused on the derivation of the few-group macroscopic cross-section libraries and associated uncertainties.

Exercise I-3: “Core Physics” focused on the core steady state stand-alone neutronics calculations and associated uncertainties.

The special issue is devoted to Phase I of the above-described OECD/NEA UAM-LWR benchmark. The special issue contains thirteen papers devoted to the advances in the uncertainty and sensitivity analysis related to reactor physics modeling. The authors of these papers are active participants

in the OECD/NEA UAM-LWR benchmark and in this publication they present their work and developments related to the benchmark exercises. Most of the papers are focused on propagation of cross-sections uncertainties at different stages of reactor calculations and some papers also discuss in addition the propagation of manufacturing uncertainties in lattice physics calculations. The topic of the paper of M. Pusa is the development of sensitivity and uncertainty analysis capability for the reactor physics code CASMO-4. The development of two complementary techniques direct perturbation (DP) and stochastic sampling (SS) as well as their implementation in CASMO-5MX is described by W. Wieselquist et al. The development and application of SS technique using MCNPX was also presented in the same paper. The variance-based global sensitivity analysis technique has been modified to be applied to calculations of reactor parameters that are dependent on group-wise neutron cross-sections as reported by B. A. Adetula and P. M. Bokov. Furthermore, P. M. Bokov presented asymptotic analysis for the variance-based global sensitivity indices in a companion paper. L. Mercatali et al. performed sensitivity and uncertainty analysis using SCALE-6.1 code package (based on the generalized perturbation theory) in order to assess the prediction uncertainty of some selected reactor integral parameters due to the uncertainty in the basic nuclear data. Moreover, the reference solutions for the test cases of Exercise I-1 obtained using Monte Carlo methodologies together with a comparison between deterministic and stochastic solutions are presented in the same paper. Studies involving criticality and uncertainty analysis calculations on both pin cell and fuel assembly level were performed using TSUNAMI-2D sequence in SCALE 6.1 and subsequently presented by C. C. Arenas et al. Uncertainty variations due to temperatures changes and different fuel compositions were the main focus of this analysis. C. J. Díez et al. reported sensitivity calculations using the “sandwich formula” to propagate cross-section uncertainties. Two different codes were employed to calculate the sensitivity coefficients of  $k_{\text{eff}}$  to cross-sections in criticality calculations: MCNPX-2.7e (using differential operator technique) and SCALE-6.1 (using adjoint-weighted technique). The effects of the numerical discretization error and the manufacturing tolerances on fuel pin lattice integral parameters (multiplication factor and macroscopic cross-sections) through sensitivity calculations were discussed by E. Canuti et al. Evaluation of uncertainties in depletion calculations is the subject of the papers of O. Cabellos and H. J. Park et al., based on the PWR pin-cell burnup subexercise of Exercise I-1. Two methods for propagating cross-section uncertainties through core simulators (the XSUSA statistical approach and the “two-step” method) were compared and analyzed by A. Yankov et al. The paper of C. Mesado et al. studies the propagation of uncertainties of neutron kinetics parameters in the coupled core transient response. G. Strydom summarized the results of an uncertainty and sensitivity quantification investigation performed with statistical methodology, utilizing a typical high temperature reactor benchmark and the coupled code PEBBED-THERMIX.

The obtained results from sensitivity and uncertainty analysis for the test cases of Exercises I-1 and I-2 indicated

that the largest contributors to prediction uncertainties of infinite multiplication factor are the neutron capture reaction  $^{238}\text{U}(n, \gamma)$  and corresponding cross-section (for UOX fuel) and  $^{238}\text{U}(n, n')$  reaction and corresponding cross-section (for MOX fuel and UOX fuel with  $\text{Gd}_2\text{O}_3$  burnable poison). When depletion is involved for UOX fuel the major contributor  $^{238}\text{U}(n, \gamma)$  is replaced by  $^{239}\text{Pu}$  nubar (average number of neutrons per fission reaction) as the burnup process progresses (at approximately 15 GWd/MTU).

The cross-section uncertainty information is considered as the most important source of input uncertainty for Phase I of the OECD/NEA UAM-LWR benchmark. The cross-section related uncertainties are propagated through the 3 exercises of Phase I. In Exercise I-2 manufacturing and geometry (technological) uncertainties are added to account for them in lattice physics calculations. It was found that the contribution of manufacturing uncertainties to prediction uncertainty of neutronics parameters of interest is generally smaller than the contribution of cross-section uncertainties. New and improved methods have been developed and implemented in several calculation sequences from the participants during benchmark activities related to Phase I of the OECD/NEA UAM-LWR benchmark. Such diversity is important for the progress of the project and is important for the collaboration of the UAM benchmark group with the SCALE team at the Oak Ridge National Laboratory (ORNL), USA. One of the outcomes was the finding that the propagation of cross-section uncertainties, uncertainties of depletion and kinetics parameters, and manufacturing uncertainties in core calculations can be done simultaneously in a practical manner by combining deterministic and statistical uncertainty and sensitivity analysis methodologies.

As the OECD/NEA UAM-LWR activities advance, the intention is to publish similar special issues on the remaining two phases of the benchmark. For more information about the OECD/NEA UAM-LWR benchmark please visit <http://www.oecd-nea.org/science/wprs/egrsltb/UAM>.

## Acknowledgments

The editors would like to thank the members of the Expert Group on UAM (EGUAM) at OECD/NEA, the members of the UAM-LWR Scientific Board, and Dr. Enrico Sartori, Dr. Jim Gulliford, and Dr. Akifumi Yamaji from OECD/NEA, whose support, help, contributions, and encouragement in establishing and carrying out this benchmark are invaluable. Finally, our thanks go to the many authors and researchers who contributed to the technical success of Phase I of this benchmark.

*Kostadin Ivanov  
Carlo Parisi  
Oscar Cabellos*

## Research Article

# Propagation of Cross-Section Uncertainties in Criticality Calculations in the Framework of UAM-Phase I Using MCNPX-2.7e and SCALE-6.1

C. J. Díez,<sup>1</sup> J. J. Herrero,<sup>1</sup> O. Cabellos,<sup>1,2</sup> and J. S. Martínez<sup>1</sup>

<sup>1</sup> Department of Nuclear Engineering, Universidad Politécnica de Madrid, C/José Gutiérrez Abascal 2, 28006 Madrid, Spain

<sup>2</sup> Institute of Nuclear Fusion, Universidad Politécnica de Madrid, C/José Gutiérrez Abascal 2, 28006 Madrid, Spain

Correspondence should be addressed to C. J. Díez; [cj.diez@upm.es](mailto:cj.diez@upm.es)

Received 22 August 2012; Accepted 7 December 2012

Academic Editor: Kostadin Ivanov

Copyright © 2013 C. J. Díez et al. This is an open access article distributed under the Creative Commons Attribution License, which permits unrestricted use, distribution, and reproduction in any medium, provided the original work is properly cited.

In the framework of the OECD/NEA project on Benchmark for Uncertainty Analysis in Modeling (UAM) for Design, Operation, and Safety Analysis of LWRs, several approaches and codes are being used to deal with the exercises proposed in Phase I, “Specifications and Support Data for Neutronics Cases.” At UPM, our research group treats these exercises with sensitivity calculations and the “sandwich formula” to propagate cross-section uncertainties. Two different codes are employed to calculate the sensitivity coefficients of  $k_{\text{eff}}$  to cross sections in criticality calculations: MCNPX-2.7e and SCALE-6.1. The former uses the Differential Operator Technique and the latter uses the Adjoint-Weighted Technique. In this paper, the main results for exercise I-2 “Lattice Physics” are presented for the criticality calculations of PWR. These criticality calculations are done for a  $15 \times 15$  TMI fuel assembly at four different states: HZP-Unrodded, HZP-Rodded, HFP-Unrodded, and HFP-Rodded. The results of the two different codes above are presented and compared. The comparison proves a good agreement between SCALE-6.1 and MCNPX-2.7e in  $k_{\text{eff}}$  uncertainty that comes from the sensitivity coefficients calculated by both codes. Differences are found when the sensitivity profiles are analysed, but they do not lead to differences in the  $k_{\text{eff}}$  uncertainty.

## 1. Introduction

As stated in the Introduction of [1], “This benchmark project (...) responds to the needs of estimating confidence bounds for the results from simulations and analysis in real applications.” Phase I deals with the neutronics cases.

- (i) *Exercise I-1.* Cell Physics focused on the derivation of the multigroup microscopic cross section libraries and their uncertainties.
- (ii) *Exercise I-2.* Lattice Physics focused on the derivation of the few-group macroscopic cross section libraries and their uncertainties.
- (iii) *Exercise I-3.* Core Physics focused on the core steady state stand-alone neutronics calculations and their uncertainties.

For these calculations, the main source of uncertainty taken into account is the cross section uncertainties which are propagated throughout the different simulation levels.

There are mainly two different approaches to propagate uncertainties: The first one is based on a Monte Carlo approach where a large amount of calculations are performed sampling the problem parameters as random variables, and then carrying out a statistical analysis; the second one relies on sensitivity coefficients and the “sandwich formula.” The latter approach is the one employed in this work.

The way of obtaining the sensitivity coefficients of the response functions depends on which code is used. In this case, two different techniques are used: the Adjoint-Weighted Technique by SCALE-6.1 [2] and the Differential Operator Technique by MCNPX-2.7e [3]. Previous works [4, 5] have compared both techniques showing their pros and cons.

This work is aimed to present how the uncertainty quantification is carried out using the sensitivity approach and how the sensitivity coefficients are calculated with SCALE-6.1 and MCNPX-2.7e. Afterwards, in the framework of Exercise I-2, both codes are used to perform the uncertainty quantification on the  $k_{\text{eff}}$  of a  $15 \times 15$  TMI fuel assembly.

Finally, their results are compared and conclusions are drawn.

## 2. Uncertainty Quantification Based on Sensitivity Coefficients

The uncertainty quantification based on sensitivity coefficients relies on the “sandwich formula” obtained with the propagation of moments, as presented in [6, Section III.F] and summarized here.

Being  $R$  the calculated response function of a system which depends on  $(\alpha_1, \dots, \alpha_n)$  parameters,  $R$  can be approximated by a linear function of  $(\alpha_1, \dots, \alpha_n)$  using the Taylor series approximation around a nominal value  $(\alpha_1^0, \dots, \alpha_n^0)$ , as presented in (1), where  $\delta\alpha_i = \alpha_i - \alpha_i^0$ :

$$R(\alpha_1, \dots, \alpha_n) = R(\alpha_1^0, \dots, \alpha_n^0) + \sum_{i=1}^n \left( \frac{\partial R}{\partial \alpha_i} \right)_{(\alpha_1^0, \dots, \alpha_n^0)} \delta\alpha_i. \quad (1)$$

Then, taking the parameters of the system as random variables,  $R$  becomes a random variable for which its mean coincides with the response function at the nominal value, (2), and its variance is calculated with (3) known as the “sandwich formula” or the “sandwich rule”:

$$E(R) = R(\alpha_1^0, \dots, \alpha_n^0), \quad (2)$$

$$\text{var}(R) = S V_\alpha S^T, \quad (3)$$

where

(i)  $S = (\partial R / \partial \alpha_1, \dots, \partial R / \partial \alpha_n)$  is the vector of the sensitivity coefficients.

(ii)  $V_\alpha$  is the covariance matrix of the system parameters defined as

$$(V_\alpha)_{ij} = \begin{cases} \text{cov}(\alpha_i, \alpha_j), & i \neq j, \\ \text{var}(\alpha_i), & i = j. \end{cases} \quad (4)$$

Because usually the sensitivity coefficients are calculated as relative values,

$$S'_i = \frac{\partial R / R}{\partial \alpha_i / \alpha_i}. \quad (5)$$

Equation (3) can be rewritten as (6), where the value obtained is the relative standard deviation (rel.std.dev.( $R$ )) and  $V'_\alpha$  is the relative covariance matrix:

$$\begin{aligned} (\text{rel.std.dev.}(R))^2 &= \frac{\text{var}(R)}{R^2} \\ &= \sum_{i=1, j=1}^n \left( S'_i \frac{\text{cov}(\alpha_i, \alpha_j)}{\alpha_i \alpha_j} S'_j \right) = S' V'_\alpha S'^T. \end{aligned} \quad (6)$$

Both values, the standard deviation  $\sqrt{\text{var}(R)}$  provided by (3) and the rel.std.dev.( $R$ ) calculated in (6), are used as a measure of the uncertainty on the response function. Therefore, the sensitivity coefficients of the response function to the system parameters,  $S_i$  or  $S'_i$ , should be calculated and the covariance matrix ( $V_\alpha$ ) or the relative covariance matrix ( $V'_\alpha$ ) should be provided.

**2.1. Calculating the Sensitivity Coefficients.** The two codes which perform the criticality calculations in this paper use different methods for calculating the sensitivity coefficients necessary to carry out the uncertainty quantification:

- (i) SCALE-6.1 uses the Adjoint-Weighted Technique.
- (ii) MCNPX-2.7e uses the Differential Operator Technique.

**2.1.1. SCALE-6.1—The Adjoint-Weighted Technique.** The Adjoint-Weighted Technique is used in SCALE-6.1 inside the TSUNAMI sequence, and the theory applied is stated in the SAMS module manual [2, Section F22]. Every sensitivity coefficient is calculated as a sum of two terms: explicit and implicit, as presented in

$$(S_k)_{\text{complete}} = (S_k)_{\text{explicit}} + (S_k)_{\text{implicit}}. \quad (7)$$

The explicit term,  $(S_k)_{\text{explicit}}$ , is calculated using the Adjoint-Weighted Technique (called adjoint-based perturbation in the SAMS manual), based on the perturbation  $\delta k$  of the  $k_{\text{eff}}$  given in (8). There,  $\phi$  is the neutron flux of the problem defined by  $[A - \lambda B]\phi = 0$ , where  $A$  is the operator that represents all of the transport equations except for the fission term,  $B$  is the operator that represents the fission term, and  $\lambda$  represents the eigenvalues where the largest one is  $1/k_{\text{eff}}$ .  $\phi^\dagger$  is the adjoint neutron flux of the adjoint problem defined as  $[A^\dagger - \lambda B^\dagger]\phi^\dagger = 0$  where  $A^\dagger$  and  $B^\dagger$  are the adjoint operators corresponding to  $A$  and  $B$ .  $\delta A$  and  $\delta B$  are the perturbed operators due to a perturbation in the cross sections:

$$\frac{\delta k_{\text{eff}}}{k_{\text{eff}}} = - \frac{\langle \phi^\dagger (\delta A - \lambda \delta B) \phi \rangle}{\langle \phi^\dagger (\lambda \delta B) \phi \rangle}. \quad (8)$$

The implicit term,  $(S_k)_{\text{implicit}}$ , is calculated in order to take into account the effect on  $k_{\text{eff}}$  of perturbing one cross section that affects the resonance-shielded values of other cross sections. This term appears because the transport calculations should be done using groupwise cross sections which require an initial self-shielding adjustment.

In any TSUNAMI sequence, the forward and adjoint transport problems are solved in order to calculate the neutron flux and its adjoint using XSDRNPM module for TSUNAMI-1D, NEWT module for TSUNAMI-2D, and KENO-V.a or KENO-VI for TSUNAMI-3D. Then, the SAMS module is applied for calculating the sensitivity coefficients for every energy-group reaction cross section. The sensitivity to the average number of neutrons per fission,  $\bar{\nu}$ , and to the fission spectrum,  $\chi$ , is estimated. Also, SAMS module performs the uncertainty quantification on the  $k_{\text{eff}}$  due to the cross section uncertainties.

**2.1.2. MCNPX-2.7e—The Differential Operator Technique.** The Differential Operator Technique is applied in MCNPX-2.7e to calculate the change  $\Delta k_{\text{eff}}$  due to a perturbation in a cross section,  $\Delta\sigma$ , by means of the PERT card. It is based on the Taylor series expansion as presented in (9), where  $\sigma_x$

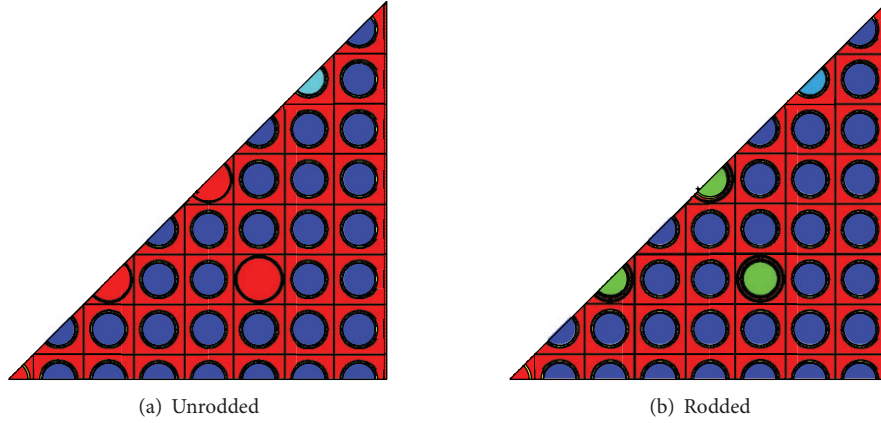


FIGURE 1: Geometrical model implemented in MCNPX-2.7e for 1/8 of the 15 × 15 TMI fuel assembly.

is the cross section perturbed,  $\sigma_{x,0}$  is its nominal value, and  $\Delta\sigma = \sigma_x - \sigma_{x,0}$ , is the perturbation:

$$\begin{aligned} \Delta k_{\text{eff}} &= k_{\text{eff}}(\sigma_x) - k_{\text{eff}}(\sigma_{x,0}) = \left( \frac{\partial k}{\partial \sigma} \bigg|_{\sigma_{x,0}} \Delta\sigma \right)_{1\text{st}} \\ &+ \left( \frac{1}{2} \frac{\partial^2 k}{\partial \sigma^2} \bigg|_{\sigma_{x,0}} (\Delta\sigma)^2 \right)_{2\text{nd}} + \dots \quad (9) \\ &= [\Delta k_{\text{eff}}]_{\text{PERT},1\text{st}} + [\Delta k_{\text{eff}}]_{\text{PERT},2\text{nd}} + \dots \end{aligned}$$

The first derivative means the derivative of the probability of the random walk occurring. The second one is the derivative of the tally response itself. There is an additional derivative for the changes in the fission source distribution that MCNPX-2.7e does not take into account, but methodologies about how to calculate it have been developed in [4, 7–9] showing also its effect. In [4, 10], it was pointed out that because the scattering affects the fission source spatial distribution more than capture, the sensitivity to scattering cross sections could be wrong. Other limitations are stated in the MCNPX manual [3, Section 5.2.2].

For the sensitivity coefficient, only the first derivative is required. Using the first term provided by the PERT card (using the keyword METHOD=+2), the sensitivity coefficient is calculated with (10), just dividing by  $k_{\text{eff},0}$  and  $p_x$ , which is the variation of the cross section from  $\sigma_x = \sigma_{x,0}(1 + p_x)$ . Because  $[\Delta k_{\text{eff}}]_{\text{PERT},1\text{st}}$  is lineal with respect to the size of the perturbation  $p_x$ , so choosing one value for  $p_x$  is trivial:

$$S_i = \frac{1}{k_0 p_x} [\Delta k_{\text{eff}}]_{\text{PERT},1\text{st}}. \quad (10)$$

The statistical uncertainty is propagated to the sensitivity coefficient by (11), obtaining the relative standard deviation:

$$\frac{\sqrt{\text{var}(S_i)}}{S_i} = \sqrt{\frac{\text{var}([\Delta k_{\text{eff}}]_{\text{PERT},1\text{st}})}{[\Delta k_{\text{eff}}]_{\text{PERT},1\text{st}}^2} + \frac{\text{var}(k_0)}{k_0^2}}. \quad (11)$$

TABLE 1: Reaction cross sections perturbed using PERT cards in the MCNPX-2.7e calculations.

Reaction	Isotopes
$\sigma(n, n)$	<sup>152,154,155,156,157,158,160</sup> Gd, <sup>238</sup> U, <sup>107,109</sup> Ag, <sup>113</sup> Cd, <sup>115</sup> In
$\sigma(n, n')$	<sup>238</sup> U
$\sigma(n, f)$	<sup>235,238</sup> U
$\sigma(n, \gamma)$	<sup>152,154,155,156,157,158,160</sup> Gd, <sup>238</sup> U, <sup>107,109</sup> Ag, <sup>113</sup> Cd, <sup>115</sup> In

### 3. PWR Calculations on Exercise I-2

**3.1. Specifications and Modeling Exercise I-2.** Exercise I-2 [2, Chapter 3] proposes uncertainty propagation of the input parameters through the lattice physics to output variables for different Light Water Reactors (LWRs). Here, only the first one of three proposed test problems regarding PWR geometry is carried out. It consists in propagating the cross section uncertainties in a 2D fuel assembly model with reflective boundary conditions which will be used later as the standard model for fuel assembly cross-section generation in PWR core analysis.

The specifications of the fuel assembly are given in [1, Section 3.2]. It is a 15 × 15 TMI fuel assembly model which contains gadolinia pins as burnable poison. Also, the specifications of the control rods are found there. The definition of the pin cell is the same as used in Exercise I-1 [1, Section 2.4]. The fuel assembly configuration is presented in Figure 1(a) for the unrodded case and in Figure 1(b) for the rodded case. The fuel pins are in blue, the gadolinia pins in light blue, the control rods in green, cladding in yellow, and water in red.

The criticality calculations for the 15 × 15 TMI fuel assembly are carried out at Hot Zero Power (HZZP) and at Hot Full Power (HFP) conditions for both cases, unrodded and rodded, together with uncertainty quantification on  $k_{\text{eff}}$  due to the cross section uncertainties.

**3.1.1. SCALE-6.1.** For the criticality calculations with sensitivity analysis and uncertainty quantification of SCALE-6.1, the TSUNAMI-2D sequence is chosen. There, the NEWT

TABLE 2:  $k_{\text{eff}}$  values for the different states of the  $15 \times 15$  TMI fuel assembly obtained by MCNPX-2.7e and SCALE-6.1, taking the SCALE results as the reference for the difference in pcm.

	Unrodded		Rodded	
	HZP	HFP	HZP	HFP
MCNPX-2.7e	$1.41768 \pm 16$ pcm	$1.40441 \pm 16$ pcm	$1.07386 \pm 22$ pcm	$1.06146 \pm 25$ pcm
SCALE-6.1	1.41227	1.39802	1.07160	1.05834
Difference	383 pcm	457 pcm	211 pcm	295 pcm

TABLE 3: Comparison of the uncertainty contribution to  $k_{\text{eff}}$  of each variance-covariance matrix of the reaction pair presented in the first two columns given in rel.std.dev.(%) calculated by SCALE-6.1 and MCNPX-2.7e for unrodded case.

(a) HZP

Reaction	Reaction	MCNP-2.7e	SCALE-6.1	Ratio
$^{238}\text{U}$ ( $n, \gamma$ )	$^{238}\text{U}$ ( $n, \gamma$ )	0.23145	0.24582	0.942
$^{235}\text{U}$ ( $n, \gamma$ )	$^{235}\text{U}$ ( $n, \gamma$ )	0.19674	0.19970	0.985
$^{235}\text{U}$ ( $n, f$ )	$^{235}\text{U}$ ( $n, \gamma$ )	0.10733	0.10895	0.985
$^{238}\text{U}$ ( $n, n'$ )	$^{238}\text{U}$ ( $n, n'$ )	0.09078	0.09455	0.960
$^{235}\text{U}$ ( $n, f$ )	$^{235}\text{U}$ ( $n, f$ )	0.08368	0.08500	0.985
$^{238}\text{U}$ ( $n, f$ )	$^{238}\text{U}$ ( $n, f$ )	0.01363	0.01366	0.998
$^{238}\text{U}$ ( $n, n$ )	$^{238}\text{U}$ ( $n, \gamma$ )	<b>0.01215</b>	<b>-0.00474</b>	<b>-2.566</b>
$^{238}\text{U}$ ( $n, n$ )	$^{238}\text{U}$ ( $n, n$ )	<b>0.01185</b>	<b>0.02265</b>	<b>0.523</b>
$^{157}\text{Gd}$ ( $n, \gamma$ )	$^{157}\text{Gd}$ ( $n, \gamma$ )	0.00645	0.00683	0.945
$^{155}\text{Gd}$ ( $n, \gamma$ )	$^{155}\text{Gd}$ ( $n, \gamma$ )	0.00476	0.00488	0.977
$^{238}\text{U}$ ( $n, f$ )	$^{238}\text{U}$ ( $n, \gamma$ )	0.00246	0.00257	0.957
$^{156}\text{Gd}$ ( $n, \gamma$ )	$^{156}\text{Gd}$ ( $n, \gamma$ )	0.00129	0.00128	1.006
$^{238}\text{U}$ ( $n, n$ )	$^{238}\text{U}$ ( $n, f$ )	<b>-0.00116</b>	<b>0.00065</b>	<b>-1.787</b>
$^{238}\text{U}$ ( $n, n$ )	$^{238}\text{U}$ ( $n, n'$ )	-0.00476	-0.00504	0.944
	Total	0.34577	0.35940	0.962
$^{235}\text{U}$ $\bar{\nu}$	$^{235}\text{U}$ $\bar{\nu}$	—	0.26937	
$^{235}\text{U}$ $\chi$	$^{235}\text{U}$ $\chi$	—	0.08531	
	Total SCALE		0.46441	0.774

(b) HFP

Reaction	Reaction	MCNP-2.7e	SCALE-6.1	Ratio
$^{238}\text{U}$ ( $n, \gamma$ )	$^{238}\text{U}$ ( $n, \gamma$ )	0.23793	0.25293	0.941
$^{235}\text{U}$ ( $n, \gamma$ )	$^{235}\text{U}$ ( $n, \gamma$ )	0.19738	0.20025	0.986
$^{235}\text{U}$ ( $n, f$ )	$^{235}\text{U}$ ( $n, \gamma$ )	0.10697	0.10860	0.985
$^{238}\text{U}$ ( $n, n'$ )	$^{238}\text{U}$ ( $n, n'$ )	0.09808	0.09962	0.985
$^{235}\text{U}$ ( $n, f$ )	$^{235}\text{U}$ ( $n, f$ )	0.08333	0.08470	0.984
$^{238}\text{U}$ ( $n, n$ )	$^{238}\text{U}$ ( $n, n'$ )	<b>0.02302</b>	<b>-0.00562</b>	<b>-4.093</b>
$^{238}\text{U}$ ( $n, n$ )	$^{238}\text{U}$ ( $n, \gamma$ )	0.01634	0.00943	1.732
$^{238}\text{U}$ ( $n, f$ )	$^{238}\text{U}$ ( $n, f$ )	0.01407	0.01412	0.997
$^{238}\text{U}$ ( $n, n$ )	$^{238}\text{U}$ ( $n, n$ )	<b>0.01358</b>	<b>0.02520</b>	<b>0.539</b>
$^{157}\text{Gd}$ ( $n, \gamma$ )	$^{157}\text{Gd}$ ( $n, \gamma$ )	0.00653	0.00693	0.943
$^{155}\text{Gd}$ ( $n, \gamma$ )	$^{155}\text{Gd}$ ( $n, \gamma$ )	0.00480	0.00496	0.967
$^{238}\text{U}$ ( $n, f$ )	$^{238}\text{U}$ ( $n, \gamma$ )	0.00259	0.00272	0.953
$^{156}\text{Gd}$ ( $n, \gamma$ )	$^{156}\text{Gd}$ ( $n, \gamma$ )	0.00135	0.00132	1.023
$^{238}\text{U}$ ( $n, n$ )	$^{238}\text{U}$ ( $n, f$ )	<b>-0.00137</b>	<b>0.00070</b>	<b>-1.959</b>
	Total	0.35331	0.36607	0.965
$^{235}\text{U}$ $\bar{\nu}$	$^{235}\text{U}$ $\bar{\nu}$	—	0.26834	
$^{235}\text{U}$ $\chi$	$^{235}\text{U}$ $\chi$	—	0.08823	
	Total SCALE		0.46984	0.779

TABLE 4: Comparison of the uncertainty contribution to  $k_{\text{eff}}$  of each variance-covariance matrix of the reaction pair presented in the first two columns given in rel.std.dev.(%) calculated by SCALE-6.1 and MCNPX-2.7e for rodged case.

(a) HZP						
Reaction		Reaction		MCNP-2.7e	SCALE-6.1	Ratio
$^{238}\text{U}$	( $n, \gamma$ )	$^{238}\text{U}$	( $n, \gamma$ )	0.21670	0.23086	0.939
$^{235}\text{U}$	( $n, \gamma$ )	$^{235}\text{U}$	( $n, \gamma$ )	0.17403	0.17602	0.989
$^{238}\text{U}$	( $n, n'$ )	$^{238}\text{U}$	( $n, n'$ )	0.16286	0.16089	1.012
$^{235}\text{U}$	( $n, f$ )	$^{235}\text{U}$	( $n, \gamma$ )	0.11027	0.11189	0.985
$^{235}\text{U}$	( $n, f$ )	$^{235}\text{U}$	( $n, f$ )	0.10708	0.10936	0.979
$^{109}\text{Ag}$	( $n, \gamma$ )	$^{109}\text{Ag}$	( $n, \gamma$ )	0.07569	0.07831	0.967
$^{107}\text{Ag}$	( $n, \gamma$ )	$^{107}\text{Ag}$	( $n, \gamma$ )	0.06786	0.06965	0.974
$^{115}\text{In}$	( $n, \gamma$ )	$^{115}\text{In}$	( $n, \gamma$ )	0.03640	0.03627	1.003
$^{238}\text{U}$	( $n, f$ )	$^{238}\text{U}$	( $n, f$ )	0.02242	0.02237	1.002
$^{238}\text{U}$	( $n, n$ )	$^{238}\text{U}$	( $n, \gamma$ )	<b>0.01812</b>	<b>0.01185</b>	<b>1.529</b>
$^{238}\text{U}$	( $n, n$ )	$^{238}\text{U}$	( $n, n$ )	<b>0.01357</b>	<b>0.02340</b>	<b>0.580</b>
$^{157}\text{Gd}$	( $n, \gamma$ )	$^{157}\text{Gd}$	( $n, \gamma$ )	0.00747	0.00817	0.915
$^{113}\text{Cd}$	( $n, \gamma$ )	$^{113}\text{Cd}$	( $n, \gamma$ )	0.00744	0.00738	1.008
$^{155}\text{Gd}$	( $n, \gamma$ )	$^{155}\text{Gd}$	( $n, \gamma$ )	0.00556	0.00584	0.952
$^{107}\text{Ag}$	( $n, n$ )	$^{107}\text{Ag}$	( $n, n$ )	<b>0.00347</b>	<b>0.00042</b>	<b>8.193</b>
$^{238}\text{U}$	( $n, f$ )	$^{238}\text{U}$	( $n, \gamma$ )	0.00322	0.00337	0.955
$^{115}\text{In}$	( $n, n$ )	$^{115}\text{In}$	( $n, n$ )	<b>0.00310</b>	<b>0.00164</b>	<b>1.888</b>
$^{156}\text{Gd}$	( $n, \gamma$ )	$^{156}\text{Gd}$	( $n, \gamma$ )	0.00162	0.00154	1.050
$^{109}\text{Ag}$	( $n, n$ )	$^{109}\text{Ag}$	( $n, n$ )	<b>0.00145</b>	<b>0.00031</b>	<b>4.695</b>
$^{238}\text{U}$	( $n, n$ )	$^{238}\text{U}$	( $n, f$ )	<b>-0.00139</b>	<b>0.00088</b>	<b>-1.579</b>
$^{238}\text{U}$	( $n, n$ )	$^{238}\text{U}$	( $n, n'$ )	<b>-0.03164</b>	<b>-0.00757</b>	<b>4.178</b>
		Total		0.37315	0.38518	0.969
$^{235}\text{U}$	$\bar{\nu}$	$^{235}\text{U}$	$\bar{\nu}$	—	0.25594	
$^{235}\text{U}$	$\chi$	$^{235}\text{U}$	$\chi$	—	0.13360	
Total SCALE					0.49199	0.783
(b) HFP						
Reaction		Reaction		MCNP-2.7e	SCALE-6.1	Ratio
$^{238}\text{U}$	( $n, \gamma$ )	$^{238}\text{U}$	( $n, \gamma$ )	0.22281	0.23783	0.937
$^{235}\text{U}$	( $n, \gamma$ )	$^{235}\text{U}$	( $n, \gamma$ )	0.17426	0.17639	0.988
$^{238}\text{U}$	( $n, n'$ )	$^{238}\text{U}$	( $n, n'$ )	0.16419	0.16909	0.971
$^{235}\text{U}$	( $n, f$ )	$^{235}\text{U}$	( $n, \gamma$ )	0.10985	0.11143	0.986
$^{235}\text{U}$	( $n, f$ )	$^{235}\text{U}$	( $n, f$ )	0.10703	0.10925	0.980
$^{109}\text{Ag}$	( $n, \gamma$ )	$^{109}\text{Ag}$	( $n, \gamma$ )	0.07689	0.07969	0.965
$^{107}\text{Ag}$	( $n, \gamma$ )	$^{107}\text{Ag}$	( $n, \gamma$ )	0.06925	0.07100	0.975
$^{115}\text{In}$	( $n, \gamma$ )	$^{115}\text{In}$	( $n, \gamma$ )	0.03707	0.03690	1.005
$^{238}\text{U}$	( $n, f$ )	$^{238}\text{U}$	( $n, f$ )	0.02313	0.02310	1.001
$^{238}\text{U}$	( $n, n$ )	$^{238}\text{U}$	( $n, \gamma$ )	<b>0.02141</b>	<b>0.01592</b>	<b>1.345</b>
$^{238}\text{U}$	( $n, n$ )	$^{238}\text{U}$	( $n, n'$ )	<b>0.01567</b>	<b>-0.00854</b>	<b>-1.835</b>
$^{238}\text{U}$	( $n, n$ )	$^{238}\text{U}$	( $n, n$ )	<b>0.01276</b>	<b>0.02589</b>	<b>0.493</b>
$^{157}\text{Gd}$	( $n, \gamma$ )	$^{157}\text{Gd}$	( $n, \gamma$ )	0.00770	0.00825	0.934
$^{113}\text{Cd}$	( $n, \gamma$ )	$^{113}\text{Cd}$	( $n, \gamma$ )	0.00762	0.00748	1.019
$^{107}\text{Ag}$	( $n, n$ )	$^{107}\text{Ag}$	( $n, n$ )	<b>0.00587</b>	<b>0.00043</b>	<b>13.758</b>
$^{155}\text{Gd}$	( $n, \gamma$ )	$^{155}\text{Gd}$	( $n, \gamma$ )	0.00569	0.00592	0.961
$^{109}\text{Ag}$	( $n, n$ )	$^{109}\text{Ag}$	( $n, n$ )	<b>0.00450</b>	<b>0.00031</b>	<b>14.391</b>
$^{238}\text{U}$	( $n, f$ )	$^{238}\text{U}$	( $n, \gamma$ )	0.00341	0.00356	0.958

(b) Continued.

Reaction		Reaction		MCNP-2.7e	SCALE-6.1	Ratio
$^{115}\text{In}$	$(n, n)$	$^{115}\text{In}$	$(n, n)$	<b>0.00262</b>	<b>0.00167</b>	<b>1.569</b>
$^{156}\text{Gd}$	$(n, \gamma)$	$^{156}\text{Gd}$	$(n, \gamma)$	0.00166	0.00159	1.048
$^{238}\text{U}$	$(n, n)$	$^{238}\text{U}$	$(n, f)$	<b>-0.00151</b>	<b>0.00094</b>	<b>-1.599</b>
Total				0.37973	0.39380	0.964
$^{235}\text{U}$	$\bar{\nu}$	$^{235}\text{U}$	$\bar{\nu}$	—	0.25451	
$^{235}\text{U}$	$\chi$	$^{235}\text{U}$	$\chi$	—	0.13788	
Total SCALE					0.49966	0.788

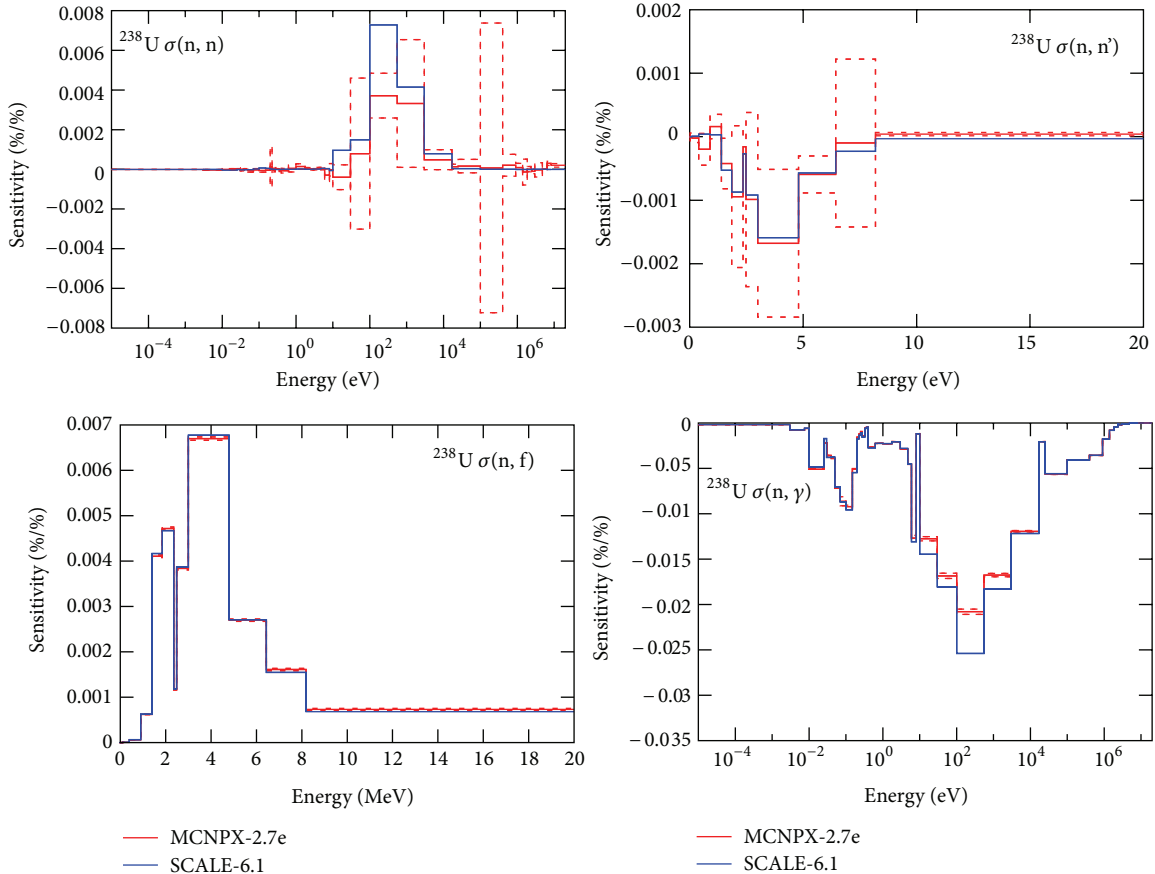


FIGURE 2: Sensitivity profiles of  $^{238}\text{U}$  reaction cross sections calculated by MCNPX-2.7e and SCALE-6.1 for unrodded case at HZP.

module [2, Section F21] is used for solving the forward and adjoint transport problems. NEWT is an algorithm for two-dimensional analysis in nonorthogonal geometries combining a step characteristics approach plus discrete ordinates. The 238 energy group cross section library of the ENDF/B-VII.0 [2, Section M4] is used with NEWT (using the keyword v7-238). Then, the SAMS module [2, Section F22] is invoked to calculate the sensitivity coefficients in 238 energy groups. Because SCALE-6.1 provides a set of covariance matrices to perform the uncertainty quantification, “SCALE Nuclear Data Covariance Library” [2, Section M19] that is given in 44 energy group [2, Table M4.2.1], the sensitivity profiles are collapsed from 238 to 44 energy group structure inside SAMS, but the latter profile is not supplied to the user. But collapsing to 44 energy groups can be done with the VIBE tool [11].

3.1.2. *MCNPX-2.7e*. For the criticality calculations of MCNPX-2.7e, the KCODE card [3, Section 5.2.2] is applied and activated only for neutrons. The ENDF/B-VII.0 cross section library is used, taking the processed cross section files for MCNPX from [12]. Because the cross section library used for  $^{107}\text{Ag}$  in [12] comes from JEFF-3.1.1, the  $^{107}\text{Ag}$  ENDF/B-VII.0 cross section file is processed and included in the set of cross section libraries used by MCNPX-2.7e to substitute the previous one.

After preparing the inputs for the criticality calculations, PERT cards are added in order to calculate the sensitivity coefficients of  $k_{\text{eff}}$  to the reaction cross sections given in Table 1.

To calculate the same sensitivity coefficients as SCALE-6.1, the keyword that sets to which reaction cross section is

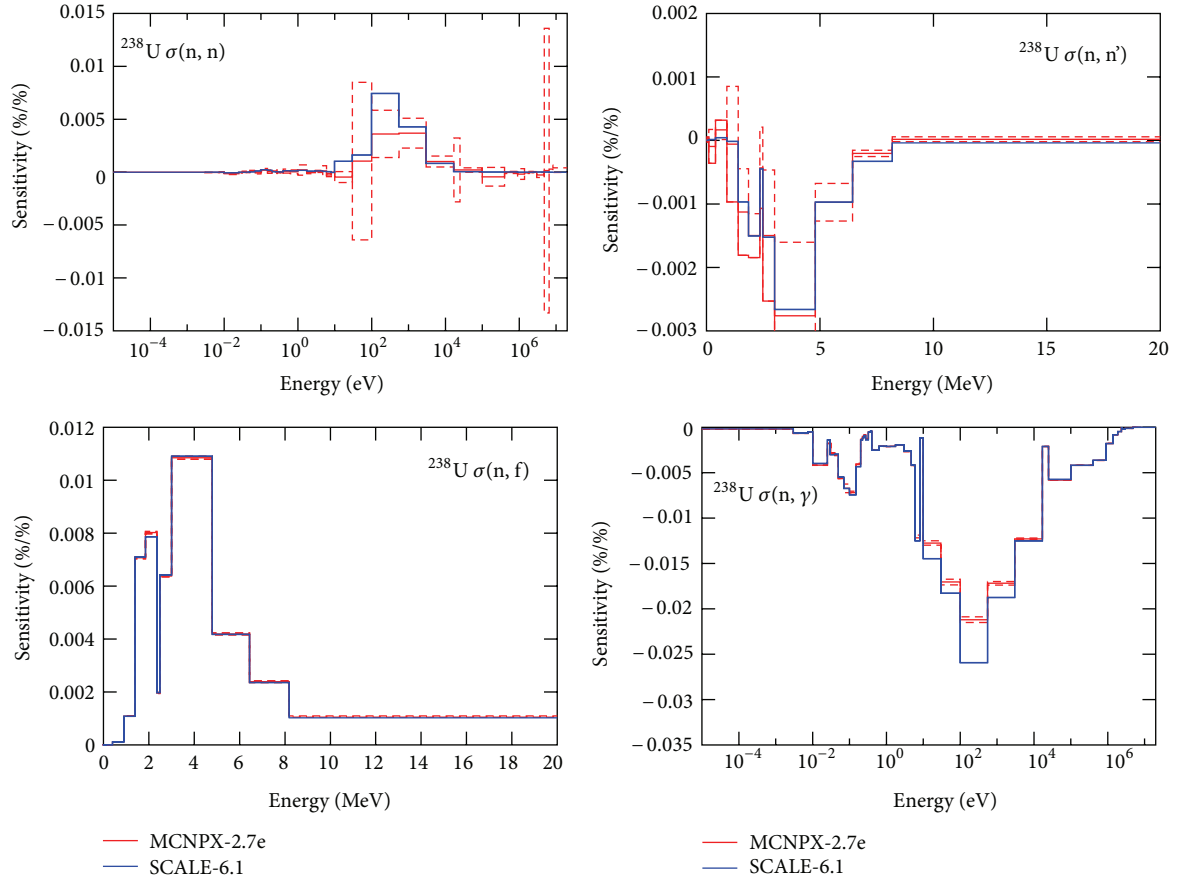


FIGURE 3: Sensitivity profiles of  $^{238}\text{U}$  reaction cross sections calculated by MCNPX-2.7e and SCALE-6.1 for rodded case at HZP.

assigned the perturbation on the  $k_{\text{eff}}$ , RXN, is specified taking into account the equivalences between RXN and the identifiers of the SCALE reaction cross sections presented in [4, Table V]. In order to compare the sensitivity profiles provided by SCALE-6.1 and MCNPX-2.7e, the PERT cards should use the same 44 energy group structure used by SCALE-6.1.  $p_x$  is set to 100 to calculate the sensitivity coefficients by (10).

Once the sensitivity coefficients are calculated, the “SCALE Nuclear Data Covariance Library” is processed by the VIEWCVX code (provided as a module of ERRORJ code [13]) to obtain the relative covariance matrix of the reactions given in Table 1. Then, the “sandwich formula” given in (6) is calculated, obtaining the uncertainty on  $k_{\text{eff}}$ .

**3.2. Comparison of  $k_{\text{eff}}$  Values.** The  $k_{\text{eff}}$  values are presented in Table 2. MCNPX-2.7e provides larger values than SCALE-6.1 for all cases, but the difference between codes is reduced when going from unrodded to rodded case. These differences appear due to the use of multigroup cross-sections or continuous energy cross-sections, the different methodologies used in each code to solve the neutron transport equations, and the different processing codes used for preparing the cross section data files: NJOY v99.364 for MCNPX-2.7e and AMPX for SCALE-6.1.

**3.3. Comparison of the  $k_{\text{eff}}$  Uncertainty.** The uncertainty results obtained by SCALE-6.1 and MCNPX-2.7e are presented in the tables: for the unrodded fuel assembly at HZP (Table 3(a)), and at HFP (Table 3(b)); for the rodded case at HZP (Table 4(a)), and at HFP (Table 4(b)). These tables present in the first two columns the reaction pair of the variance-covariance matrix that contributes to the  $k_{\text{eff}}$  uncertainty. The contribution is given in rel.std.dev.(%) in the third and fourth columns. Only the contributions with  $|\text{rel.std.dev.}(\%)| > 0.001$  are presented, sorted in descending order. The square root of the sum of the square rel.std.dev. provides the total uncertainty in  $k_{\text{eff}}$  as rel.std.dev.(%). The ratio between MCNPX-2.7e and SCALE-6.1 values is given for each contribution and for the total values. Two more rows are added to show the importance of the  $^{235}\text{U } \bar{\nu}$  and  $^{235}\text{U } \chi$  uncertainty contributions to  $k_{\text{eff}}$ , calculated by SCALE-6.1. The last row shows the total uncertainty given by SCALE-6.1, taking into account all the possible reactions for which there is uncertainty information, and the ratio to the total uncertainty provided by MCNPX-2.7e.

There is a good agreement between MCNPX-2.7e and SCALE-6.1 results except when the  $(n, n)$  reaction cross section is involved. There is a contribution in the HZP unrodded case in which the  $(n, n)$  reaction is involved and both codes remain in good agreement: the  $^{238}\text{U } (n, n)$ - $^{238}\text{U}$

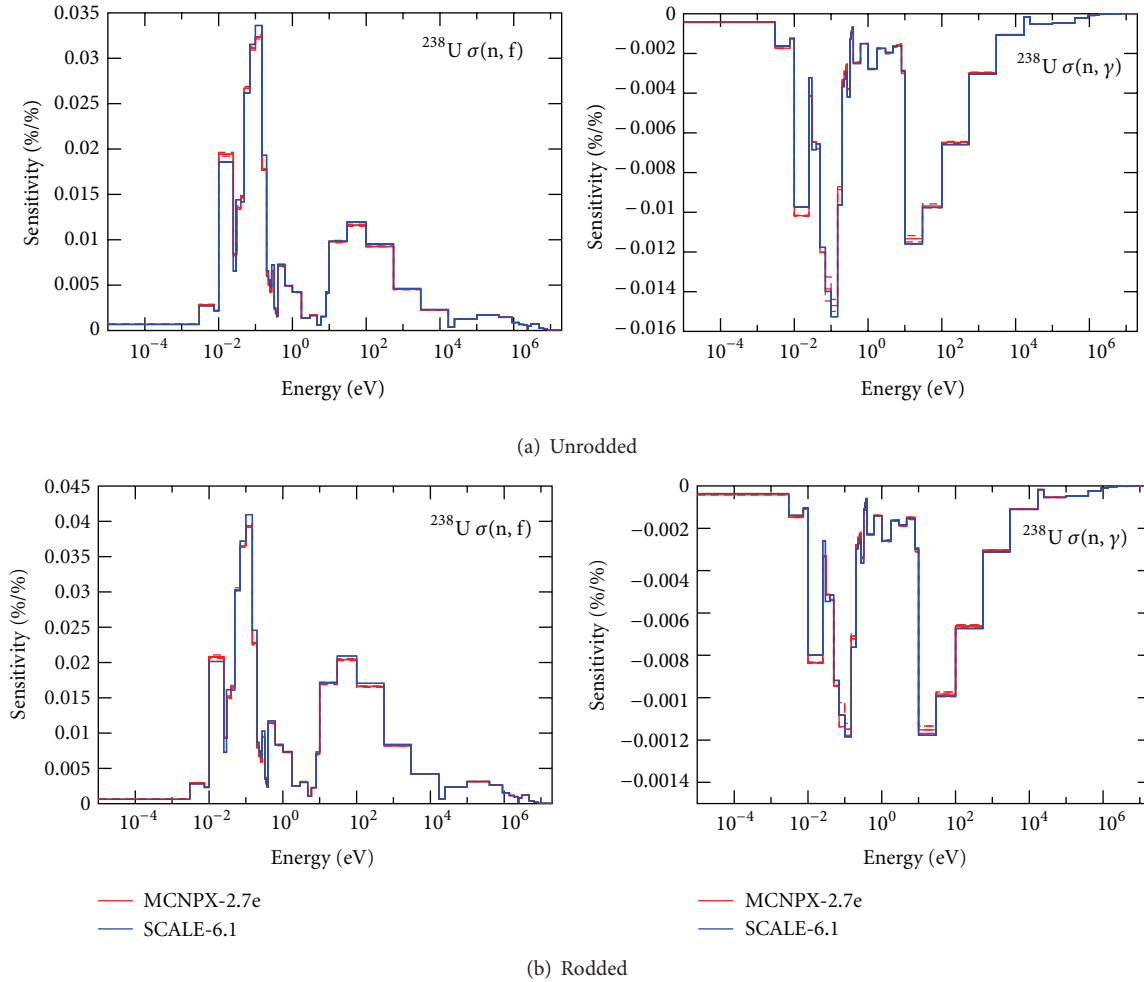


FIGURE 4: Sensitivity profiles of  $^{238}\text{U}$  reaction cross sections calculated by MCNPX-2.7e and SCALE-6.1 for unrodded and rodded cases at HZP.

$(n, n')$  covariance matrix contribution. But this result is obtained by chance, because as showed later, there are large differences in the  $^{238}\text{U}$   $(n, n)$  sensitivity profile between both codes, while for the  $^{238}\text{U}$   $(n, n')$  sensitivity profile there is almost no difference. Therefore, after applying the “sandwich formula,” the contribution given by each code is almost the same due to the combination of the differences in the  $^{238}\text{U}$   $(n, n)$  sensitivity profile.

However, the  $(n, n)$  reactions are included in the total values given by MCNPX; they have no impact because their contribution to the total is negligible.

It is necessary to implement more PERT cards in MCNPX-2.7e, because only with the ones calculated, the total uncertainty in the  $k_{\text{eff}}$  is being underestimated around a 23%. This 23% comes mainly because MCNPX-2.7e is not able to calculate the sensitivities to  $^{235}\text{U}$   $\bar{\nu}$  and  $^{235}\text{U}$   $\chi$  yet. But this capability could be implemented as presented in [14].

The differences between HZP and HFP are explained later through the comparison of the sensitivity profiles, because the variance-covariance matrices used in the “sandwich formula” do not change between cases.

**3.4. Comparison of Sensitivity Profiles.** The sensitivity profiles of  $^{238}\text{U}$  reaction cross sections calculated by MCNPX-2.7e and SCALE-6.1 are presented in Figures 2 and 3, and for  $^{235}\text{U}$  reaction cross sections in Figure 4, both for unrodded and rodded cases at HZP. MCNPX values are given in red, with dashed lines for their statistical uncertainty because of the Monte Carlo approach of solving the transport problem, and SCALE ones are in blue.

There is good agreement between all reaction cross sections except for  $(n, n)$ . Special remark should be done for the large statistical uncertainty on the  $(n, n')$  reaction while its mean value remains in good agreement with the SCALE-6.1 values. For the other isotope-reaction cross sections, the same trend is observed: good agreement for all reaction cross section except for the  $(n, n)$  reaction. These kinds of differences in  $(n, n)$  reaction were found before in [4], where the scattering reactions did not agree well with the SCALE results because of the deficiencies of the Differences Operator Technique used in the PERT card.

The temperature effect on the sensitivity profiles is analysed. Only for the unrodded case there is a noticeable change

TABLE 5: Largest integrated sensitivity coefficients of the reaction cross sections for the unrodded case at HZP and HFP sorted in descending order provided by SCALE-6.1.

(a) HZP		
Reaction		Int.sen.coef.
$^{235}\text{U}$	$\bar{\nu}$	$9.4533E - 01$
$^{235}\text{U}$	$(n, f)$	$2.7342E - 01$
$^{238}\text{U}$	$(n, \gamma)$	$-1.9175E - 01$
$^1\text{H}$	$(n, n)$	$1.5701E - 01$
$^{235}\text{U}$	$(n, \gamma)$	$-1.4756E - 01$
$^{238}\text{U}$	$\bar{\nu}$	$5.4659E - 02$
$^1\text{H}$	$(n, \gamma)$	$-4.5765E - 02$
$^{238}\text{U}$	$(n, f)$	$2.6307E - 02$
$^{238}\text{U}$	$(n, n)$	$1.4825E - 02$
(b) HFP		
Reaction		Int.sen.coef.
$^{235}\text{U}$	$\bar{\nu}$	$9.4404E - 01$
$^{235}\text{U}$	$(n, f)$	$2.7389E - 01$
$^{238}\text{U}$	$(n, \gamma)$	$-1.9659E - 01$
$^1\text{H}$	$(n, n)$	$1.6365E - 01$
$^{235}\text{U}$	$(n, \gamma)$	$-1.4806E - 01$
$^{238}\text{U}$	$\bar{\nu}$	$5.5948E - 02$
$^1\text{H}$	$(n, \gamma)$	$-4.4564E - 02$
$^{238}\text{U}$	$(n, f)$	$2.7192E - 02$
$^{238}\text{U}$	$(n, n)$	$1.5870E - 02$

in the  $^{238}\text{U}(n, \gamma)$  sensitivity profile; the sensitivity coefficients of the low energy groups are increased when going from HZP to HFP due to the Doppler broadening.

The effect of the control rods can be observed comparing Figures 2 (unrodded) and 3 (rodded). The  $^{238}\text{U}(n, f)$  and  $(n, n')$  reactions are affected: the sensitivity coefficients of the low energy groups are increased when going from unrodded to rodded case. The  $^{157}\text{Gd}(n, \gamma)$  sensitivity coefficients follow the same trend: they are increased at low energies. The effect on  $^{235}\text{U}$  reactions can be seen comparing Figures 4(a) and 4(b). The  $^{235}\text{U}(n, f)$  sensitivity coefficients are increased in the whole range while the  $^{235}\text{U}(n, \gamma)$  ones are decreased only at low energies, when changing from unrodded to rodded configuration. These changes provoke the variations observed in the contributions of these reactions to the  $k_{\text{eff}}$  uncertainty.

Another source of difference, apart from the methodology used by each code to calculate the sensitivity coefficients, is that SCALE-6.1 provides the sensitivity profiles in 238 energy groups, while for MCNPX-2.7e the sensitivity profiles are calculated in 44 energy groups. Therefore, the energy group structure could lead to differences in between both codes.

**3.5. Ranking the Importance of the Reactions.** SCALE-6.1 provides a useful result: the integrated sensitivity coefficients of every reaction involved in the criticality calculations. It is the sum of the sensitivity coefficients over all energy groups

TABLE 6: Largest integrated sensitivity coefficients of the reaction cross sections for the rodded case at HZP and HFP sorted in descending order provided by SCALE-6.1.

(a) Rodded at HZP		
Reaction		Int.sen.coef.
$^{235}\text{U}$	$\bar{\nu}$	$9.2720E - 01$
$^{235}\text{U}$	$(n, f)$	$3.6753E - 01$
$^1\text{H}$	$(n, n)$	$2.3743E - 01$
$^{238}\text{U}$	$(n, \gamma)$	$-1.8097E - 01$
$^{235}\text{U}$	$(n, \gamma)$	$-1.2798E - 01$
$^{238}\text{U}$	$\bar{\nu}$	$7.1728E - 02$
$^{238}\text{U}$	$(n, f)$	$4.3054E - 02$
$^1\text{H}$	$(n, \gamma)$	$-3.3060E - 02$
$^{109}\text{Ag}$	$(n, \gamma)$	$-2.1940E - 02$
$^{238}\text{U}$	$(n, n)$	$1.6606E - 02$
$^{107}\text{Ag}$	$(n, \gamma)$	$-1.3914E - 02$
$^{115}\text{In}$	$(n, \gamma)$	$-1.2778E - 02$
(b) Rodded at HFP		
Reaction		Int.sen.coef.
$^{235}\text{U}$	$\bar{\nu}$	$9.2540E - 01$
$^{235}\text{U}$	$(n, f)$	$3.6931E - 01$
$^1\text{H}$	$(n, n)$	$2.4283E - 01$
$^{238}\text{U}$	$(n, \gamma)$	$-1.8549E - 01$
$^{235}\text{U}$	$(n, \gamma)$	$-1.2804E - 01$
$^{238}\text{U}$	$\bar{\nu}$	$7.3537E - 02$
$^{238}\text{U}$	$(n, f)$	$4.4462E - 02$
$^1\text{H}$	$(n, \gamma)$	$-3.2066E - 02$
$^{109}\text{Ag}$	$(n, \gamma)$	$-2.2270E - 02$
$^{238}\text{U}$	$(n, n)$	$1.7615E - 02$
$^{107}\text{Ag}$	$(n, \gamma)$	$-1.4158E - 02$
$^{115}\text{In}$	$(n, \gamma)$	$-1.2976E - 02$

of the same reaction. This value reflects how sensitive is the  $k_{\text{eff}}$  to this reaction. Then, the reactions can be ranked as a function of their relevance to  $k_{\text{eff}}$  with their integrated sensitivity coefficient.

With the sensitivity profiles provided by MCNPX-2.7e, the integrated sensitivity values can be calculated. Because comparing the integrated sensitivity coefficients is equivalent to compare sensitivity profiles, only the SCALE-6.1 results are shown in this section.

Table 5 presents the integrated sensitivity values for the unrodded case at HZP and HFP, while Table 6 shows the results for the rodded case at HZP and HFP. The most relevant reactions are the ones for  $^{235}\text{U}$ ,  $^{238}\text{U}$ , and  $^1\text{H}$ . In the rodded case, the  $(n, \gamma)$  reactions of  $^{107}\text{Ag}$ ,  $^{109}\text{Ag}$ , and  $^{115}\text{In}$  arise as important.

## 4. Conclusions

The propagation of cross section uncertainties in criticality calculations for a  $15 \times 15$  TMI fuel assembly in two different configurations, unrodded and rodded, at two different states, HZP and HFP, has been performed using two

different approaches carried out by each of the codes used: (i) MCNPX-2.7e—Differential Operator Technique and (ii) SCALE-6.1—Adjoint-Weighted Technique.

The two approaches have been presented and compared through this exercise. The  $k_{\text{eff}}$  and its uncertainty due to cross-section uncertainties have been calculated, distinguishing between its different contributors. The most important ones for this exercise are  $^{235}\text{U}-\bar{\nu}$ ,  $\chi$ ,  $(n, f)$ ,  $(n, \gamma)$ ,  $^{238}\text{U}-(n, n')$ ,  $(n, f)$ ,  $(n, \gamma)$ , and the covariance  $^{235}\text{U}(n, f)-^{235}\text{U}(n, \gamma)$ . Additionally, the sensitivity coefficients and the integrated sensitivity coefficients have been calculated and compared.

In general, both approaches/codes are in good agreement, in spite of the differences in the  $k_{\text{eff}}$  values. There are only two exceptions observed: one is for the contribution of the  $(n, n)$  reaction cross sections which are not properly calculated by MCNPX-2.7e because the deficiencies of the PERT card to calculate the  $(n, n)$  sensitivity coefficients, and the another is for the contribution of  $^{238}\text{U}(n, n)-(n, n')$  covariance whose agreement between codes comes by chance because of the combination of the differences in the  $(n, n)$  sensitivity profile. The good agreements between codes are corroborated by the comparison of the sensitivity profiles given by each code.

The inability of calculating the contribution due to  $\bar{\nu}$  and  $\chi$  values makes MCNPX-2.7e to underestimate the uncertainty in  $k_{\text{eff}}$  at least in a 23% compared with SCALE-6.1. It is important to remark that the most relevant reactions are not always the main source of the uncertainty, such as the case of  $^1\text{H}$  which is in the top list of reactions for which  $k_{\text{eff}}$  is sensitive to, but it is not in the list of the most important contributions to the  $k_{\text{eff}}$  uncertainty because of the low uncertainty of its reactions.

Thus, MCNPX-2.7e can deal with the uncertainty quantification problem as SCALE-6.1 does, but improvements should be done in the PERT card capabilities such as the proper calculation of the sensitivity coefficients of  $(n, n)$  reaction cross sections, the inclusion of the perturbation due to the change in the fission source distribution, and the implementation of the perturbation of the  $\bar{\nu}$  and  $\chi$  values.

## Acknowledgments

The research leading to these results has received funding from specific collaborative agreement P110530207 between CSN and UPM in the area of “uncertainty propagation in nuclear criticality safety.” Also, this work is also partially supported by the Spanish Ministry of Education of Spain through the FPU Program for teaching and researching formation under Grant AP2009-1801 for the first author.

## References

- [1] K. Ivanova, M. Avramova, S. Kamerow et al., *Benchmark For Uncertainty Analysis in Modeling (UAM) For Design, Operation and Safety Analysis of LWRs*, NEA/NSC/DOC, 2012.
- [2] Oak Ridge National Laboratory, “SCALE: a comprehensive modeling and simulation suite for nuclear safety analysis and design,” ORNL/TM-2005/39, version 6.1, Radiation Safety Information Computational Center, Oak Ridge National Laboratory as CCC-785, 2011.
- [3] D. B. Pelowitz, “MCNPX user’s manual,” Tech. Rep. LA-CP-07-1473, Los Alamos National Laboratory, 2008.
- [4] J. Favorite, “Eigenvalue sensitivity analysis using the MCNP5 perturbation capability,” in *Proceedings of the Nuclear Criticality Safety Division Topical Meeting on Realism, Robustness and the Nuclear Renaissance*, pp. 245–255, American Nuclear Society, 2009.
- [5] B. C. Kiedrowski and F. B. Brown, “Comparison of the Monte Carlo adjoint-weighted and di perturbation methods,” *Progress in Nuclear Science and Technology*, vol. 2, pp. 836–841, 2011.
- [6] D. G. Cacuci, *Sensitivity and Uncertainty Analysis*, Chapman Hall/CRC, London, UK, 2003.
- [7] Y. Nagaya and F. B. Brown, “Estimation of the change in k-effective due to perturbed fission source distribution in MCNP,” in *Proceedings of the ANS Mathematics & Computation Topical Meeting (M&C '03)*, Gatlinburg, Tenn, USA, 2003.
- [8] Y. Nagaya and F. B. Brown, “Implementation of a method to estimate change in eigenvalue due to perturbed fission source distribution into MCNP,” Tech. Rep. LA-UR-03-1387, Los Alamos National Laboratory, 2003.
- [9] K. Raskach, “An improvement of the monte carlo generalized differential first- and second-order perturbations of fission source,” *Nuclear Science and Engineering*, vol. 162, no. 2, pp. 158–166, 2009.
- [10] J. A. Favorite, “On the accuracy of the differential operator Monte Carlo perturbation method for eigenvalue problems,” Technical Report LA-UR-09-4207, Los Alamos National Laboratory, 2009.
- [11] B. Rearden and R. Lefebvre, “Getting Started with VIBE as a DICE Plug-in Module,” Tech. Rep. ORNL/TM-2010/60, Oak Ridge National Laboratory, 2010.
- [12] T. Viitanen and J. Leppanen, “ZZ SERPENT117-ACELIB, Continuous-energy X-sec lib., radioactive decay, fission yield data for SERPENT in ACE,” Tech. Rep. NEA-1854, 2010.
- [13] G. Chiba, “ERRORJ—a code to process neutron-nuclide reaction cross section covariance, version 2.3,” JAEA-Data/Code 2007-007, Japan Atomic Energy Agency, 2007.
- [14] R. L. Perel, “Sensitivities of  $k_{\text{eff}}$  calculated with Monte-Carlo methods: theory and first results,” Tech. Rep. JEF-DOC-1123, Nuclear Energy Agency, 2005.

## Research Article

# Uncertainty Analysis of Light Water Reactor Fuel Lattices

C. Arenas,<sup>1</sup> R. Bratton,<sup>2</sup> F. Reventos,<sup>1</sup> and K. Ivanov<sup>2</sup>

<sup>1</sup> Department of Physics and Nuclear Engineering, Technical University of Catalonia, 08034 Barcelona, Spain

<sup>2</sup> Department of Mechanical and Nuclear Engineering, The Pennsylvania State University, University Park, PA 16802, USA

Correspondence should be addressed to C. Arenas; [carenas@tinnet.org](mailto:carenas@tinnet.org)

Received 20 August 2012; Accepted 18 November 2012

Academic Editor: Carlo Parisi

Copyright © 2013 C. Arenas et al. This is an open access article distributed under the Creative Commons Attribution License, which permits unrestricted use, distribution, and reproduction in any medium, provided the original work is properly cited.

The study explored the calculation of uncertainty based on available cross-section covariance data and computational tool on fuel lattice levels, which included pin cell and the fuel assembly models. Uncertainty variations due to temperatures changes and different fuel compositions are the main focus of this analysis. Selected assemblies and unit pin cells were analyzed according to the OECD LWR UAM benchmark specifications. Criticality and uncertainty analysis were performed using TSUNAMI-2D sequence in SCALE 6.1. It was found that uncertainties increase with increasing temperature, while  $k_{\text{inf}}$  decreases. This increase in the uncertainty is due to the increase in sensitivity of the largest contributing reaction of uncertainty, namely, the neutron capture reaction  $^{238}\text{U}(n, \gamma)$  due to the Doppler broadening. In addition, three types (UOX, MOX, and UOX-Gd<sub>2</sub>O<sub>3</sub>) of fuel material compositions were analyzed. A remarkable increase in uncertainty in  $k_{\text{inf}}$  was observed for the case of MOX fuel. The increase in uncertainty of  $k_{\text{inf}}$  in MOX fuel was nearly twice the corresponding value in UOX fuel. The neutron-nuclide reaction of  $^{238}\text{U}$ , mainly inelastic scattering ( $n, n'$ ), contributed the most to the uncertainties in the MOX fuel, shifting the neutron spectrum to higher energy compared to the UOX fuel.

## 1. Introduction

The demand for the best estimate calculations in nuclear reactor core modeling and design has increased in recent years. Uncertainty analysis has been highlighted as an important part of the design and safety analysis of modern nuclear reactors. The modeling aspects of uncertainty analysis and sensitivity analysis are to be further developed and validated on scientific grounds in support of their performance. The Organization for Economic Cooperation and Development (OECD)/Nuclear Energy Agency (NEA) initiated the Benchmark for Uncertainty Analysis in Modeling, Design, Operation, and Safety Analysis of Light Water Reactor (OECD LWR UAM benchmark). The general objective of the benchmark is to propagate the uncertainty through complex coupled multiphysics and multiscale simulations. The benchmark is divided into three phases with Phase I highlighting the uncertainty propagation in neutronics calculations, while Phases II and III are focused on uncertainty analysis of reactor core and reactor system, respectively.

In Phase I of the OECD LWR UAM benchmark, the exercises are divided into three parts: cell physics (Exercise I),

lattice physics (Exercise II), and core physics (Exercise III) [1]. This paper will discuss Exercises I and II.

## 2. Uncertainty Calculations

In general, uncertainty is calculated based on covariance matrix and weighting factor coefficients [2]:

$$\Delta^2 = \alpha [\text{cov}] \alpha^T, \quad (1)$$

where  $\alpha$  is the weighting factor matrix,  $\alpha^T$  is the transpose of the weighting factor matrix,  $[\text{cov}]$  is the covariance matrix, and  $\Delta^2$  is the uncertainty.

In order to obtain the uncertainty of the response of interest, which may be the critical eigenvalue, the reactivity difference between two reactor states, or the ratio of reactions rates, sensitivity coefficients (S) are used as weighting factors to the covariance matrix

$$\Delta_{k \text{ eff}}^2 = S [\text{cov}] S^T. \quad (2)$$

**2.1. Covariance Matrix of Nuclear Data.** The evaluation of nuclear data induced uncertainty is possible by the use of nuclear cross-section variance and covariance data. By including the uncertainty or covariance information, the analyst can propagate cross-section data uncertainties through sensitivity studies to the final calculated quantities of interest. The covariance data files provide the estimated variance for the individual data as well as any correlation that may exist. In principle, the covariance matrices can be now self-shielded in the same way as the cross-sections, although in practice this is rarely done. The impact of this treatment on the obtained covariance matrices and their dependence on energy group structure needs to be studied. The SCALE 6.1/TSUNAMI-2D [3] sequence uses a completely different approach to address the impact of self-shielding in sensitivity and uncertainty analysis. Rather than modifying the covariance data, the sensitivity coefficients are modified to include the “implicit effects” of perturbations in the group cross-sections caused by perturbations in self-shielding. Implicit effects account for impact of resonance self-shielding on sensitivity coefficients and uncertainty evaluations. This allows the use of unshielded covariance data. Treatment of implicit effects is a standard part of the TSUNAMI-2D analysis and has been shown to be a significant sensitivity component in some cases.

The SCALE 6.1 covariance library data corresponds also to 44-group relative uncertainties assembled from a variety of sources, including evaluations from ENDF/B-VII, ENDF/B-VI, JENDL-3.3, and more than 300 approximated uncertainties from a collaborative project performed by Brookhaven National Laboratory (BNL), Los Alamos National Laboratory (LANL), and Oak Ridge National Laboratory (ORNL).

It is assumed that the same relative (rather than absolute) uncertainties can be applied to all cross-section libraries, even if these are not strictly consistent with the nuclear data evaluations. In addition, the assumption that there are no covariance correlations between energy groups is applied [1].

**2.2. Sensitivity Coefficients.** For light water reactors, two components of sensitivity coefficient are needed. Explicit sensitivity represents the sensitivity of the calculated  $k_{\text{inf}}$  to components of the group-wise cross-section data. Implicit sensitivity addresses the impact of resonance self-shielding effect in a system. Together, the explicit and implicit sensitivity are combined to produce the total sensitivity:

$$S_{\text{Total}} = S_{\text{Explicit}} + S_{\text{Implicit}}. \quad (3)$$

**2.3. Computational Tools.** The SCALE 6.1/TSUNAMI-2D sequence is used to perform the study. First, the ENDF/B-VII.0 based 238-group microscopic cross-section data library is processed using BONAMIST and CENTRM/PMC. Next, forward and adjoint calculations are performed using NEWT, a 2D transport solver. Finally, sensitivity coefficients are calculated, and uncertainty data is generated by SAMS using the default covariance data library in 44 groups (44groupcov).

The SCALE 6.1 sensitivity and uncertainty methodology is based on the first-order perturbation theory to calculate response sensitivity coefficients, which are then folded with nuclear data covariances to obtain the response uncertainty.

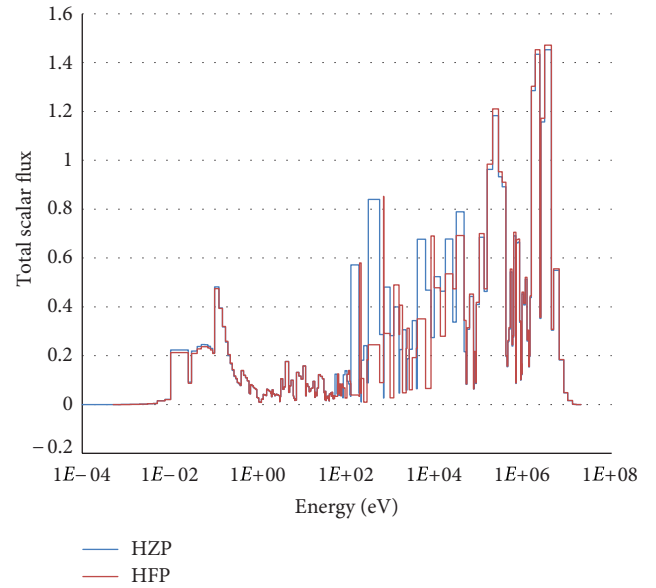


FIGURE 1: The neutron flux of PWR unit cell at two different operating conditions.

TSUNAMI-2D applies the generalized perturbation theory (GPT) to generate uncertainties associated with the few-group assembly homogenized neutron cross-section data [2].

### 3. Temperature Sensitivity Study

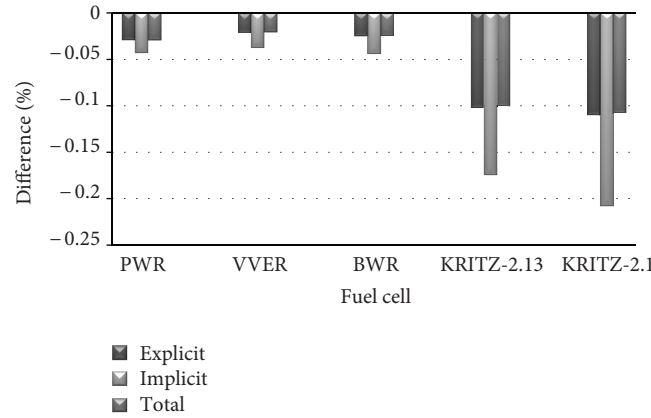
The study begins with specification of fuel pin cells of three light water reactor types and two critical experiments provided by the OECD LWR UAM benchmark within Exercise I-1 [4]. This exercise evaluates the multigroup microscopic cross-section uncertainties associated with multigroup cross-section libraries used as an input in lattice physics codes. The details of the specifications are available in [1].  $k_{\text{inf}}$  and propagated cross-section uncertainties obtained for different pin cell test problems are shown in Table 1.

Observations of the results showed that  $k_{\text{inf}}$  reduces as the temperature rises. This is due to the effect of Doppler broadening and the reduction in moderation due to the changing moderator density. The uncertainty in  $k_{\text{inf}}$  seemed to increase with increasing temperature. The largest contributor to the uncertainty is due to  $^{238}\text{U}(n, \gamma)$  reaction. The majority of neutron capture in  $^{238}\text{U}$  occurs at intermediate energy, and thus as the temperature increases, the neutron spectrum shifts into the epithermal range. Figure 1 shows such a shift of the neutron spectrum into the epithermal range when changing from Hot Zero Power (HZZ) to Hot Full Power (HFP) conditions.

The resonance absorption due to Doppler broadening is reflected in the calculation of the sensitivity, mainly the implicit sensitivity. This implicit sensitivity accounts for the self-shielding effect. Figure 2 illustrates the relative change in sensitivity of  $^{238}\text{U}(n, \gamma)$  in each unit cell analyzed between HZZ and HFP conditions.

TABLE 1: Uncertainty in  $k_{\text{inf}}$  in LWR unit cells.

Fuel	Operating conditions	$k_{\text{inf}}$	Uncertainty in $k_{\text{inf}}$ (% $\Delta k/k$ )	Largest uncertainty-contributing reaction
BWR	HZP	1.3382	0.52	$^{238}\text{U}(n, \gamma)$
	HFP (40% void)	1.2208	0.62	$^{238}\text{U}(n, \gamma)$
PWR	HZP	1.4206	0.48	$^{238}\text{U}(n, \gamma)$
	HFP	1.4017	0.49	$^{238}\text{U}(n, \gamma)$
VVER	HZP	1.3448	0.51	$^{238}\text{U}(n, \gamma)$
	HFP	1.3270	0.52	$^{238}\text{U}(n, \gamma)$
KRITZ 2.1	HZP	1.2323	0.59	$^{238}\text{U}(n, \gamma)$
	HFP	1.1837	0.63	$^{238}\text{U}(n, \gamma)$
KRITZ 2.13	HZP	1.2642	0.55	$^{238}\text{U}(n, \gamma)$
	HFP	1.2329	0.58	$^{238}\text{U}(n, \gamma)$

FIGURE 2: Relative change in the sensitivity of  $^{238}\text{U}(n, \gamma)$ .

In addition, three fuel assemblies of three light water reactor types provided by the OECD LWR UAM benchmark were analyzed. The details of the specifications are readily available [1]. The  $k_{\text{inf}}$  and uncertainties obtained are shown in Table 2.

Similar to the fuel pin models, in fuel assembly models, the uncertainty in  $k_{\text{inf}}$  increases with increasing temperature, while  $k_{\text{inf}}$  decreases [5]. As explained earlier, this effect arises because of the increase in sensitivity of the largest contributor of uncertainty, the  $^{238}\text{U}(n, \gamma)$  reaction. The majority of neutron capture in  $^{238}\text{U}$  occurs at intermediate energy, and thus as the temperature increases, the spectrum shifts to the epithermal range (i.e., becomes harder). Likewise, 40% void exhibit larger uncertainty in  $k_{\text{inf}}$  also due to a harder flux spectrum.

The fuel assembly analysis (as part of Exercise I-2) includes the propagation of multigroup cross-section uncertainties (multigroup covariance matrix) to two-group homogenized cross-section uncertainties (two-group covariance matrix). The two-group cross-section uncertainties are obtained using the SCALE-6.0 44-group covariance matrix as input to the TSUNAMI-2D sequence with GPT in SCALE 6.1. The obtained results are shown in Table 3.

One can define nine-dimensional response vector  $\mathbf{R} = [\Sigma_{a1}, \Sigma_{a2}, \Sigma_{f1}, \Sigma_{f2}, \nu\Sigma_{f1}, \nu\Sigma_{f2}, D_1, D_2, \Sigma_{12}]$  for two-group

assembly homogenized cross-sections and obtain a corresponding covariance matrix in which the diagonal elements are the relative standard deviations, while off-diagonal elements are the correlation coefficients. The covariance matrices for the BWR and PWR cases are displayed in Figures 3, 4, 5, and 6.

The obtained results for different LWR types and cases indicate the following tendencies.

- (a) Group 1 (fast) cross-section uncertainty is ~2-3 times larger than Group 2 (thermal) cross-sections uncertainty.
- (b) Uncertainty contributions:
  - (i) a major contributor to Group 1 (fast) cross-section uncertainties is U-238 inelastic scattering;
  - (ii) U-238 inelastic scattering uncertainty is quite large;
  - (iii) 40% void (and higher) exhibit larger uncertainty in  $k_{\infty}$  due to harder flux spectrum.
- (c) Uncertainty (correlation) contribution:
  - (i) U-238 inelastic scattering uncertainty is quite large and dominates correlation coefficient.

TABLE 2: Assembly  $k_{\text{inf}}$  values and associated uncertainties.

Fuel	Operating conditions	$k_{\text{inf}}$	Uncertainty in $k_{\text{inf}}$ (% $\Delta k/k$ )	Largest uncertainty-contributing reaction
BWR	HZP	1.1116	0.50	$^{238}\text{U}(n, \gamma)$
	HFP (40% void)	1.0779	0.56	$^{238}\text{U}(n, \gamma)$
PWR	HZP	1.4130	0.46	$^{23}\text{U}(n, \gamma)$
	HFP	1.3968	0.47	$^{238}\text{U}(n, \gamma)$
VVER	HZP	1.3164	0.47	$^{238}\text{U}(n, \gamma)$
	HFP	1.3115	0.47	$^{238}\text{U}(n, \gamma)$

TABLE 3: Two-group cross-section uncertainty in LWR fuel assembly.

Response cross-section	Uncertainty (% $\Delta R/R$ )		Uncertainty (% $\Delta R/R$ )		Uncertainty (% $\Delta R/R$ )	
	BWR		PWR		VVER	
	HZP	HFP	HZP	HFP	HZP	HFP
$\Sigma_{t1}$	0.84	0.91	0.87	0.88	0.81	0.82
$\Sigma_{t2}$	0.13	0.15	0.14	0.14	0.12	0.12
$D_1$	0.84	0.91	0.87	0.88	0.81	0.82
$D_2$	0.13	0.15	0.14	0.14	0.12	0.12
$\Sigma_{a1}$	0.78	0.83	0.86	0.87	0.81	0.82
$\Sigma_{a2}$	0.20	0.22	0.22	0.22	0.21	0.21
$\Sigma_{f1}$	0.68	0.72	0.36	0.36	0.47	0.47
$\Sigma_{f2}$	0.32	0.32	0.32	0.32	0.32	0.32
$\Sigma_{11}$	0.84	0.91	0.87	0.87	0.81	0.81
$\Sigma_{12}$	1.10	1.22	1.20	1.21	1.03	1.03
$\Sigma_{21}$	0.27	0.34	0.30	0.33	0.26	0.29
$\Sigma_{22}$	0.13	0.16	0.15	0.15	0.13	0.13

	$\Sigma_{a1}$	$\Sigma_{a2}$	$\Sigma_{f1}$	$\Sigma_{f2}$	$\nu\Sigma_{f1}$	$\nu\Sigma_{f2}$	$D_1$	$D_2$	$\Sigma_{12}$
$\Sigma_{a1}$	0.78								
$\Sigma_{a2}$	0.25	0.20							
$\Sigma_{f1}$	-0.47	0.00	0.68						
$\Sigma_{f2}$	-0.04	0.18	0.13	0.32					
$\nu\Sigma_{f1}$	-0.43	0.00	0.87	0.08	0.98				
$\nu\Sigma_{f2}$	-0.03	0.13	0.10	0.72	0.13	0.45			
$D_1$	-0.69	-0.02	0.58	-0.02	0.55	-0.02	0.84		
$D_2$	0.03	0.09	0.01	0.02	0.00	0.01	0.04	0.13	
$\Sigma_{12}$	0.70	-0.01	-0.68	0.03	-0.64	0.02	-0.90	-0.03	1.01

FIGURE 3: BWR HZP covariance matrix.

	$\Sigma_{a1}$	$\Sigma_{a2}$	$\Sigma_{f1}$	$\Sigma_{f2}$	$\nu\Sigma_{f1}$	$\nu\Sigma_{f2}$	$D_1$	$D_2$	$\Sigma_{12}$
$\Sigma_{a1}$	0.83								
$\Sigma_{a2}$	0.22	0.22							
$\Sigma_{f1}$	-0.57	0.01	0.72						
$\Sigma_{f2}$	-0.04	0.19	0.14	0.32					
$\nu\Sigma_{f1}$	-0.52	0.01	0.89	0.10	1.01				
$\nu\Sigma_{f2}$	-0.03	0.14	0.10	0.72	0.14	0.45			
$D_1$	-0.67	0.01	0.59	-0.01	0.56	0.00	0.91		
$D_2$	0.72	-0.05	0.02	0.03	0.01	0.02	0.04	0.15	
$\Sigma_{12}$	0.03	0.18	-0.72	0.01	-0.68	0.01	-0.84	-0.04	1.22

FIGURE 4: BWR HFP covariance matrix.

	$\Sigma_{a1}$	$\Sigma_{a2}$	$\Sigma_{f1}$	$\Sigma_{f2}$	$\nu\Sigma_{f1}$	$\nu\Sigma_{f2}$	$D_1$	$D_2$	$\Sigma_{12}$
$\Sigma_{a1}$	0.86								
$\Sigma_{a2}$	0.13	0.22							
$\Sigma_{f1}$	0.18	0.13	0.36						
$\Sigma_{f2}$	0.00	0.44	0.33	0.32					
$\nu\Sigma_{f1}$	-0.07	0.09	0.72	0.22	0.51				
$\nu\Sigma_{f2}$	0.00	0.31	0.24	0.71	0.33	0.44			
$D_1$	-0.74	0.01	-0.26	0.00	0.04	0.00	0.87		
$D_2$	0.03	0.09	0.07	0.01	0.04	0.01	0.05	0.14	
$\Sigma_{12}$	0.76	-0.04	0.25	0.00	-0.07	0.00	-0.89	-0.04	1.20

FIGURE 5: TMI HZP covariance matrix.

	$\Sigma_{a1}$	$\Sigma_{a2}$	$\Sigma_{f1}$	$\Sigma_{f2}$	$\nu\Sigma_{f1}$	$\nu\Sigma_{f2}$	$D_1$	$D_2$	$\Sigma_{12}$
$\Sigma_{a1}$	0.87								
$\Sigma_{a2}$	0.13	0.22							
$\Sigma_{f1}$	0.17	0.13	0.36						
$\Sigma_{f2}$	0.00	0.44	0.33	0.32					
$\nu\Sigma_{f1}$	-0.08	0.09	0.72	0.22	0.51				
$\nu\Sigma_{f2}$	0.00	0.32	0.24	0.71	0.33	0.44			
$D_1$	-0.74	0.01	-0.26	0.00	0.04	0.00	0.88		
$D_2$	0.03	0.10	0.06	0.01	0.04	0.01	0.05	0.14	
$\Sigma_{12}$	0.77	-0.04	0.25	0.00	-0.07	0.00	-0.89	-0.04	1.21

FIGURE 6: TMI HFP covariance matrix.

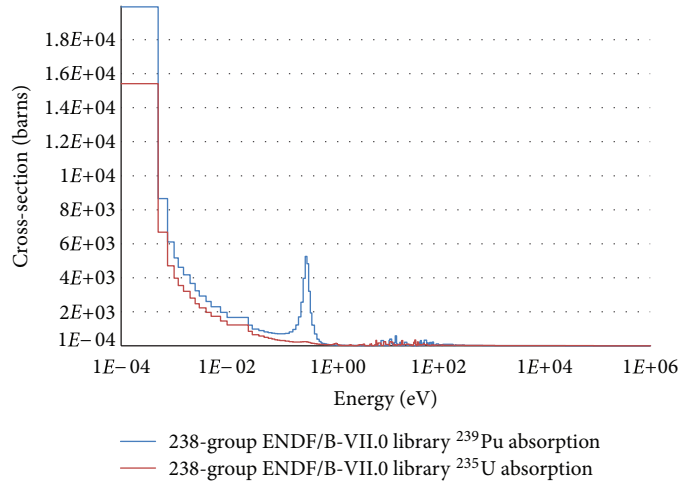


FIGURE 7: Plot of  $^{239}\text{Pu}$  absorption cross-sections compared to  $^{235}\text{U}$  absorption cross-sections.

TABLE 4: Uncertainty in  $k_{\text{inf}}$  in GEN-III unit cells.

Fuel	Compositions	$k_{\text{inf}}$	Uncertainty in $k_{\text{inf}}$ (% $\Delta k/k$ )	Largest uncertainty-contributing reaction
MOX	9.8% $^{239}\text{Pu}$	1.0921	0.94	$^{238}\text{U}(n, n')$
	6.5% $^{239}\text{Pu}$	1.0540	0.97	$^{238}\text{U}(n, n')$
	3.7% $^{239}\text{Pu}$	1.0115	0.99	$^{238}\text{U}(n, n')$
UOX	4.2% $^{235}\text{U}$	1.2431	0.51	$^{238}\text{U}(n, \gamma)$
	3.2% $^{235}\text{U}$	1.1741	0.54	$^{238}\text{U}(n, \gamma)$
	2.1% $^{235}\text{U}$	1.0490	0.59	$^{238}\text{U}(n, \gamma)$
UOX-Gd <sub>2</sub> O <sub>3</sub>	2.2% $^{235}\text{U}$	0.2166	1.79	$^{238}\text{U}(n, n')$
	1.9% $^{235}\text{U}$	0.1997	1.94	$^{238}\text{U}(n, n')$

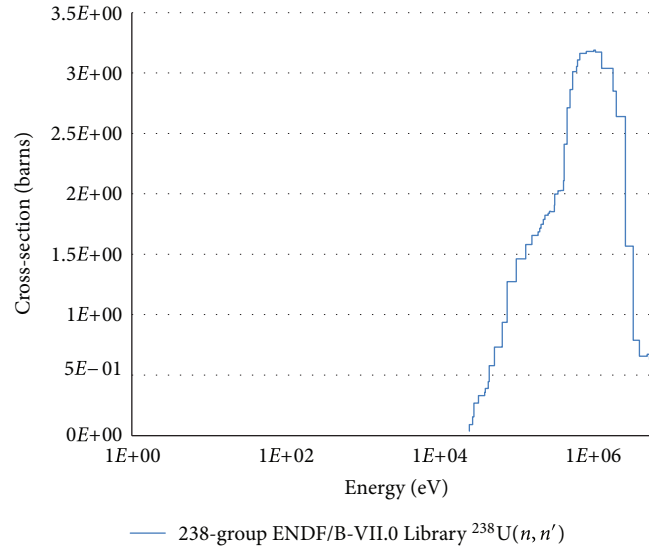
FIGURE 8: The plot of inelastic cross-section of  $^{238}\text{U}$  as a function of energy.

TABLE 5: Macroscopic fission cross-sections in MOX fuel cells.

Fuel	Composition	$k_{\text{inf}}$	$^{235}\text{U} \sum_f$ (1/cm)	$^{239}\text{Pu} \sum_f$ (1/cm)
MOX	3.7% Pu329	1.0115	6.70	13.74
MOX	6.5% Pu329	1.0540	4.65	8.40
MOX	9.8% Pu329	1.0921	3.69	5.88

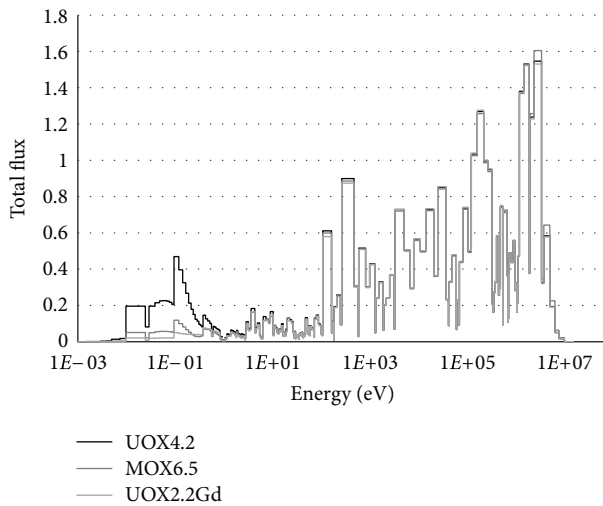


FIGURE 9: The neutron flux spectra of three unit cell compositions.

TABLE 6: LWR neutronics parameters [6, Table 3-1 page 88].

Parameter	$^{235}\text{U}$	$^{239}\text{Pu}$
Average $\nu$	2.4	2.9
Average $\eta$	2.0	1.9
Average $\sigma_{\text{fission}}$	280 barns	790 barns

#### 4. Composition Sensitivity Study

Selected fuel pin cells and four types of fuel assemblies from a representative Generation III LWR (GEN-III) specification were analyzed for the purpose of comparing effect of the compositions on the uncertainty calculations. The specifications of the GEN-III unit cells and fuel assemblies are readily available [1].

Three types of unit cells were analyzed at Hot Full Power; these include MOX, UOX, and UOX with  $\text{Gd}_2\text{O}_3$ . The multiplication factors and their uncertainties are presented in Table 4.

For each group of the fuel cells, several factors influence the changes in the uncertainty in  $k_{\text{inf}}$ , and each will be examined separately.

For each unit cell, the calculated  $k_{\text{inf}}$  increases with increasing enrichment of fissile material, while the uncertainty in  $k_{\text{inf}}$  decreases.

For the MOX fuel cells, the amount of  $^{238}\text{U}$  is reduced as the amount of  $^{239}\text{Pu}$ , the fissile material, is increased. The reduction in the amount of  $^{238}\text{U}$  means that there is less neutrons absorption by  $^{238}\text{U}$  nuclides. This is later found to be the most important nuclide contributor to uncertainty in  $k_{\text{inf}}$  in the unit cell. Thus, with less absorption by  $^{238}\text{U}$  nuclides, the uncertainty is reduced when comparing only the changes in the enrichment of  $^{239}\text{Pu}$  in MOX fuel cell.

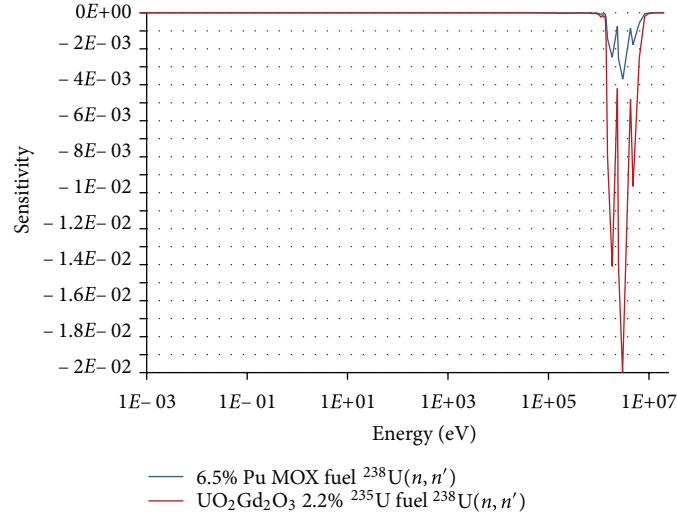


FIGURE 10: The sensitivity of  $^{238}\text{U}(n, n')$  as function of energy.

TABLE 7: Uncertainty in  $k_{\text{inf}}$  in GEN-III fuel assembly.

Fuel	Compositions	$k_{\text{inf}}$	Uncertainty in $k_{\text{inf}}$ (% $\Delta k/k$ )	Largest uncertainty-contributing reaction
GEN III	Type 1	1.2501	0.49	$^{238}\text{U}(n, \gamma)$
	Type 2	1.1228	0.49	$^{238}\text{U}(n, \gamma)$
	Type 3	0.9564	0.53	$^{238}\text{U}(n, \gamma)$
	Type 4	1.0700	0.97	$^{238}\text{U}(n, n')$

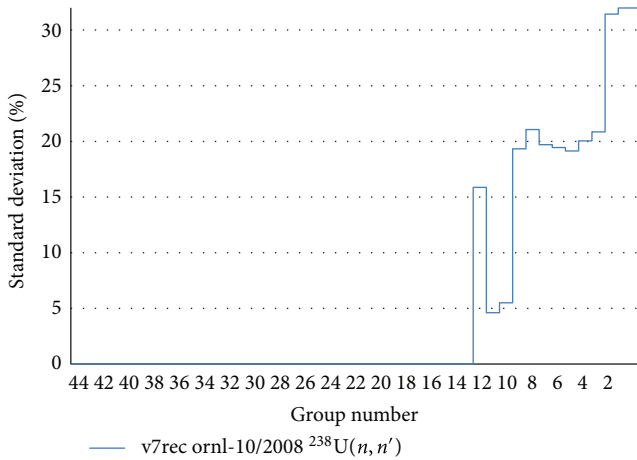


FIGURE 11: The 2D plot of  $^{238}\text{U}(n, n')$  covariance by energy group.

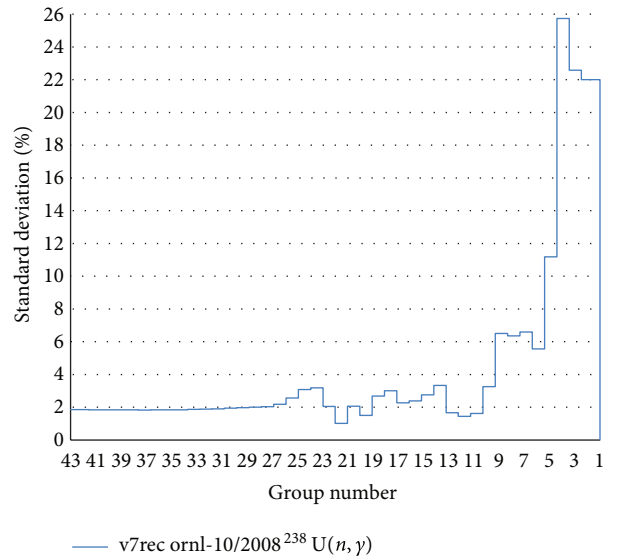


FIGURE 12: The 2D plot of  $^{238}\text{U}(n, \gamma)$  covariance by energy group.

However, the uncertainties of the MOX fuel cells were nearly twice than that of UOX fuel. The presence of  $^{239}\text{Pu}$  plays an important role in the increase in uncertainty. Figure 7 shows that the neutron absorption by  $^{239}\text{Pu}$  outcompeted the neutron absorption by  $^{235}\text{U}$ .

As a consequence, from the fact that more neutrons are absorbed by  $^{239}\text{Pu}$  than  $^{235}\text{U}$ , more neutrons are produced by fission due to  $^{239}\text{Pu}$ . Table 5 shows the dependency of fission macroscopic cross-sections to the composition of the

fuel, and Table 6 displays the comparison of the neutrons production parameters of each nuclide.

Neutrons produced by  $^{239}\text{Pu}$ , in general, will have higher energy than that of  $^{235}\text{U}$ . In this case, the neutron spectrum is harder because more neutrons with higher energies are produced by  $^{239}\text{Pu}$ , the dominant fission nuclide.

TABLE 8: Two-group cross-section uncertainty ( $\% \Delta R/R$ ) in GEN-III fuel assembly.

Response cross-section	GEN III type 1	GEN III type 2	GEN III type 3	GEN III type 4
$\Sigma_{t1}$	0.90	0.90	0.90	0.97
$\Sigma_{t2}$	0.14	0.14	0.14	0.14
$D_1$	0.90	0.90	0.90	0.97
$D_2$	0.14	0.14	0.14	0.14
$\Sigma_{a1}$	0.89	0.89	0.89	1.00
$\Sigma_{a2}$	0.21	0.19	0.19	0.24
$\Sigma_{f1}$	0.37	0.37	0.50	0.44
$\Sigma_{f2}$	0.32	0.32	0.33	0.62
$\Sigma_{11}$	0.90	0.90	0.90	0.97
$\Sigma_{12}$	1.25	1.25	1.24	1.47
$\Sigma_{21}$	0.33	0.32	0.31	0.37
$\Sigma_{22}$	0.15	0.15	0.15	0.16

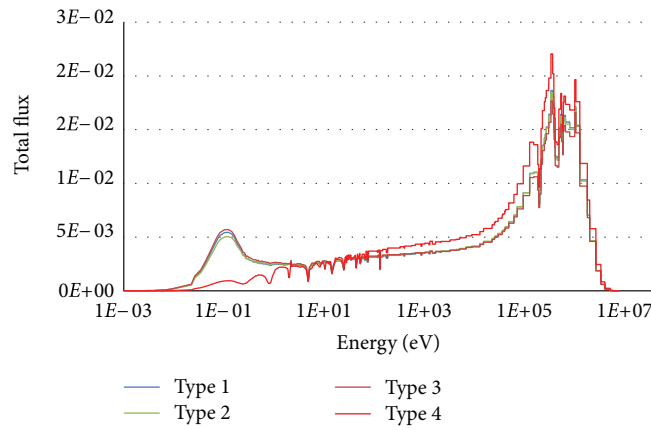


FIGURE 13: The neutron flux spectra of GEN-III LWR fuel assembly.

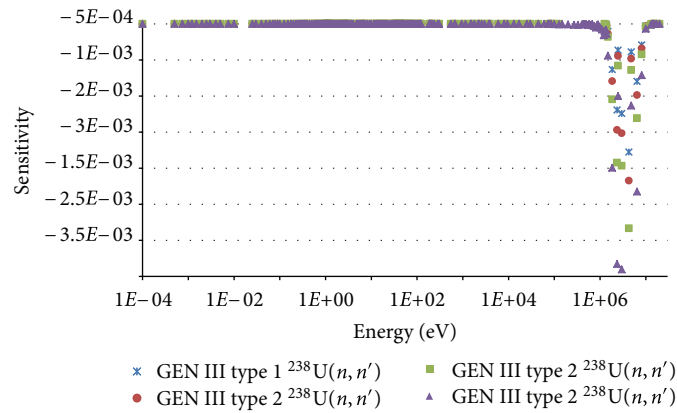


FIGURE 14: The sensitivity of  $^{238}\text{U}(n, n')$  as function of energy.

On the other hand, for UOX fuel cell with  $Gd_2O_3$  added, similar finding (hardening of the neutron spectrum) occurred but due to a very different mechanism. The uncertainties in  $k_{inf}$  are nearly triple of the fuel cell with similar  $^{235}U$  enrichment. This is due to the fact that gadolinium is a major thermal neutron absorber. The significant reduction in the thermal neutrons shifted the fission reactions toward neutrons with higher energy. Once again, the neutron spectrum is harder than that of UOX fuel cell without  $Gd_2O_3$  added.

The uncertainties in fuel cells with harder neutron spectrum seemed to be higher than fuel cells with softer neutron spectrum. This is due to the absorption of the  $^{238}U$ . The resonance absorption of  $^{238}U$  that occurs at higher neutron energy is very large.

The absorption of thermal neutrons by  $^{239}Pu$  dominates the fission process. Since fission in  $^{239}Pu$  produces more fast neutrons, the neutron spectrum becomes harder. The harder the spectrum, the higher the  $^{238}U(n, n')$  reaction rates. This effect can be seen in Figure 8, which depicts the cross-section of  $^{238}U(n, n')$  reaction. When  $Gd_2O_3$  is added, the largest nuclide reaction cross-section contributor to the uncertainty in  $k_{inf}$  changed from  $^{238}U(n, \gamma)$  to  $^{238}U(n, n')$ . These changes are due to the presence of gadolinium, mainly a thermal neutron absorber, causing significant reductions in thermal neutron populations. The neutron flux spectrum is harder, and it can be seen in Figure 9.

The sensitivity profiles were compared in Figure 10. It was found that the unit cell containing gadolinium is very sensitive to the  $^{238}U(n, n')$  reaction, and this large sensitivity contributes to increase in uncertainty.

The covariance matrix of  $^{238}U(n, n')$  is presented in Figure 11, while the covariance matrix of  $^{238}U(n, \gamma)$  is shown in Figure 12. It should be noted that at high energy, the coefficients of relative covariance of  $^{238}U(n, n')$  cross-section reach 30% of the standard deviation. Thus, for a reactor with a harder spectrum, it produces a large contribution to the uncertainty of  $k_{inf}$ .

Four types of fuel assembly from a representative Generation III LWR specification (as part of Exercise I-2) were analyzed at Hot Full Power condition:

- (i) type 1 (UOX 4.2%  $^{235}U$ );
- (ii) type 2 (UOX 4.2%  $^{235}U$  +  $UO_2Gd_2O_3$  2.2%  $^{235}U$ );
- (iii) type 3 (UOX 3.2%  $^{235}U$  +  $UO_2Gd_2O_3$  1.9%  $^{235}U$ );
- (iv) type 4 (MOX).

The details of the specifications are readily available [1]. The values calculated for  $k_{inf}$  and their uncertainties are presented in Table 7.

Results show that  $k_{inf}$  increases with increasing enrichment of fissile material, while the uncertainty in  $k_{inf}$  decreases. Unlike the effect we found earlier for UOX fuel pin cell with  $Gd_2O_3$  added, in this case the presence of  $Gd_2O_3$  does not lead to a significant increase in uncertainty because of the homogenization process. For the MOX fuel assembly, there is a remarkable increase in uncertainty in  $k_{inf}$ , and this

result is similar to that observed in the corresponding pin cell analysis.

Additionally, the two-group cross-section uncertainties are presented in Table 8.

These results show, as expected, a larger uncertainty for the MOX fuel assembly (type 4) than for the UOX assemblies (types 1 through 3).

Figure 13 depicts the neutron flux of fuel assemblies from a representative GEN-III LWR at HFP condition. There is a significant reduction in the thermal neutrons for the MOX fuel assembly. The harder the spectrum, the higher the  $^{238}U(n, n')$  reaction rates.

Sensitivity profiles of  $^{238}U(n, n')$  were compared in Figure 14. Fuel assembly containing Pu is very sensitive to  $^{238}U(n, n')$  reaction, and its contribution to uncertainty is noticeable.

## 5. Conclusions

Sensitivity studies have been performed using SCALE [7] to investigate the effect of temperature and material composition on cross-section uncertainty propagation at two levels—pin cell models (within the framework of Exercise I-1) and assembly models (within the framework of Exercise I-2). It was found that the uncertainty in  $k_{inf}$  is dominated by neutron interactions with  $^{238}U$  in both studies with varying temperatures and compositions. The following tendencies have been observed:

- (a) increasing temperature leads to increasing uncertainty in  $k_{inf}$ ;
- (b) decreasing  $^{238}U$  in fuel composition leads to decreasing uncertainty in  $k_{inf}$ ;
- (c) major contributor to uncertainty is affected by the neutron spectrum.

The fast group cross-section uncertainties are much larger than the thermal cross-section uncertainties due to the larger role of  $^{238}U$ .

## 6. Future Work

The future studies will be focused on Exercise I-3—propagation of few-group cross-section uncertainties to the core steady state stand-alone neutronics calculations using statistical methodology similar to the one reported in [8].

## Acknowledgments

The authors would like to acknowledge the two Ph.D. fellowship grants, one at the Technical University of Catalonia (sponsored by the Spanish Nuclear Security Council) and the other at the Pennsylvania State University (sponsored by the US Nuclear Regulatory Commission), which supported the graduate students performing the studies reported in this paper.

## References

- [1] “OECD/NEA benchmark for Uncertainty Analysis in Modelling (UAM) for design, operation and safety analysis of LWRs,” in *Specification and Support Data For the Neutronics Cases (Phase I)*, vol. 1, Version 2. 0. NEA/NSC/DOC(2012), 2012.
- [2] D. Cacuci, *Sensitivity and Uncertainty Analysis: Theory*, vol. 1, Chapman & Hall/CRC, 2003.
- [3] “SCALE: a comprehensive modeling and simulation suite for nuclear safety analysis and design,” ORNL/TM-2005/39, Version 6. 1, Oak Ridge National Laboratory, Oak Ridge, Tenn, USA, 2011.
- [4] S. Kamerow, C. Arenas Moreno, and K. Ivanov, “Uncertainty analysis of light water reactor unit fuel pin cells,” in *Proceedings of the International Conference on Mathematics and Computational Methods Applied to Nuclear Science and Engineering (M&C ’11)*, Rio de Janeiro, Brazil, May 2011.
- [5] M. Avramova, C. Arenas Moreno, and K. Ivanov, “Extension of BEPU methods to sub-channel thermal-hydraulics and to coupled three-dimensional neutronics/thermal-hydraulics codes,” in *Proceedings of The OECD/CSNI Workshop*, Barcelona, Spain, November 2011.
- [6] J. Duderstadt and L. Hamilton, *Nuclear Reactor Analysis*, John Wiley & Sons, New York, NY, USA, 1976.
- [7] B. T. Rearden, M. Williams, M. Jessee, D. Mueller, and D. Wiarda, “Sensitivity and uncertainty analysis capabilities and data in SCALE,” *Nuclear Technology*, vol. 174, no. 2, pp. 236–288, 2011.
- [8] M. Klein, L. Gallner, B. Krzykacz-Hausmann, A. Pautz, and W. Zwermann, “Influence of nuclear data uncertainties on reactor core calculations,” *Kerntechnik*, vol. 76, no. 3, pp. 174–178, 2011.

## Research Article

# PSI Methodologies for Nuclear Data Uncertainty Propagation with CASMO-5M and MCNPX: Results for OECD/NEA UAM Benchmark Phase I

W. Wieselquist, T. Zhu, A. Vasiliev, and H. Ferroukhi

Laboratory for Reactor Physics Systems Behaviour, Paul Scherrer Institut, 5232 Villigen, Switzerland

Correspondence should be addressed to W. Wieselquist; [william.wieselquist@gmail.com](mailto:william.wieselquist@gmail.com)

Received 22 August 2012; Accepted 22 November 2012

Academic Editor: Carlo Parisi

Copyright © 2013 W. Wieselquist et al. This is an open access article distributed under the Creative Commons Attribution License, which permits unrestricted use, distribution, and reproduction in any medium, provided the original work is properly cited.

Capabilities for uncertainty quantification (UQ) with respect to nuclear data have been developed at PSI in the recent years and applied to the UAM benchmark. The guiding principle for the PSI UQ development has been to implement nonintrusive “black box” UQ techniques in state-of-the-art, production-quality codes used already for routine analyses. Two complimentary UQ techniques have been developed thus far: (i) direct perturbation (DP) and (ii) stochastic sampling (SS). The DP technique is, first and foremost, a robust and versatile sensitivity coefficient calculation, applicable to all types of input and output. Using standard uncertainty propagation, the sensitivity coefficients are folded with variance/covariance matrices (VCMs) leading to a local first-order UQ method. The complementary SS technique samples uncertain inputs according to their joint probability distributions and provides a global, all-order UQ method. This paper describes both DP and SS implemented in the lattice physics code CASMO-5MX (a special PSI-modified version of CASMO-5M) and a preliminary SS technique implemented in MCNPX, routinely used in criticality safety and fluence analyses. Results are presented for the UAM benchmark exercises I-1 (cell) and I-2 (assembly).

## 1. Introduction

The OECD/NEA benchmark for uncertainty analysis in modeling (UAM) was launched a few years ago to promote the development, assessment, and integration of comprehensive uncertainty quantification (UQ) methods in best-estimate multiphysics coupled simulations of LWRs during normal as well as transient conditions [1]. Although very ambitious by nature (due to the complexity of the task to treat all potential sources of uncertainties), the benchmark has nevertheless achieved one of its first objectives, namely, to constitute a major (if not the main) international framework to drive forward the development of methodologies for the propagation of nuclear data uncertainties in reactor simulations. This topic was proposed as the first phase of the benchmark, and since research in precisely this area was at the same time being launched within the STARS project [2] at the Paul Scherrer Institut (PSI), participation to this benchmark was considered as a timely and highly valuable opportunity to complement the development and assessment of the PSI methods. In that context, two parallel lines of development were in fact

initiated at PSI. On the one hand, the development of a UQ methodology for the propagation of neutronic uncertainties in the deterministic CASMO/SIMULATE/SIMULATE-3 K chain of reactor analysis codes and used for safety assessment of the Swiss reactors was launched. On the other hand, the development of a corresponding UQ methodology for neutron transport simulations with the stochastic continuous-energy MCNPX and with primary emphasis on criticality safety was recently initiated. In this paper, the principles and concepts of both methodologies are first summarized. Then, the results obtained for the UAM Phase I benchmark cases analyzed so far are presented. The primary focus is given to the CASMO-5M analyses conducted so far for Phase I-1, aimed at cell physics, and Phase I-2, dedicated to lattice physics. Regarding MCNPX, the first set of solutions obtained for the hot-zero-power pin cell cases of Phase I-1 will also be presented.

*1.1. Motivation.* In order to rigorously establish the accuracy (or bias) of the so-called best-estimate codes, the precision (or

uncertainty) must be quantified. (The measure of accuracy is bias: low accuracy implies a large bias and high accuracy implies a small bias. The measure of precision is uncertainty: low precision implies large uncertainty and high precision implies small uncertainty.) This includes propagation of input uncertainty (all inputs are really distributions) to output uncertainty, which is the basic task of UQ. The most straightforward benefit of UQ is the new information about the distribution of outputs which can be used to qualify designs and/or provide confidence in results. However, with UQ a much more rigorous validation procedure is also available and the value of this should not be underestimated. With UQ, one can compare *calculations with uncertainty*  $C \pm \sigma_C$  to experimental results with uncertainty  $E \pm \sigma_E$  using overlap testing, instead of the conservative assumption of no uncertainty in calculations ( $\sigma_C = 0$ ) or subjective use of expert judgment to decide if  $C$  is close enough to  $E \pm \sigma_E$ . A best-estimate code (and its validation) should avoid such conservative assumptions and expert judgment by definition.

*1.2. Preliminaries.* Consider input,  $x$ , and output,  $y$ , with nominal values  $x_0$  and  $y_0$  and perturbed values  $x'$  and  $y'$ . When sampling perturbed values  $x'$  from a distribution, the  $n$ th sample of the input is  $x'^{(n)}$  and the corresponding output is  $y'^{(n)}$ . With computer codes, there is typically a large set of input and output, which may be denoted  $\mathbf{x}_0$  and  $\mathbf{y}_0$  for nominal sets and  $\mathbf{x}'$ , and  $\mathbf{y}'$  for perturbed sets.

*1.3. First-Order UQ Using Uncertainty Propagation.* The cornerstone of local, first-order UQ methods is the capability to calculate sensitivity coefficients:

$$S \equiv \left. \frac{\partial y}{\partial x} \right|_{x=x_0, y_0}, \quad (1)$$

which are vital to sensitivity analysis (SA). It is very convenient to introduce the definition of a *perturbation factor*,  $p$ , such that the perturbed input  $x' = px_0$  and the corresponding output factor,  $q$ ,  $y' = qy_0$ . Thus the sensitivity coefficient may be written simply as

$$S \equiv \left. \frac{\partial q}{\partial p} \right|_{p=1}; \quad (2)$$

Nonintrusive SA can then be implemented simply as a numerical differentiation of  $q$  with respect to  $p$ , referred to here as direct perturbation (DP) as in [3]. Two factors make it difficult to use DP in an automated manner to obtain accurate estimates of  $S$ : (i) due to finite-precision arithmetic, “too small” perturbations do not change the output significantly and (ii) due to unknown relationships between inputs and outputs, “too small” perturbations for one input may be “too large” for another. With low-order numerical differentiation formulas (e.g., first-order finite differences) especially, “too large” perturbation can greatly increase the approximation error. Due to the relatively high cost of calculations in nuclear simulations, low-order formulas are typically used.

Although DP can be straightforwardly extended to simultaneously estimate  $S$  for multiple outputs, it cannot handle

simultaneous input perturbations; that is, input perturbations are always one at a time. Thus with many more input parameters than output parameters, DP is not very efficient. For nuclear data uncertainty propagation, this was the basic reason behind the development of very efficient (but intrusive) perturbation theory-based algorithms for sensitivity coefficient estimation, for example, in the SCALE code system [4].

Using the calculated sensitivity coefficients in UQ simply requires the classic first-order uncertainty propagation formula [5], shown below for *multiple input and output parameters*:

$$\mathbf{V}_Y = \mathbf{S}^T \mathbf{V}_X \mathbf{S}, \quad (3)$$

with *relative* variance/covariance matrix (VCM) of the outputs  $\mathbf{V}_Y$  in terms of the *relative* VCM of the inputs  $\mathbf{V}_X$  and the sensitivity coefficients,  $\mathbf{S}$ , now a matrix defined as  $S_{ij} = \partial q_j / \partial p_i$  for input parameter index (row)  $i$  and output parameter index (column)  $j$ .

*1.4. Sampling-Based UQ.* Sampling-based UQ, or stochastic sampling (SS), has been historically used for nonlinear systems with few correlated parameters [6]. However, currently SS is increasingly applied for all types of UQ, including neutronics, due to its nonintrusive nature [7], flexibility to handle many uncertain parameters [8], theory for non-parametric tolerance intervals (i.e., Wilks’ formula), and global sampling of the solution space. In order to implement an SS method, one simply has to sample inputs from their distributions (choosing appropriate distributions is another matter), run the code with each sampled set, and analyze the distribution of outputs.

*1.4.1. Simple Random Sampling from Multivariate Gaussian Distributions.* In the case of the distribution of nuclear data, one generally assumes that the input  $\mathbf{x}$  obeys an  $M$ -dimensional Gaussian (normal) distribution [5]:

$$f_X(\mathbf{x}) = \frac{1}{(2\pi)^{M/2} |\mathbf{V}_X|^{1/2}} \exp\left(-\frac{(\mathbf{x}-\mathbf{x}_0) \mathbf{V}_X^{-1} (\mathbf{x}-\mathbf{x}_0)^T}{2}\right), \quad (4)$$

with input VCM  $\mathbf{V}_X$  of dimension  $M \times M$ ,  $|\mathbf{V}_X|$  the determinant, and mean  $\mathbf{x}_0$  of dimension  $1 \times M$ . A matrix of  $N$  simple random samples  $\mathbf{X}'$  ( $N \times M$ ) which respects the correlations of data may be constructed as described in [9].

- (1) Decompose VCM  $\mathbf{V}_X$  using a “Cholesky-like” decomposition (see below),  $\mathbf{T}^T \mathbf{T} = \mathbf{V}$ , where  $\mathbf{T}$  is  $M^* \times M$ .
- (2) Make  $N \times M^*$  random samples from the standard normal distribution (zero mean and unit variance) and store the results in the  $N \times M^*$  matrix  $\mathbf{Z}$ .
- (3) The random samples are then given as  $\mathbf{x}'^{(n)} = \mathbf{x}_0 + \mathbf{Z}^{(n)} \mathbf{T}$ , where  $\mathbf{Z}^{(n)}$  is the  $n$ th row of  $\mathbf{Z}$ .

The term “Cholesky-like” is used because a true Cholesky factorization requires a (square) symmetric positive definite

(SPD) matrix whereas a general VCM can be symmetric positive *semidefinite* (SPSD), for example, due to perfect (anti) correlation of parameters. In this case the matrix is rank-deficient with rank  $M^*$  and  $\mathbf{T}$  is rectangular, with  $M^* < M$ , and (4) must use the generalized inverse and pseudodeterminant.

**1.4.2. Nonparametric Statistics and Wilks' Formula.** Given  $N$  random samples of a quantity, the formula for the tolerance interval in terms of coverage ( $a$ ) and confidence ( $b$ ), *without assuming a particular distribution*, is known colloquially as Wilks' formula, due to the seminal work of S. S. Wilks in nonparametric statistics [10]. Nonparametric (or order) statistics is the name given to the set of statistical techniques which does not require data belonging to a particular distribution (e.g. normal) and frequently requires ordering samples, for instance, from least to greatest. For a more complete discussion of nonparametric statistics applied to neutronics calculations, see [8]. In order for Wilks' formula to be valid, a simple random sampling process must be used; that is, stratified sampling or variance reduction is not allowed according to the theory. For example, with  $N = 93$  samples, a two-sided tolerance interval can be declared as  $[y_{\min}, y_{\max}]$ , where  $y_{\min}$  and  $y_{\max}$  are the minimum and maximum results from the 93 samples. Such a tolerance interval is guaranteed to contain the (middle)  $a = 95\%$  of the distribution with  $b = 95\%$  confidence. Note that, with  $a = b$ , the behavior of  $\log(N)$  versus  $\log(1 - a)$  is roughly linear.

**1.4.3. Sample Statistics.** In neutronics UQ, the variance (or standard deviation) is used most often as the measure of uncertainty. With UQ methods based on the uncertainty propagation formula (e.g., DP), the variance of outputs is simply the diagonal of the output VCM. With SS, it is convenient to use the sample variance from sample statistics:

$$v = \frac{1}{N} \sum_{n=1}^N (y^{(n)} - y_0)^2, \quad (5)$$

where  $y^{(n)}$  is the (perturbed) result of sample  $n$ ,  $y_0$  is the nominal calculation value, and  $N$  is the total number of samples. It is well known in statistics that the sample variance of a normal distribution is a scaled chi-square distribution of  $N - 1$  degrees of freedom which can be used to provide  $N$ -dependent bounds on the sample variances as shown in [6].

## 2. Methodology

Although both direct perturbation (DP) and stochastic sampling (SS) schemes are "nonintrusive" by nature, in order to develop UQ techniques for the CASMO-5 M lattice physics code, some source code modifications were necessary as CASMO-5M's nuclear data library is stored in a proprietary binary format and "perturbed libraries" could not be easily created.

For the relatively newer developments concerning UQ with MCNPX, ACE format libraries may be created directly and thus no source code modifications of MCNPX are required. The following sections will first describe the

CASMO-5MX code, then the DP and SS techniques as designed for use with CASMO-5MX, and finally the SS technique development for MCNPX.

**2.1. General Development of CASMO-5MX.** The capability to perturb the nuclear data library of the lattice physics code is the first step in order to perform any "nonintrusive" UQ with respect to nuclear data. Because of the aforementioned proprietary nature of CASMO-5M's 586-group ENDF/B-VII.R0-based nuclear data library, source code modifications were the easiest way to gain access to this library to perform perturbations. For this purpose, a special module called "PERTXS" and a corresponding cross-section (XS) "perturbation file" was developed. The perturbation file can simply be thought of as a new (optional) input file that demands nuclear data perturbations to apply to the nominal library at runtime. This PSI-modified version of CASMO-5 M will hereon be referred to as CASMO-5MX and the DP technique has been described in [3] and SS technique in [9]. Here, for the reader's convenience, all necessary elements will be reviewed.

**2.1.1. Allowed Nuclear Data Perturbations.** Currently CASMO-5MX allows *nuclear data* perturbations to the following microscopic data for all nuclides in the library (ENDF MT numbers in parentheses).

- (1) elastic scattering (MT = 2),
- (2) inelastic scattering (MT = 4),
- (3)  $(n, 2n)$  (MT = 16),
- (4) fission (MT = 18),
- (5) capture (MT = 101),
- (6) average neutrons per fission (MT = 452), and
- (7) average fission spectrum (MT = 1018).

In addition, external utilities have been created to perturb any parameter contained in the standard input file, facilitating sensitivity/uncertainty analysis with respect to such parameters as clad thickness, fuel enrichment, and so forth. With nuclear data perturbations, it is important to understand that perturbations are made *relative to the existing data on the library*; that is, values on the library are not replaced with new perturbed values but increased/decreased by a perturbation factor  $p$ .

**2.1.2. Perturbation Formulas.** A very convenient feature of CASMO-5MX is that perturbations may be supplied in any group structure, for example, the 19-group "coarse" structure used by default in CASMO-5 M for UO<sub>2</sub> assembly method of characteristics (MOC) transport calculations, an arbitrary two-group structure, or the full 586-group library structure. However, using coarse groups for perturbations keeps data files smaller and in most cases, it has been found that using a very fine group structure (e.g., 586 library groups) does not significantly alter the final output uncertainty estimates. (A small study of this will be provided later.) Additionally, because the underlying VCM data is in the SCALE6 44-group structure, it does not make too much sense to go beyond this.

Inside CASMO-5MX, the following perturbation formulas are used to map perturbations from the input group structure to the 586-group library structure:

$$p_{\chi}^g = \frac{\sum_h p_I^h \chi_I^h w_0^{g,h}}{\sum_h \chi_I^h w_0^{g,h}}, \quad (6)$$

$$p_{\sigma}^g = \frac{\sum_h p_I^H \sigma_I^h w_1^{g,h}}{\sum_h \sigma_I^h w_1^{g,h}}. \quad (7)$$

Equation (6) defines the perturbation factor to be applied to the library fission spectrum in library group  $g$  with input fission spectrum  $\chi_I^h$  and input perturbation  $p_I^h$ , where the input (coarse) energy groups use index  $h$ . Equation (7) defines the perturbation factor for a cross-section with standard flux weighting. The weights  $w_0^{g,h}$  and  $w_1^{g,h}$  are given by the following equations:

$$w_0^{g,h} = \frac{\int_{E^{\text{lower}(g,h)}}^{E^{\text{upper}(g,h)}} dE}{\int_{E^h}^{E^{h-1}} dE} = \frac{\Delta E^{g,h}}{\Delta E^h}, \quad (8)$$

$$w_1^{g,h} = \frac{\int_{E^{\text{lower}(g,h)}}^{E^{\text{upper}(g,h)}} \phi(E) dE}{\int_{E^g}^{E^{g-1}} \phi(E) dE}. \quad (9)$$

The upper and lower bounds of the numerator integrals are basically the union grid boundaries for the union of group  $g$  and group  $h$ ; therefore, the weights are only nonzero where groups overlap. If the supplied perturbation group structure and the library group structure are aligned and there is only one  $h$  group for one or more  $g$  groups (i.e., the input structure is coarser) and the formulas reduce considerably to  $p^g = p_I^h$  (Figure 1). This means one may perturb the library using only relative information, that is, a set of  $p$  values. However, when the perturbation group structure is nonaligned with the library, then both the weights and cross-section factors, for example,  $\sigma_I^h$  and  $w_1^{g,h}$ , do not cancel in (6) and (7) and dependence on the intragroup weighting functions and cross-sections are introduced. This means that one cannot simply use the perturbations  $p$  and an approximate spectrum, for example,  $\phi(E) \propto 1/E$ , and reference values for the data in the perturbation group structure, for example,  $\sigma_I^h$ , must be provided as well. In CASMO-5MX, the weighting is assumed  $1/E$  and the reference values in the SCALE6 VCM library are used.

The ability to supply perturbations in any group structure effectively gives the user the ability to generate sensitivity profiles at different resolutions for different reactions. For example, to simply evaluate the order-of-magnitude effect for a particular reaction, two-group perturbations could be supplied. If the sensitivity is high, perturbations in a finer structure could be made to generate a refined sensitivity profile. The limiting resolution is simply that of the underlying 586-group library.

**2.1.3. Nuclear Data Variance/Covariance Matrices.** The uncertainty in groupwise nuclear data is typically expressed

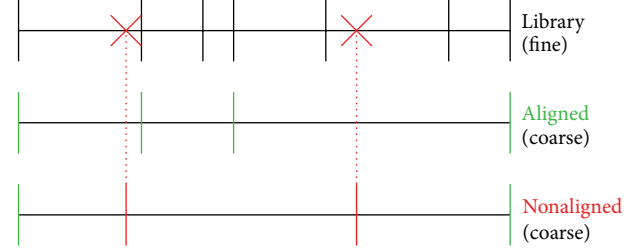


FIGURE 1: Aligned and nonaligned coarse perturbation group structures.

only in terms of variance/covariance matrices (VCMs), which implies an underlying Gaussian (normal) distribution of the data. At the single-nuclide, single-reaction level with  $G$  energy groups, this is a matrix of size  $G \times G$  with the diagonal elements giving the groupwise variance and off-diagonal elements giving the covariance between two groups. Close groups tend to be highly correlated, for example, it is improbable that the data in one fast group would increase and the next one down would decrease. Component cross-sections (e.g., scattering and capture) tend to be anticorrelated, as they must sum to the total cross section. Because measurements are frequently made on compounds, not single nuclides, there is additional correlation between some of the single-nuclide data.

With correlations that cannot be neglected and huge datasets (e.g., 300 nuclides with 44 energy groups and 6 reactions is about 80,000 “inputs”), nuclear data uncertainty propagation is difficult and unique. Because this data is only recently being fully utilized, there are few choices for robust and reasonable VCM evaluations. The SCALE6 VCM [4] data is among the most widely used and developed for these purposes and has been used exclusively in this work, with one single additional approximation due to current limitations in some of the processing tools: cross-nuclide covariances (e.g.,  $\text{Pu}^{239}$  fission anticorrelated with  $\text{Pu}^{241}$  fission) are neglected. The data available on the VCM library and the data which may be perturbed with CASMO-5MX are for the most part consistent. Two exceptions are that the VCM library contains data for each partial capture reaction  $\text{MT} = 102-109$  and the CASMO-5 M data library combines elastic, inelastic,  $(n, 2n)$ , and  $(n, 3n)$  into a single “scattering matrix.” The first issue is easily circumvented using the uncertainty propagation formula in (3) to combine the partial VCMs for  $\text{MT} = 102$  to 109 into a single  $\text{MT} = 101$  VCM [11]. The second issue dealing with combined scattering is described in the next section.

Because the SCALE6 VCM library is provided in a 44-group structure, *nonaligned* with the CASMO-5MX library structure, there are two options to use this data:

- (1) make perturbations in the 44-group structure, relying on (6) and (7) to map these perturbations to 586-groups,
- (2) convert the 44-group VCMs to a different group structure, ideally to a coarse group structure *aligned* with the library.

The second option has been investigated and the code ANGELO which performs the conversion has been provided for the purposes of this benchmark [12]. Although its applicability has not been rigorously determined, for converting 44-group SCALE6 VCMs to coarse 8-, 19-, and 31-group structures of CASMO-5MX, the scheme seems reasonable.

**2.1.4. Scattering Matrix Perturbations and External Scattering Fraction Data.** Many lattice physics codes, including CASMO-5 M, store a single “combined scattering matrix” for each nuclide, lumping elastic and inelastic scattering with the  $(n, 2n)$  and  $(n, 3n)$  reactions. Additionally, on the VCM library, uncertainty information for these reactions is only present in “1D” or “vector” form; that is, it has been “summed” over all final energy groups. With these two constraints, perturbations could originally [3] only be applied in the following manner to the combined scattering matrix:

$$\sigma_s^{I g \rightarrow g'} = p_S^g \sigma_s^{g \rightarrow g'}, \quad (10)$$

where perturbation  $p_S^g$  depends only on the initial group  $g$  and is applied identically to all final groups,  $g'$ , in combined scattering matrix,  $\sigma_s^{g \rightarrow g'}$ . One upside to this type of perturbation is that the mapping formula from (9) can still be used for scattering perturbations. To denote this type of special perturbation, the special MT number MT = 13 was introduced to denote “combined scattering” perturbations within the CASMO-5MX system.

However, it became apparent that the combined treatment tends to underestimate the uncertainty due, in particular, to inelastic scattering in U-238 [11], which is actually one of the dominant sources of uncertainty for many responses. However, an approach to separate these effects was described in [9], where one can perform additional NJOY calculations to estimate the so-called “scattering fractions,” that is, fractions of the combined scattering matrix which are due to elastic, inelastic, and so forth. The scattering fractions become an auxiliary library to be used when separation of effects is important. In this case, the scattering matrix perturbation formula becomes

$$\sigma_s^{I g \rightarrow g'} = \left( p_{S,el}^g f_{el}^{g \rightarrow g'} + p_{S,in}^g f_{in}^{g \rightarrow g'} + p_{n,2n}^g f_{n,2n}^{g \rightarrow g'} + p_{n,3n}^g f_{n,3n}^{g \rightarrow g'} \right) \sigma_s^{g \rightarrow g'}, \quad (11)$$

where the  $f$  terms are the scattering fractions, tabulated for each nonzero  $g, g'$  pair for that reaction. Currently the scattering fractions have been prepared for U-235 and U-238 only, and only at a temperature of 500 K and a background cross section of 40 barns, after some initial studies, found them to be remarkably constant with respect to temperature and background cross-section variations.

**2.1.5. Resonance Self-Shielding.** The way that resonance self-shielding is performed in CASMO-5M makes it difficult to perturb nuclear data *before* the resonance self-shielding calculation. Therefore, the resonance self-shielded and infinitely dilute data are perturbed by the same factor  $p$ , which

neglects the effect *changes* in the data have on self-shielding. Because self-shielding is a “negative” type of feedback, the current approach in CASMO-5MX is thought to produce slightly higher uncertainties, but comparisons to SCALE6 TSUNAMI, which does include the effect, have not shown a significant effect [3, 9]. The difference should be most noticeable with strong *and* highly uncertain resonances, for which perhaps the U-238 dominated systems tested so far do not qualify.

**2.2. Direct Perturbation with CASMO-5MX/DP.** The main difficulties applying the DP technique to calculate sensitivity coefficients, namely, fixed-precision and eliminating second-order and higher effects, have been overcome using an adaptive technique [3] in which

- (1) a scoping calculation is used to assess the magnitude of the response change;
- (2) then extra calculations are made which satisfy precision requirements;
- (3) finally a polynomial fit (linear or parabolic) is constructed from the pool of available calculations and used to estimate the sensitivity coefficient.

Numerous schemes have been designed within this general framework, for example, using one or two scoping calculations and one or two extra calculations, for a range of two to four calculations per input parameter. Clearly with nuclear data one cannot hope to perform DP on all 80,000 parameters. However, CASMO-5MX/DP serves numerous purposes:

- (1) provide sensitivity profiles for code-to-code comparisons (e.g., with SCALE6 TSUNAMI),
- (2) provide reference local, first-order uncertainty results to assess other CASMO-5MX methodologies, such as SS,
- (3) provide sensitivity coefficients for nonnuclear data parameters, for example, fuel enrichment.

Figure 2 shows a flow chart for the CASMO-5MX/DP technique. The basic sequence is to begin with a perturbation factor of unity, that is,  $p = 1$ , and perform the nominal calculation. After the base calculation, depending on the specific DP mode chosen (see Table 1), the DP driver will select and perform additional perturbed cases. Using the resultant  $y^{(1)}$  from the first perturbed case, the DP driver can now calculate a sensitivity coefficient,  $S$ . In the “2-point simple” mode, DP would stop here, using simple finite differences (i.e., linear fit) for the estimate of  $S$ . In the “3-point adaptive” mode, a second calculation is performed with  $p$  estimated such that the new  $y^{(2)}$  satisfies a “small but not too small” criterion; for example, only the three least significant digits show variation.  $S$  is updated using a linear fit of  $y$  and  $y^{(2)}$ . In the “4-point adaptive” mode, one additional perturbed case allows a parabolic fit with  $S$  estimated as the slope of the fit at  $p = 1$ .

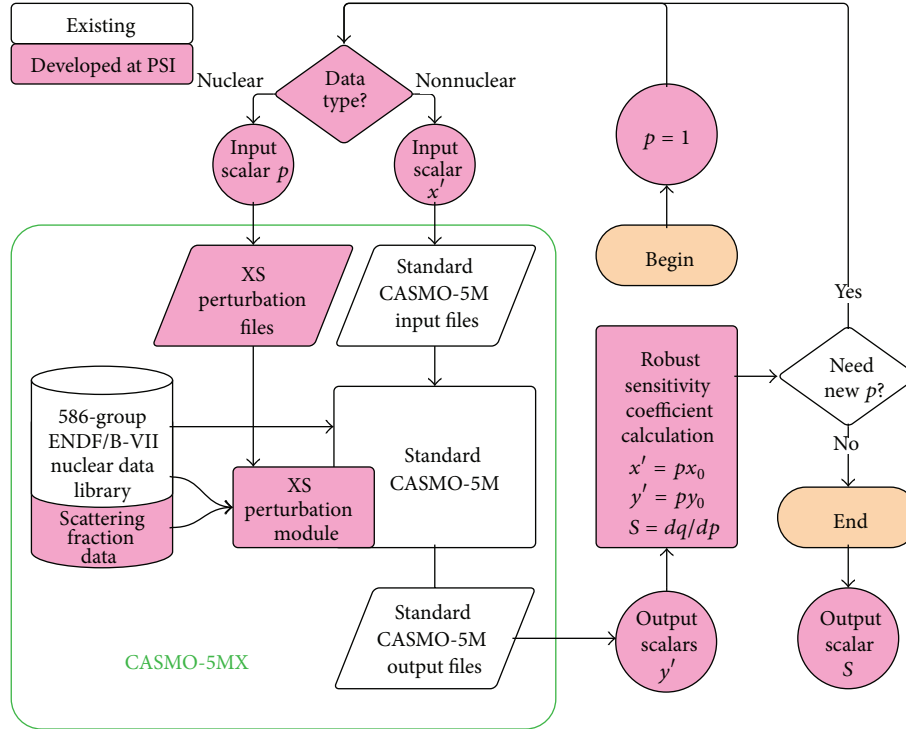


FIGURE 2: Flowchart of CASMO-5MX/DP direct perturbation methodology.

TABLE 1: Summary of DP modes.

DP mode	Available results	Fit used to estimate $S$
2-point simple	$y, y^{(1)}$	Linear (not robust)
3-point adaptive	$y, y^{(1)}, y^{(2)}$	Linear using $y, y^{(2)}$
4-point adaptive	$y, y^{(1)}, y^{(2)}, y^{(3)}$	Parabolic using $y, y^{(2)}, y^{(3)}$

Although Figure 2 is shown assuming a single output, CASMO-5MX/DP can effectively produce sensitivity coefficients for all outputs simultaneously, especially with the 4-point adaptive scheme. Figure 2 also makes the distinction that nuclear data perturbations are based on relative perturbation  $p$  and affect the XS perturbation file, whereas perturbations of general input file parameters result in replacement of  $x$  in the standard input file with  $x'$ . Once sensitivity coefficients  $S$  are available, UQ may be performed using standard first-order uncertainty propagation via (3).

**2.3. Stochastic Sampling with CASMO-5MX.** The CASMO-5MX stochastic sampling (SS) methodology from [9], shown in Figure 3, uses a very similar framework to the DP methodology (Figure 2). The major differences are summarized below.

- (1) DP varies a single input parameter at a time ( $x_0 \rightarrow x'$ ) whereas SS varies them all simultaneously ( $\mathbf{x}_0 \rightarrow \mathbf{x}'$ ).
- (2) DP is first a sensitivity analysis technique and with UQ possible through local and first-order uncertainty propagation, whereas SS is first a UQ technique

(global and all-order) with approximation due to a finite sample size.

- (3) Due to the adaptive nature, the robust DP presented requires serial execution of up to 4 cases (although sensitivities of different inputs may be investigated simultaneously) whereas SS is inherently parallel.

The basic sequence in SS (refer to Figure 3) is as follows.

- (1) Each input is sampled  $N$  times according to their underlying probability distributions and respecting correlation to other inputs, if any. The  $n$ th sample input set contains is denoted  $\mathbf{x}^{(n)}$ , and note that the main data of the XS perturbation file is just the relative perturbations  $\mathbf{p}^{(n)}$ .
- (2) CASMO-5MX is run  $N$  times with each set of data; that is,  $n = 1, 2, \dots, N$ .
- (3) The distribution of the  $N$  sets of output is analyzed statistically, for example, with the sample variance.

Note that, in Figure 3, stages of the calculation which result in  $N$  sets of data/files are shown with a “shadow.”

**2.4. Stochastic Sampling with MCNPX/NUSS.** In parallel to CASMO-5MX/SS, activities to implement SS in the Monte Carlo code MCNPX have led to the development of MCNPX plus nuclear data uncertainty with stochastic sampling, MCNPX/NUSS, which functions very similarly to CASMO-5MX/SS, except that due to the open nature of the MCNPX ACE library format, it is possible to create perturbed nuclear

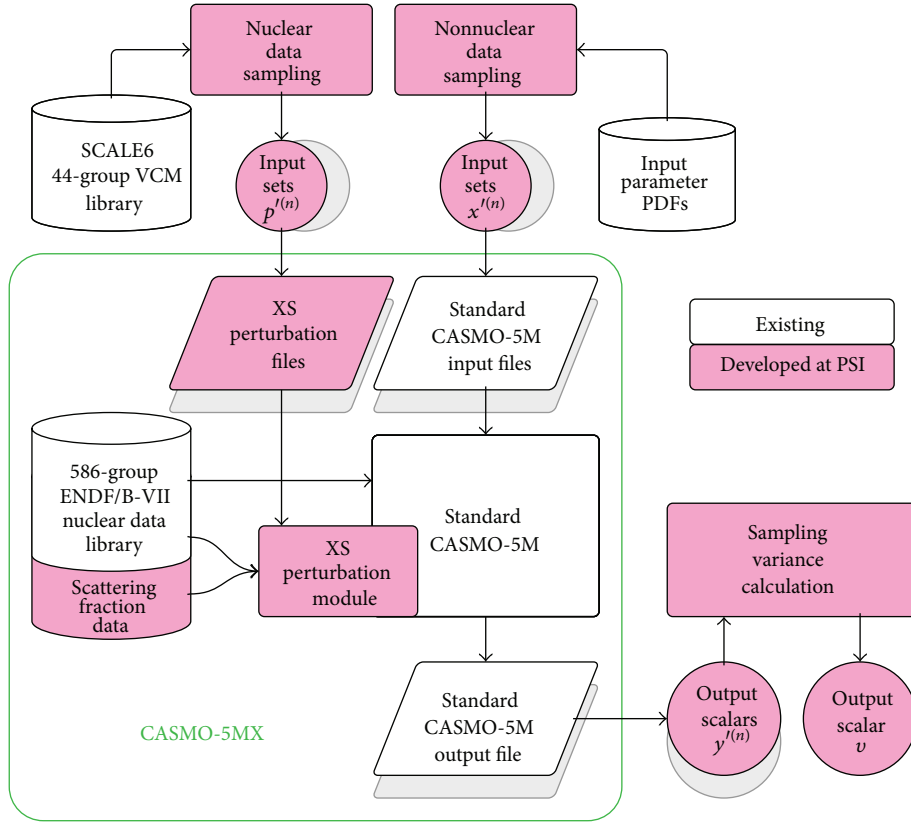


FIGURE 3: Flowchart of CASMO-5MX/SS stochastic sampling methodology.

data libraries and source code modification are not necessary, as shown in Figure 4. As in CASMO-5MX, the same simple random sampling procedure is used but a new tool is needed to apply perturbations  $\mathbf{p}^{(n)}$  to create the perturbed ACE library from the nominal one. Note that the decision to perturb data at the ACE library stage, instead of upstream when data is in the ENDF format, is mainly motivated by the relative ease of access to data in the ACE format. Future versions of MCNXP/NUSS may modify data at the ENDF stage.

Because the currently used VCM library is based on the SCALE 44-group structure, data perturbations  $\mathbf{p}^{(n)}$  are provided in this structure; however, the system is not restricted to any particular group structure for perturbations. In the “library rewriting” stage, a constant perturbation is applied to pointwise data:

$$x'(E) = p_g x_0(E) \quad \text{for } E^g \leq E < E^{g-1}, \quad (12)$$

for the perturbation  $p_g$  of group  $g$  which ranges from lower to upper energies,  $E^g$  and  $E^{g-1}$ . Note that with perturbation of partial cross-sections in the ACE library, the total and absorption cross-section must also be adjusted to preserve consistency in the nuclear data files. The final procedure of the MCNXP/NUSS tool is to systematically supply MCNXP calculations with the generated random ACE-formatted nuclear data files. The MCNXP outputs of interest can be analyzed by the same statistical means as in CASMO-5MX/SS, except for

a statistical error term which is inherent to the Monte Carlo calculations. When the distribution of an MCNXP output is characterized, it is important to separate the statistical variance from the variance due to data variations:

$$v = v_{\text{stats}} + v_{\text{data}}. \quad (13)$$

The magnitude of  $v_{\text{stats}}$  is related to the number of neutron histories in the Monte Carlo calculations and has been estimated to be small compared to data contribution (i.e., nuclear data) for all cases considered here.

### 3. Results

An overview of the UAM Phase I cases analyzed in this paper is provided in Table 2. Notably, there is no depletion and no soluble boron for any of these cases. In the cell cases of exercise I-1, there is no thermal expansion; however, in the PWR lattice case of exercise I-2, thermal expansion has been assumed which decreases the density and increases the size of all materials. The operating conditions of hot zero power (HZIP) and hot full power (HFP) dictate the fuel temperature ( $T_{\text{fuel}}$ ), moderator temperature ( $\rho$ ), void fraction ( $V$ ), and control rod insertion.

**3.1. CASMO-5MX Results.** This section presents CASMO-5MX results for both exercises I-1 and I-2. All uncertainty

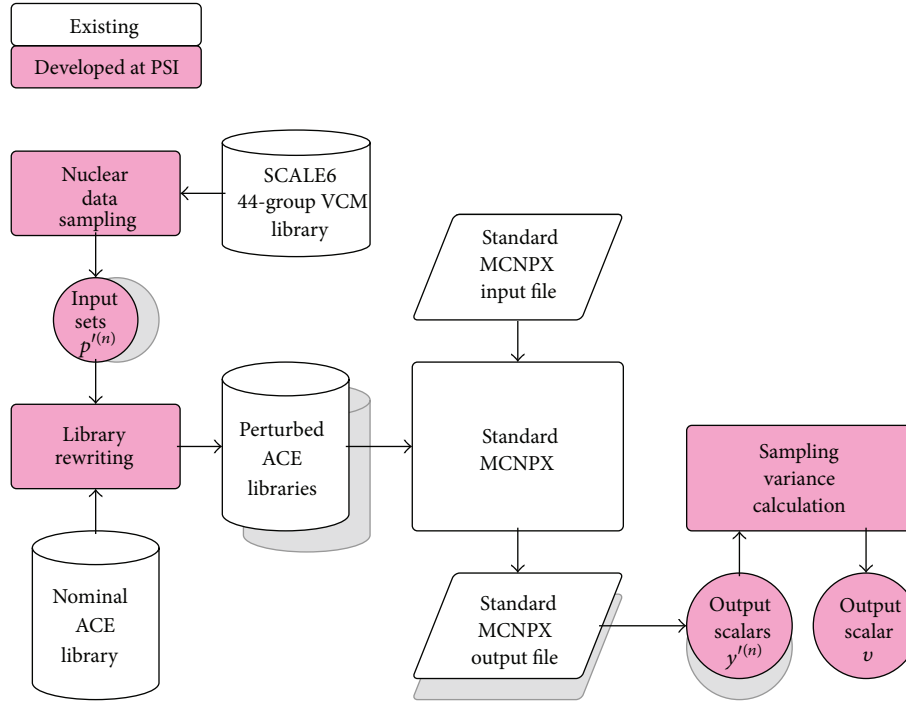


FIGURE 4: Flowchart of nuclear data UQ with MCNPX/NUSS.

TABLE 2: Overview of UAM Phase 1 cases analyzed with CASMO-5MX (C5) and MCNPX/NUSS (MC).

Exercise	Model	Fuel	Cond.	Bor. (ppm)	State point parameters				Code	
					$T_{\text{fuel}}$ (K)	$\rho$ (g/cm <sup>3</sup> )	V (%)	CR	C5	MC
I-1	PB-2 BWR cell	UO <sub>2</sub>	HZP	0	552.83	0.754	0	No	X	X
			HFP	0	900	0.461	40	No	X	—
	TMI-1 PWR cell	UO <sub>2</sub>	HZP	0	551	0.748	0	No	X	X
			HFP	0	900	0.766	0	No	X	—
GenIII cell	MOX	HFP	0	900	0.701	0	No	X	—	
I-2	TMI-1 PWR lattice	UO <sub>2</sub>	HFP	0	900	0.748	0	Yes/No	X	—

results are in terms of relative standard deviation in percent. For both CASMO-5MX/DP and SS, perturbations are made in the 19-group CASMO-5M group structure, unless otherwise noted. The number of samples used was  $N = 1000$  in all cases. *With CASMO-5MX calculations, uncertainty was assumed for all nuclides present in each problem and all reactions available in the SCALE6 VCM library.*

**3.1.1. Exercise I-1: Cell Physics.** The uncertainty summary of exercise I-1 cases is given in Table 3 for the PB-2 (BWR) cases, including results for both CASMO-5MX/DP (C5MX/DP) and CASMO-5MX/SS (C5MX/SS), and in Table 4 for the TMI-1 and Generation III (Gen-III) MOX cases, only with CASMO-5MX/SS. Results show the general trend in eigenvalue uncertainty of approximately 0.5% and 1-group cross section uncertainty of about 1% for most absorption cross sections and nuclides which have mainly thermal fission, but about 4% for nuclides which have significant fast fission. Making the spectrum harder, by introduction of 40% void

in the PB-2 HFP case or by using MOX fuel (in the Gen-III case), increases the influence of the fast spectrum, which almost always has higher uncertainty than the nuclear data in the thermal range.

To assess the effect of the perturbation group structure, two additional group structures were investigated as shown in Table 5: the next finer 31-group structure in CASMO-5 M and the 44-group structure of SCALE6. CASMO-5MX/DP was used in order to investigate the breakdown of the uncertainty, that is, which uncertain nuclear data contributed most to an uncertain output. This is presented in terms of the variance fraction, that is, the variance due to that parameter divided by the total variance, which naturally sums to unity.

The most influential parameters are easily defined by sorting from greatest to least variance fraction, and the cumulative value can be used to limit the important parameters, for example, the set representing 99% of the total variance, as shown in Figure 5 for the eigenvalue uncertainty and in Figure 6 for the 1-group U-235 fission and U<sup>238</sup> absorption

TABLE 3: Uncertainty summary for exercise I-1 PB-2 cases.

Parameter	PB-2 HZP		PB-2 HFP	
	C5MX/DP	C5MX/SS	C5MX/DP	C5MX/SS
Eigenvalue	1.3454 ± 0.55%	0.54%	1.2290 ± 0.66%	0.66%
U-235 abs.	60.5 b ± 0.99%	1.01%	40.7 b ± 1.22%	1.23%
U-235 fis.	49.7 b ± 1.01%	1.02%	32.8 b ± 1.23%	1.23%
U-238 abs.	0.915 b ± 1.08%	1.09%	0.852 b ± 1.07%	1.10%
U-238 fis.	0.0939 b ± 3.70%	3.76%	0.0882 b ± 4.51%	4.55%

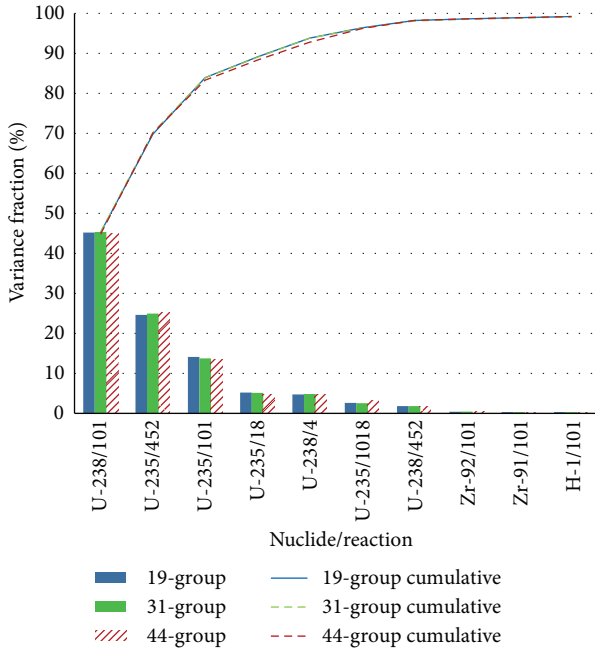


FIGURE 5: Breakdown of eigenvalue uncertainty as function of perturbation group structure for the PB-2 HZP cell case.

cross section uncertainty. Good agreement between the uncertainty breakdowns is observed except for the U-235 fission spectrum (MT = 1018) component which increases considerably with the 44-group structure. As shown in Figure 7, this was found due to the coarse fast groups in the CASMO-5 M 19- and 31-group structures and the highly varying U-235 fission spectrum uncertainty in the fast range in the native 44-groups. Because all perturbations are applied to the CASMO-5MX 586-group library structure, detailed sensitivity profiles may be generated as shown in Figure 7.

3.1.2. *Exercise I-2: Lattice Physics.* The lattice physics cases in exercise I-2 are concerned with propagating both nuclear data uncertainty and the so-called “technological parameter” uncertainty to the two-group nodal data used in conventional core simulators based on two-group nodal diffusion. The output parameters of interest here are mainly the homogenized macroscopic cross sections for fast and thermal absorption ( $\Sigma_a^1$  and  $\Sigma_a^2$ ), neutron production ( $\nu\Sigma_f^1$  and  $\nu\Sigma_f^2$ ), removal ( $\Sigma_{rem}$ ), diffusion coefficients ( $D^1$  and  $D^2$ ), and assembly

TABLE 4: Uncertainty summary for exercise I-1 TMI-1 and Gen-III MOX cases.

Parameter	TMI-1 HZP	TMI-1 HFP	Gen-III MOX
Eigenvalue	1.4293 ± 0.50%	1.4099 ± 0.51%	1.1076 ± 0.95%
U-235 abs.	43.6 b ± 1.05%	42.4 b ± 1.06%	15.2 b ± 1.37%
U-235 fis.	35.3 b ± 1.05%	34.3 b ± 1.07%	11.0 b ± 1.19%
U-238 abs.	0.911 b ± 1.10%	0.934 b ± 1.11%	0.893 b ± 1.14%
U-238 fis.	0.101 b ± 3.59%	0.101 b ± 3.62%	0.118 b ± 3.69%
Pu-239 abs.			27.3 b ± 1.23%
Pu-239 fis.			17.6 b ± 1.30%
Pu-240 abs.			21.7 b ± 1.33%
Pu-240 fis.			0.639 b ± 2.10%
Pu-241 abs.			31.6 b ± 1.28%
Pu-241 fis.			23.7 b ± 1.30%
Pu-242 abs.			11.9 b ± 5.03%
Pu-242 fis.			0.492 b ± 4.85%
Am-241 abs.			32.8 b ± 4.41%
Am-241 fis.			0.753 b ± 2.62%

TABLE 5: Effect of changing the perturbation group structure for the PB-2 HZP cell case.

Parameter	Perturbation group structure		
	19-group	31-group	44-group
Eigenvalue	0.55%	0.55%	0.54%
U-235 abs.	0.99%	0.99%	0.92%
U-235 fis.	1.01%	1.02%	0.94%
U-238 abs.	1.08%	1.07%	1.03%
U-238 fis.	3.70%	3.67%	3.73%

discontinuity factors (ADF<sup>1</sup> and ADF<sup>2</sup>). A summary of nodal parameters’ nominal values and uncertainties are shown in Table 6 for the TMI-1 PWR assembly at HFP conditions only, with control rods out (unrodded) and in (rodded), considering only nuclear data uncertainty. Additionally, the uncertainty in pin powers was examined at 3 locations: (i) the location of the unrodded case peak power (unr. peak loc.), (ii) the location of the rodded case peak power (rod. peak loc.), and (iii) the gadolinium pin power (Gd pin loc.). See Figure 8 for the locations in the southeast quarter of the 17×17 PWR assembly. The uncertainty in unrodded assembly pin powers was remarkably low; only for the gadolinium pin

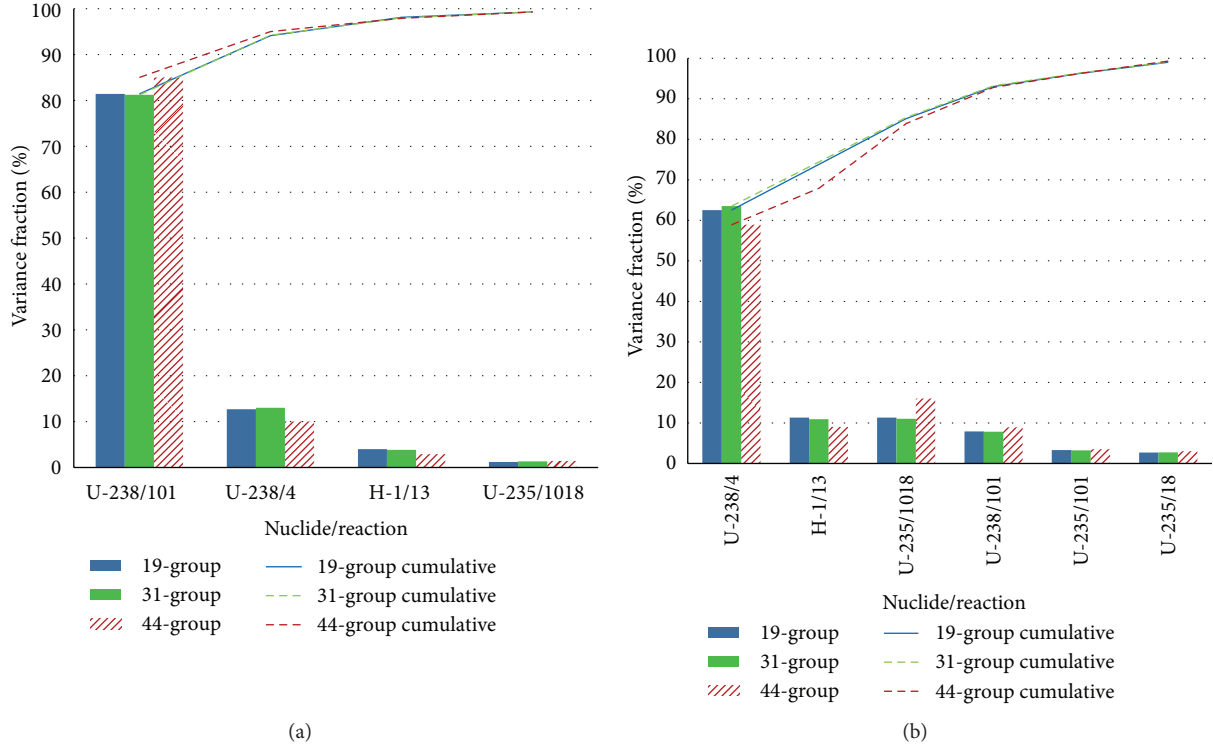


FIGURE 6: Breakdown of 1-group U-238 absorption cross section uncertainty (a) and U-235 fission cross section uncertainty (b) in terms of variance fractions for the PB-2 HZP cell case.

TABLE 6: Uncertainty summary for the exercise I-2 TMI-1 HFP case, assuming only nuclear data uncertainty.

Parameter	Unrodded		Rodded	
	DP	SS	DP	SS
Eigenvalue	$1.3997 \pm 0.50\%$	0.50%	$1.0284 \pm 0.53\%$	0.53%
$\Sigma_a^1$	$0.01 \pm 0.87\%$	0.91%	$0.0133 \pm 0.94\%$	0.99%
$\Sigma_a^2$	$0.108 \pm 0.21\%$	0.22%	$0.136 \pm 0.18\%$	0.18%
$\nu\Sigma_f^1$	$0.00861 \pm 0.50\%$	0.51%	$0.00851 \pm 0.49\%$	0.49%
$\nu\Sigma_f^2$	$0.186 \pm 0.44\%$	0.45%	$0.190 \pm 0.44\%$	0.45%
$\Sigma_{rem}$	$0.0158 \pm 1.03\%$	1.07%	$0.0137 \pm 1.18\%$	1.20%
$D^1$	$1.43 \pm 0.83\%$	0.86%	$1.39 \pm 0.88\%$	0.89%
$D^2$	$0.372 \pm 0.01\%$	0.02%	$0.376 \pm 0.02\%$	0.02%
Unr. peak loc.	$1.09 \pm 0.03\%$	0.04%	$0.802 \pm 0.06\%$	0.11%
Gd pin loc.	$0.405 \pm 0.56\%$	0.51%	$0.506 \pm 0.63\%$	0.50%
Rod. peak loc.	$0.951 \pm 0.04\%$	0.05%	$1.26 \pm 0.14\%$	0.12%
ADF <sup>1</sup>	$0.975 \pm 0.04\%$	0.04%	$1.020 \pm 0.05\%$	0.05%
ADF <sup>2</sup>	$1.070 \pm 0.03\%$	0.03%	$1.470 \pm 0.06\%$	0.06%

is the uncertainty greater than 0.1%. In the rodded assembly, pin power uncertainty was slightly greater, on the order of 0.2% for most pins.

At the time of this publication, the probability distributions of the technological parameters were not generally agreed upon, and so only a sensitivity analysis has been

performed using CASMO-5MX/DP which can easily compute sensitivity coefficients of any input file parameter. As in the benchmark specification, five technological parameters were considered: fuel density ( $fdens$ ), fuel enrichment ( $enr$ ), fuel pellet radius ( $rfuel$ ), clad thickness ( $tclad$ ), and gap thickness ( $tgap$ ). The sensitivity coefficients with respect to each technological parameter are shown in Table 7. One generally sees the highest sensitivity to the radius of the fuel pellet ( $rfuel$ ) which can be over 1% variation in an output per 1% variation in pellet radius.

**3.2. MCNPX Results.** Results obtained with MCNPX/NUSS for eigenvalue uncertainty in the PB-2 and TMI-1 cell models at HZP are shown in Table 8. Simultaneous variations were performed for U-235 and U-238 reactions, consistent with CASMO-5MX/SS with one exception; the  $(n, \gamma)$  partial cross-section (MT = 102) is considered explicitly in MCNPX and not the total capture (MT = 101) as in CASMO-5 M. For some nuclides with significant  $(n, \alpha)$  reactions, comparisons would not be consistent as MT = 101 includes  $(n, \alpha)$  but MT = 102 does not, but for U-235 and U-238, the difference between  $(n, \gamma)$  and total capture is minor. Due to the long runtimes of MCNPX calculations, only  $N = 80$  samples were made; however, this achieved statistical uncertainty more than two orders of magnitude less than the data uncertainty for these cases.

Although the number of samples was fairly small at 80, a study of the running average eigenvalue and uncertainty

TABLE 7: Sensitivity summary with respect to technological parameters for exercise I-2 TMI-1 HFP (values > 0.5 shown in bold).

Parameter	Unrodded					Rodded				
	<i>enr</i>	<i>fdens</i>	<i>tgap</i>	<i>tclad</i>	<i>rfuel</i>	<i>enr</i>	<i>fdens</i>	<i>tgap</i>	<i>tclad</i>	<i>rfuel</i>
eigenvalue	0.13	-0.05	0.00	-0.03	-0.29	0.26	0.11	-0.01	-0.05	-0.10
$\Sigma_a^1$	0.27	<b>0.72</b>	0.00	-0.01	<b>1.41</b>	0.16	<b>0.51</b>	0.00	-0.01	<b>0.92</b>
$\Sigma_a^2$	<b>0.61</b>	<b>0.67</b>	0.00	-0.02	<b>1.39</b>	<b>0.51</b>	<b>0.56</b>	0.00	-0.02	<b>1.17</b>
$\nu\Sigma_f^1$	<b>0.63</b>	<b>0.87</b>	0.00	-0.03	<b>1.59</b>	<b>0.63</b>	<b>0.86</b>	0.00	-0.03	<b>1.52</b>
$\nu\Sigma_f^2$	<b>0.76</b>	<b>0.73</b>	0.00	-0.02	<b>1.57</b>	<b>0.77</b>	<b>0.75</b>	0.00	-0.03	<b>1.56</b>
$\Sigma_{rem}$	-0.17	-0.16	-0.03	-0.19	<b>-1.77</b>	-0.20	-0.18	-0.03	-0.22	<b>-2.06</b>
$D^1$	0.02	<b>-0.42</b>	0.01	-0.03	-0.35	0.02	-0.42	0.01	-0.04	-0.36
$D^2$	-0.02	-0.15	0.02	0.10	<b>0.61</b>	-0.02	-0.17	0.02	0.10	<b>0.61</b>
Unr. Peak Loc.	0.00	0.02	0.00	0.01	0.13	0.00	0.00	0.00	0.00	0.26
Gd Pin Loc.	0.33	0.23	0.01	0.07	<b>0.72</b>	0.25	0.10	0.01	0.05	<b>1.02</b>
Rod. Peak Loc.	0.07	0.07	0.00	0.00	0.15	0.00	0.00	0.00	0.00	0.00

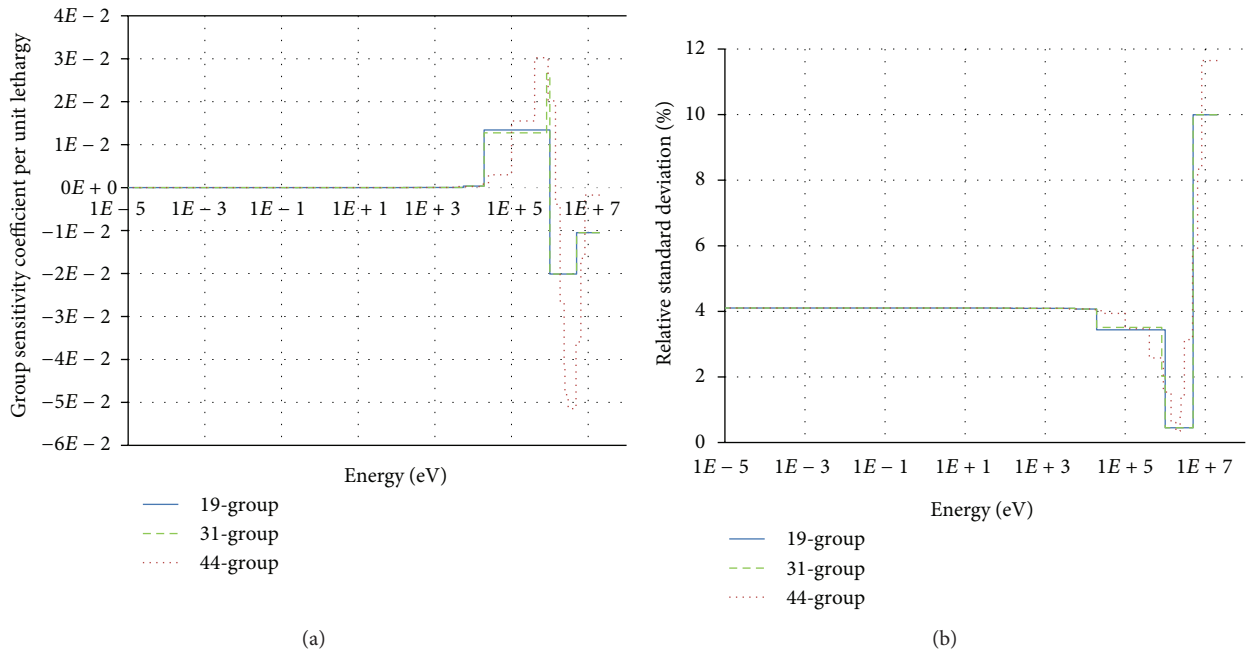


FIGURE 7: SCALE6 nuclear data uncertainty for U-235 fission spectrum, MT = 1018, (a) and sensitivity profile of the 1-group U-235 fission cross section to the U-235 fission spectrum (b) for the PB-2 HZP cell case.

TABLE 8: Uncertainty summary using MCNPX/NUSS for HZP cases.

Parameter	PB-2 HZP	TMI-1 HZP
Eigenvalue	1.3443 ± 0.54%	1.4305 ± 0.49%

(one-sigma error bars) in Figure 9 shows little sample bias in the sample mean and stable behavior of the sample standard deviation. Additional discussion may be found in [13].

#### 4. Discussion

In this section, various results from the previous section will be further discussed, namely,

TABLE 9: Comparison of top 5 contributors for MCNPX/NUSS versus CASMO-5MX/DP for exercise I-1 PB-2 HZP.

Nuclide/reaction	MCNPX/NUSS	CASMO-5MX/DP
U-238/102	0.32%	0.37%
U-235/452	0.30%	0.27%
U-235/102	0.17%	0.20%
U-238/4	0.12%	0.12%
U-235/18	0.10%	0.12%
Total	0.54% (0.50% in top 5)	0.54% (0.53% in top 5)

- (i) BWR uncertainties predicted by both the CASMO-5MX/DP and SS methodologies,
- (ii) BWR versus PWR uncertainties,

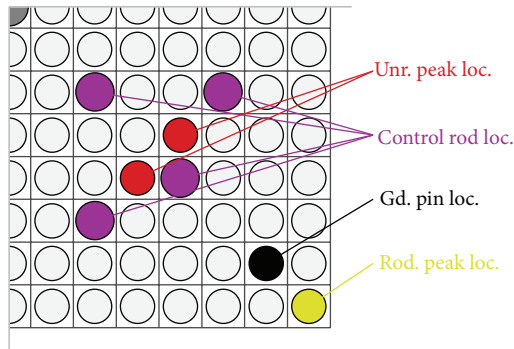


FIGURE 8: PWR assembly locations (southeast quarter shown).

- (iii) UO<sub>2</sub> versus MOX uncertainties,
- (iv) CASMO-5MX versus MCNPX/NUSS results.

**4.1. Comparison of BWR Uncertainties versus UQ Methodology.** Consistent trends are observed with both methodologies for the exercise I-1 PB-2 (BWR) case, with slightly higher uncertainties observed at HFP, both in eigenvalue (denoted “K-inf”) and 1-group cross sections, especially U-238 fission. This is due to spectrum hardening in the HFP case, with nearly 40% void, which acts to increase uncertainty because data in the fast range is generally more uncertain. For the 1-group cross sections, a faster spectrum also increases the impact of U-238 inelastic scattering, which contributes greatly to the overall uncertainty [9]. Assuming DP as a reference solution, SS shows excellent agreement (see Figure 10), with smaller eigenvalue uncertainty by less than 4% and larger cross section uncertainty by at most 3% (U-238 absorption at HFP).

**4.2. Comparison of Stochastic Sampling Uncertainties versus LWR Reactor Type.** At HZP conditions, almost identical uncertainties are observed for the exercise I-1 PB-2 (BWR) and TMI-1 (PWR) cases (see Figure 11). There is slightly larger uncertainty at HZP for the U-235 1-group cross sections due to higher enrichment in the PWR (4.85 wt%) compared to the BWR (2.93 wt%). Because of the previously discussed hardening of the spectrum for the BWR case at HFP, the uncertainty in the U-238 1-group fission cross section is noticeably higher.

**4.3. Comparison of Uncertainties for UO<sub>2</sub> and MOX Fuel Types.** For MOX fuel from the exercise I-1 Gen-III MOX case, nearly double the uncertainty (0.95%) in eigenvalue is observed compared to UOX fuel (0.51%). See the graphical summary in Figure 12. This marked increase is not only due to the higher uncertainty for the Pu isotopes but also due to the faster spectrum in those cases, which increases uncertainty due to the shift to the more uncertain fast range. Notably, Pu<sup>242</sup> and Am<sup>241</sup> 1-group cross section uncertainties are greater than 4%.

**4.4. Comparison of Uncertainties for CASMO-5MX/SS and MCNPX/NUSS.** The MCNPX results showed a total uncertainty in eigenvalue of 0.54% using MCNPX/NUSS which was very consistent with both the CASMO-5MX/SS and CASMO-5MX/DP results using the same nuclear data uncertainty but different nuclear data libraries and codes systems. Additional tests cases with one-at-a-time perturbations of single reactions have been prepared for a more detailed investigation, comparing to a breakdown from CASMO-5MX/DP, with perturbations in the SCALE6 44-group for maximum consistency with MCNPX/NUSS. The results in Table 9 show the top 5 contributors according to each methodology, and in general one sees excellent agreement. It is perhaps only interesting that CASMO-5MX/DP shows 0.53% uncertainty in the top 5 whereas MCNPX/NUSS shows 0.50%.

## 5. Conclusions

The UAM benchmark has provided the opportunity to develop state-of-the-art methodologies for uncertainty quantification (UQ) and the framework for international collaboration and comparison. At PSI, within the STARS project, the first development was CASMO-5MX, a modification of the production CASMO-5M code to perturb nuclear data libraries through an auxiliary input file with the capabilities to provide perturbations in any group structure and perturb individually the inelastic (MT = 4) and elastic (MT = 2) scattering components despite the internal use of a combined scattering matrix with elastic and inelastic scattering lumped together. Building on this capability, a sensitivity analysis (SA) tool using direct perturbation (DP) was developed, CASMO-5MX/DP, which performs adaptive perturbations in order to robustly estimate sensitivity coefficients of arbitrary outputs with respect to arbitrary inputs, including nuclear data. Using standard first-order uncertainty propagation, CASMO-5MX/DP can also be used for local, first-order UQ. However, to be used for production UQ, CASMO-5MX/DP requires too many calculations, and for these reasons, a second UQ methodology based on stochastic sampling (SS) was developed, CASMO-5MX/SS, which can provide uncertainty estimates for arbitrary outputs at a fixed cost of 100 to 1000 calculations. Most recently, development of an SS methodology for a continuous-energy, Monte Carlo code, MCNPX, was initiated, called MCNPX/NUSS.

Results for the UAM benchmark exercises were presented, including the LWR cell cases from exercise I-1 and the PWR assembly case from exercise I-2. For the cell cases, uncertainty in the eigenvalue and 1-group collapsed microscopic cross sections (in terms of relative standard deviation) was found to be about 0.5% and 1%, respectively. For the Gen-III MOX case, the eigenvalue uncertainty was nearly double (1%) and Pu-242 and Am-241 1-group cross sections uncertainties’ reached 5%. In UO<sub>2</sub> fuel, the most important contributors to the eigenvalue uncertainty were found to be U<sup>238</sup> capture (MT = 101), U<sup>235</sup> neutrons per fission (MT = 452), and U-235 capture (MT = 101), accounting for over 80% of the total variance in eigenvalue. For 1-group cross section uncertainty, U-238 inelastic scattering (MT = 4)

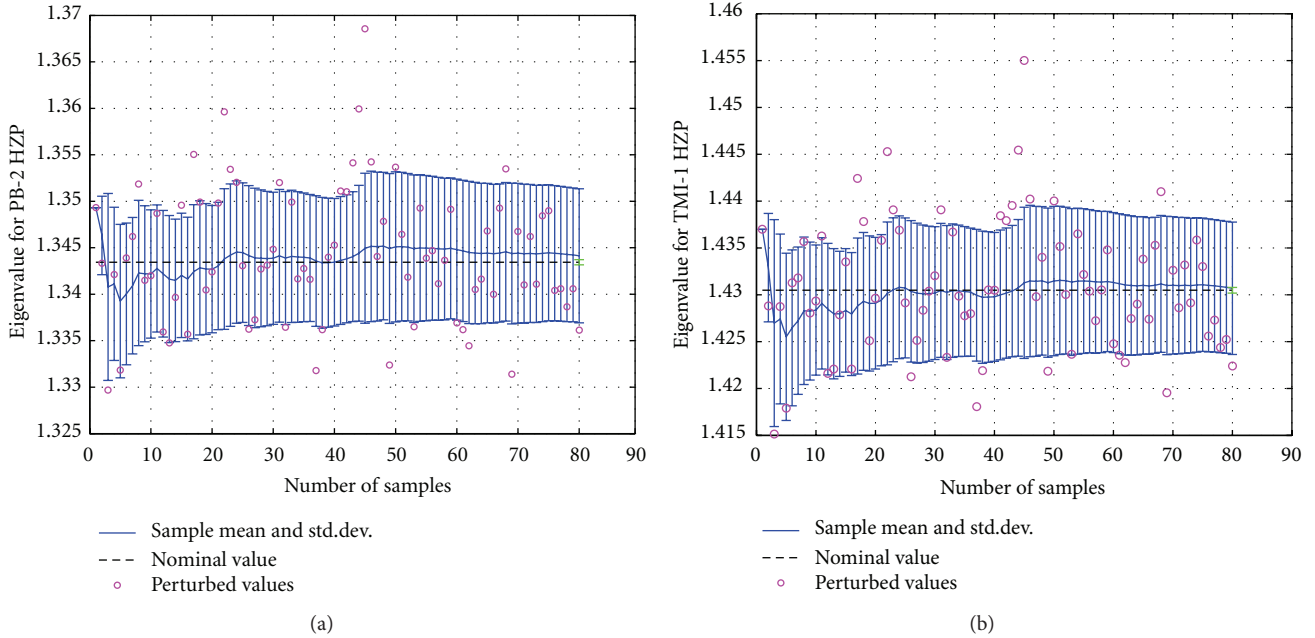


FIGURE 9: Cumulative moving average of eigenvalue with MCNPX/NUSS versus number of samples for exercise I-1 PB-2 HZP (a) and TMI-1 HZP cases (b).

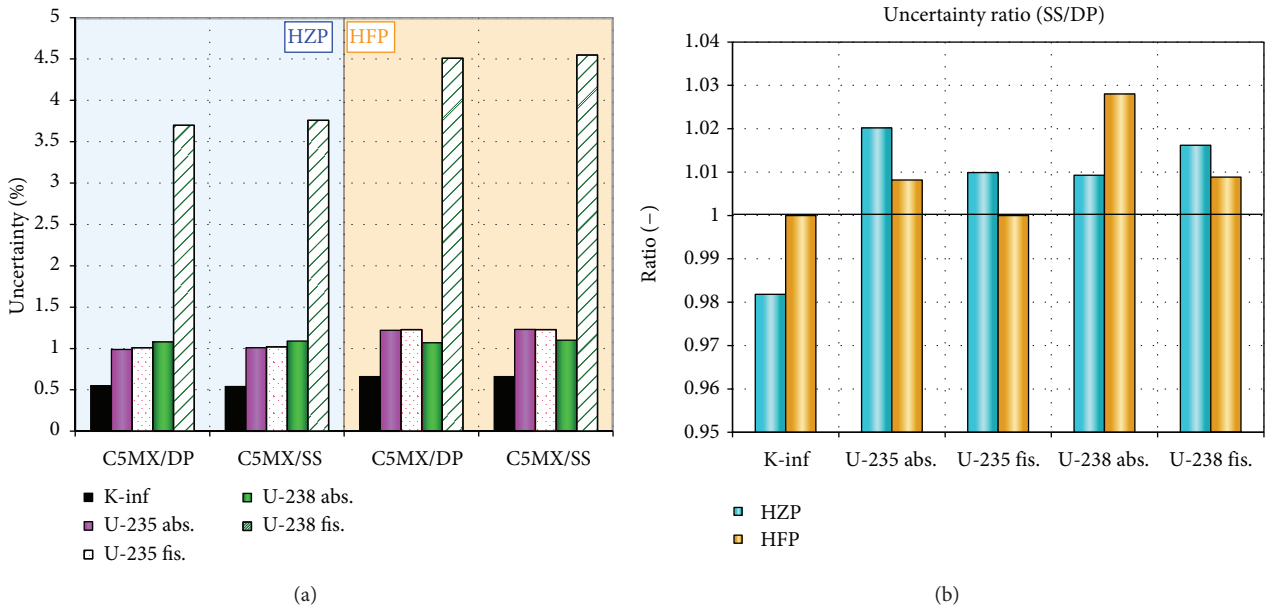


FIGURE 10: Comparison of CASMO-5MX/DP and/SS methods.

accounted for well over 50% of variance alone and usually more. For the TMI-1 PWR assembly case, uncertainty in eigenvalue was consistent with the cell cases at about 0.5%. Uncertainty in other assembly outputs ranged from less than 0.1% for the assembly discontinuity factors (ADFs), powers at the nominal peak pin locations, and the thermal diffusion coefficient ( $D^2$ ) to 1% for the fast diffusion coefficient ( $D^1$ ) and the fast absorption cross section ( $\Sigma_a^1$ ). Both rodged and unrodged cases were analyzed and uncertainty was found to

remain the same or slightly increase when control rods were inserted.

Finally, sensitivity coefficients were calculated for technological parameters for the exercise I-2 TMI-1 PWR assembly and it was found that the radius of the fuel pellet is the most sensitive parameter, having sensitivity coefficients of absolute value from 1 to 2 for many outputs. For example, the sensitivity coefficient of the removal cross section ( $\Sigma_{rem}$ ) with respect to pellet radius is  $-2.1$  for unrodged case, which

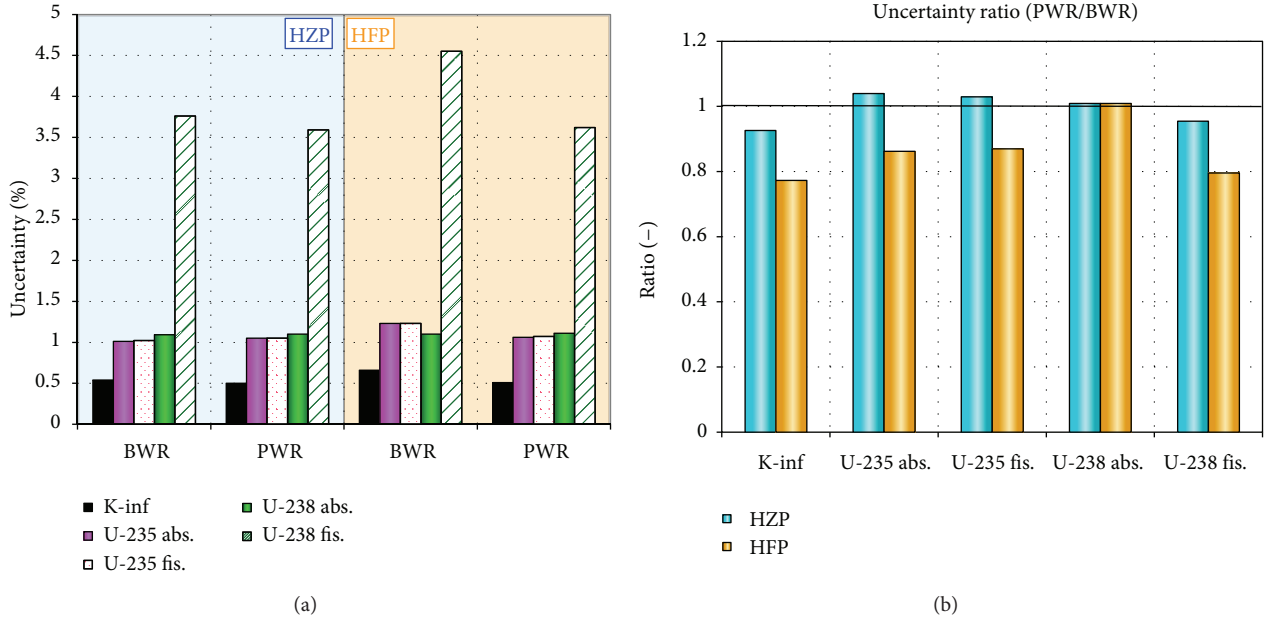


FIGURE 11: Comparison of PWR and BWR uncertainties with CASMO-5MX/SS.

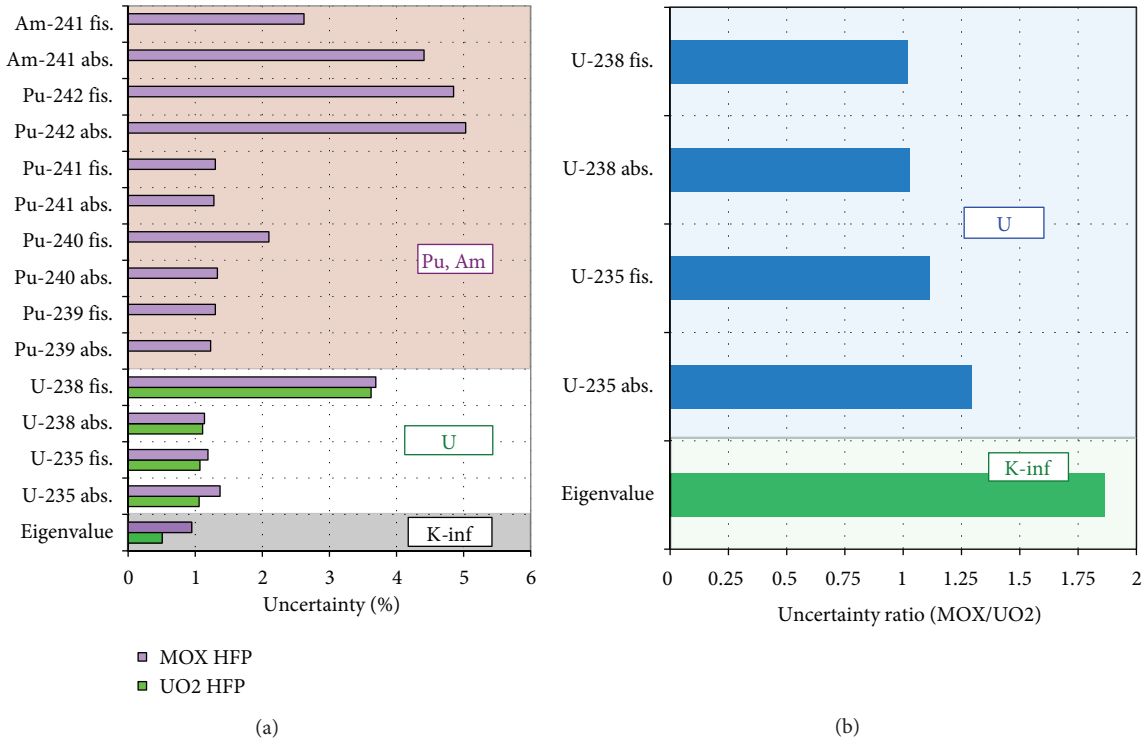


FIGURE 12: Comparison of MOX and UO2 fuel uncertainty.

means that, for a 1% change in pellet radius,  $\Sigma_{rem}$  will decrease by 2%! It is clear, however, that a better understanding of the distributions of the technological parameters is necessary, and in particular, how the batch-based nature of manufacturing introduces correlations across the fuel pellets, assemblies. For example, should all the fuel pellets in a single assembly be considered to come from the same batch, different batches, or

a fixed number of batches? If a fixed number of batches, how is it determined which pellets are from which batch? Answering these questions requires either more knowledge of how a particular fuel assembly was manufactured or simulation of the actual manufacturing processes! Otherwise, conservative, limiting cases must be created, which is in direct opposition to the overarching goal of best estimate analyses with UQ.

Future work in the area of neutronics UQ at PSI includes enhancement of the MCNPX/NUSS continuous-energy Monte Carlo strategy, implementing the capability to perturb fission product yields and decay constants, and extension of the SS methodology from the lattice code CASMO-5 M to the core simulator SIMULATE-3.

## References

- [1] OECD Report, "Technology relevance of the uncertainty analysis in modelling project for nuclear reactor safety," NEA/NSC/DOC, 2007.
- [2] <http://stars.web.psi.ch>.
- [3] W. Wieselquist, A. Vasiliev, and H. Ferroukhi, "Towards an uncertainty quantification methodology with CASMO-5," in *Proceedings of the Mathematics and Computations Division of the American Nuclear Society Topical Meeting (M&C '11)*, Rio de Janeiro, Brazil, May 2011, CD-ROM.
- [4] "SCALE: A Modular Code System for Performing Standardized Computer Analyses for Licensing Evaluations," ORNL/TM-2005/39, Version 6, Vols. III, 2009.
- [5] D. L. Smith, *Probability, Statistics, and Data Uncertainties in Nuclear Science and Technology*, American Nuclear Society, USA, 1991.
- [6] M. Klein, L. Gallner, I. Pasichnyk, A. Pautz, and W. Zwermann, "Influence of nuclear data covariance on reactor core calculations," in *Proceedings of the Mathematics and Computations Division of the American Nuclear Society Topical Meeting (M&C '11)*, on CD-ROM, Rio de Janeiro, Brazil, May 2011.
- [7] D. Rochman, A. J. Koning, S. C. Van Der Marck, A. Hogenbirk, and C. M. Sciolla, "Nuclear data uncertainty propagation: perturbation vs. Monte Carlo," *Annals of Nuclear Energy*, vol. 38, no. 5, pp. 942–952, 2011.
- [8] R. Macian, M. A. Zimmermann, and R. Chawla, "Statistical uncertainty analysis applied to fuel depletion calculations," *Journal of Nuclear Science and Technology*, vol. 44, no. 6, pp. 875–885, 2007.
- [9] W. Wieselquist, A. Vasiliev, and H. Ferroukhi, "Nuclear data uncertainty propagation in a lattice physics code using stochastic sampling," in *Proceedings of the International Topical Meeting on Advances in Reactor Physics (PHYSOR '12)*, Knoxville, Tenn, USA, April 2012, on CD-ROM.
- [10] S. S. Wilks, "Determination of sample sizes for setting tolerance limits," *The Annals of Mathematical Statistics*, vol. 12, no. 1, pp. 91–96, 1941.
- [11] M. Pusa, "Incorporating sensitivity and uncertainty analysis to a lattice physics code with application to CASMO-4," *Annals of Nuclear Energy*, vol. 40, no. 1, pp. 153–162, 2012.
- [12] I. Kodeli, "ANGELO-LAMBDA Covariance matrix interpolation and mathematical verification," NEA-DB Computer Code Collection, NEA-1798/02, 2008.
- [13] T. Zhu, A. Vasiliev, W. Wieselquist, and H. Ferroukhi, "Stochastic sampling method with MCNPX for nuclear data uncertainty propagation in criticality safety applications," in *Proceedings of the International Topical Meeting on Advances in Reactor Physics (PHYSOR '12)*, Knoxville, Tenn, USA, April 2012, on CD-ROM.

## Research Article

# SCALE Modeling of Selected Neutronics Test Problems within the OECD UAM LWR's Benchmark

Luigi Mercatali,<sup>1</sup> Kostadin Ivanov,<sup>2</sup> and Victor Hugo Sanchez<sup>1</sup>

<sup>1</sup> Karlsruhe Institute of Technology (KIT), Campus Nord, Hermann-von-Helmholtz-Platz 1, 76344 Eggenstein-Leopoldshafen, Germany

<sup>2</sup> The Pennsylvania State University (PSU), 206 Reber Building, University Park, PA 16803, USA

Correspondence should be addressed to Luigi Mercatali; [luigi.mercatali@kit.edu](mailto:luigi.mercatali@kit.edu)

Received 20 July 2012; Accepted 20 December 2012

Academic Editor: Oscar Cabellos

Copyright © 2013 Luigi Mercatali et al. This is an open access article distributed under the Creative Commons Attribution License, which permits unrestricted use, distribution, and reproduction in any medium, provided the original work is properly cited.

The OECD UAM Benchmark was launched in 2005 with the objective of determining the uncertainty in the simulation of Light Water Reactors (LWRs) system calculations at all the stages of the coupled reactor physics—thermal hydraulics modeling. Within the framework of the “Neutronics Phase” of the Benchmark the solutions of some selected test cases at the cell physics and lattice physics levels are presented. The SCALE 6.1 code package has been used for the neutronics modeling of the selected exercises. Sensitivity and Uncertainty analysis (S/U) based on the generalized perturbation theory has been performed in order to assess the uncertainty of the computation of some selected reactor integral parameters due to the uncertainty in the basic nuclear data. As a general trend, it has been found that the main sources of uncertainty are the  $^{238}\text{U}$  ( $n,\gamma$ ) and the  $^{239}\text{Pu}$  nubar for the UOX- and the MOX-fuelled test cases, respectively. Moreover, the reference solutions for the test cases obtained using Monte Carlo methodologies together with a comparison between deterministic and stochastic solutions are presented.

## 1. Introduction

In recent years there has been an increasing demand from nuclear research, industry, safety, and regulation bodies for best estimate predictions of Light Water Reactors (LWRs) performances to be provided with their confidence bounds. In addition to the establishment of LWRs best-estimate calculations for design and safety analysis, understanding uncertainties of evaluated reactor parameters is important for introducing appropriate design margins and deciding where additional efforts should be undertaken to reduce those uncertainties. In order to address those issues, an in-depth discussion on “Uncertainty Analysis in Modeling” started to take place in 2005 within the OECD/NEA Nuclear Science Committee, which led to the creation of a dedicated Expert Group and to the launching of a Benchmark exercise, the OECD UAM (Uncertainty Analysis in Modeling) LWR Benchmark [1]. The proposed technical approach is to establish a benchmark for uncertainty analysis in best-estimate modeling and coupled multiphysics and multi-scale LWR analysis, using as bases a series of well-defined problems with complete sets of input specifications and

reference experimental data. The objective is to determine the uncertainty in LWR system calculations at all stages of coupled reactor physics/thermal hydraulics calculation. The UAM benchmark has been conceived to be structured in three different phases, being Phase I the “Neutronics Phase,” Phase II the “Core Phase,” and Phase III the “System Phase.” Additionally, each benchmark phase is subdivided in a number of different Exercises in order to propagate the full chain of uncertainty in the modeling across different scales (multi-scale) and physics phenomena (multi-physics). The present paper is devoted to the solutions of some selected test problems within the Exercises I-1 and I-2 of Phase I. The Exercise I-1 is entitled “Cell Physics” and is focused on derivation of the multigroup microscopic cross-section libraries. Its objective is to address the uncertainties due to the basic nuclear data as well as the impact of processing the nuclear and covariance data, selection of multi-group structure, and self-shielding treatment. Within Exercise I-1 the uncertainties in the evaluated Nuclear Data Libraries (NDLs) are propagated into multigroup microscopic cross-sections. In Exercise I-2 multi-group cross-section uncertainties are input uncertainties which are then propagated

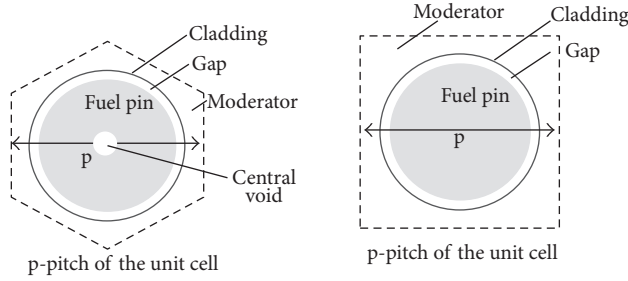


FIGURE 1: Types of geometries for the fuel pin-cell test cases within Exercise I-1.

through the lattice physics calculations to few-group cross-section uncertainties.

## 2. Description of the Test Cases

Within the framework of Exercise I-1 different fuel pin-cell test problems have been defined representing both square and triangular pitches. The two types of basic geometries for the unit cells are schematized in Figure 1.

In this paper the following test cases have been considered.

- Two-dimensional fuel pin-cell problems representative of Boiling Water Reactor (BWR) Peach Bottom 2 (PB-2) [2], Pressurized Water Reactor (PWR) Three Mile Island 1 (TMI-1) [3], and Koyloduz-6 VVER-1000 [4]. Each pin-cell model has to be analyzed at Hot Full Power conditions (HFP) as well as at Hot Zero Power conditions (HZP). To enhance the differences between the three cases (PWR, BWR, and VVER) the HFP case of the BWR is defined to be calculated at 40% void fraction (with a corresponding moderator density ( $\rho$ ) of  $460.72 \text{ kg/m}^3$ ) instead of 0%. Hence the PWR and BWR cases are for square pitch but with different spectra, while the VVER case is for triangular pitch.
- Fuel pin-cell test problems from the KRITZ-2 LEU critical experiments [5].
- PWR MOX (MOX 9.8% Pu) pin-cell case representative of Generation 3 PWR designs, which in the following text of this paper will be referred to as GEN-III [6].

Within Exercise I-2, different stand-alone neutronics single Fuel Assembly (FA) and minicore test problems have been proposed. In this paper we will present the solutions for the following test cases.

- BWR PB-2 assembly model [2]: the assembly “type 2” of the initial loading of the Peach Bottom 2 nuclear power plant is chosen for this exercise.
- PWR TMI-1 assembly model [3].
- GEN-III assembly models [6]: one MOX and three UOX FAs types with different  $^{235}\text{U}$  enrichment and Gd content are available for this exercise.

The parameter specifications as well as the operating conditions for all the test cases analyzed in the present paper are summarized in Table 1. The six types of FAs considered in our analysis are shown in Figure 2.

## 3. Theoretical Approach and Computational Method

The basic problem of the neutronics is the solution of the integral-differential Boltzmann equation for the neutron transport, which is a linear equation requiring the treatment of seven independent variables: three in space, two in angle, one in energy of the incident neutrons, and time. As a consequence of such a complexity, one has to keep in mind that even if the accuracy in the predictions of the modern transport codes (both Monte Carlo and deterministic) is continuously improving, there will be always approximations introduced in the calculational procedure. Examples of uncertainties are the ones originated from the basic nuclear reaction data, from the geometrical description of the problem, and from the material compositions. The knowledge of the approximations used in the analysis and of the overall calculational uncertainties is therefore essential to gain confidence in the results obtained, and sensitivity analysis and uncertainty evaluation (S/U) are the main instruments for dealing with the sometimes scarce knowledge of the input parameters used in the simulation tools [8]. For sensitivity analysis, sensitivity coefficients are the key quantities that have to be evaluated. They are determined and assembled, using different methodologies, in a way that when multiplied by the variation of the corresponding input parameter, they will quantify the impact on the targeted quantities whose sensitivity is referred to. There are two main methodologies developed for sensitivity and uncertainty analysis. One is the forward (direct) calculation method based either on the numerical differentiation or on a stochastic method, and the other is the adjoint method based on the perturbation theory [9]. In general, the forward approach is preferable when there are few input parameters that can vary and many output parameters of interest. The contrary is true for the adjoint methodology, which is the one mainly adopted in reactor physics, as the source of uncertainty is mainly related to the neutron cross-sections that can represent a very notable number of variables (up to several hundred thousand). Moreover, the linear property of the Boltzmann equation makes the adjoint approach even more attractive. Since all the analysis for the benchmark cases presented in this paper has been carried out using perturbation methodologies, let us briefly recall the theoretical background of these techniques.

From a general point of view one can represent a generic integral reactor parameter  $Q$  (i.e., the  $k_{\text{eff}}$ , a reactivity coefficient, a reaction rate, etc.) as a function of cross-sections:

$$Q = f(\sigma_1, \sigma_2, \dots, \sigma_j), \quad (1)$$

where  $\sigma_1, \sigma_2, \dots, \sigma_j$  represent cross sections by isotope, type of reaction, and energy range (or energy group in a multi-group representation).

TABLE 1: Pin-cell data for the test cases of Exercises I-1 and Exercise I-2.

Parameter	BWR	PWR	VVER	KRITZ-2:1	GEN-III
FA geometry	7 × 7	15 × 15	—	—	17 × 17
FA pitch (mm)	152.4	218.11	—	—	216.1
Fuel rods per assembly	49	208	—	—	265
Number of guide tubes per FA	—	16	—	—	24
Number of instrumentation tubes per FA	—	1	—	—	—
Number of Gd pins per FA	—	4	—	—	—
Guide tube outside diameter (mm)	—	13.462	—	—	12.07
Guide tube inside diameter (mm)	—	12.649	—	—	11.27
Instrumentation tube outside diameter (mm)	—	12.522	—	—	—
Instrumentation tube inside diameter (mm)	—	11.201	—	—	—
Unit cell (mm)	18.75	14.427	12.75	14.85	12.62
Fuel pellet diameter (mm)	12.1158	9.391	7.56	10.58	8.253
Fuel pellet material	UO <sub>2</sub>	UO <sub>2</sub>	UO <sub>2</sub>	UO <sub>2</sub>	MOX
Fuel density (g/cm <sup>3</sup> )	10.42	10.283	10.4	—	—
Fuel enrichment (w/o)	2.93	4.85	3.3	1.86	9.8 (Pu)
Central void diameter (mm)	—	—	1.4	—	—
Central void material	—	—	Dry air	—	—
Cladding outside diameter (mm)	14.3002	10.928	9.1	12.25	9.487
Cladding thickness (mm)	0.9398	0.673	0.69	0.74	0.578
Cladding material	Zircaloy-2	Zircaloy-4	Zr + 1% Nb	Zircaloy-2	Zircaloy-4
Cladding density (g/cm <sup>3</sup> )	6.55	6.55	—	—	—
Gap material	He	He	He	He	He
Moderator material	H <sub>2</sub> O				
Fuel temperature (K)					
HZP	552.833	551	552.15	292.7	—
HFP	900	900	900	521.5	900
Cladding temperature (K)					
HZP	552.833	551	552.15	—	—
HFP	600	600	600	—	610
Moderator temperature (K)					
HZP	552.833	551	552.15	—	—
HFP	557	562	560	—	584
Moderator density (kg/m <sup>3</sup> )					
HZP	753.978	766	767	—	—
HFP	460.72	748.4	752.5	—	—

The variation of  $Q$  due to variations of cross-sections  $\sigma$  can be expressed using perturbation theories to evaluate the sensitivity coefficients  $S$  as follows [8–12]:

$$\frac{\delta Q}{Q} = \sum_j S_j \frac{\delta \sigma_j}{\sigma_j}, \quad (2)$$

where the sensitivity coefficients are formally given by

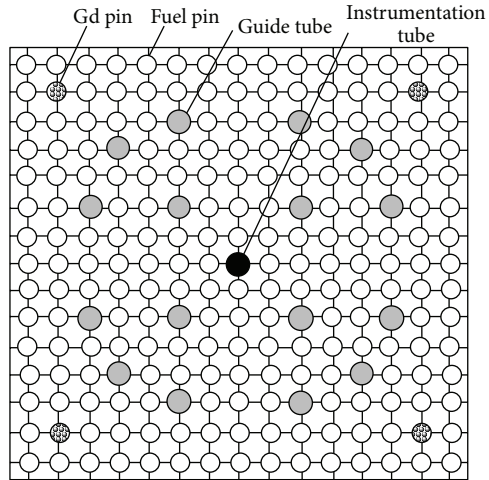
$$S_j = \frac{\partial Q}{\partial \sigma_j} \cdot \frac{\sigma_j}{Q}. \quad (3)$$

For practical purposes, one can consider the sensitivity coefficient as divided into two components as follows:

$$\frac{\delta Q}{Q} = \sum_j S_j \frac{\delta \sigma_j}{\sigma_j} + \left( \frac{\partial Q}{\partial \sigma^e} \cdot \frac{\sigma^e}{Q} \right) \cdot \frac{\delta \sigma^e}{\sigma^e} = I + D, \quad (4)$$

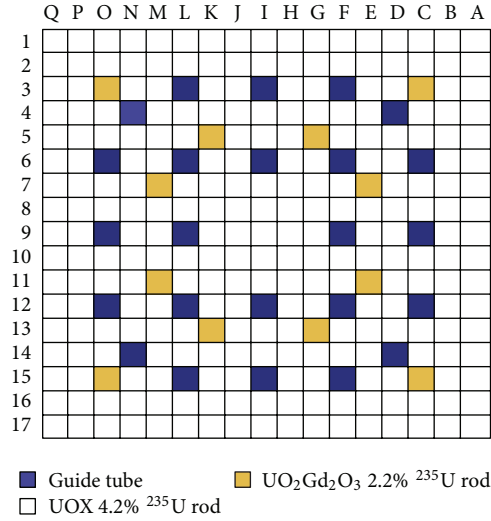
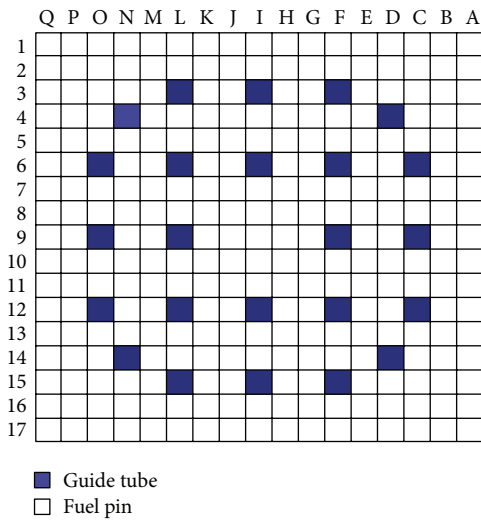
where the terms  $I$  and  $D$  are generally referred to as “indirect” and “direct” effect, respectively. The  $D$  term in (4) reflects the hypothesis of a direct dependence of the parameter  $Q$  on only the energy dependent detector cross-section  $\sigma^e$ . The  $I$  term in (4) is the response perturbation due to flux perturbations. The indirect term of (4) consists also of two components, namely, the explicit and implicit ones [13]. The explicit component of the indirect effect comes from the flux perturbation caused by perturbing any multi-group cross-section appearing explicitly in the transport equation. The implicit component of the indirect effect is associated with self-shielding perturbations; in other words perturbing the cross section of one nuclide may change the self-shielded cross section of another nuclide, which causes additional flux perturbations. As an example if one considers the hydrogen, perturbing the H elastic value has an explicit effect because

4	3	3	2	2	2	3
3	2	1	1	1	1	2
3	1	5A	1	1	5A	1
2	1	1	1	1	1	1
2	1	1	1	6B	1	1
2	1	5A	1	1	1	2
3	2	1	1	1	2	2



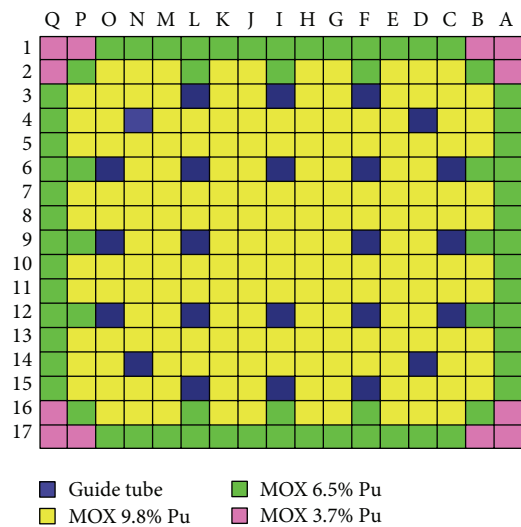
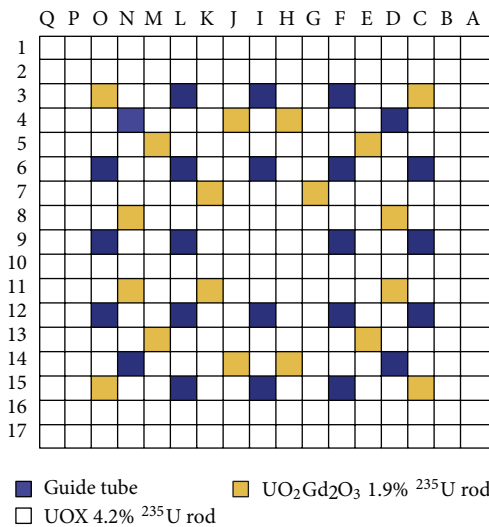
(a)

(b)



(c)

(d)



(e)

(f)

FIGURE 2: FAs for the test cases of Exercise I-2: BWR (a), PWR (b), GEN-III Type 1 (c), GEN-III Type 2 (d), GEN-III Type 3 (e), and GEN-III Type 4 (f).

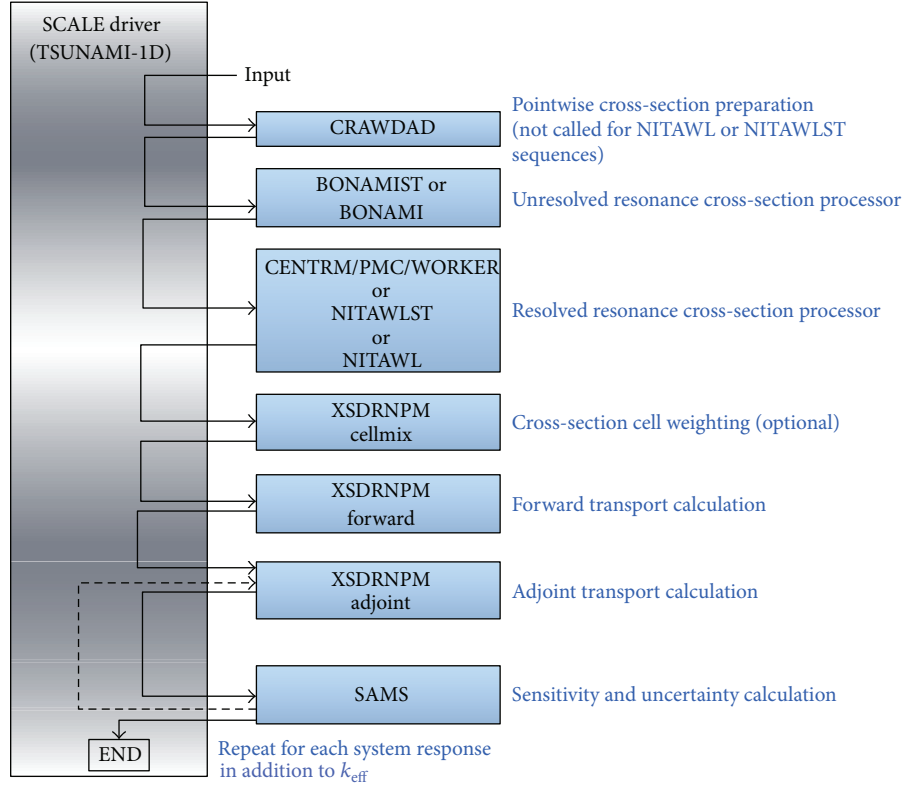


FIGURE 3: General flow diagram of the TSUNAMI code [7].

the flux is perturbed due to changes in H moderation. However there is also an implicit effect because changing the H data perturbs the self-shielded  $^{238}\text{U}$  absorption cross section, which causes another flux perturbation.

Let us now consider a ratio response  $R$  characterized by the macroscopic cross-sections  $\Sigma_1$  and  $\Sigma_2$  as follows:

$$R = \frac{\langle \Sigma_1 \Phi \rangle}{\langle \Sigma_2 \Phi \rangle}, \quad (5)$$

where in (5) the brackets  $\langle, \rangle$  indicate the integration over the phase space and  $\Phi$  is the homogeneous flux. In this case the sensitivity coefficients are given by

$$S_j^R = \langle \underline{\Psi}, \sigma_j \Phi \rangle, \quad (6)$$

where  $\underline{\Psi}_R^*$  is the solution of

$$M^* \underline{\Psi}_R^* = \frac{dR}{d\Phi}, \quad (7)$$

where  $M^*$  is the adjoint Boltzmann operator. The uncertainties associated to the cross-section can be represented in the form of a variance-covariance matrix:

$$D_\sigma = \begin{bmatrix} d_{11} & \cdots & d_{1J} \\ \vdots & \ddots & \vdots \\ d_{1J} & \cdots & d_{JJ} \end{bmatrix}, \quad (8)$$

where the elements  $d_{ij}$  represent the variances and covariances of the nuclear data. Once the sensitivity coefficients and

the  $D_\sigma$  matrix are available, the variance (i.e., the uncertainty) of the generic integral parameter  $Q$  can be expressed as

$$\text{var}(Q) = \sum_{j,i}^J S_j S_i d_{ij}. \quad (9)$$

All the calculations presented in this paper have been performed by means of the SCALE 6.1 code system [14] using ENDF/B-VII.0 nuclear data [15]. SCALE (Standardized Computer Analysis for Licensing Evaluations) is a modular code system developed at Oak Ridge National Laboratory to perform analysis for criticality safety, reactor physics and radiation shielding applications. SCALE calculations typically use sequences that execute a predefined series of executable modules to compute particle fluxes and responses (multiplication factor, reaction rates, etc.). SCALE also includes modules for sensitivity and uncertainty analysis (S/U) of calculated responses. The S/U codes in SCALE are collectively referred to as TSUNAMI (Tools for Sensitivity and Uncertainty Analysis Methodology Implementation) [7, 16]. The techniques used in TSUNAMI to generate sensitivity information are based on the widely used adjoint-based perturbation theory approach described above. The flow diagram of the TSUNAMI calculations is shown in Figure 3.

The calculation procedure for the multi-group cross-section processing is based on a rigorous mechanism using the continuous energy solvers BONAMI and CENTRM [17] for self-shielding in the unresolved and resolved resonance regions, respectively, for appropriately weighting multi-group

cross-sections using a continuous energy spectrum. The CENTRM module performs transport calculation using ENDF-based point data on an ultrafine energy grid (typically 30.000–70.000 energy points) to generate effectively continuous energy neutron flux solutions in the resonance and thermal ranges. This is used to weight the multi-group cross-sections to be utilized in the subsequent transport calculations. After the cross-sections are processed, the TSUNAMI-ID sequence performs two criticality calculations, solving the forward and adjoint forms of the Boltzmann equation, respectively, using the XSDRNPM discrete ordinate code [18]. In this step an energy discretization based on a 238-group structure is adopted. The sequence then calls the SAMS module, specifically SAMS5 [19], in order to compute the sensitivity coefficients. Once sensitivities are available, the uncertainty on the integral parameters of interest due to the uncertainty in the basic nuclear data are evaluated according to (9) using the so-called 44GROUPOV covariance matrix [20]. The 44GROUPOV matrix comprehends a total of 401 materials in a 44-group energy structure. The library includes evaluated covariances obtained from ENDF/B-VII, ENDF/B-VI, and JENDL3.3 for more than 50 materials. It is assumed [20] that covariances taken from one data evaluation, such as ENDF/B-VI or JENDL-3.3, can also be applied to other evaluations of the same data, such as ENDF/B-VII. All other nuclear data uncertainties have been estimated from approximations in which the uncertainty assessment is decoupled from the original evaluation procedure.

#### 4. Results

Results for the  $k_{\text{eff}}$  values and associated uncertainties related to the benchmark test cases of Exercises I-1 and I-2 are summarized in Table 2. As expected, because of the negative fuel Doppler coefficient, the reactivities computed for all the test cases at HFP conditions are consistently lower than those at HZP conditions. The total uncertainties of the  $k_{\text{eff}}$  have been evaluated to be  $\sim 0.5\%$ – $0.6\%$  for all the test cases with the exception of the GEN-III Type 4 case within Exercise I-2 where the computed uncertainty is higher by around a factor of two because of the presence of the plutonium isotopes in the fuel (MOX fuel). In Figure 4 the five reaction cross-sections which contribute the most to the  $k_{\text{eff}}$  uncertainty for the test cases of Exercise I-1 are shown. While for the UOX-fuelled test cases the main contribution to the total uncertainty is due to the  $^{238}\text{U}(n,\gamma)$  followed by the  $^{235}\text{U}$  nubar (average number of neutrons per fission reaction— $\nu$ ) and  $^{235}\text{U}(n,\gamma)$ ; for the MOX-fuelled test case considered (GEN-III) the predominant component to the total uncertainty comes from the  $^{239}\text{Pu}$  nubar followed by the  $^{238}\text{U}(n,n')$  and  $^{239}\text{Pu}(n,\text{fission})$ . By definition the reason for these main contributions to the uncertainty can be due to the highest sensitivities associated to such reactions, to the highest value of the associated covariances, or to a combination of both. As an example, in the case of the  $^{238}\text{U}(n,\gamma)$ , on one hand, the  $k_{\text{eff}}$  is quite sensitive to its value (especially in the unresolved resonance regions), and on the other hand its evaluation is still quite “uncertain”, and evaluated cross-sections from various

TABLE 2: Exercises I-1 and I-2 results:  $k_{\text{eff}}$ .

Test cases	$k_{\text{eff}}$	Uncertainty (% $\Delta R/R$ )
Exercise I-1		
BWR		
HZP	1.34050	$5.23E-01$
HFP	1.22270	$6.16E-01$
PWR		
HZP	1.42290	$4.82E-01$
HFP	1.40424	$4.89E-01$
VVER		
HZP	1.34498	$5.13E-01$
HFP	1.32725	$5.20E-01$
KRITZ-2:1		
Cold	1.23394	$5.87E-01$
Hot	1.18584	$6.31E-01$
GEN-III		
HFP	1.09591	$5.20E-01$
Exercise I-2		
PWR		
HZP	1.11029	$5.00E-01$
HFP	1.07736	$5.56E-01$
BWR		
HZP	1.41009	$4.64E-01$
HFP	1.39351	$4.71E-01$
GEN-III Type 1	1.25325	$4.87E-01$
GEN-III Type 2	1.12304	$4.94E-01$
GEN-III Type 3	1.04501	$5.03E-01$
GEN-III Type 4	1.07008	$9.68E-01$

sources differ by more than their assigned uncertainties [21]. In Table 3 the explicit and implicit contributions to the total sensitivity coefficient of the  $^{238}\text{U}$  absorption cross-sections are given. One can observe that for some oxygen and uranium isotopes cross-sections the implicit part computed by the TSUNAMI code is not negligible.

Also, the most relevant sensitivity profiles for the BWR PB-2 and GEN-III unit-cell cases are shown in Figures 5 and 6, respectively. One of the benchmark requirements was the evaluation of the uncertainty associated to the calculation of the one-group absorption and fission microscopic cross-sections for  $^{235}\text{U}$  and  $^{238}\text{U}$  within the test cases of Exercise I-1. The results are given in Table 4. The uncertainty of the microscopic cross-section values is around one order of magnitude higher than the one of the  $k_{\text{eff}}$  cases, ranging in between  $\sim 1\%$  and  $\sim 4\%$ . The highest uncertainty value was systematically found for the fission cross-section of  $^{238}\text{U}$ . As far as the test cases of Exercise I-2 are concerned, as required from the benchmark specification, some selected homogenized macroscopic cross sections with the associated uncertainties have been evaluated in a two-group structure with a cut-off energy of 0.625 eV. Results are provided in Table 5. The first energy group ( $E \leq 0.625$  eV) was systematically found to be the one with the lower associated uncertainties. Also, as a general trend the uncertainties have been evaluated to

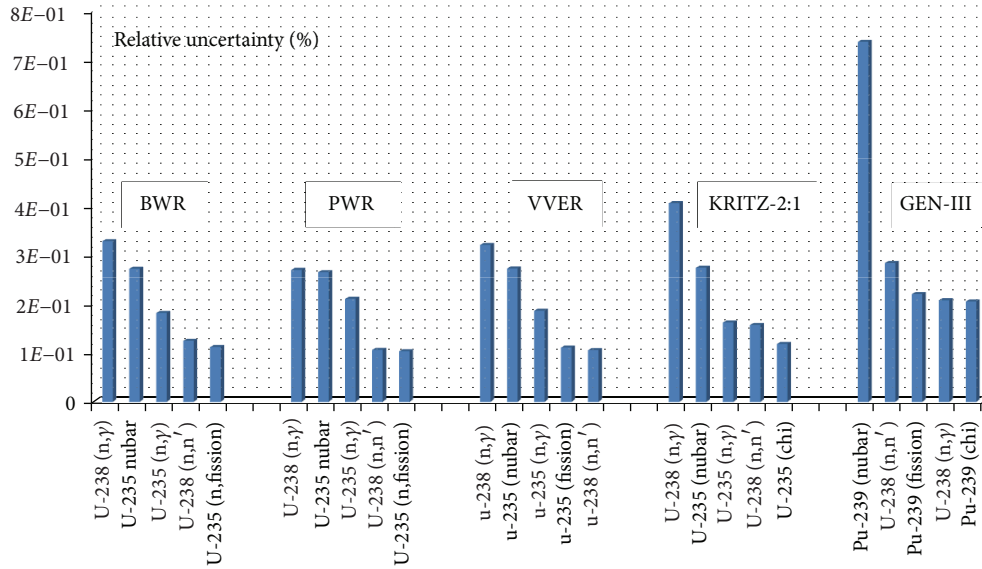


FIGURE 4: The five reaction cross-sections with the highest contribution to the  $k_{eff}$  uncertainty for the test cases within Exercise I-1.

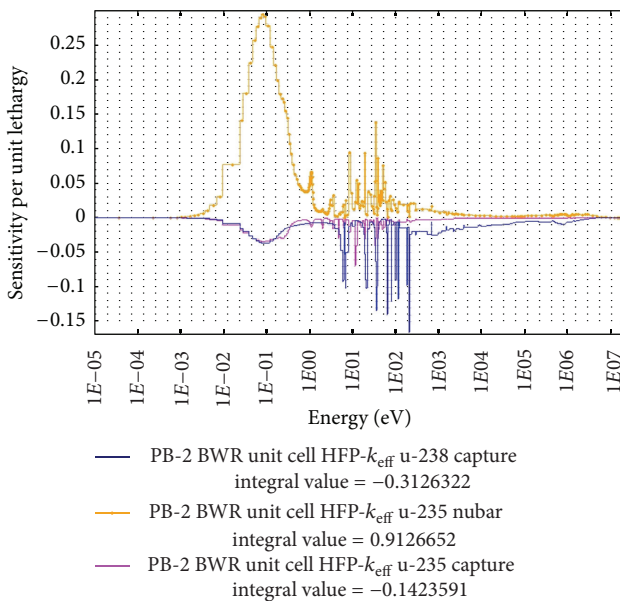


FIGURE 5:  $k_{eff}$  sensitivity profiles for the BWR PB-2 unit cell case (HFP conditions).

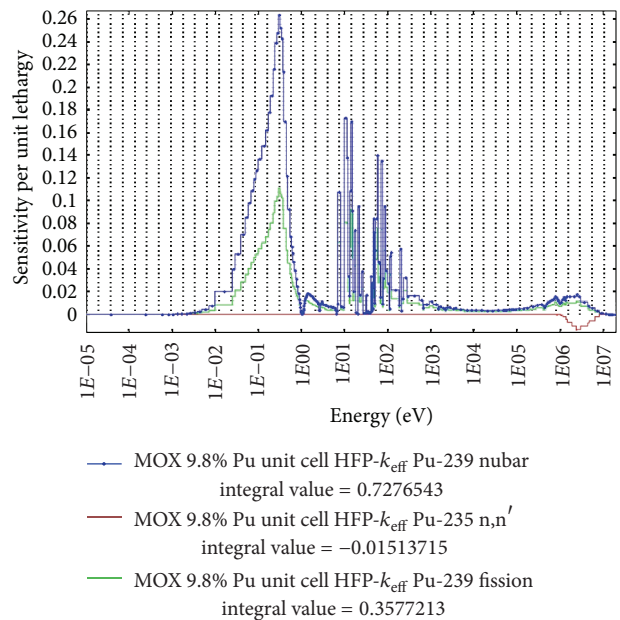


FIGURE 6:  $k_{eff}$  sensitivity profiles for the GEN-III unit cell case (HFP conditions).

be very consistent within all the test cases, and higher values (in the order of 1.35%) were computed for the homogenized absorption cross-section.

### 5. The Reference Solutions

As part of the activities within the UAM benchmark. KIT and PSU are also working on the development of reference solutions for the test cases by means of Monte Carlo methodologies. As it is well known, the Monte Carlo method can be considered as a “numerical experiment” that represents a high quality reference solution for the validation of deterministic

codes. For this purpose we are mainly using the SERPENT code [22], a Monte Carlo code designed for lattice physics calculations [23]. A comparison between absorption and fission microscopic cross sections values as computed with SERPENT and SCALE and relative to three test cases within Exercise I-1 is summarized in Table 6. A very good agreement between the two approaches can be observed.  $k_{eff}$  values computed by means of the SERPENT code (v. 1.1.16) with different sets of NDIs are summarized in Table 7. As far as the modeling, a good statistics in the criticality calculations has been achieved by simulating  $5.0E + 6$  neutron histories

TABLE 3: Exercise I-1: PWR test case at HFP: energy integrated sensitivity coefficients of the  $^{238}\text{U}$  absorption cross-section with respect to different cross-section isotopes.

Nuclide	Reaction	Explicit	Implicit	Sensitivity
$^{16}\text{O}$	<i>Total</i>	$3.00E - 02$	$1.19E - 02$	$4.19E - 02$
$^{16}\text{O}$	Scattering	$2.99E - 02$	$1.19E - 02$	$4.18E - 02$
$^{16}\text{O}$	Elastic	$2.99E - 02$	$1.19E - 02$	$4.18E - 02$
$^{16}\text{O}$	n,n'	$1.37E - 05$	$-1.95E - 08$	$1.37E - 05$
$^{16}\text{O}$	n,2n	$4.32E - 12$	$-2.24E - 17$	$4.32E - 12$
$^{16}\text{O}$	n, $\gamma$	$-8.21E - 07$	$1.00E - 08$	$-8.11E - 07$
$^{16}\text{O}$	n,p	$-1.90E - 07$	$-2.02E - 11$	$-1.90E - 07$
$^{16}\text{O}$	n,d	$-4.02E - 08$	$-1.07E - 12$	$-4.02E - 08$
$^{16}\text{O}$	n,t	$-5.75E - 13$	$-5.14E - 18$	$-5.75E - 13$
$^{16}\text{O}$	n,alpha	$1.12E - 04$	$2.69E - 08$	$1.12E - 04$
$^{234}\text{U}$	<i>Total</i>	$-4.27E - 05$	$2.05E - 06$	$-4.07E - 05$
$^{234}\text{U}$	Scattering	$-9.13E - 08$	$1.47E - 06$	$1.37E - 06$
$^{234}\text{U}$	Elastic	$-9.43E - 07$	$1.47E - 06$	$5.23E - 07$
$^{234}\text{U}$	n,n'	$8.50E - 07$	$3.27E - 10$	$8.50E - 07$
$^{234}\text{U}$	n,2n	$1.99E - 09$	$-1.12E - 13$	$1.99E - 09$
$^{234}\text{U}$	Fission	$4.15E - 08$	$4.34E - 09$	$4.58E - 08$
$^{234}\text{U}$	n, $\gamma$	$-4.27E - 05$	$5.83E - 07$	$-4.21E - 05$
$^{234}\text{U}$	Nubar	$4.36E - 08$	—	$4.36E - 08$
$^{234}\text{U}$	Chi	$-3.13E - 15$	—	$-3.13E - 15$
$^{235}\text{U}$	<i>Total</i>	$-1.01E - 01$	$3.36E - 03$	$-9.75E - 02$
$^{235}\text{U}$	Scattering	$1.08E - 03$	$8.97E - 04$	$1.97E - 03$
$^{235}\text{U}$	Elastic	$-9.45E - 05$	$8.96E - 04$	$8.01E - 04$
$^{235}\text{U}$	n,n'	$1.16E - 03$	$8.01E - 07$	$1.16E - 03$
$^{235}\text{U}$	n,2n	$1.38E - 05$	$-1.14E - 09$	$1.38E - 05$
$^{235}\text{U}$	Fission	$-7.56E - 02$	$1.39E - 03$	$-7.42E - 02$
$^{235}\text{U}$	n, $\gamma$	$-2.63E - 02$	$1.07E - 03$	$-2.53E - 02$
$^{235}\text{U}$	Nubar	$-2.75E - 04$	—	$-2.75E - 04$
$^{235}\text{U}$	Chi	$1.22E - 11$	—	$1.22E - 11$
$^{238}\text{U}$	<i>Total</i>	$7.85E - 01$	$-8.43E - 02$	$7.01E - 01$
$^{238}\text{U}$	Scattering	$3.25E - 02$	$-5.69E - 02$	$-2.44E - 02$
$^{238}\text{U}$	Elastic	$4.68E - 03$	$-5.69E - 02$	$-5.22E - 02$
$^{238}\text{U}$	n,n'	$2.75E - 02$	$8.91E - 06$	$2.75E - 02$
$^{238}\text{U}$	n,2n	$3.38E - 04$	$8.26E - 08$	$3.38E - 04$
$^{238}\text{U}$	Fission	$1.04E - 01$	$-3.16E - 07$	$1.04E - 01$
$^{238}\text{U}$	n, $\gamma$	$6.48E - 01$	$-2.74E - 02$	$6.21E - 01$
$^{238}\text{U}$	Nubar	$1.38E - 04$	—	$1.38E - 04$
$^{238}\text{U}$	Chi	$-1.12E - 12$	—	$-1.12E - 12$

over 1000 active cycles (5000 neutron source  $\times$  1000 cycles). Continuous cross-section libraries in SERPENT are given in steps of 300 K (300 K, 600 K, etc.), and the “actual” problem temperatures have been simulated by defining a mix of two materials with proportions equal to the weighted averages in between the two closest temperatures sets as available in SERPENT package. One can observe quite a good agreement in between the results with the different NDLS. Also, a systematic slight increase in the prediction of the  $k_{\text{eff}}$  when switching from JEFF3.1 to JEFF3.1.1 up to ENDF/B-VII, respectively, can be noted.  $k_{\text{eff}}$  computed with JEFF3.1.1

are larger by  $\sim 100$  pcm with respect to those obtained from JEFF3.1, and this is mainly due to the improvement of the  $^{16}\text{O}(n,\alpha)$  cross section which was decreased by 30% in the JEFF3.1.1 evaluation [24]. The comparison of these values with the correspondent ones obtained from the SCALE6.1 code (see Table 2) shows some discrepancies. One of the reasons for these differences was found to be due to the different Boundary Conditions (BCs) used in the SERPENT modeling; the “white” BC is not yet implemented in SERPENT, and therefore the “reflective” BC has been adopted for our simulations. In order to assess the impact of the

TABLE 4: Exercises I-1: one-group microscopic cross-sections.

Exercise I-1 test cases	Microscopic cross-section (barn)			
	<sup>235</sup> U absorption (uncertainty %)	<sup>238</sup> U absorption (uncertainty %)	<sup>235</sup> U fission (uncertainty %)	<sup>238</sup> U fission (uncertainty %)
BWR				
HZP	2.01E + 01 (1.04E + 00)	3.10E - 01 (9.80E - 01)	1.65E + 01 (1.06E + 00)	3.01E - 02 (4.07E + 00)
HFP	4.15E + 01 (1.22E + 00)	8.80E - 01 (9.70E - 01)	3.34E + 01 (1.22E + 00)	8.57E - 02 (4.79E + 00)
PWR				
HZP	4.41E + 01 (1.09E + 00)	9.42E - 01 (9.65E - 01)	3.57E + 01 (1.10E + 00)	9.91E - 02 (3.92E + 00)
HFP	4.30E - 01 (1.10E + 00)	9.64E - 01 (9.71E - 01)	3.47E + 01 (1.11E + 00)	9.91E - 02 (3.94E + 00)
VVER				
HZP	5.98E + 01 (1.02E + 00)	1.02E + 00 (9.88E + 01)	4.90E + 01 (1.04E + 00)	9.26E - 02 (3.86E + 00)
HFP	5.84E + 01 (1.03E + 00)	1.04E + 00 (9.90E - 01)	4.78E + 01 (1.05E + 00)	9.27E - 02 (3.88E + 00)
KRITZ-2:1				
Cold	8.23E + 01 (1.07E + 00)	1.01E + 00 (1.02E + 00)	6.83E + 01 (1.09E + 00)	8.90E - 02 (4.20E + 00)
Hot	2.71E + 01 (1.13E + 00)	3.84E - 01 (1.01E + 00)	2.24E - 01 (1.15E + 00)	3.38E - 02 (4.51E + 00)
GEN-III				
HFP	1.53E + 01 (1.38E + 00)	9.18E - 01 (1.01E + 00)	1.10E + 01 (1.22E + 00)	1.17E - 01 (3.83E + 00)

TABLE 5: Exercise I-2 results: macroscopic cross-sections.

Cross-section	Energy group	Value (cm <sup>-1</sup> ) (Uncertainty %)					
		PWR	BWR	GEN-III Type 1	GEN-III Type 2	GEN-III Type 3	GEN-III Type 4
Total	1	1.44E + 00	1.58E + 00	1.31E + 00	1.32E + 00	1.33E + 00	1.50E + 00
		(1.38E - 01)	(1.29E - 01)	(1.41E - 01)	(1.39E - 01)	(1.39E - 01)	(1.39E - 01)
	2	5.69E - 01	5.79E - 01	5.33E - 01	5.34E - 01	5.34E - 01	5.24E - 01
		(8.78E - 01)	(8.40E - 01)	(9.04E - 01)	(9.03E - 01)	(9.01E - 01)	(9.73E - 01)
Absorption	1	1.11E - 01	5.72E - 02	1.07E - 01	1.17E - 01	3.45E - 1	1.24E - 01
		(8.77E - 01)	(6.06E - 01)	(7.00E - 01)	(5.61E - 01)	(9.79E - 01)	(5.11E - 01)
	2	1.06E - 02	7.32E - 03	1.04E - 02	1.06E - 02	5.09E - 01	1.07E - 02
		(1.33E + 00)	(1.38E + 00)	(1.35E + 00)	(1.34E + 00)	(1.47E + 00)	(1.34E + 00)
Fission	1	7.95E - 01	2.94E - 02	6.86E - 02	6.60E - 02	1.90E - 01	6.42E - 02
		(3.17E - 03)	(3.23E - 01)	(3.23E - 01)	(3.24E - 01)	(6.26E - 01)	(3.24E - 01)
	2	3.59E - 03	1.95E - 03	3.17E - 03	3.10E - 03	4.97E - 01	3.05E - 03
		(3.55E - 01)	(6.81E - 01)	(3.71E - 01)	(3.75E - 01)	(4.45E - 01)	(3.80E - 01)
Nufission	1	1.94E - 01	7.02E - 02	1.67E - 1	1.61E - 01	5.45E - 01	1.56E - 01
		(4.44E - 01)	(4.49E - 01)	(4.48E - 01)	(4.49E - 01)	(1.09E + 00)	(4.49E - 01)
	2	9.08E - 03	4.69E - 03	8.02E - 03	7.86E - 03	1.44E - 02	7.73E - 3
		(5.12E - 01)	(1.01E + 00)	(5.71E - 01)	(5.82E - 01)	(7.75E - 01)	(5.92E - 01)

different BCs on the computed reactivities, three test cases at HZP conditions have been modeled with the MCNP5 code (v. 1.40) [25] with “white” BCs. The corresponding results, which are given in Table 7 and have been obtained by simulating 1500 generation of 2000 neutrons each, show how the discrepancies are then reduced.

## 6. Conclusions

The neutronics modeling of some selected test cases within the “Neutronics Phase” of the OECD UAM Benchmark

has been presented. A S/U analysis on the impact of the uncertainty in the basic nuclear data on the calculation of the multiplication factor and microscopic and macroscopic cross-sections have been performed using the perturbation methodologies implemented in the TSUNAMI code. Uncertainties were found to be ~0.5% on  $k_{\text{eff}}$  and higher (up to ~4%) for the cross-sections. The <sup>238</sup>U capture cross-section and the <sup>239</sup>Pu nubar were found to be the highest contributors to the total uncertainty for the UOX and MOX LWR’s representative test cases. The deterministic solutions were also compared with the corresponding reference solutions obtained using Monte Carlo methods, and a good

TABLE 6: Phase I-1 Exercises.

Micro-XS	SCALE 6.1	SERPENT	Uncertainty due to nuclear data (%)	Unit cell
$^{235}\text{U}$ absorption	41.48	$40.41 \pm 0.0086$	1.22	BWR
$^{238}\text{U}$ absorption	0.88	$0.80 \pm 0.0011$	0.97	
$^{235}\text{U}$ fission	33.43	$32.56 \pm 0.00069$	1.22	
$^{238}\text{U}$ fission	0.086	$0.089 \pm 0.00097$	4.79	
$^{235}\text{U}$ absorption	42.95	$42.18 \pm 0.00088$	1.09	PWR
$^{238}\text{U}$ absorption	0.96	$0.93 \pm 0.0011$	0.97	
$^{235}\text{U}$ fission	34.72	$34.10 \pm 0.00064$	1.11	
$^{238}\text{U}$ fission	0.099	$0.10 \pm 0.00096$	3.94	
$^{235}\text{U}$ absorption	58.13	$57.26 \pm 0.00085$	1.03	VVER
$^{238}\text{U}$ absorption	1.042	$1.005 \pm 0.0012$	0.99	
$^{235}\text{U}$ fission	47.84	$47.76 \pm 0.00063$	1.05	
$^{238}\text{U}$ fission	0.093	$0.095 \pm 0.00100$	3.88	

TABLE 7: Phase I-1 Exercise:  $k_{\text{eff}}$  evaluation with SERPENT and MCNP\*.

Test case	JEFF3.1	$k_{\text{eff}}$ JEFF 3.1.1	ENDFB-7
VVER			
HZP	$1.34764 \pm 0.00028$	$1.34937 \pm 0.00026$	$1.34986 \pm 0.00027$ $1.34542 \pm 0.00029^*$
HFP	$1.33152 \pm 0.00028$	$1.33356 \pm 0.00029$	$1.33435 \pm 0.00029$
PWR			
HZP	$1.42785 \pm 0.00027$	$1.42888 \pm 0.00025$	$1.42923 \pm 0.00027$ $1.42018 \pm 0.00030^*$
HFP	$1.41136 \pm 0.00026$	$1.41315 \pm 0.00028$	$1.41401 \pm 0.00026$
BWR			
HZP	$1.34541 \pm 0.00027$	$1.34673 \pm 0.00025$	$1.34691 \pm 0.00026$ $1.34191 \pm 0.00034^*$
HFP	$1.23046 \pm 0.00032$	$1.23080 \pm 0.00032$	$1.23295 \pm 0.00032$
KRITZ-2:1			
Cold	$1.23762 \pm 0.00028$	$1.23846 \pm 0.00027$	$1.23984 \pm 0.00027$
Hot	$1.22632 \pm 0.00028$	$1.22864 \pm 0.00026$	$1.22863 \pm 0.00027$
GEN-III			
HFP	$1.01485 \pm 0.00039$	$1.01602 \pm 0.00039$	$1.01805 \pm 0.00037$

agreement has been found for several cases, particularly in the evaluation of the microscopic cross-sections.

## References

- [1] K. Ivanov et al., “Benchmark for Uncertainty Analysis in Modeling (UAM) for Design, Operation and Safety Analysis of LWRs,” NEA/NSC/DOC, 2012.
- [2] J. Solis, K. Ivanov, B. Sarikaya, A. Olson, and K. Hunt, “BWR TT Benchmark. Volume I: Final Specifications,” NEA/NSC/DOC, 2001.
- [3] K. Ivanov, T. Beam, A. Baratta, A. Irani, and N. Trikouros, “PWR MSLB Benchmark. Volume I: Final Specifications,” NEA/NSC/DOC(99), 1999.
- [4] B. Ivanov, K. Ivanov, P. Groudev, M. Pavlova, and V. Hadjiev, “VVER-1000 Coolant Transient Benchmark (V1000-CT). Phase 1—Final Specification,” NEA/NSC/DOC, 2002.
- [5] “Benchmark on the KRITZ-2 LEU and MOX Critical Experiments—Final Report,” NEA/NSC/DOC, 2005.
- [6] C. Vaglio and A. Santamarina, “Assembly and core specification of generation 3 PWR,” CEA Report, 2010.
- [7] B. Rearden, C. M. Hopper, K. R. Elam et al., “Applications of the TSUNAMI sensitivity and uncertainty analysis methodology,” in *Proceedings of the 7th International Conference on Nuclear Criticality Safety (ICNC '03)*, Tokai-mura, Japan, October 2003.
- [8] G. Palmiotti and M. Salvatores, “Developments in sensitivity methodologies and the validation of reactor physics calculations,” *Science and Technology of Nuclear Installations*, vol. 2012, Article ID 529623, 14 pages, 2012.
- [9] H. Brooks, “Perturbation Theory for Boltzmann Equation,” KAPL-304, 1950.
- [10] G. Aliberti, L. Mercatali, G. Palmiotti, and M. Salvatores, “A systematic approach to nuclear data uncertainties and their

- impact on transmutation strategies,” in *Proceedings of the International Workshops on Nuclear Data for Transmutation*, Darmstadt, Germany, September 2003.
- [11] A. Gandini, “Uncertainty analysis and experimental data transposition methods based on perturbation theory,” in *Uncertainty Analysis*, Y. Ronen, Ed., CRC Press, Boca Raton, Fla, USA, 1988.
- [12] E. Greenspan, “Developments in perturbation theory,” in *Advances in Nuclear Science and Technology*, J. Lewins and A. Becker, Eds., vol. 14, Plenum Press, 1982.
- [13] M. L. Williams, B. L. Broadhead, and C. V. Parks, “Eigenvalue sensitivity theory for resonance-shielded cross sections,” *Nuclear Science and Engineering*, vol. 138, no. 2, pp. 177–191, 2001.
- [14] “SCALE: A Comprehensive Modeling and Simulation Suite for Nuclear Safety Analysis and Design,” ORNL/TM-2005/39, Version 6.1. Oak Ridge National Laboratory. Radiation Safety Information Computational Center at Oak Ridge National Laboratory as CCC-785, 2011.
- [15] M. B. Chadwick, P. Obložinský, M. Herman et al., “ENDF/B-VII.0: next generation evaluated nuclear data library for nuclear science and technology,” *Nuclear Data Sheets*, vol. 107, pp. 2931–3060, 2006.
- [16] B. T. Rearden, M. L. Williams, M. A. Jessee, D. E. Mueller, and D. A. Wiarda, “Sensitivity and uncertainty analysis capabilities and data in SCALE,” *Nuclear Technology*, vol. 174, no. 2, pp. 236–288, 2011.
- [17] M. L. Williams, “Resonance self-shielding methodologies,” *Nuclear Technology*, vol. 174, pp. 149–168, 2011.
- [18] N. M. Greene, L. M. Petrie, and M. L. Williams, “XSDRNPM: A One-Dimensional Discrete-Ordinates Code for Transport Analysis,” ORNL/TM-2005/39, 2011.
- [19] B. T. Rearden, L. M. Petrie, M. A. Jessee, and M. L. Williams, “SAMS: Sensitivity Analysis Module for SCALE,” ORNL/TM-2005/39, 2011.
- [20] M. L. Williams, D. Wiarda, G. Arbanas, and B. L. Broadhead, “SCALE Nuclear Data Covariance library,” ORNL/TM-2005/39, 2011.
- [21] A. Trkov, G. L. Molnár, Z. Révay et al., “Revisiting the  $^{238}\text{U}$  thermal capture cross section and gamma-ray emission probabilities from  $^{239}\text{Np}$  decay,” *Nuclear Science and Engineering*, vol. 150, no. 3, pp. 336–348, 2005.
- [22] J. Leppänen, *Development of a new Monte Carlo reactor physics code [D. Sc. Thesis]*, Helsinki University of Technology, 2007.
- [23] E. Fridman and J. Leppänen, “On the use of the Serpent Monte Carlo code for few-group cross section generation,” *Annals of Nuclear Energy*, vol. 38, no. 6, pp. 1399–1405, 2011.
- [24] “The JEFF-3.1.1 Nuclear Data Library,” NEA JEFF Report 22, OECD, 2009.
- [25] X-5 Monte Carlo Team, “MCNP—A General Monte Carlo N-Particle Transport Code (Version 5),” Los Alamos National Laboratory. LA-CP-03-0245, 2003.

## Research Article

# Presentation and Discussion of the UAM/Exercise I-1b: “Pin-Cell Burn-Up Benchmark” with the Hybrid Method

**O. Cabellos**

*Department of Nuclear Engineering, Universidad Politécnica de Madrid, C/José Gutiérrez Abascal, 2, 28006 Madrid, Spain*

Correspondence should be addressed to O. Cabellos; oscar.cabellos@upm.es

Received 6 September 2012; Accepted 10 December 2012

Academic Editor: Kostadin Ivanov

Copyright © 2013 O. Cabellos. This is an open access article distributed under the Creative Commons Attribution License, which permits unrestricted use, distribution, and reproduction in any medium, provided the original work is properly cited.

The aim of this work is to present the Exercise I-1b “pin-cell burn-up benchmark” proposed in the framework of OECD LWR UAM. Its objective is to address the uncertainty due to the basic nuclear data as well as the impact of processing the nuclear and covariance data in a pin-cell depletion calculation. Four different sensitivity/uncertainty propagation methodologies participate in this benchmark (GRS, NRG, UPM, and SNU&KAERI). The paper describes the main features of the UPM model (hybrid method) compared with other methodologies. The requested output provided by UPM is presented, and it is discussed regarding the results of other methodologies.

## 1. Introduction to the UAM/Exercise I-1b “Pin-Cell Burn-Up Benchmark”

The general frame of the OECD LWR UAM benchmark consists of three phases with different exercises for each phase [1]. In the Phase I (“*Neutronics Phase*”), the Exercise 1 (I-1) “*Cell Physics*” is focused on the derivation of the multigroup microscopic cross-section libraries. Since the OECD LWR UAM benchmark establishes a framework for propagating cross-section uncertainties in LWR design and safety calculations, the objective of the extension of this Exercise I-1 to I-1b (cell burn-up physics) is to address the uncertainties in the depletion calculation due to the basic nuclear data as well as the impact of processing of nuclear and covariance data. The SCALE-6.0/1 covariance library [2] is the recommended source of cross-section data uncertainty. However, covariance data coming from other source of uncertainty together with evaluated nuclear data files can be used without any inconvenience.

To address this problem different sensitivity/uncertainty (S/U) tools can be used to propagate nuclear data (e.g., cross-section) uncertainties. The requested output of Exercise I-1b is criticality value, reactions rates, collapsed cross-sections and nuclide concentrations as well as their uncertainties for depletion in a PWR pin-cell model.

*1.1. Specifications of the “Pin-Cell Burn-Up Benchmark”.* The specification of this pin-cell benchmark is given in Tables 1 and 2 (geometry and material specifications), showing a typical configuration of a TMI-1 PWR unit cell.

The linear fuel density (gU/cm) calculated according to values taken from Tables 1 and 2 is 6.2784 gU/cm. The average power density (W/gU) can be assumed to be equal to 33.58 W/gU. The fuel sample is burned for a unique complete cycle, the length of the burn time, and subsequent cooling time is given in Table 3. The specific power and the final cumulative burnup are also given, 61.28 GWd/MTU.

Concerning boundary conditions, the following type of boundary conditions can be used: (a) for a “cylindrical pin-cell” model, reflective boundary conditions are utilized at the center-line boundary while white boundary conditions are applicable at the peripheries of the cell model; (b) for a “square pin-cell” model, reflective boundary conditions on all surfaces are applied. For depletion, it can be considered an infinite burn-up spectrum mode.

*1.2. Requested Output of the “Pin-Cell Burn-Up Benchmark”.* Results and associated uncertainties are provided at eight burn-up steps: 0, 10, 20, 30, 40, 50, 60, and shutdown (61.28) GWd/MTU. And, six additional decay steps are required at 1, 3, 5, 10, 50, and 100 years of cooling time. The requested

TABLE 1: Hot full power (HFP) conditions for fuel pin-cell burn-up benchmark.

Fuel temperature (K)	900.0
Cladding temperature (K)	600.0
Moderator (coolant) temperature (K)	562.0
Moderator (coolant) density (g/cm <sup>3</sup> )	0.7484
Reactor power (MWt)	2772.0
Total number of fuel assemblies in the reactor core	177
Number of fuel rods per fuel assembly	208
Active core length (mm)	3571.20

TABLE 2: Configuration of pin-cell burn-up benchmark.

Unit cell pitch (mm)	14.427
Fuel pellet diameter (mm)	9.391
Fuel pellet material	UO <sub>2</sub>
Fuel density (g/cm <sup>3</sup> )	10.283
Fuel enrichment (w/o)	4.85
Cladding outside diameter (mm)	10.928
Cladding thickness (mm)	0.673
Cladding material	Zircaloy-4
Cladding density (g/cm <sup>3</sup> )	6.55
Gap material	He
Moderator material	H <sub>2</sub> O

TABLE 3: Simplified operating history data for pin-cell burn-up benchmark and specific power.

Operating cycle	1
Burn time (days)	1825.0
Final Burnup (GWd/MTU)	61.28
Downtime (days)	1870.0
Specific power (kW/kgU)	33.58

output can be summarized in the following three sets of information:

- (i) criticality values:  $K_{inf}$  and nuclide reactions that contribute the most to the uncertainty in  $k_{inf}$ ;
- (ii) reaction rates and collapsed macroscopic cross-sections:
  - (a) Reaction rates (capture and fission) and uncertainties for major isotopes: <sup>235,238</sup>U and <sup>239,240,241</sup>Pu;
  - (b) Two-group macroscopic cross-sections, fast and thermal, and associated uncertainties for the homogenized pin cell: absorption, fission, nu-fission, and diffusion coefficient. The thermal energy cutoff is 0.625 eV.
- (iii) Number densities:
  - (a) actinides (15): <sup>233,234,235,236,238</sup>U; <sup>237</sup>Np; <sup>238,239,240,241,242</sup>Pu; <sup>241,243</sup>Am; <sup>244,246</sup>Cm;

- (b) fission products (36): <sup>95</sup>Mo; <sup>99</sup>Tc; <sup>101,106</sup>Ru; <sup>103</sup>Rh; <sup>109</sup>Ag; <sup>133,134,135,137</sup>Cs; <sup>139</sup>La; <sup>140,142,144</sup>Ce; <sup>142,143,145,146,148,150</sup>Nd; <sup>147,148,149,150,151,152,154</sup>Sm; <sup>151,153,154,155</sup>Eu; <sup>154,155,156,158,160</sup>Gd.

## 2. Summary of Propagation Uncertainty Methodologies in Burn-Up Calculations

The first phase of participation in this exercise was completed in April 2012 with a total of 4 participants: GRS, NRG, UPM, and SNU&KAERI. Table 4 summarizes the main calculation methodologies and nuclear data libraries and their uncertainties. The results were presented at the Sixth Workshop (UAM-6) of OECD Benchmark for Uncertainty Analysis in Best-Estimate Modelling (UAM).

On one hand, depletion calculations are performed by GRS and UPM with SCALE6 code system [3], while NRG uses SERPENT code [4] and SNU&KAERI participates in the benchmark with its own McCARD code [5], both Monte Carlo codes. On the other side, for uncertainty calculations, GRS and NRG use Monte Carlo techniques, GRS with a sampling methodology (XSUSA [6]) of multigroup cross-section libraries provided in SCALE6 format and NRG using the technique of Total Monte Carlo [7] with TENDL2011. UPM applies a hybrid method [8] based on determining the sensitivity coefficients with TSUNAMI code [9] and performing a Monte Carlo sampling to determine the uncertainty of the number densities; these uncertainties are computed with ACAB code [10]. McCARD code makes use of the technique of Adjoint Weighted Perturbation (AWP) method to predict the sensitivity coefficients.

Regarding cross-section covariance data, GRS, SNU&KAERI, and UPM use SCALE6/COVA-44 groups. In addition, SNU&KAERI provides results with uncertainties coming from JENDL3.3 and ENDF/B-VII.0. Figure 1 shows an example of cross-section covariance data taken from SCALE6.1/COVA-44G. In this figure, the original <sup>235</sup>U COVERX/SCALE6.1 file is processed with ANGELO, LAMBDA, and NJOY codes to visualize the correlation matrix. NRG uses TENDL2011 and their uncertainty for cross-section data libraries. In addition, NRG and UPM have carried out some calculations with the uncertainty provided in Fission Yields (TENDL2011, JEFF-3.1.1) and Decay Data (JEFF-3.1.1) libraries.

Next, the main characteristics of the uncertainty propagation methodologies used in this Benchmark are summarized, and the uncertainty propagation in number density is used as an example in the following Figures 2, 3, and 6.

- (1) Figure 2 shows the calculation scheme of the Monte Carlo methodologies. NRG uses for each sampling a different nuclear data library TENDL2011; the generation of this library is done using the TASMAN code [7]. TASMAN is a computer code for the production of covariance data using results of the nuclear model code TALYS, and for automatic optimization of the TALYS results with respect to experimental data. It is assumed that each nuclear model (i.e., TALYS input)

TABLE 4: List of participants and brief description of their methodologies used in this benchmark.

Institution (country)	Methodology/codes (Nuclear data library)	Covariance data library	Criticality calculation methodology	Uncertainty methodology
GRS (Germany)	XSUSA/SCALE6.0	SCALE 6.0 (44 groups)	2-D-SN	Sampling multigroups libraries based on uncertainties in nuclear data libraries
	TRITON (BONAMI-CENTRM-NEWT-ORIGENS) (ENDF/B-VII.0)			
NRG (The Netherlands)	TMC/SERPENT (TENDL2011)	XS and FYs TENDL2011	Monte Carlo	Total Monte Carlo
SNU&KAERI (South Korea)	McCARD (ENDF/B-VII.0)	ENDF/B-VII.0 JENDL3.3 SCALE6.1	Monte Carlo	Monte Carlo uncertainty propagation
UPM (Spain)	SCALE6.1 TRITON/ACAB Hybrid method (TSUNAMI) (ENDF/B-VII.0)	SCALE 6.1 (44groups) FY & Decay data JEFF3.1.1	2-D-SN	Hybrid method: TSUNAMI and sampling in inventory calculations

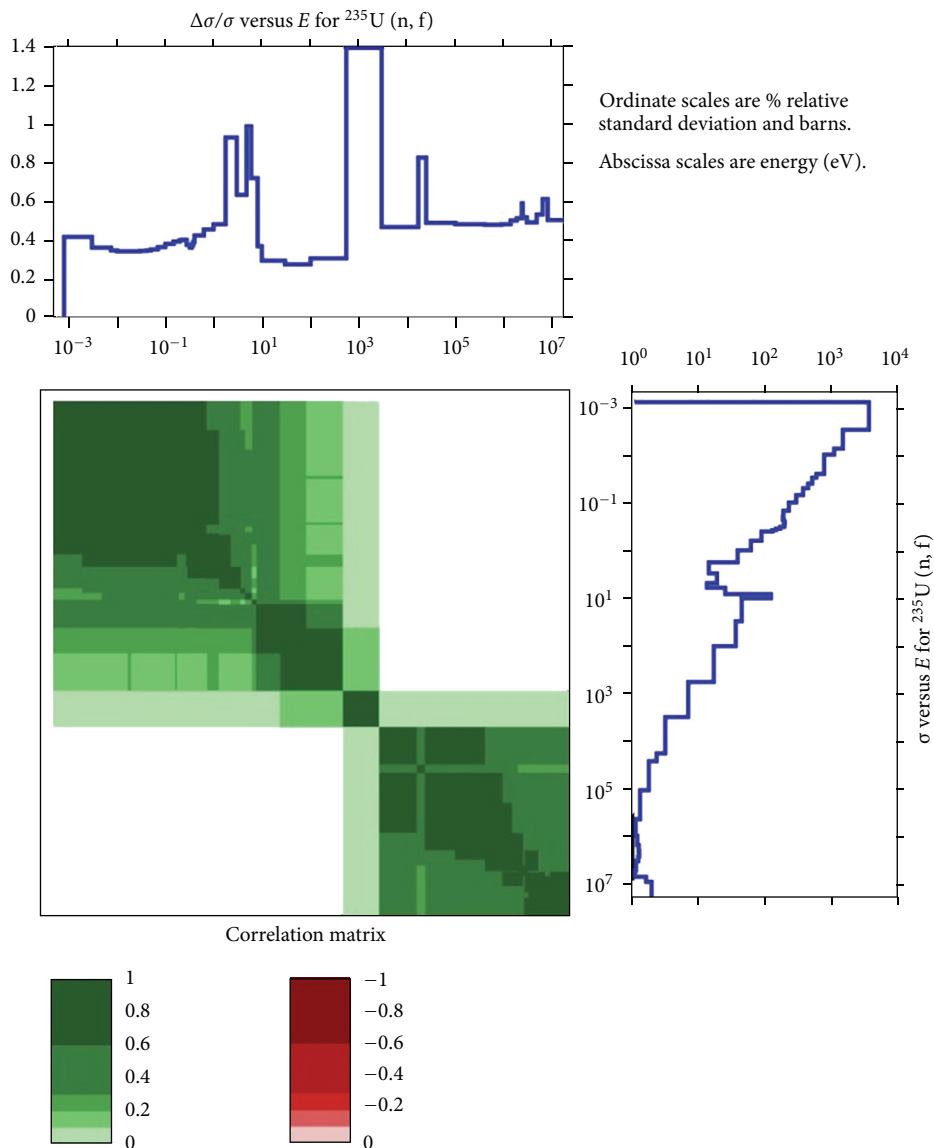


FIGURE 1: SCALE6.1 <sup>235</sup>U-fission covariance data processed in 44 groups with ANGELO, LAMBDA, and NJOY99-364 codes.

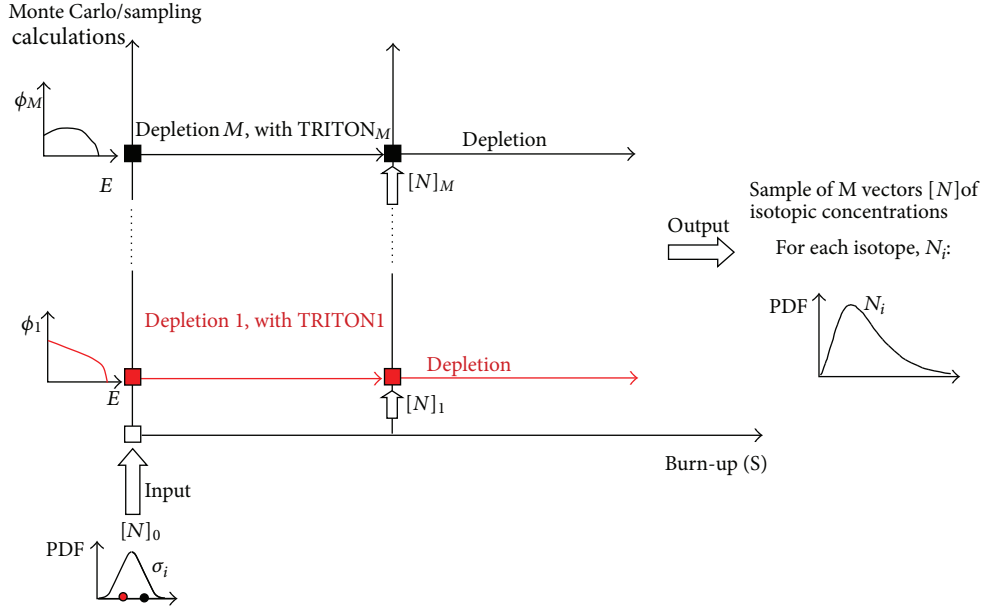


FIGURE 2: Simultaneous random sampling of the PDF of all the input parameters.

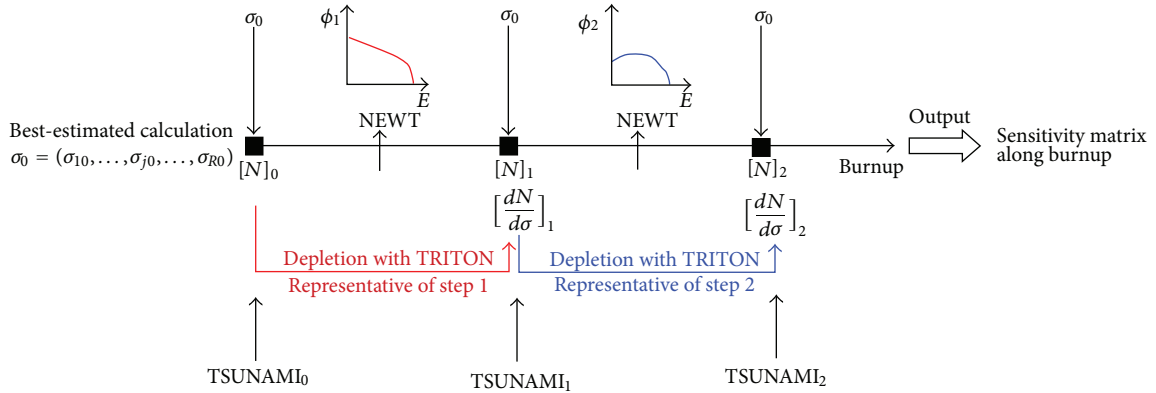


FIGURE 3: Procedure based on S/U.

parameter has its own uncertainty; running TALYS many times, it provides a sampling of ENDF files or a single file with full covariance information. GRS will generate a set of multigroup libraries in SCALE6 format; this sampling is done with the SCALE6.1/44-groups covariance library using XSUSA code.

- (2) The sensitivity/uncertainty procedure is based on a first order Taylor series approach. So, the number density can be written as

$$N_i(\sigma^{\text{eff}}) = N_i(\widehat{\sigma}^{\text{eff}}) + \sum_{j=1}^R \left[ \frac{\partial N_i}{\partial \sigma_j} \right]_{\widehat{\sigma}^{\text{eff}}} (\sigma_j^{\text{eff}} - \widehat{\sigma}_j^{\text{eff}}) + \dots, \quad (1)$$

where  $\sigma_j^{\text{eff}} = \sum_g \sigma_j^g \phi^g$ .

We can define the sensitivity coefficients as  $\rho_{ij} = [\partial N_i / \partial \sigma_j]_{\widehat{\sigma}^{\text{eff}}}$ , and  $\varepsilon_j = (\sigma_j^{\text{eff}} - \widehat{\sigma}_j^{\text{eff}})$  is the error in the 1-group effective cross-sections. This 1-group error depends explicitly

on the uncertainty of cross-sections, and implicitly on the neutron-flux uncertainty,

$$\varepsilon_j = \sum_{g=1}^G \phi^g (\sigma_j^g - \widehat{\sigma}_j^g) + \sum_{g=1}^G \sigma_j^g (\phi^g - \widehat{\phi}^g) = \phi^T \varepsilon_{\sigma_j} + \sigma_j^T \varepsilon_{\phi}. \quad (2)$$

Here,  $\varepsilon_{\sigma_j}$  is the error due to nuclear data and  $\varepsilon_{\phi}$  is the error due to neutron-flux. The variance in the number density can be obtained using the sandwich formula:

$$\begin{aligned} \text{var } N &\approx \mathbf{S} [\text{COV}_{\sigma^{\text{eff}}}] \mathbf{S}^T \\ &\approx \mathbf{S} \left\{ \begin{bmatrix} \ddots & & & & 0 \\ & \ddots & & & \\ & & \widehat{\phi}^T & & \\ & & & [\text{COV}_{\sigma_j}] & \\ & & & & \widehat{\phi} \\ & & & & & \ddots \end{bmatrix} \right. \\ &\quad \left. + \begin{bmatrix} \ddots & & & & 0 \\ & \ddots & & & \\ & & \widehat{\sigma}_j^T & & \\ & & & [\text{COV}_{\phi}] & \\ & & & & \widehat{\sigma}_j \\ & & & & & \ddots \end{bmatrix} \right\} \mathbf{S}^T. \quad (3) \end{aligned}$$

The first term propagates the multigroup cross-section uncertainty with no uncertainty in the neutron flux. And, the second term propagates the effect of this uncertainty with the uncertainty in the neutron flux.

If the uncertainty in the neutron flux can be considered negligible, a simple scheme of S/U can be illustrated in Figure 3. In this case, TRITON code [3] is run to determine the number densities at different burn-up steps, as a reference or nominal calculation without uncertainties. And, the number densities calculated in the nominal case are used to generate TSUNAMI [9] inputs at each burn-up step. With TSUNAMI code, S/U analysis can be provided for criticality ( $dk/d\sigma, dk/dN, \dots$ ), two-group cross-sections ( $d \sum_{abs1}/d\sigma, d \sum_{abs1}/dN, \dots$ ) and reaction rates ( $dRR_{U235cap}/d\sigma, dRR_{U235cap}/dN, \dots$ ). However, number density sensitivities ( $dN/d\sigma$ ) are not calculated with TSUNAMI code.

Once, the sensitivity coefficients are calculated by TSUNAMI code, the criticality uncertainty analysis based on “nuclear data uncertainties” can be formulated as follows:  $k_{eff}$  it is explicitly dependent on the nuclear data (e.g., cross-sections, nu-bar, ...) and implicitly dependent on the number density which characterizes the system:

$$\text{var}(k) \approx S_k V_\sigma S_k^T + S_N V_N S_N^T = \text{var}(k_\sigma) + \text{var}(k_N). \quad (4)$$

$S_k$  is the sensitivity coefficient explicitly of cross-sections ( $\Delta k/\Delta\sigma$ ) and  $S_N$  is the sensitivity coefficient of number density, ( $\Delta k/\Delta N$ ); both are calculated by TSUNAMI code. Figures 4 and 5 show the  $k$ -eff integrated sensitivity coefficients for cross-section and number density at each burn-up step. In Figure 4, the evolution of  $S_k$  shows the importance of  $^{239}\text{Pu}$  at high burnups, mainly for nu-bar nuclear reaction. For  $^{238}\text{U}$ , ( $n, \gamma$ ) and ( $n, n'$ ) reactions are the most important for all burnup. For  $^{235}\text{U}$ , sensitivity decreases with burn-up, being nu-bar with the highest value. Evolution of  $^{135}\text{Xe}(n, \gamma)$  is also shown. Some “fission-gamma” cross-correlations for  $^{239}\text{Pu}$  and  $^{235}\text{U}$  are also illustrated. Figure 5 shows the integrated sensitivities,  $S_N$ , for the most important isotopes related with criticality:  $^{239,240,241}\text{Pu}$ ,  $^{235,238}\text{U}$ . Also, some important fission products are shown:  $^{135}\text{Xe}$  and  $^{103}\text{Rh}$ .

$V_\sigma$  is the covariance cross-section data taken from SCALE6.1/COVA, and  $V_N$  is the covariance number densities predicted by ACAB code. It can be calculated with the uncertainty due to cross-section, fission yield and/or decay data.

- (3) Our ACAB code is used to propagate nuclear data uncertainty (cross-section, fission yield, and decay data) in the prediction of number density uncertainty:

$$\text{var}(N) \approx S_N V_\sigma S_N^T = \text{var}(N_\sigma). \quad (5)$$

ACAB accounts for the impact of nuclear data uncertainty as follows (see Figure 6). (i) In a first step, a coupled neutron-depletion calculation (without uncertainties) is carried out only once, taken the best-estimated values for all the parameters involved in the problem. (ii) In a second step, ACAB

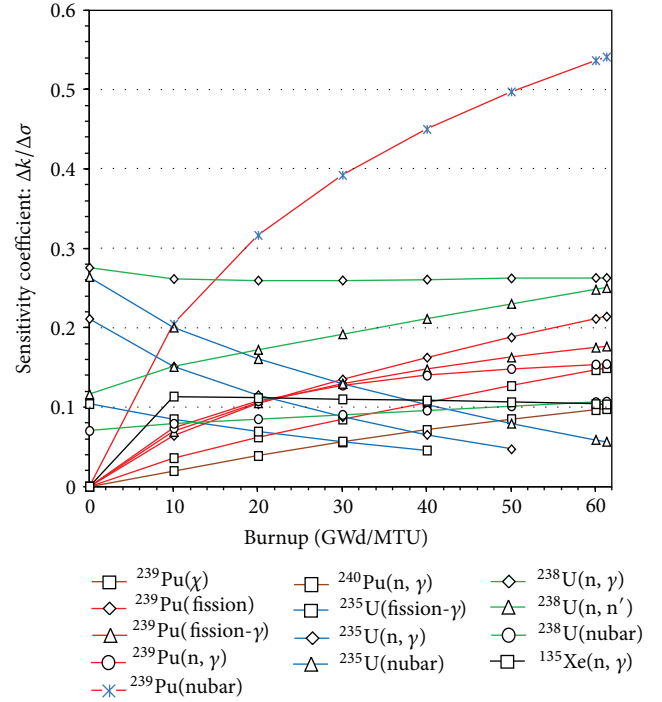


FIGURE 4: Sensitivity coefficients calculated with SCALE6.1/TRITON/TSUNAMI.

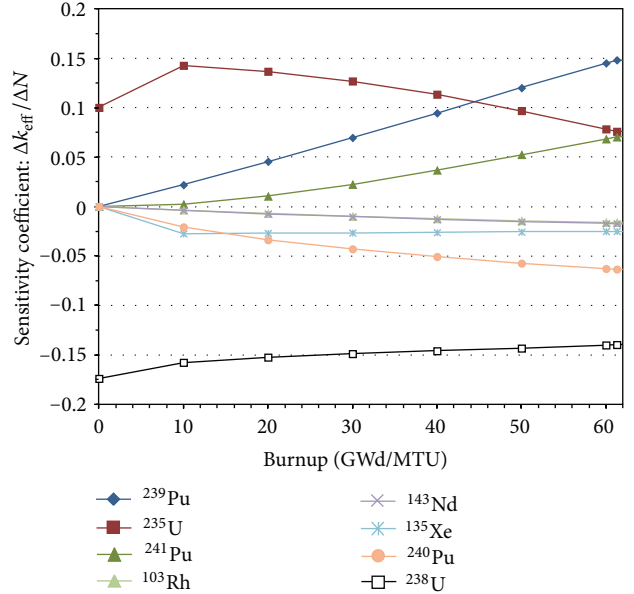


FIGURE 5: Sensitivity coefficients calculated with SCALE6.1/TRITON/TSUNAMI.

performs a simultaneous random sampling of the probability density functions (PDF) of all these variables: cross-section, fission yield, and decay data. Then, ACAB computes the isotopic concentrations at the end of each burn step, taking the fluxes halfway through each burn step determined in the best-estimated calculation. Then, only the depletion

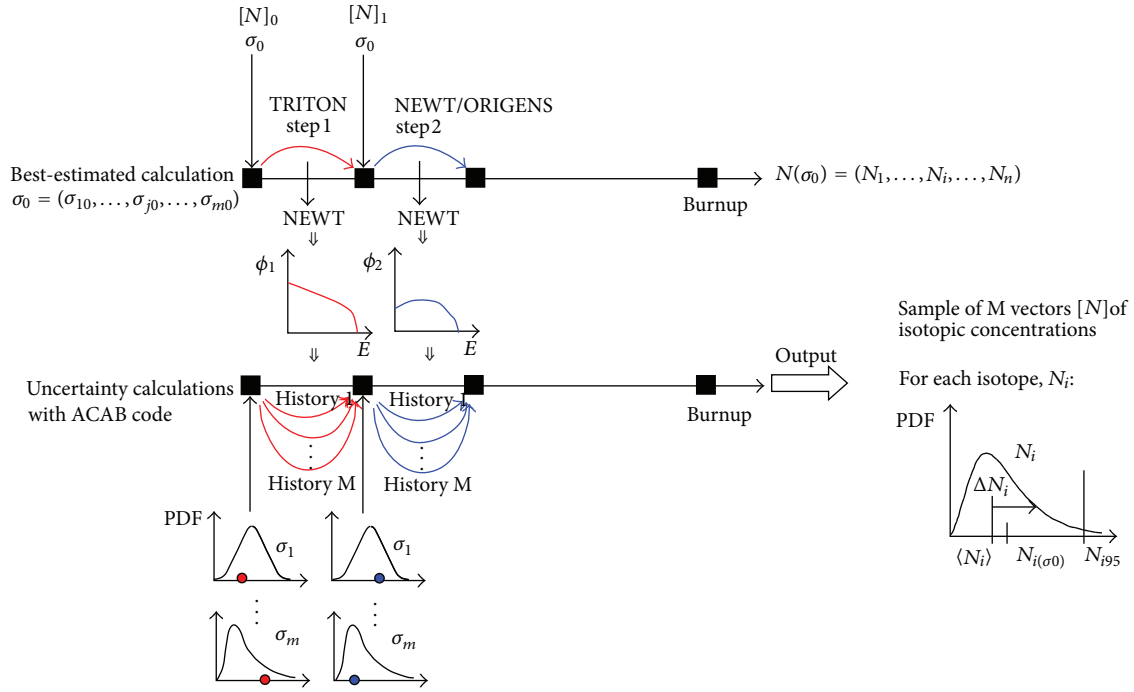


FIGURE 6: A Hybrid method used by ACAB code.

calculations are repeated or run many times. A statistical analysis of the results allows assessing the uncertainty in the calculated number density and determining  $V_N$ . Table 5 shows an example of this type of information.

### 3. Results with the Hybrid Method

In Table 6,  $k_{\text{eff}}$  and their associated uncertainty for PWR unit-cell are summarized at four different burnups. The five most important nuclide reactions that contribute to uncertainty are identified: (i) for fresh fuel,  $U^{238}(n, \gamma)$ ,  $U^{235}(v)$  and  $(n, \gamma)$ ,  $U^{238}(n, n')$ ,  $U^{235}(n, \text{fiss-}\gamma)$ , and (ii) for high burnup:  $Pu^{239}(v)$ ,  $U^{238}(n, \gamma)$  and  $(n, n')$ ,  $Pu^{239}(n, \text{fiss})$ , and  $(n, \text{fiss-}\gamma)$ . In addition, the contribution of number density uncertainty,  $\text{var}(k_N)$ , is evaluated, being the cross-sections and fission yields the most important contributions, and it can be concluded that the contribution of decay data uncertainty is negligible.

Table 7 shows the uncertainty of two-group cross-sections:  $\sum_{\text{abs-1}}$ ,  $\sum_{\text{abs-2}}$ ,  $\sum_{\text{fis-1}}$ ,  $\sum_{\text{fis-2}}$ ,  $v \sum_{\text{fis-1}}$ ,  $v \sum_{\text{fis-2}}$ ,  $\text{diff}_1$ , and  $\text{diff}_2$  (subscript 1 refers to fast group and subscript 2 to the thermal group). The low contribution of the uncertainty due to number density uncertainty except for thermal groups can be seen. The total uncertainty is about 1%, and the contribution due to the uncertainty in fission yields is negligible.

As an example of integrated sensitivities of macroscopic two-group cross-sections, Figures 7 and 8 show these values for  $\sum_{\text{abs-1}}$ .  $^{238}\text{U}$  is the most important contributor with the  $(n, n)$  and  $(n, \gamma)$  reactions.

Table 8 shows the uncertainty for the following capture and fission reaction rates:  $^{235,238}\text{U}$  and  $^{239,240,241}\text{Pu}$ . The

total uncertainty is in the range of 1%–3%. In general, the uncertainty contribution due to the uncertainty in the number density ( $\text{var}(\text{RR}_N)$ ) is below the contribution due to cross-section ( $\text{var}(\text{RR}_\sigma)$ ), except for  $^{240}\text{Pu}$  and  $^{241}\text{Pu}$  reaction rates where this contribution is larger.

In Table 9, it can be seen that the number density uncertainty for some major and minor actinides due to cross-section data remains below 3%. Larger uncertainties are predicted for minor actinides (e.g.,  $^{246}\text{Cm}$ ) and the uncertainty throughout irradiation period rises. And, it can be concluded that the uncertainty due to decay data uncertainty is negligible.

In Table 10, the uncertainty in the number of fission products due to cross-sections, decay, and fission yields data has been predicted. Some isotopes,  $^{155}\text{Gd}$ ,  $^{154,155}\text{Eu}$ , and  $^{149}\text{Sm}$  show a relative error above 10%, being the high uncertainty in cross-section data, the reason of this large uncertainty. In general, the uncertainty due to fission yields remain below 3%, except for  $^{95}\text{Mo}$  with 4.5% (with high sensitivity to  $^{95}\text{Zr}$  fission yield) and  $^{149}\text{Sm}$  with 4.7% (with high sensitivity to  $^{149}\text{Pm}$  fission yield) [11]. For decay data uncertainties, the isotope  $^{151}\text{Eu}$  reaches a maximum uncertainty of 3.2% as a consequence of the 6.7% relative error in the half-life of  $^{151}\text{Sm}$ .

### 4. Conclusions and Comparison with Other Methodologies

There has been a very small contribution of participants in the pin-cell burn-up benchmark, Exercise I-1b, with only

TABLE 5: Correlation matrix,  $V_N$ , calculated at shutdown (61.28 GWd/TU) using SCALE6.1 cross-section data uncertainty. Column “ $e$  (%)” is the relative error in % for each isotope.

	$e$ (%)	U <sup>233</sup>	U <sup>234</sup>	U <sup>235</sup>	U <sup>236</sup>	U <sup>238</sup>	Np <sup>237</sup>	Pu <sup>238</sup>	Pu <sup>239</sup>	Pu <sup>240</sup>	Pu <sup>241</sup>	Pu <sup>242</sup>	Am <sup>241</sup>	Am <sup>242</sup>	Am <sup>243</sup>	Cm <sup>242</sup>	Cm <sup>243</sup>	Cm <sup>244</sup>
U <sup>233</sup>	2.2	<b>1.0</b>	0.6															
U <sup>234</sup>	3.2	0.6	<b>1.0</b>															
U <sup>235</sup>	0.6			<b>1.0</b>	0.3							-0.1						-0.1
U <sup>236</sup>	0.4			0.3	<b>1.0</b>		0.2											
U <sup>238</sup>	0.1					<b>1.0</b>		-0.2	-0.3	-0.2	-0.2	-0.3	-0.2		-0.2	-0.2		-0.2
Np <sup>237</sup>	0.8			0.2		<b>1.0</b>												
Pu <sup>238</sup>	0.9				-0.2		<b>1.0</b>			0.1	0.4				0.2	0.4	0.1	0.3
Pu <sup>239</sup>	1.4				-0.3			<b>1.0</b>	-0.4	-0.2								
Pu <sup>240</sup>	2.0				-0.2				<b>1.0</b>	0.3		0.1						
Pu <sup>241</sup>	1.4				-0.2		0.1	-0.2	0.3	<b>1.0</b>	0.3	0.5			0.1	0.2		
Pu <sup>242</sup>	1.4		-0.1		-0.3		0.4			0.3	<b>1.0</b>	0.4	0.2			0.5	0.1	0.1
Am <sup>241</sup>	1.9				-0.2			0.1	0.5	0.4	<b>1.0</b>	-0.2			-0.2			0.1
Am <sup>242</sup>	5.8									0.2	-0.2	<b>1.0</b>				0.6	0.1	
Am <sup>243</sup>	2.0		-0.1		-0.2		0.2			0.1			<b>1.0</b>		0.3	0.1	0.2	
Cm <sup>242</sup>	1.7				-0.2		0.4			0.2	0.5	-0.2	0.6	0.3	<b>1.0</b>			
Cm <sup>243</sup>	6.0			-0.1			0.1				0.1		0.1	0.1		<b>1.0</b>	0.1	
Cm <sup>244</sup>	2.1				-0.2		0.3				0.1	0.1	0.2			0.1	<b>1.0</b>	

TABLE 6: Uncertainties in criticality value,  $k_{\text{eff}}$ , with the main source of contributions. Cross-section uncertainties are taken from SCALE6.1/44-GROUP and fission yields and decay data source of uncertainty from JEFF-3.1.1.

	0 GWd/MTU		10 GWd/MTU		30 GWd/MTU		60 GWd/MTU				
Mean $k_{\text{eff}}$	1.40	Rel. std. dev. (%)	Mean $k_{\text{eff}}$	1.25	Rel. std. dev. (%)	Mean $k_{\text{eff}}$	1.08	rel. std. dev. (%)	Mean $k_{\text{eff}}$	0.90	Rel. std. dev. (%)
U <sup>238</sup> ( $n, \gamma$ )		0.28	U <sup>238</sup> ( $n, \epsilon\gamma$ )	0.26	Pu <sup>239</sup> (nubar)	0.39	Pu <sup>239</sup> (nubar)	0.54			
U <sup>235</sup> (nubar)		0.26	Pu <sup>239</sup> (nubar)	0.20	U <sup>238</sup> ( $n, \gamma$ )	0.26	U <sup>238</sup> ( $n, \gamma$ )	0.26			
U <sup>235</sup> ( $n, \gamma$ )		0.21	U <sup>235</sup> (nubar)	0.20	U <sup>238</sup> ( $n, n'$ )	0.19	U <sup>238</sup> ( $n, n'$ )	0.25			
U <sup>238</sup> ( $n, n'$ )		0.12	U <sup>235</sup> ( $n, \gamma$ )	0.15	Pu <sup>239</sup> (fis)	0.13	Pu <sup>239</sup> (fis)	0.21			
U <sup>235</sup> ( $n, \gamma$ -fiss)		0.10	U <sup>238</sup> ( $n, n'$ )	0.15	U <sup>235</sup> (nubar)	0.13	Pu <sup>239</sup> ( $n, \gamma$ -fiss)	0.18			
...		...	...	...	...	...	...	...			
Total var( $k_{\sigma}$ )		0.49		0.51		0.63		0.79			
var( $k_N$ )_XS/SCALE		0.00		0.19		0.25		0.35			
var( $k_N$ )_FYs		0.00		0.22		0.22		0.21			
var( $k_N$ )_Decay		0.00		0.00		0.00		0.00			
Total var( $k$ )		0.49		0.58		0.71		0.89			

four institutions: GRS, NRG, UPM, and SNU&KAERI. However, the most representative methodologies in propagation uncertainties in depletion calculation are involved. Other institutions such as AREVA/NP and PSI have shown interest in participating in this exercise. Here, a comparison of these methodologies is summarized.

- (1) Regarding the uncertainty in criticality, Table 6 shows the  $k_{\text{eff}}$  relative uncertainty for the fresh fuel: approximately 0.5%, and it reaches approximately 0.80% at high burn-up. GRS with XSUSA and SNU&KAERI with McCARD code have obtained similar prediction. For fresh fuel, the most important contribution is due to the reaction <sup>238</sup>U( $n, \gamma$ ) and, at shutdown is, <sup>239</sup>Pu(nubar). Only, elastic reactions for <sup>235</sup>U and <sup>238</sup>U are predicted by GRS/XSUSA as important reactions to be taken into account. NRG/TENDL2011

includes <sup>235</sup>U and <sup>239</sup>Pu ( $\chi$ ) as other important reaction to be considered.

- (2) The importance of different source of cross-section uncertainty has been evaluated by SNU&KAERI. Thus, for fresh fuel the  $k_{\text{eff}}$  relative uncertainty is 0.79% or 0.30%, with uncertainty cross-section data ENDF/B.VII.1 or JENDL/-3.3, respectively.
- (3) Comparing results between UPM and GRS (using both institutions similar uncertainty data and codes), it can be concluded that the linear approximation used by UPM neglects the possible correlation between the prediction of number densities and neutron transport calculation. At high burn-up the lower uncertainty in  $k_{\text{eff}}$  predicted by GRS (0.75%) with respect to UPM (0.89%) shows a possible negative correlation between these terms.

TABLE 7: Uncertainty in two-group cross-section data. Cross-section uncertainties are taken from SCALE6.1/44-GROUP.

		0 GWd/MTU	10 GWd/MTU	30 GWd/MTU	60 GWd/MTU	
$\Sigma_{\text{abs-1}}$	Mean value	$1.16E-02$	$1.20E-02$	$1.26E-02$	$1.31E-02$	
	Relative uncertainty (%)	$\text{var}(\Sigma_{\sigma})$	0.9	0.9	0.9	0.9
		$\text{var}(\Sigma_N)_\Delta\text{XS}$	0.0	0.1	0.1	0.1
		$\text{var}(\Sigma_N)_\Delta\text{FY}$	0.0	0.0	0.0	0.0
	Total Uncertainty	0.9	0.9	0.9	0.9	
$\Sigma_{\text{abs-2}}$	Mean value	$1.16E-01$	$1.30E-01$	$1.31E-01$	$1.20E-01$	
	Relative uncertainty (%)	$\text{var}(\Sigma_{\sigma})$	0.2	0.2	0.2	0.3
		$\text{var}(\Sigma_N)_\Delta\text{XS}$	0.0	0.3	0.4	0.6
		$\text{var}(\Sigma_N)_\Delta\text{FY}$	0.0	0.2	0.2	0.2
	Total Uncertainty	0.2	0.4	0.5	0.7	
$\Sigma_{\text{fis-1}}$	Mean value	$3.87E-03$	$3.42E-03$	$2.72E-03$	$2.02E-03$	
	Relative uncertainty (%)	$\text{var}(\Sigma_{\sigma})$	0.4	0.4	0.5	0.9
		$\text{var}(\Sigma_N)_\Delta\text{XS}$	0.0	0.1	0.2	0.3
		$\text{var}(\Sigma_N)_\Delta\text{FY}$	0.0	0.0	0.0	0.0
	Total Uncertainty	0.4	0.4	0.6	1.0	
$\Sigma_{\text{fis-2}}$	Mean value	$8.64E-02$	$8.48E-02$	$7.52E-02$	$5.84E-02$	
	Relative uncertainty (%)	$\text{var}(\Sigma_{\sigma})$	0.3	0.3	0.4	0.5
		$\text{var}(\Sigma_N)_\Delta\text{XS}$	0.0	0.2	0.4	0.7
		$\text{var}(\Sigma_N)_\Delta\text{FY}$	0.0	0.1	0.1	0.0
	Total Uncertainty	0.3	0.4	0.5	0.8	
$\nu\Sigma_{\text{fis-1}}$	Mean value	$9.76E-03$	$8.79E-03$	$7.20E-03$	$5.57E-03$	
	Relative uncertainty (%)	$\text{var}(\Sigma_{\sigma})$	0.5	0.6	0.7	1.1
		$\text{var}(\Sigma_N)_\Delta\text{XS}$	0.0	0.1	0.2	0.3
		$\text{var}(\Sigma_N)_\Delta\text{FY}$	0.0	0.0	0.0	0.0
	Total Uncertainty	0.5	0.6	0.8	1.2	
$\nu\Sigma_{\text{fis-2}}$	Mean value	$2.11E-01$	$2.15E-01$	$1.99E-01$	$1.62E-01$	
	Relative uncertainty (%)	$\text{var}(\Sigma_{\sigma})$	0.4	0.5	0.6	0.8
		$\text{var}(\Sigma_N)_\Delta\text{XS}$	0.0	0.3	0.4	0.7
		$\text{var}(\Sigma_N)_\Delta\text{FY}$	0.0	0.1	0.1	0.0
	Total Uncertainty	0.4	0.5	0.7	1.1	
diff-1	Mean value	$2.51E+00$	$1.41E+00$	$1.99E-01$	$1.62E-01$	
	Relative uncertainty (%)	$\text{var}(\Sigma_{\sigma})$	0.9	0.9	0.9	0.9
		$\text{var}(\Sigma_N)_\Delta\text{XS}$	0.0	0.0	0.0	0.0
		$\text{var}(\Sigma_N)_\Delta\text{FY}$	0.0	0.0	0.0	0.0
	Total Uncertainty	0.9	0.9	0.9	0.9	
diff-2	Mean value	$4.33E-01$	$3.62E-01$	$3.56E-01$	$3.54E-01$	
	Relative uncertainty (%)	$\text{var}(\Sigma_{\sigma})$	0.2	0.2	0.2	0.2
		$\text{var}(\Sigma_N)_\Delta\text{XS}$	0.0	0.0	0.0	0.0
		$\text{var}(\Sigma_N)_\Delta\text{FY}$	0.0	0.0	0.0	0.0
	Total Uncertainty	0.2	0.2	0.2	0.2	

(4) The importance of fission yields is analyzed by UPM and NRG with a relative uncertainty contribution to  $k_{\text{eff}}$  approximately 0.2–0.3%. The importance of decay data studied by UPM shows a negligible effect.

(5) For two group cross-sections and reaction rates, the relative uncertainty is in the range of 1-2%. And comparing GRS between UPM, a positive correlation in two-group cross-sections between the prediction of number densities and neutron transport calculation

due to the highest uncertainty values predicted by GRS is shown. For reaction rates, a negative correlation is found. NRG predicts larger uncertainties above 2% because of the TENDL2011 library.

(6) The uncertainty in the number density of major isotopes ( $^{235}\text{U}$ ,  $^{239}\text{Pu}$ ,...) is in the range of 1–3% increasing with burnup; higher uncertainty is predicted by GRS/XSUSA (3.5% for  $^{242}\text{Pu}$ ). For minor actinides, the highest uncertainty value is for  $^{246}\text{Cm}$

TABLE 8: Uncertainty in reaction rates. Cross-section uncertainties are taken from SCALE6.1/44-GROUP.

		0 GWd/MTU	10 GWd/MTU	30 GWd/MTU	60 GWd/MTU
<sup>235</sup> U-cap	Mean value	9.10E-02	7.27E-02	4.76E-02	2.12E-02
	Relative uncertainty (%)	var(RR <sub>σ</sub> )	1.8	1.8	1.8
		var(RR <sub>N</sub> ) <sub>ΔXS</sub>	0.0	0.2	0.8
<sup>235</sup> U-fis	Mean value	3.85E-01	2.97E-01	1.92E-01	8.70E-02
	Relative uncertainty (%)	var(RR <sub>σ</sub> )	1.1	1.1	1.1
		var(RR <sub>N</sub> ) <sub>ΔXS</sub>	0.0	0.2	0.8
<sup>238</sup> U-cap	Mean value	1.83E-01	2.01E-01	2.29E-01	2.76E-01
	Relative uncertainty (%)	var(RR <sub>σ</sub> )	1.4	1.3	1.3
		var(RR <sub>N</sub> ) <sub>ΔXS</sub>	0.0	0.2	0.4
<sup>238</sup> U-fis	Mean value	2.15E-02	2.43E-02	2.78E-02	3.27E-02
	Relative uncertainty (%)	var(RR <sub>σ</sub> )	4.0	3.7	3.6
		var(RR <sub>N</sub> ) <sub>ΔXS</sub>	0.0	0.2	0.4
<sup>239</sup> Pu-cap	Mean value	—	3.93E-02	7.41E-02	1.00E-01
	Relative uncertainty (%)	var(RR <sub>σ</sub> )	—	1.6	1.5
		var(RR <sub>N</sub> ) <sub>ΔXS</sub>	—	0.9	0.7
<sup>239</sup> Pu-fiss	Mean value	—	6.91E-02	1.33E-01	1.81E-01
	Relative uncertainty (%)	var(RR <sub>σ</sub> )	—	1.3	1.3
		var(RR <sub>N</sub> ) <sub>ΔXS</sub>	—	0.9	0.7
<sup>240</sup> Pu-cap	Mean value	—	1.68E-02	5.00E-02	8.66E-02
	Relative uncertainty (%)	var(RR <sub>σ</sub> )	—	1.3	1.3
		var(RR <sub>N</sub> ) <sub>ΔXS</sub>	—	2.4	1.3
<sup>240</sup> Pu-fiss	Mean value	—	6.10E-05	2.95E-04	6.67E-04
	Relative uncertainty (%)	var(RR <sub>σ</sub> )	—	2.4	2.2
		var(RR <sub>N</sub> ) <sub>ΔXS</sub>	—	3.1	2.1
<sup>241</sup> Pu-cap	Mean value	—	1.13E-03	8.50E-03	2.05E-02
	Relative uncertainty (%)	var(RR <sub>σ</sub> )	—	1.5	1.4
		var(RR <sub>N</sub> ) <sub>ΔXS</sub>	—	2.0	1.5
<sup>241</sup> Pu-fiss	Mean value	—	3.11E-03	2.37E-02	5.73E-02
	Relative uncertainty (%)	var(RR <sub>σ</sub> )	—	1.3	1.3
		var(RR <sub>N</sub> ) <sub>ΔXS</sub>	—	2.9	1.5

TABLE 9: Uncertainty in number density for some important major and minor actinides. Cross-section uncertainties are taken from SCALE6.1/44-GROUP (ΔXS) and decay data (ΔDD) source of uncertainty from JEFF-3.1.1.

	0 GWd/MTU		10 GWd/MTU		30 GWd/MTU		60 GWd/MTU			
	Mean	Mean	Rel. std. dev. (%)	Mean	Rel. std. dev. (%)	Mean	Rel. std. dev. (%)			
			ΔXS	ΔDD	ΔXS	ΔDD	ΔXS	ΔDD		
<sup>233</sup> U	0.00E+00	5.94E-11	3.1	0.0	1.29E-10	2.1	0.0	1.41E-10	2.1	0.0
<sup>234</sup> U	1.17E-05	1.03E-05	1.0	0.0	7.94E-06	1.9	0.0	5.04E-06	3.1	0.0
<sup>235</sup> U	1.13E-03	8.71E-04	0.2	0.0	4.97E-04	0.3	0.0	1.74E-04	0.6	0.0
<sup>236</sup> U	0.00E+00	4.87E-05	0.8	0.0	1.15E-04	0.5	0.0	1.58E-04	0.4	0.0
<sup>238</sup> U	2.18E-02	2.17E-02	0.0	0.0	2.14E-02	0.1	0.0	2.08E-02	0.1	0.0
<sup>237</sup> Np	0.00E+00	1.70E-06	1.2	0.0	8.76E-06	0.8	0.0	2.03E-05	0.8	0.0
<sup>238</sup> Pu	0.00E+00	1.24E-07	2.3	0.0	2.08E-06	1.4	0.0	1.07E-05	0.9	0.0
<sup>239</sup> Pu	0.00E+00	8.08E-05	1.2	0.0	1.46E-04	1.1	0.0	1.60E-04	1.3	0.0
<sup>240</sup> Pu	0.00E+00	9.36E-06	3.1	0.0	4.01E-05	2.1	0.0	7.59E-05	1.9	0.0
<sup>241</sup> Pu	0.00E+00	3.55E-06	2.9	0.0	2.46E-05	1.7	0.0	4.68E-05	1.5	0.0
<sup>242</sup> Pu	0.00E+00	1.98E-07	3.7	0.0	4.95E-06	1.9	0.0	2.31E-05	1.4	0.0
<sup>241</sup> Am	0.00E+00	3.66E-08	3.3	0.1	7.18E-07	1.9	0.1	1.99E-06	1.8	0.1
<sup>243</sup> Am	0.00E+00	9.64E-09	5.9	0.0	8.18E-07	3.0	0.0	7.00E-06	1.9	0.0
<sup>244</sup> Cm	0.00E+00	5.70E-10	6.9	0.0	1.76E-07	3.4	0.0	3.61E-06	2.1	0.0

TABLE 10: Uncertainty in number density of some important fission products. Cross-section uncertainties are taken from SCALE6.1/44-GROUP ( $\Delta XS$ ). Fission yields ( $\Delta FYs$ ) and decay data ( $\Delta DD$ ) source of uncertainty from JEFF-3.1.1.

	0 GWd/MTU		10 GWd/MTU			30 GWd/MTU			60 GWd/MTU				
	Mean	Mean	Rel. std. dev. (%)			Mean	Rel. std. dev. (%)			Mean	Rel. std. dev. (%)		
			$\Delta XS$	$\Delta DD$	$\Delta FYs$		$\Delta XS$	$\Delta DD$	$\Delta FYs$		$\Delta XS$	$\Delta DD$	$\Delta FYs$
<sup>154</sup> Gd	0.00E+00	1.45E-09	11.8	0.1	2.3	4.20E-08	7.2	0.0	1.1	2.69E-07	5.2	0.0	0.8
<sup>155</sup> Gd	0.00E+00	5.06E-10	12.4	0.2	5.1	2.23E-09	15.2	0.2	2.4	5.80E-09	15.4	0.2	1.1
<sup>156</sup> Gd	0.00E+00	1.59E-07	3.9	0.1	3.0	1.34E-06	3.6	0.0	1.4	7.71E-06	4.1	0.0	0.8
<sup>158</sup> Gd	0.00E+00	6.06E-08	5.5	0.0	2.9	3.51E-07	5.3	0.0	1.8	1.43E-06	6.8	0.0	1.2
<sup>160</sup> Gd	0.00E+00	3.80E-09	1.3	0.0	4.8	2.25E-08	0.9	0.0	3.3	7.28E-08	0.7	0.0	2.9
<sup>151</sup> Eu	0.00E+00	5.98E-10	1.9	3.3	3.1	8.30E-10	2.0	3.1	2.5	7.89E-10	2.3	3.2	2.0
<sup>153</sup> Eu	0.00E+00	6.72E-07	2.2	0.0	2.1	3.31E-06	3.8	0.0	1.0	7.30E-06	6.0	0.0	0.7
<sup>154</sup> Eu	0.00E+00	6.87E-08	15.3	0.0	2.1	6.72E-07	11.3	0.0	1.0	1.94E-06	11.2	0.0	0.7
<sup>155</sup> Eu	0.00E+00	4.36E-08	14.1	0.0	5.9	1.98E-07	16.6	0.0	2.9	5.64E-07	18.6	0.0	1.3
<sup>147</sup> Sm	0.00E+00	4.24E-07	0.8	0.0	2.9	2.57E-06	0.8	0.0	1.6	5.23E-06	1.0	0.0	1.2
<sup>148</sup> Sm	0.00E+00	4.48E-07	2.6	0.0	3.0	3.65E-06	1.4	0.0	1.6	1.19E-05	0.8	0.0	1.2
<sup>149</sup> Sm	0.00E+00	1.17E-07	14.0	0.0	6.4	1.21E-07	14.3	0.0	5.7	1.05E-07	15.5	0.0	5.1
<sup>150</sup> Sm	0.00E+00	2.75E-06	1.3	0.0	2.4	9.21E-06	1.0	0.0	1.4	1.88E-05	0.9	0.0	1.0
<sup>151</sup> Sm	0.00E+00	3.92E-07	1.7	0.0	4.0	5.26E-07	1.8	0.0	3.3	6.33E-07	2.2	0.0	2.5
<sup>152</sup> Sm	0.00E+00	1.30E-06	1.0	0.0	1.9	3.47E-06	1.2	0.0	1.3	5.26E-06	1.6	0.0	0.9
<sup>154</sup> Sm	0.00E+00	2.54E-07	1.0	0.0	2.8	9.81E-07	0.6	0.0	1.8	2.47E-06	0.4	0.0	1.2
<sup>142</sup> Nd	0.00E+00	3.74E-08	3.8	0.0	3.0	4.40E-07	2.2	0.0	1.6	2.08E-06	1.5	0.0	1.1
<sup>143</sup> Nd	0.00E+00	1.23E-05	0.6	0.0	2.6	3.23E-05	0.5	0.0	1.4	4.79E-05	0.5	0.0	1.1
<sup>145</sup> Nd	0.00E+00	9.10E-06	0.7	0.0	2.8	2.46E-05	0.5	0.0	1.6	4.18E-05	0.5	0.0	1.1
<sup>146</sup> Nd	0.00E+00	7.51E-06	0.7	0.0	2.5	2.34E-05	0.5	0.0	1.3	5.03E-05	0.4	0.0	0.9
<sup>148</sup> Nd	0.00E+00	4.20E-06	0.7	0.0	2.1	1.24E-05	0.5	0.0	1.3	2.45E-05	0.4	0.0	0.9
<sup>150</sup> Nd	0.00E+00	1.76E-06	0.8	0.0	2.7	5.57E-06	0.5	0.0	1.8	1.18E-05	0.4	0.0	1.2
<sup>133</sup> Cs	0.00E+00	1.55E-05	0.7	0.0	2.0	4.36E-05	0.5	0.0	1.1	7.63E-05	0.4	0.0	0.9
<sup>134</sup> Cs	0.00E+00	4.83E-07	2.5	0.0	2.2	3.74E-06	1.6	0.0	1.1	1.16E-05	1.5	0.0	0.9
<sup>135</sup> Cs	0.00E+00	6.23E-06	1.4	0.1	2.5	1.82E-05	0.9	0.0	1.5	3.43E-05	0.8	0.0	1.0
<sup>137</sup> Cs	0.00E+00	1.51E-05	0.7	0.1	2.6	4.43E-05	0.5	0.0	1.6	8.59E-05	0.4	0.0	1.2
<sup>139</sup> La	0.00E+00	1.54E-05	0.7	0.0	2.4	4.46E-05	0.5	0.0	1.6	8.57E-05	0.3	0.0	1.2
<sup>140</sup> Ce	0.00E+00	1.39E-05	0.7	0.0	2.6	4.29E-05	0.5	0.0	1.5	8.48E-05	0.3	0.0	1.1
<sup>142</sup> Ce	0.00E+00	1.40E-05	0.7	0.0	2.6	4.05E-05	0.5	0.0	1.5	7.75E-05	0.3	0.0	1.1
<sup>144</sup> Ce	0.00E+00	9.12E-06	0.7	0.0	2.3	1.45E-05	0.5	0.0	1.7	1.44E-05	0.5	0.0	1.6
<sup>95</sup> Mo	0.00E+00	8.36E-06	1.0	0.0	9.7	3.55E-05	0.7	0.0	6.8	6.90E-05	0.5	0.0	4.8
<sup>99</sup> Tc	0.00E+00	1.47E-05	0.7	0.0	2.6	4.15E-05	0.5	0.0	1.6	7.44E-05	0.4	0.0	1.3
<sup>101</sup> Ru	0.00E+00	1.29E-05	0.7	0.0	2.8	3.82E-05	0.5	0.0	1.8	7.40E-05	0.4	0.0	1.2
<sup>106</sup> Ru	0.00E+00	1.80E-06	1.2	0.0	3.9	6.14E-06	0.7	0.0	2.2	1.18E-05	0.5	0.0	1.8
<sup>103</sup> Rh	0.00E+00	6.45E-06	1.3	0.0	3.0	2.11E-05	1.7	0.0	1.8	3.66E-05	2.4	0.0	1.3
<sup>109</sup> Ag	0.00E+00	4.50E-07	1.6	0.0	3.9	2.55E-06	1.9	0.0	1.8	7.00E-06	2.6	0.0	1.2

with 13.9% and 4.0%, predicted by GRS and UPM, respectively. NRG with TENDL2011 predicts similar values to UPM.

- (7) For number density of fission products, NRG predicts larger uncertainty values than UPM and GRS, with a maximum uncertainty in <sup>147</sup>Sm of 31.7%. For this isotope, GRS and UPM predict an uncertainty approximately 2%. So, the influence of TENDL2011 in the prediction of fission products is quite large. Decay data uncertainty is analyzed by UPM showing only an important uncertainty of 3.3% in <sup>151</sup>Eu.

The contribution of fission yield data uncertainty is also studied by UPM; the predicted number density uncertainty is in the range of 1–4%, with a maximum value for <sup>95</sup>Mo with 4.8%. And, for uncertainty cross-section, the largest uncertainties found by UPM are <sup>155</sup>Gd (15.4%), <sup>155</sup>Eu (18.6%), and <sup>149</sup>Sm (15.5%). For these isotopes, GRS predicts lower uncertainty: <sup>155</sup>Gd (5.3%), <sup>155</sup>Eu (5.5%), and <sup>149</sup>Sm (2.5%).

- (8) In the case of <sup>155</sup>Gd (generated by  $\beta$ -decay of <sup>155</sup>Eu), it shows higher sensitivities to <sup>153,155</sup>Eu( $n, \gamma$ ) reaction

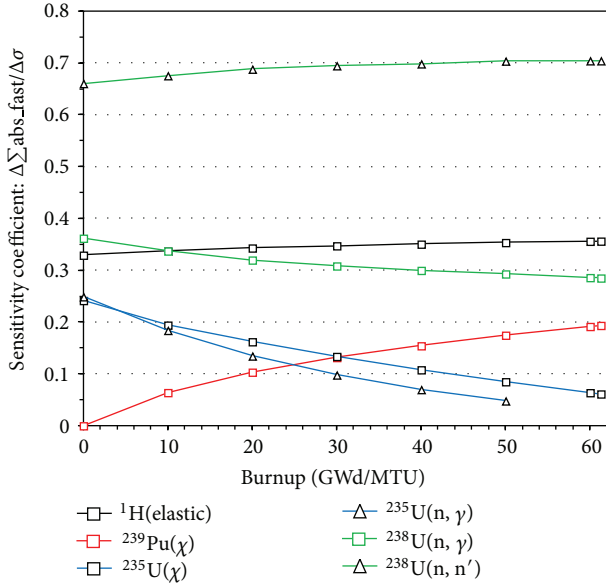


FIGURE 7: Sensitivity coefficients calculated with SCALE6.1/TRITON/Tsunami.

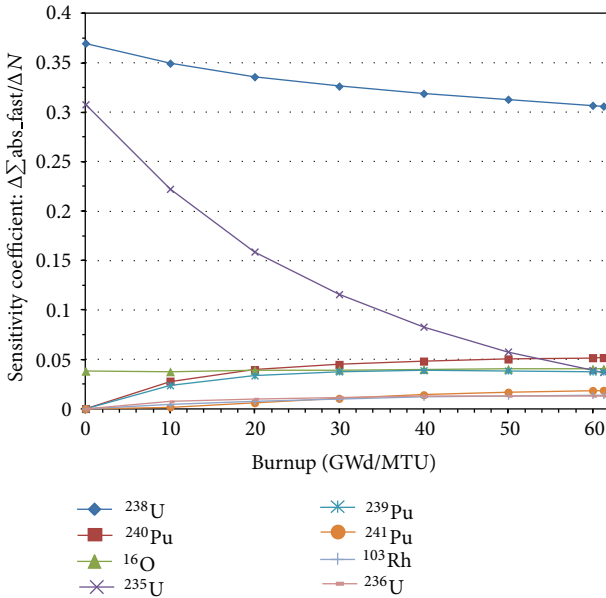


FIGURE 8: Sensitivity coefficients calculated with SCALE6.1/TRITON/Tsunami.

and <sup>155</sup>Eu fission yield. For <sup>149</sup>Sm (important contribution generated by β-decay of <sup>149</sup>Pm) the higher sensitivities are due to <sup>149</sup>Sm(n, γ) and <sup>149</sup>Pm fission yield.

It is expected that new contributions for this benchmark will supply additional information to define the output range of uncertainty of this Exercise I-1b. And, as complete covariance data in ENDF/B-VII.1, JEFF-3.2, and JENDL-4.x

become available, exercise I-1b can be performed as originally designed and results compared with the SCALE6/44-GROUPS library supplying additional valuable information.

Finally, a general recommendation of this work should be the definition of input uncertainties for the following UAM Exercises. In particular one of the next steps in the roadmap of OECD LWR UAM benchmark is Phase II (“Core Phase”) and in particular is the “Exercise II-2: Time-Dependent Neutronics”: where neutron kinetics and fuel depletion stand-alone performance will be assessed. From the point of view of burn-up calculations, it can be considered a long-term time phenomena described by fuel assembly depletion performance (used for core design and fuel management). The objective of this Exercise II-2 will be to determine the uncertainty in predicting the relative power over time of a core after a short-term reactivity change as well as during longer-term depletion cases.

### Acknowledgment

This work is performed in the framework of the agreement in the area of Burn-Up Credit (P090531725) and Propagation of Uncertainties (P110530207) in Criticality Safety between the Spanish Nuclear Safety Council (CSN) and the Universidad Politécnica de Madrid (UPM).

### References

- [1] M. N. Avramova and K. N. Ivanov, “Verification, validation and uncertainty quantification in multi-physics modeling for nuclear reactor design and safety analysis,” *Progress in Nuclear Energy*, vol. 52, no. 7, pp. 601–614, 2010.
- [2] ZZ-SCALE6. 0/COVA-44G, USCD1236/02 OECD-NEA Data Bank.
- [3] B. T. Rearden et al., ORNL/TM-2005/39 Version 6, vol. I, Sect. C9.
- [4] J. Leppänen and M. Pusa, “Burnup calculation capability in the PSG2/Serpent Monte Carlo reactor physics code,” in *Proceedings of the International Conference on Mathematics, Computational Methods and Reactor Physics (M and C ’09)*, pp. 1662–1673, Saratoga Springs, New York, NY, USA, May 2009.
- [5] H. J. Park, H. J. Shim, and C. H. Kim, “Uncertainty propagation in monte carlo depletion analysis,” *Nuclear Science and Engineering*, vol. 167, no. 3, pp. 196–208, 2011.
- [6] M. Klein, L. Gallner, B. Krzykacz-Hausmann, A. Pautz, and W. Zwermann, “Influence of nuclear data uncertainties on reactor core calculations,” *Kerntechnik*, vol. 76, no. 3, pp. 174–178, 2011.
- [7] D. Rochman, A. J. Koning, S. C. van der Marck, A. Hogenbirk, and C. M. Sciolla, “Nuclear data uncertainty propagation: perturbation vs. Monte Carlo,” *Annals of Nuclear Energy*, vol. 38, no. 5, pp. 942–952, 2011.
- [8] N. García-Herranz, O. Cabellos, J. Sanz, J. Juan, and J. C. Kuijper, “Propagation of statistical and nuclear data uncertainties in Monte Carlo burn-up calculations,” *Annals of Nuclear Energy*, vol. 35, no. 4, pp. 714–730, 2008.
- [9] B. T. Rearden, “TSUNAMI sensitivity and uncertainty analysis capabilities in SCALE 5. no. 1,” *Transactions of the American Nuclear Society*, vol. 97, pp. 604–605, 2007.

- [10] J. Sanz, O. Cabellos, and N. García-Herranz, ACAB-2008: Activation Code V2008, NEA-1839, OECD/NEA Data Bank, 2008.
- [11] G. Chiba, K. Okumura, A. Oizumi, and M. Saito, "Sensitivity analysis of fission product concentrations for light water reactor burned fuel," *Journal of Nuclear Science and Technology*, vol. 47, no. 7, pp. 652–660, 2010.

## Research Article

# Uncertainty and Sensitivity Analyses of a Pebble Bed HTGR Loss of Cooling Event

**Gerhard Strydom**

*Nuclear Science and Engineering Division, Idaho National Laboratory (INL), 2525 N. Fremont Avenue, Idaho Falls, ID 83415, USA*

Correspondence should be addressed to Gerhard Strydom; [gerhard.strydom@inl.gov](mailto:gerhard.strydom@inl.gov)

Received 20 July 2012; Accepted 7 December 2012

Academic Editor: Kostadin Ivanov

Copyright © 2013 Gerhard Strydom. This is an open access article distributed under the Creative Commons Attribution License, which permits unrestricted use, distribution, and reproduction in any medium, provided the original work is properly cited.

The Very High Temperature Reactor Methods Development group at the Idaho National Laboratory identified the need for a defensible and systematic uncertainty and sensitivity approach in 2009. This paper summarizes the results of an uncertainty and sensitivity quantification investigation performed with the SUSA code, utilizing the International Atomic Energy Agency CRP 5 Pebble Bed Modular Reactor benchmark and the INL code suite PEBBED-THERMIX. Eight model input parameters were selected for inclusion in this study, and after the input parameters variations and probability density functions were specified, a total of 800 steady state and depressurized loss of forced cooling (DLOFC) transient PEBBED-THERMIX calculations were performed. The six data sets were statistically analyzed to determine the 5% and 95% DLOFC peak fuel temperature tolerance intervals with 95% confidence levels. It was found that the uncertainties in the decay heat and graphite thermal conductivities were the most significant contributors to the propagated DLOFC peak fuel temperature uncertainty. No significant differences were observed between the results of Simple Random Sampling (SRS) or Latin Hypercube Sampling (LHS) data sets, and use of uniform or normal input parameter distributions also did not lead to any significant differences between these data sets.

## 1. Introduction

Title 10 Part 50 (10 CFR 50.46) of the United States Code of Federal Regulations first allowed “Best Estimate” calculations rather than conservative code models of safety parameters in nuclear power plants in the 1980s, stipulating, however, that uncertainties be identified and quantified [1]. The continued development of High Temperature Gas Cooled Reactors (HTGRs) requires validation and verification of HTGR design and safety models and codes, and the predictive capability of coupled neutronics/thermal-hydraulics and depletion simulations for reactor design and safety analysis can be assessed with sensitivity analysis (SA) and uncertainty analysis (UA) methods.

In general, code uncertainty refers to uncertainty in the ability of a computer software product, coupled with a specific model, to accurately describe the actual physical system of interest. The computer model is an integration of the mathematical model, the numerical techniques used to solve those equations, and the representation of the physical model

by the input geometry and material specifications. Each element contributes to the total uncertainty in the output parameter of interest, usually referred to as the Figure of Merit (FOM) in nuclear safety studies. The mathematical model consists of one or more governing equations that describe the balance between the creation, destruction, and flow of some quantity of interest (e.g., heat, coolant mass, or neutron flux) within a homogeneous control volume. It also consists of one or more subgrid equations that relate these gross phenomena to more complex physics that are neglected at the scale of the homogeneous control volume (e.g., neutron streaming between pebbles, heat conduction from the kernels to the pebble surface, etc.).

A further complication is that very few computer codes solve the analytic form of its governing equations. Instead, the differential operators in these equations are expanded as a truncated series and cast as a set of difference equations solved over a discrete mesh. If the equations are well posed, the solution is unique and refining the mesh reduces the error between the solutions of the discretized equation and

the original differential equation. Unfortunately, unlimited mesh refinement is not possible and one must tolerate some truncation error. Furthermore, in many complex fluid system simulation codes, the combination of governing equations and subgrid correlations yields ill-posed systems of differential equations that do not converge to the analytical solution upon refinement of the mesh.

Another important source of uncertainty is that the input model is a simplification of the actual physical geometry. For example, the distribution of fuel pebbles in a HTGR core is neither regular nor uniform, but to model individual pebbles is computationally prohibitive. Complex geometrical detail in some of the prismatic HTGR designs can likewise be very difficult to model accurately. The fourth major source of input uncertainty is the material neutronic and thermophysical properties. For core analysis, these include thermal properties such as conductivity and heat capacity, fluid properties such as density and viscosity, and neutronic properties such as cross sections. Knowledge of these parameters for each material of interest may be limited in the range of conditions found in a typical HTGR. Such uncertainty can be reduced through material testing and measurement, but the amount of testing is often limited by cost and schedule constraints and must be propagated through the calculations. In some cases, the natural variability of a given parameter under even the best experimental conditions may be large enough to inject uncertainty that cannot be ignored. Finally, when modeling of an actual operating reactor is considered, it is well known that the operational conditions (power level, inlet temperature, measured mass flow rates) can also have associated uncertainty ranges.

Of the four types of uncertainty sources indicated here, the uncertainties in material properties can usually be addressed by relatively simple manipulation of the corresponding values in the input decks, and geometry simplifications can be benchmarked against higher fidelity codes (e.g., 2D versus 3D effects). In contrast, propagation of uncertainties in mathematical models and solver techniques are much more challenging, and in most cases not yet attempted in industry. Developments in uncertainty methodology are therefore currently focused on cross-section, model and material input data uncertainties, and specifically on the propagation of uncertainties through sets of coupled neutronic and thermal-fluid calculations.

Several large international uncertainty quantification programs have been developed in recent years, of which the LWR Uncertainty Analysis in Modeling (UAM) benchmark [2] and the earlier BEMUSE [3] project are two examples. Both these efforts are coordinated by the Organization for Economic Co-operation and Development/Nuclear Energy Agency (OECD/NEA). These benchmarks include code-to-code comparisons of uncertainty predictions for cell, lattice and core physics calculations using common datasets, as well as comparisons with experimental and operational Light Water Reactor (LWR), Boiling Water Reactor (BWR), and Vodo-Vodyanoi Energetichesky Reactor (VVER) facilities. The HTGR community has however only recently initialized a dedicated Coordinated Research Project (CRP) for the quantification and propagation of uncertainties in a pebble

bed and prismatic HTGR design [4]. One of the crucial advantages of the LWR community is the availability of large operational databases, where numerous measurements can support uncertainty validation efforts. In the HTGR domain, very few operational facilities exist (e.g., the Chinese HTR-10 and the Japanese HTTR), or the historical measured data is not sufficiently accurate (German AVR) or available in the public domain (USA—Fort St. Vrain).

The Very High Temperature Reactor (VHTR) Methods Development group at the Idaho National Laboratory (INL) identified the need for a defensible and systematic uncertainty and sensitivity approach that conforms to the code scaling, applicability, and uncertainty (CSAU) process in 2009. The Gesellschaft für Anlagen und Reaktorsicherheit (GRS) has incorporated a stochastic sampling CSAU approach that is particularly well suited for coupled reactor physics and thermal fluids core analysis into the Software for Uncertainty and Sensitivity Analyses (SUSA) code [5]. The stochastic sampling method is utilized by several participants in the LWR UAM benchmark [6, 7], where the use of ordered statistics to derive upper and lower tolerance intervals have been widely adopted.

This paper summarizes the results of an uncertainty quantification investigation performed with SUSA, utilizing a typical HTGR benchmark (the International Atomic Energy Agency CRP-5 Pebble Bed Modular Reactor 400 MW Exercise 2) and the INL code suite PEBBED-THERMIX. For this study, the effects of uncertainties in the cross-section data and the propagated cell-to-lattice-to-core uncertainties have not yet been included—the focus here is on the effect of model and material input uncertainties for a coupled transient case. The CRP on HTGR UAM [4] does however propose to use the established methodology from the OECD/NEA LWR UAM program, and a similar depressurized loss of forced cooling (DLOFC) transient is included as part of the pebble bed test set. At INL the modeling focus has shifted to the prismatic MHTGR-350 MW design, and propagated uncertainties for this design will also be assessed as part of the CRP on HTGR UAM. A dedicated OECD/NEA code-to-code benchmark on the MHTGR-350 design was also recently launched [8], and the same codes and models will be utilized in the core modeling part of the HTGR UAM study.

## 2. Uncertainty Methodology

Two major approaches to perform uncertainty propagation in a statistically rigorous manner can be identified [9].

- (1) Methods based on the propagation of *input* uncertainties (also known as statistical or stochastic sampling methods) as represented by SUSA and Sandia National Laboratory code DAKOTA [10].
- (2) Methods based on the propagation of *output* uncertainties (also known as deterministic methods), for example, the capability of internal assessment of uncertainty method [11].

TABLE 1: PEBBED CRP-5 PBMR 400 DLOFC uncertainty study input parameters.

Parameter	Mean value	2 Standard deviations ( $2\sigma$ ) value	PDF type
Reactor power	400 MW	$\pm 8$ MW (2%)	Normal and uniform
Reactor inlet gas temperature (RIT)	500°C	$\pm 10^\circ\text{C}$ (2%)	Normal and uniform
Decay heat multiplication factor	1.0	$\pm 0.057$ (5.7%)	Normal and uniform
Fuel specific heat multiplication factor	1.0	$\pm 0.06$ (6%)	Normal and uniform
Reflector specific heat multiplication factor	1.0	$\pm 0.10$ (10%)	Normal and uniform
Fuel conductivity multiplication factor	1.0	$\pm 0.14$ (14%)	Normal and uniform
Pebble bed effective conductivity multiplication factor	1.0	$\pm 0.08$ (8%)	Normal and uniform
Reflector conductivity multiplication factor	1.0	$\pm 0.10$ (10%)	Normal and uniform

TABLE 2: PEBBED-THERMIX CRP-5 DLOFC uncertainty study cases.

Number of model runs	Input parameter sampling method	Input parameter distribution type	Model input parameters varied
100	Latin Hypercube	Uniform	Power, RIT, decay heat only
100	Latin Hypercube	Uniform	Specific heat and thermal conductivity only
100	Latin Hypercube	Uniform	All
100	Latin Hypercube	Gaussian/normal	All
200	Latin Hypercube	Gaussian/normal	All
200	Simple Random	Gaussian/normal	All

TABLE 3: Lilliefors and K-S test results for the 100 LHS Uniform set.

Test applied for Figure of Merit (DLOFC peak fuel temperature) fit	Level of Significance for Distribution Type			
	Normal	Lognormal	Exponential	Gamma
Lilliefors	0.64	0.79	0.01	—
K-S	0.92	0.97	—	0.95

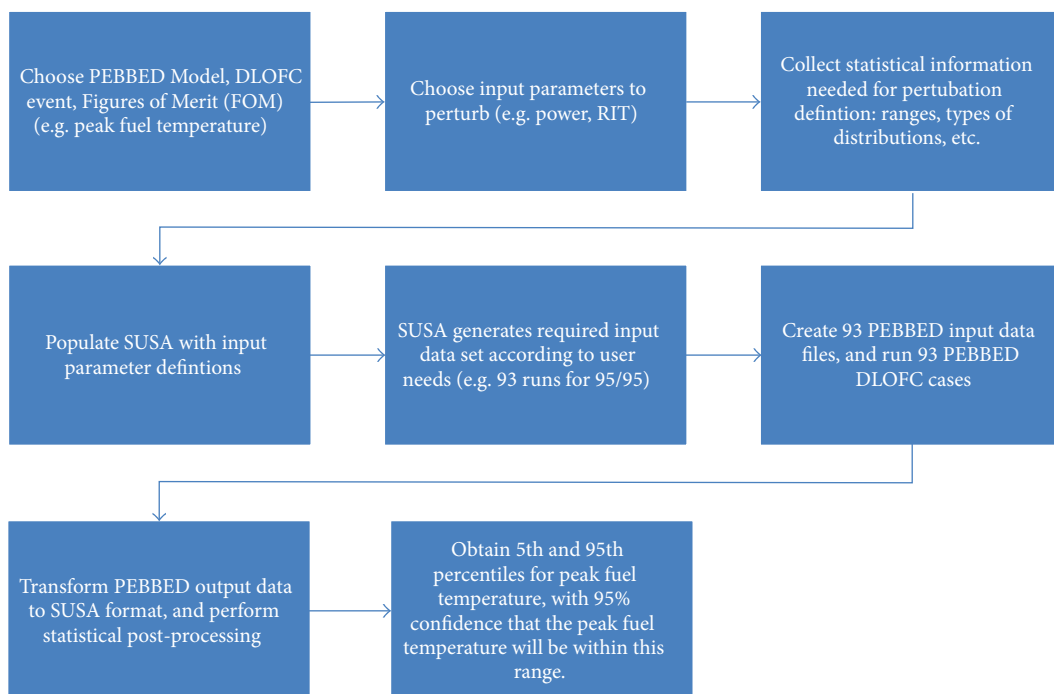


FIGURE 1: Example of the GRS methodology applied to the PEBBED-THERMIX CRP-5 PBMR 400 exercise 2 benchmark calculation.

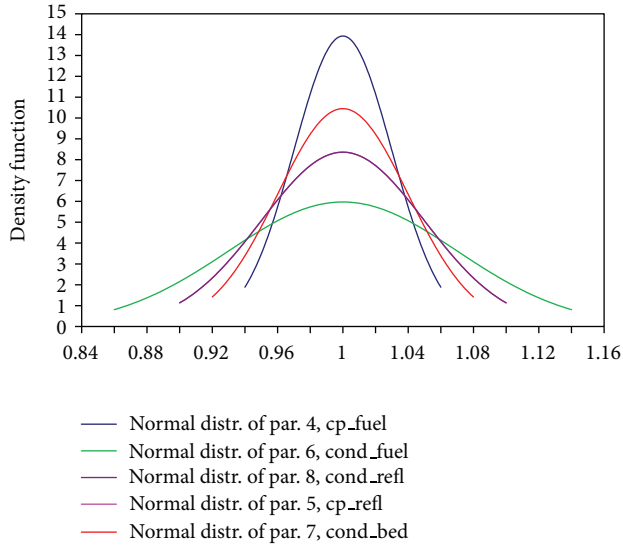


FIGURE 2: PDFs for the specific heat and thermal conductivity correlation input parameters.

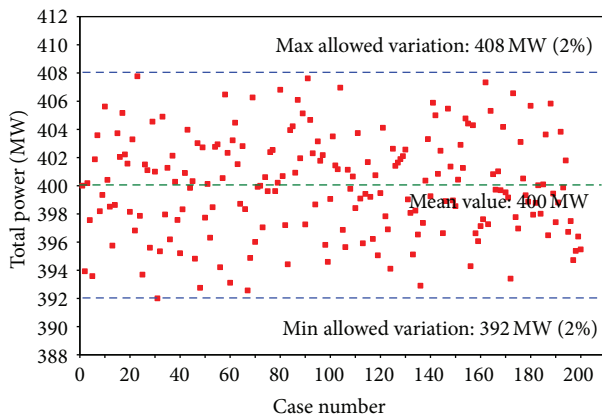


FIGURE 3: Sampled values of the total power (MW) for the 200 LHS Normal set.

(The direct perturbation method is also identified as a possible third, but expensive, approach in [6]).

The two approaches can be summarized as follows.

(i) Statistical methods (input uncertainty propagation).

- (1) Assign subjective probability ranges and distributions to (an unlimited number of) input parameters.
- (2) Propagate the combined uncertainty through the core models to determine the statistical distribution properties of the Figure of Merit (FOM). Typically lower and upper tolerance intervals can be obtained within some defined confidence level, using an ordered statistics approach.
- (3) Disadvantages include the subjective selection of input parameter distributions types and ranges, and the fact that at least 59 model

calculations are required to obtain acceptable statistical information for an one-sided 95% tolerance limit with 95% confidence.

(ii) Deterministic methods (output uncertainty propagation).

- (1) Use of a relevant set of experimental data to establish a database of uncertain data for a large number of input parameters.
- (2) Create hypercubes characterizing physical parameters and their dependencies for a wide variety of plant conditions, transients, and so forth.
- (3) Perform a single calculation utilizing all input parameters to determine the error bands enveloping the output FOM.
- (4) Disadvantages include the availability of large operational/experimental datasets for the construction of the hypercubes, and the inability of this method to distinguish the major contributors to the overall uncertainty.

Typically, because of the deterministic method requirement to have a large and comprehensive experimental database available, LWR and BWR uncertainty studies can use this method (especially for thermal fluid uncertainty studies). However, in the HTGR domain, very limited experimental and operational data exists, and the use of statistical uncertainty methods is currently the only viable approach for coupled uncertainty propagation.

The first step in the GRS method is to select the set of uncertain input parameters that will be used to evaluate the desired FOM. It is important to note that the stochastic sampling methodology is independent of the number of input parameters selected, and that all of them are sampled simultaneously as a single set. Information from the manufacture of nuclear power plant components as well as from experiments and previous calculations are used to define the mean value and probability distribution or standard deviation of uncertain parameters. Normal (and in some cases uniform) distributions are used in the absence of more knowledge about the input parameters. Once these distributions and dependencies have been established, the analyst can:

- (i) generate a random sample of size  $N$  for the input parameters from their probability distributions by a Monte Carlo module contained in the SUSA package ( $N = 93$  for two-sided 5% lower and 95% upper tolerance intervals, with a 95% confidence level—see (1) below);
- (ii) perform the corresponding  $N$  simulations with the codes. Each simulation generates one possible solution of the model, and all solutions together represent a sample from the unknown probability distribution of the model results;
- (iii) calculate quantitative uncertainty statements, for example, 5% and 95% tolerance intervals within a

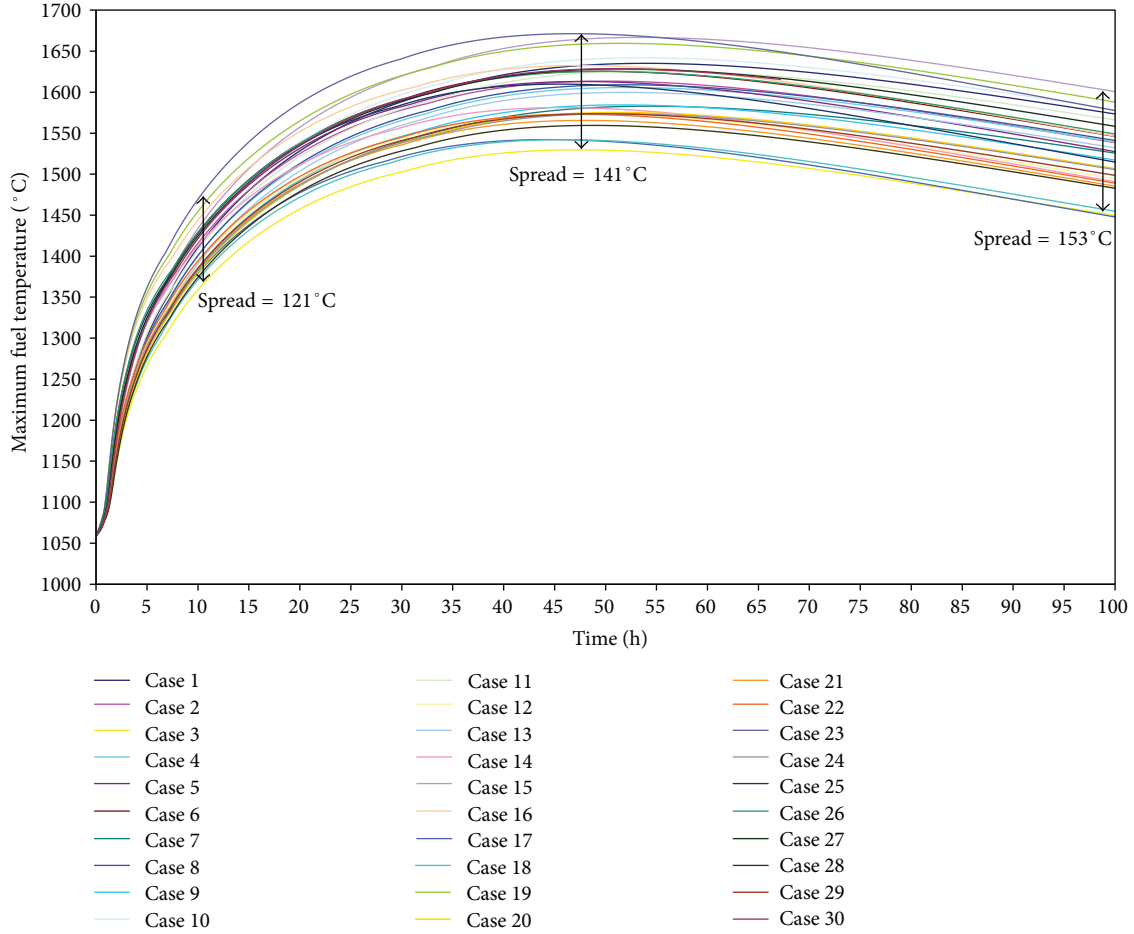


FIGURE 4: DLOFC maximum fuel temperature versus time for the first 30 cases of the 100 SRS Uniform set.

specified confidence level, usually 95% (denoted here as 95%/95%);

- (iv) calculate quantitative sensitivity measures to identify those uncertain parameters that contribute most to the uncertainty of the results.

The number of code calculations is determined by the requirement to estimate a tolerance interval for the quantity of interest with a specified confidence level. Wilks' formulae [12], shown here as (1), are used to determine the number of calculations required to obtain the desired one-sided and two-sided tolerance intervals:

$$1 - a^n \geq b, \tag{1}$$

$$(1 - a^n) - n(1 - a) a^{n-1} \geq b,$$

where  $(b \times 100)$  is the confidence level (%) that the maximum code result will not be exceeded with the probability  $(a \times 100)$  [%] of the corresponding output distribution, and  $n$  the number of calculations required. For example, the one sided “upper” 95% tolerance interval of the (unknown) peak fuel temperature distribution can be obtained with a confidence level of 95% by selecting  $n = 59$ , and the same number of model calculations would be needed for

the “lower” 5% tolerance interval. If both tolerance intervals are required (i.e., a bounding statement is desired on the lower and upper “range” of the peak fuel temperature), 93 model runs would be required for the 95%/95% two-sided tolerance intervals. It is important to note that this method does not generate the “true” distributions of the output parameters (for this to be possible, several hundred or thousand model runs would be required), but rather selected statistical information about these unknown output distributions, based on comparisons with standard statistical distributions.

*2.1. Application to the PBMR 400 Benchmark Problem.* Figure 1 presents a simplified flow diagram of the statistical sampling methodology followed for this study, utilizing the PEBBED-THERMIX codes [13] and the PBMR 400 Exercise 2 benchmark [14] test case. A combination of three reactor physics codes was utilized: COMBINE-7 for cross section preparation, PEBBED for pebble-bed reactor design and fuel cycle analysis, and THERMIX-KONVEK for thermal fluid analysis [13]. PEBBED is used for analysis of neutron flux and isotopic depletion and buildup in a pebble bed HTGR. The code can treat arbitrary pebble circulation schemes, and it permits more than one type of pebble to be specified. The large

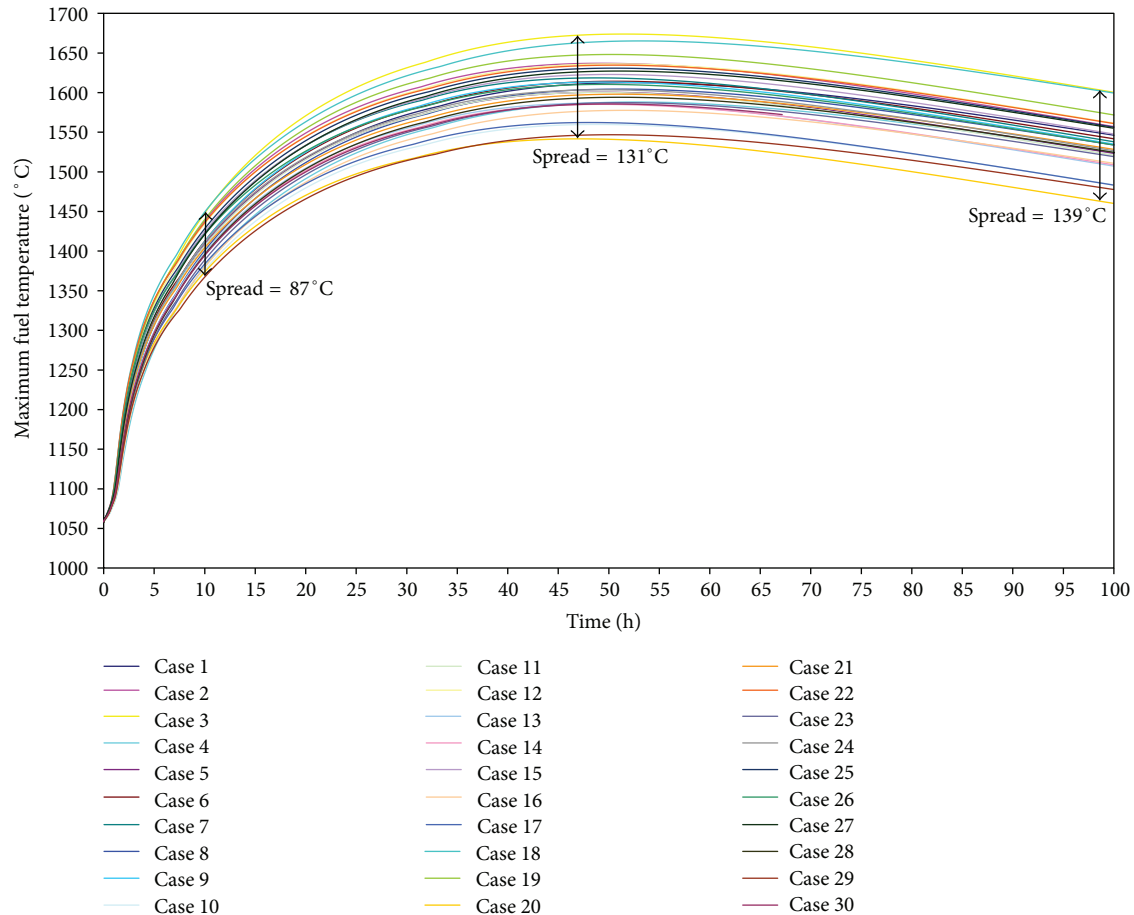


FIGURE 5: DLOFC maximum fuel temperature versus time for the first 30 cases of the 100 LHS Normal set.

temperature and burnup variations across the core require that it be discretized into many smaller “spectral zones” over which cross sections are assumed to be constant. Because the burnup and temperature profiles of the equilibrium core are not known *a priori*, the core neutronic and temperature profiles must be solved iteratively along with the generation of cross sections. To that end, PEBBED calls THERMIX-KONVEK and COMBINE after each burnup sweep and continues this iteration until the neutron source, temperatures, pebble flow maps, and zone-wise infinite medium multiplication factors are converged within tolerances specified by the user.

The THERMIX-KONVEK code was developed in Germany during the German HTGR program for the thermal fluid analysis of pebble bed HTRs [13]. It is capable of solving conduction and convection heat transfer in two dimensions (R-Z), and includes a simplified treatment of the radiative heat transport between the core structures. The code can also predict the time-dependent conduction heat transport during a DLOFC event by assuming that all convection terminates instantaneously.

An existing PEBBED-THERMIX model of the CRP-5 PBMR 400 MW benchmark was used as the starting point of the uncertainty study.

**2.2. Input Parameters, Distribution Types, and Variations.** The typical FOM for a DLOFC event is the peak fuel temperature, that is, the maximum spatial and temporal temperature reached in the fuel spheres. As a demonstration of the uncertainty methodology applied to a typical HTGR problem, eight input parameters were selected for this study, as shown in Table 1. Note that these eight parameters are an incomplete subset of all possible parameters that could affect the DLOFC peak fuel temperature, since this study is not designed to provide a complete assessment of the effect of all uncertainties.

Since the selection of the input parameters and their distributions is one of the known weak points of the stochastic sampling methodology, the results of a separate TINTE study, performed for the PBMR 400 MW design [15], was used to determine which eight parameters to include for this PEBBED DLOFC case. This study indicated that metal and graphite emissivity only influenced the metal component temperatures, and uncertainties in the helium thermal physical properties also did not result in any changes in the FOM. Out of 19 input parameters investigated in the TINTE study, six had no effect on the steady state and DLOFC peak fuel temperatures, eight had less than 10°C (0.6%) effect, and only five factors resulted in changes larger than 10°C in

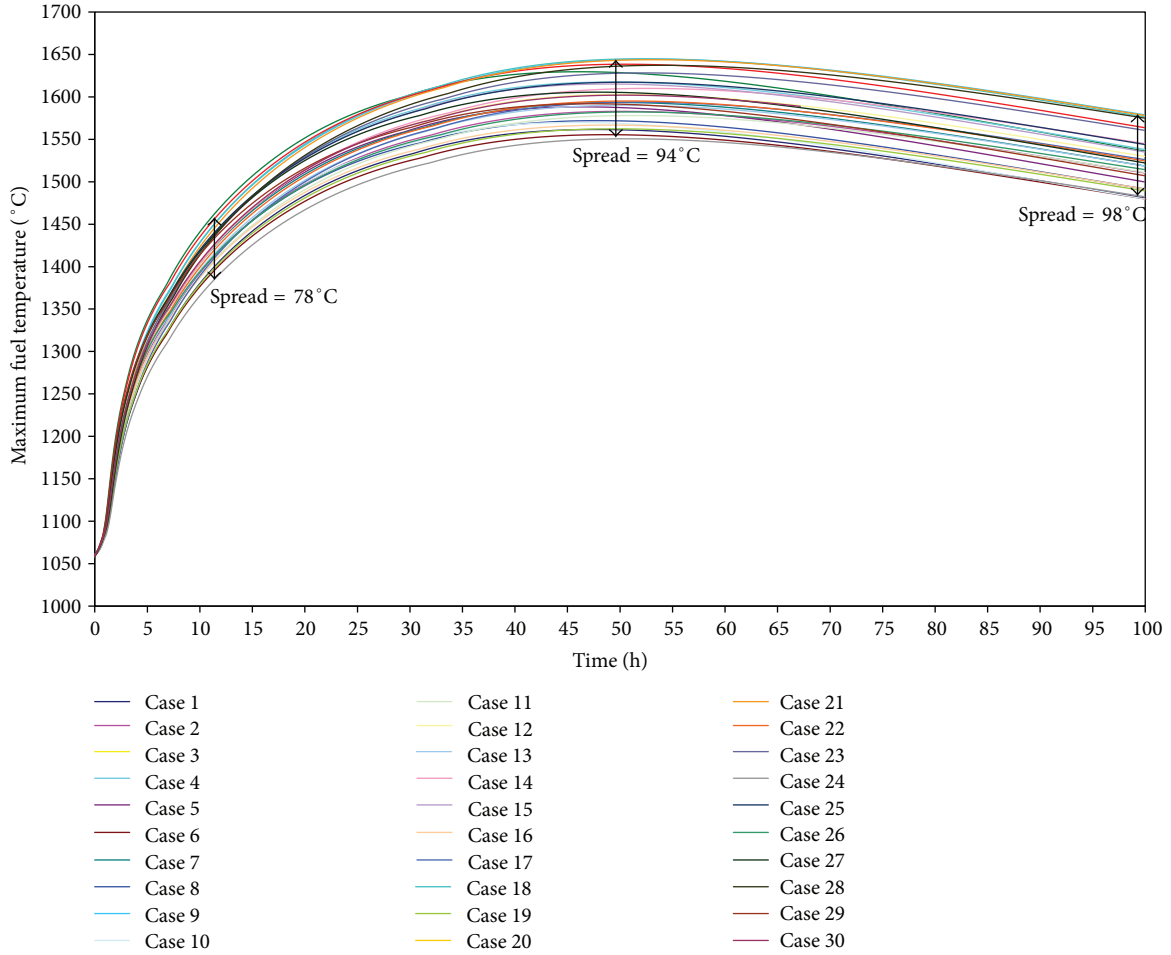


FIGURE 6: DLOFC maximum fuel temperature versus time for the first 30 cases of the 200 LHS Normal set.

the DLOFC FOM. These five input variables, together with three more that had a larger than 1% influence on the steady state temperature, were selected for inclusion in this study.

The variations on the power and reactor inlet gas temperature were applied directly on the absolute value of the input variable itself (e.g., 2% on 400 MW), in contrast to the decay heat, specific heat, and thermal conductivity, where the variations were applied as multiplication factors on the complex correlations that are used to calculate these variables. For example, the specific heat capacity of the reflector graphite material is a third-order polynomial function of temperature  $T$  and the density  $\rho$ , where

$$c_{\rho} = \rho (0.645 + 3.14T + 2.809T^2 + 0.959T^3). \quad (2)$$

The sampled multiplicative factor  $c_{\rho}$ -mod is then applied to the interim value to determine the final specific heat value in

$$c_{\rho} = c_{\rho}\text{-mod} * [\rho (0.645 + 3.14T + 2.809T^2 + 0.959T^3)]. \quad (3)$$

It should be noted that the decay heat is an almost linearly dependent variable of the long term steady state

reactor power, and as such it is not an independent input variable to this uncertainty quantification. While the SUSA code allows for input parameter dependencies (correlations) to be specified as part of the input preparation, this option was not selected for this study. It was rather decided to see if this input parameter correlation can be observed in the output data sensitivity analysis.

The mean and two standard deviations ( $2\sigma$ ) values shown in Table 1 were obtained from material manufacturers (specific heat and conductivity data for NBG-18 graphite from the SGL company), expert engineering judgment (power and inlet temperature), and from established industry standards (the German DIN standard for HTGR decay heat [16]).

A second potential weak point of the statistical method is the justification for the selection of the probability density function (PDF) types. Typical thermal physical properties, such as specific heat and thermal conductivity, can be obtained from the manufacturers, and are usually specified as normal PDFs with mean standard deviation values. More complex variable PDFs (e.g., variations in the core bypass flows) can be biased/skewed to one side, for example, gap widths grow larger or shrink over time as the graphite

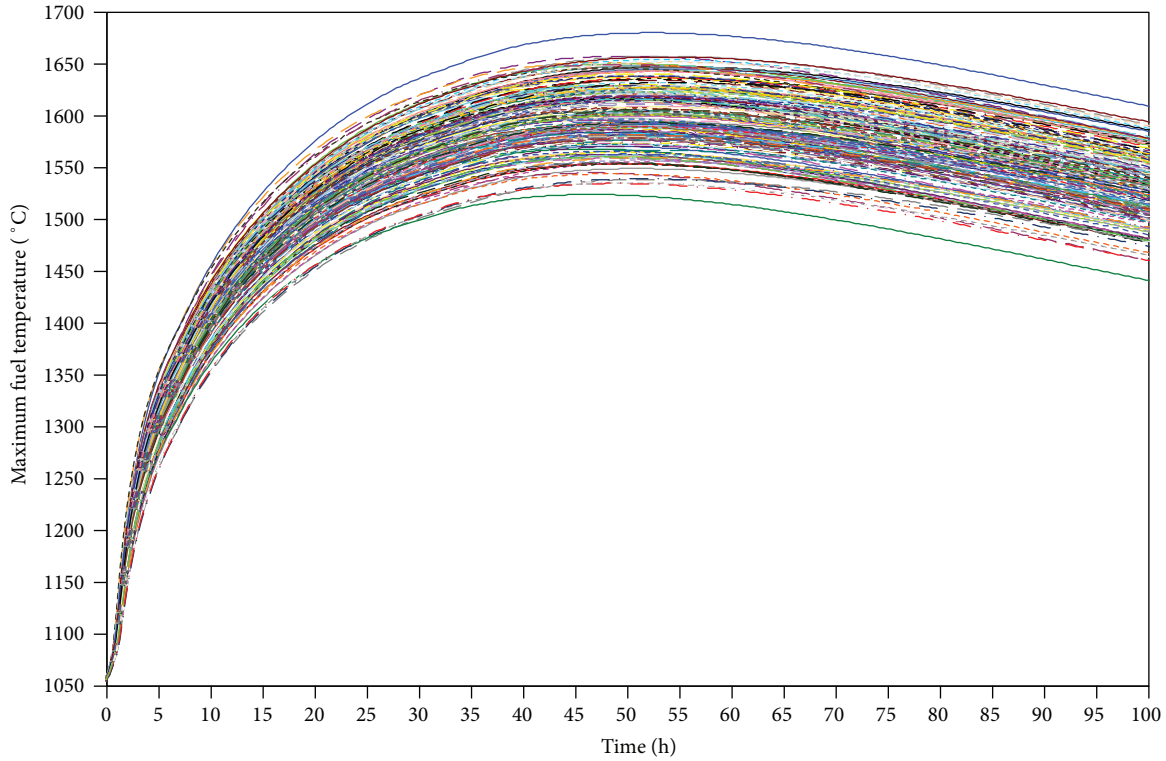


FIGURE 7: DLOFC maximum fuel temperature versus time for all 200 cases of the 200 LHS Normal set.

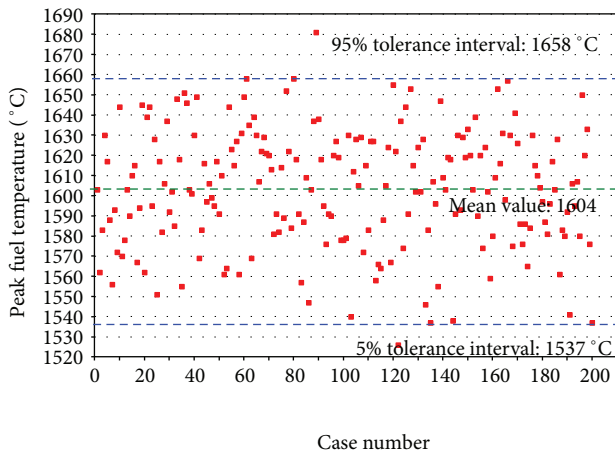


FIGURE 8: Peak DLOFC fuel temperature of the 200 LHS Normal set at 50 hours.

reflectors swell and shrink with fast fluence exposure. In cases where no definitive uncertainty information exists, a uniform or a normal/Gaussian PDF can be used with or without truncated tails. For this study, both normal and uniform PDFs were selected to assess if this factor plays a significant role in the DLOFC peak fuel temperature uncertainty. Figure 2 presents the PDF data for the specific heat and thermal conductivity input variations, with normal distributions selected and the mean and standard deviation values specified as listed in Table 1. Note that infinite tails of

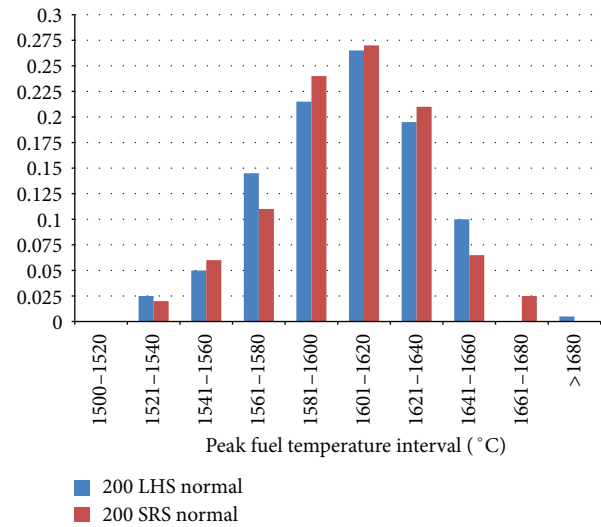


FIGURE 9: Normalized peak DLOFC fuel temperature histograms for the 200 LHS and SRS Normal sets.

the normal distributions were all truncated at their  $2\sigma$  values (at the 95.5% percentiles) to enable direct comparison with the uniform distributions' minima and maxima.

A total of six case sets (consisting of four sets of 100 and two sets of 200 model runs each) were performed for this study as described below and summarized in Table 2:

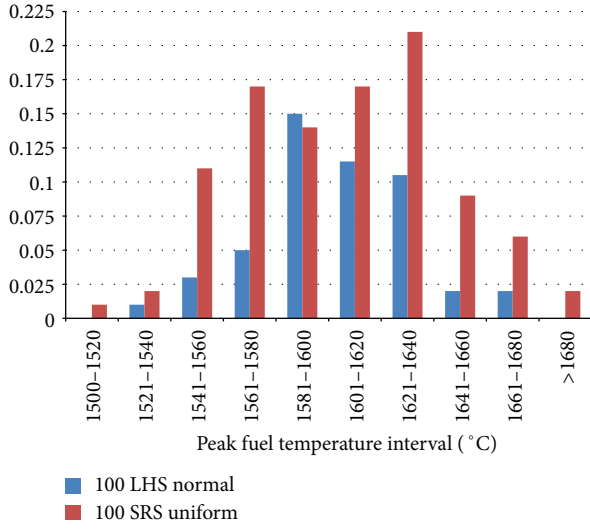


FIGURE 10: Normalized peak DLOFC fuel temperature histograms for the 100 LHS Normal and Uniform sets.

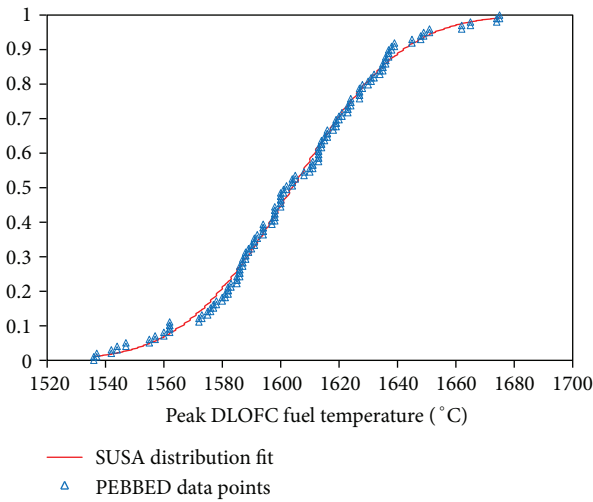


FIGURE 11: PDF and fitted normal distribution results for the 100 LHS Normal set: K-S level of significance = 0.9919.

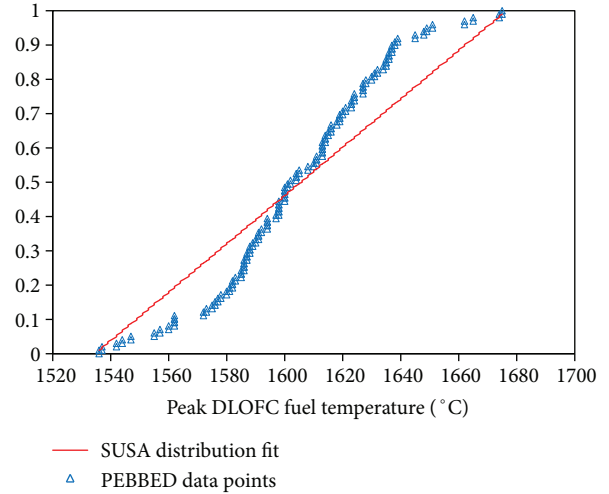


FIGURE 12: PDF and fitted uniform distribution results for the 100 LHS Normal set: K-S Level of Significance = 0.0026.

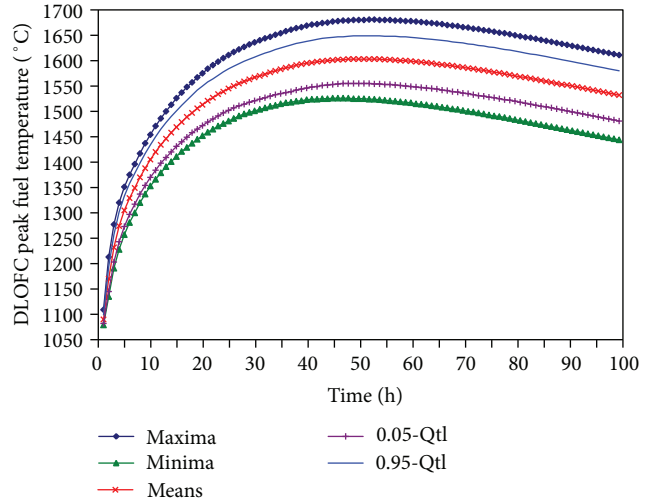


FIGURE 13: Time dependent minima, maxima, mean and 5/95 percentiles for the 200 LHS Normal set maximum fuel temperature.

- (i) Number of model runs: the number of model runs was doubled from 100 to 200 to investigate if a larger population sample produced significantly different statistical indicators.
- (ii) Sampling methodology: SUSA is capable of using either the simple random sampling (SRS) [17] or the Latin hypercube sampling (LHS) method [17] for generating the values of the input variables from their specified distributions. A comparison set of 200 model runs was performed to compare the FOM uncertainty estimates generated by these two sampling methods.
- (iii) Distribution type: two of the 100 model run sets were designed to quantify possible differences that could

result when the input parameter PDFs are changed from uniform to normal distribution types.

- (iv) Number of parameters sampled: a final point of interest was the uncertainty contribution of a few dominant input parameters compared to the combination of all eight input parameters. To this end, two sets of 100 model runs each were performed, varying only the material correlations and only the power, RIT, and decay heat correlation, respectively.

In the discussions that follow, the notation will be of the format “number, sampling method, distribution type”; for example, the first entry in Table 2 will be referred to as 100 LHS Uniform set.

The SUSA generated input data can be verified for conformance to the user’s specifications using scatter plots,

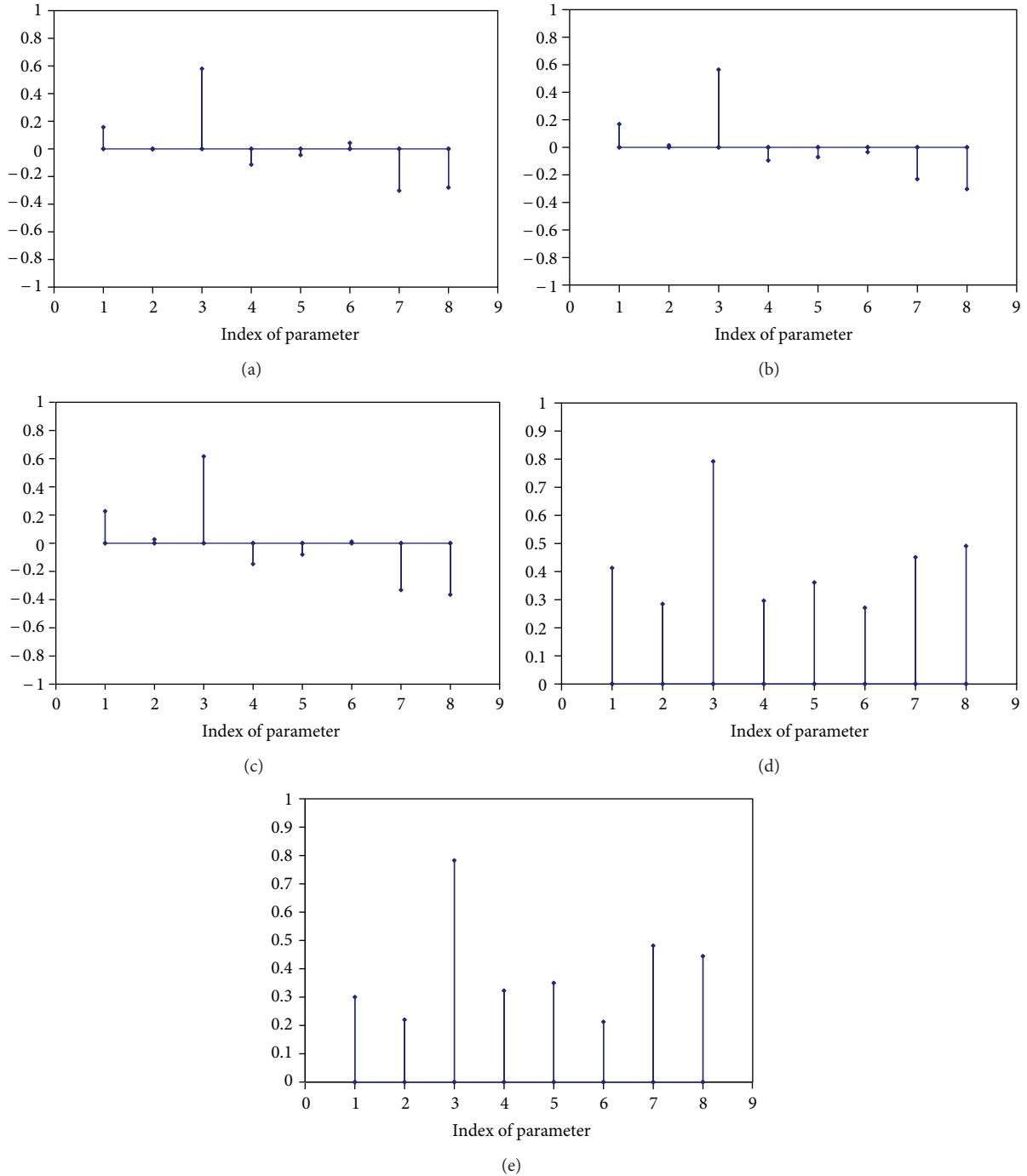


FIGURE 14: Kendall rank correlation coefficients for the 100 LHS Uniform (a) and 200 LHS Normal (b) sets. (c) Partial correlation coefficients for the Kendall correlation of the 200 LHS Normal set. Empirical correlation ratios for the 100 LHS Uniform (d) and 200 LHS Normal (e) datasets.

as shown in Figure 3 for the total power input parameter (for the 200 LHS Normal set).

### 3. Discussion of PEBBED-THERMIX Results

For the next step of the uncertainty quantification procedure, the SUSA-generated data for the eight input parameters were

used to create PEBBED and THERMIX model input files for the steady state and DLOFC calculations. The six sets listed in Table 2 required a total of 800 PEBBED-THERMIX calculations at an average run time of 35 minutes each on a single processor. Since it is possible to assign each model run to a dedicated processor on a multiprocessor cluster, the performance of large uncertainty studies is essentially

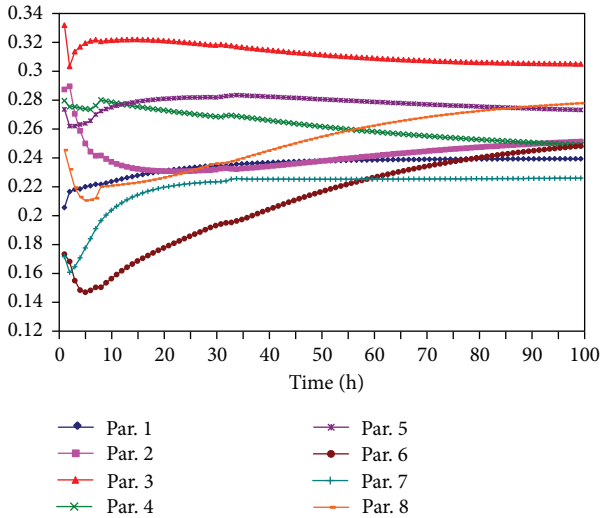


FIGURE 15: Empirical correlation ratios (peak fuel temperature) variations versus time for the 200 LHS Normal set.

determined by the number of processors available, and can in many cases be comparable to a single model run time if the cluster supports several hundred processors. The new FISSION cluster at INL has 12512 processors available.

The time behavior of the maximum fuel temperature during the DLOFC transient is shown in Figures 4, 5, and 6 for the first 30 cases of the 100 SRS Uniform, 100 LHS Normal, and 200 LHS Normal datasets, respectively. Note that the maximum fuel temperature is a *spatial* function, since the PEBBED-THERMIX model calculates temperatures in 110 core zones/meshes. The temporal maximum of this maximum fuel temperature during the DLOFC is defined as the *peak* fuel temperature, which is the FOM for this study. A few observations on the general trends can be made from this data as follows.

- (i) The PBMR core design leads to the typical HTGR loss of cooling behavior, that is, a slow increase in the maximum fuel temperature over several hours, with the peak fuel temperature reached 40–60 hours into the transient.
- (ii) The shapes of the curves in the first 30 cases are similar but the gradients are not. Although the same physical phenomena are present in all the DLOFC events, the rate of energy deposition (correlated to the decay heat) and energy removal (correlated to the fuel and reflector specific heat and thermal conductivities) differ for each of these cases, according to the sampled input values.
- (iii) Changes in the eight input parameters have opposite effects on the maximum fuel temperature: an increase in the decay heat will increase the fuel temperature, but an increase in the fuel graphite conductivity will remove heat faster from the core, and therefore lead to a lower fuel temperature. Since each DLOFC case consists of a random sampled set of the eight input parameters, the low fuel temperature curves can be

the result of a few parameters sampled low (or high) simultaneously, and an average fuel temperature curve could be caused by a cancellation of effects. These factors also cause the shift in time when the peak fuel temperature values are reached.

- (iv) The spread in maximum fuel temperatures between the first 30 cases is not constant with time. For example, it starts off with less than 5°C in the first hour and increases to 98°C for the 200 LHS Normal set, as shown in Figure 6. This divergence over time is a direct result of the sampled input parameter values, as explained above. For a time dependent event such as this DLOFC, a single and constant fuel temperature uncertainty result can therefore not be expected—it will be a function of time as well. It can be seen in Figures 4, 5 and 6 that the temperature spread between the cases continue to increase after the peak values have been reached, and a full uncertainty study should take this effect into account if it is required to determine what the maximum uncertainty bandwidth is.
- (v) The 95%/95% two-sided tolerance intervals are not compared at a fixed time point, but rather at the varying time point where a specific case reaches its peak DLOFC fuel temperature. This study therefore compares the *bounding value* fuel temperature uncertainty for the DLOFC event, regardless of when this point is reached, since the DLOFC peak fuel temperature is of major interest in HTGR reactor design safety studies.
- (vi) The temperature variation bandwidth for the 3 cases shown here seem to be quite different. The two sets that consisted of 100 runs each produced significantly larger variations than the 200 LHS Normal set (e.g., 141°C versus 94°C), and there is also a smaller difference between the 100 LHS Normal and 100 SRS Uniform sets (131°C versus 141°C). It is however important to note that the figures just show the first 30 model runs of each set for clarity sake. For the 200 LHS Normal set, the remaining 170 model runs sample a larger portion of the “true” unknown distribution, with a resultant larger bandwidth, as shown in Figure 7. (It is shown in Table 4 in the next section that the uncertainty estimates for the 6 full sets are very similar).
- (vii) The primary FOM for this study (DLOFC peak fuel temperature) results are presented in Figure 8 as a scatter plot for the 200 LHS Normal set. The mean and  $\pm 2\sigma$  values, as determined by SUSAs (see next section) are also indicated. The same data are compared in Figure 9 in a more useful format, where the normalized DLOFC peak fuel temperature histograms for the 200 LHS and SRS Normal sets are shown. The histograms both approximate normal distributions, so that (visually) no significant differences can be observed at this stage between the SRS and LHS sampling methods.

- (viii) A more pronounced visual difference can be observed in Figure 10, where the normalized histograms are shown for the 100 LHS Normal and Uniform sets. It is tempting to conclude from this figure that the uniform input sampling created a “flatter” output peak temperature distribution (but still with significant tails), and it might indeed be the case for this small population. It should however be kept in mind that both sets are subsets of the “true” empirical output peak temperature distribution, which will only be obtained after several hundred or even more than 1000 model runs, and that careful conclusions are required when the sample populations is this small. Quantitative statistical data, as determined by SUSAs and discussed in the next section, are definitely required before comparison conclusions can be made.

#### 4. SUSA Uncertainty Analysis

For the uncertainty quantification step, SUSA can perform several statistical correlation fitness tests on the output data to determine the properties of the unknown FOM distribution. For example, the Kolmogorov-Smirnov (K-S) test [18] quantifies the distance between the empirical distribution function of the sample and the cumulative distribution function of a reference distribution, and can be used to compare a population sample for conformance with a specific distribution (normal, log-normal, Weibull, uniform, Beta or Gamma). SUSA can also perform the Lilliefors test [19], which is a modification of the K-S test that tests for normal, exponential or log-normal distribution conformance. Once a statistically significant distribution match has been found, the mean, standard deviation, and other indicators of the population can be determined from the empirical distribution function of the sample population.

An illustration of the K-S test is shown in Figures 11 to 12, where the peak DLOFC fuel temperature results of the 100 LHS Normal set is compared with SUSA fits of the normal (Figure 11) and uniform (Figure 12) reference distributions. The quality of the fit can also be visually assessed, but the K-S values (0.9919 versus 0.0026) confirm that a normal distribution is a much better match to the peak DLOFC fuel temperature data set.

A second example of the Lilliefors and K-S test results for the 100 LHS Uniform set is presented in Table 3. Both tests confirm that for this uniform-distributed input sampled set, a log-normal distribution fit provides the best match for the peak fuel temperature distribution.

A summary of the mean and 95%/95% two-sided tolerance intervals at the time when the peak fuel temperature are reached are shown in Table 4 for the six SUSA-sampled sets. The number of successful model calculations is also indicated. For three of the sets, one calculation each did not complete successfully, but the remaining 99 and 199 model runs were still an adequate sample size for the statistical analysis.

The following observations can be made from this data.

*Mean Values.* The mean values for all six datasets are almost identical (e.g., 2°C variation on 1604°C), that is, regardless of the sampling method, parameters included, or distribution types, these six independent random sets predict the same mean DLOFC peak fuel temperature (1604°C).

*Dominant Input Parameters.* Even before an analytical sensitivity study is performed to determine which of the factors are responsible for most of the variations in the output data, the first two datasets shown here already show that the power, inlet gas temperature, and decay heat variations contribute significantly to the variation seen in the DLOFC peak fuel temperature. On their own, these three small input variations produced lower and upper tolerance intervals ranging between 1545°C and 1664°C (a spread of 119°C), while the much larger uncertainty variations in the five material correlations lead to values of 1555°C and 1652°C (a smaller spread of 97°C). Both these sets can be compared with the 100 LHS Uniform set where all eight input variables were included and 95%/95% two-sided tolerance intervals of 1513°C and 1686°C were obtained.

*Distribution Type (100 LHS Uniform versus 99 LHS Normal).* The use of a uniform distribution will result in the sampling of high and low input values more frequently compared to a normal distribution, since the probability of sampling a high, mean, or low value is identical for a uniform distribution, but there is a lower probability to sample from the low and high tails of the normal distribution. This effect could partly explain the lower and higher tolerance intervals on the peak fuel temperature (1513°C versus 1536°C, and 1686°C versus 1675°C) for the 100 LHS Uniform set, compared to the 99 LHS Normal set values. The difference between the two lower and upper tolerance intervals predictions is however minimal: only 23°C and 11°C on a mean value of 1604°C, respectively. The use of normal distributions for input parameter variations, as is most commonly applied when no other information is available, could therefore lead to slightly lower estimates of the tolerance limits, compared to the use of uniform distributions. This observation might however only be valid for this specific HTGR design, code and model combination and these sampled datasets.

*Sampling Method (200 LHS Normal versus 199 SRS Normal).* An interesting current issue in the uncertainty quantification community revolves around the issue of applying stratified sampling techniques (like Latin Hypercube) to improve the coverage of the input sample set ([20–22]). It can be seen in Table 4 that the lower and upper tolerance intervals for the SRS set are larger compared to the intervals for the LHS set (1531°C versus 1537°C, and 1680°C versus 1658°C). It would therefore seem that the use of simple random sampling lead to a slightly more conservative estimate of specifically the upper 95%/95% tolerance limit, which is an important safety case parameter in HTGR reactor design. This observation was also noted in a recent comparison study of SRS and LHS methodologies [23].

TABLE 4: PEBBED CRP-5 DLOFC uncertainty study results.

No of model runs	Sampling method	Input data		Output FOM (DLOFC Peak fuel temperature (°C))		
		Distribution type	Parameters varied	Lower 95%/95% Tolerance interval	Population mean value	Upper 95%/95% Tolerance interval
99	LHS	Uniform	Power, RIT, decay heat	1545	1603	1664
100	LHS	Uniform	Specific heat, thermal conductivity	1555	1605	1652
100	LHS	Uniform	All	1513	1605	1686
99	LHS	Normal	All	1536	1604	1675
200	LHS	Normal	All	1537	1604	1658
199	SRS	Normal	All	1531	1604	1680

It should again be noted however that these differences are small compared to the mean peak DLOFC fuel temperature (only 1.4% on 1604°C), so that the conclusions reached in a Sandia Laboratory study [20] can also be affirmed here: no *significant* differences are observed between the results of SRS or LHS sampled datasets. These studies recommend the use of LHS because of its enforced stratification over the sample range. On the other side of the debate an argument was also made that LHS does not conform to the requirements of the classical ordered statistics approach, and that tolerance intervals may not be obtained from LHS sampled sets [24, page 73]. In the “lessons learned” section of the latest BEMUSE report [24, page 77], the SRS method is specifically recommended for use when tolerance intervals are required. A recent effort to specifically address the use of LHS to derive asymptotically valid tolerance intervals was however reported in [22], so it seems that the use of both techniques still warrant further investigation.

*Number of Model Calculations (99 LHS Normal versus 200 LHS Normal).* Model calculations are crucial time-consuming factors for the statistical uncertainty method. This study did not observe significant differences between the tolerance intervals obtained with sets consisting of 100 or 200 model runs, that is, covering the Wilks’ formula range from the second (93 runs) to the fifth (181 runs) order. The Wilks’ formula second order application (93 runs) therefore seems to be sufficient for this core design, model and transient. This conclusion is supported by the ATHLET PWR study [5] where 100 model runs were performed for 56 uncertain input parameters, and most of the participants in the BEMUSE benchmark study [3] did between 93 and 150 model runs for 13 to 49 input parameters. Four of the BEMUSE benchmark participants found that the 95th percentile can typically be directly obtained from a converged PDF after 400 to 500 model runs, if parallel resources are available, or if the model run times are not significant. The final recommendation in the recent Phase VI BEMUSE report [24] was that Wilks’ formula should be applied at the third or fourth order (between 124 and 153 model runs), if the upper tolerance interval approaches the regulatory limit on the FOM.

A single example of the time dependent nature of the data shown in Table 4 is provided in Figure 13, which shows the data for the 200 LHS Normal set. As indicated earlier, the minima and maxima (which is the upper and lower bounds of the maximum fuel temperatures in Figure 7) vary with time, and the resultant distribution properties show similar variations. The uncertainty bandwidth increases with time beyond the time point where the peak fuel temperature is reached, that is, in this example the highest fuel temperatures and the largest uncertainty variations do not occur at the same time point.

It has been shown in this section that the input uncertainties in only eight parameters already lead to 95%/95% two-sided tolerance intervals of 1531°C and 1680°C on a mean value of 1604°C (the data for the 200 SRS Normal set has been used here). These values represents an uncertainty band/spread of approximately 4.6% around the mean value of 1604°C for the peak fuel temperature during a DLOFC transient in the PBMR design. A more complete study, taking into account all known input uncertainties could possibly lead to a larger uncertainty bandwidth. These uncertainties need to be taken into account during the HTGR reactor safety margin design process.

## 5. SUSA Sensitivity Analysis

This section presents selected results from the SUSA sensitivity analysis. An overview of the definitions, uses, and advantages of typical sensitivity parameters (regression coefficients, correlation measurements, partial and empirical coefficients, etc.) can be found in [17]. As indicated previously, SUSA can calculate several quantitative measures of correlations that might exist between the uncertainties in input parameters and the subsequent variations in the output data. Since the model calculations are usually expensive in terms of computational requirements, it is accepted practice to use the same datasets for the sensitivity and uncertainty analyses.

The Kendall rank correlation coefficients and the empirical correlations ratios shown in Figure 14 for the 100 LHS Uniform and 200 LHS Normal sets can be generated for any

TABLE 5: Indices for data in Figure 15.

Input variable number	Description
1	Reactor power
2	Reactor inlet gas temperature (RIT)
3	Decay heat multiplication factor
4	Fuel specific heat multiplication factor
5	Reflector specific heat multiplication factor
6	Fuel conductivity multiplication factor
7	Pebble bed effective conductivity multiplication factor
8	Reflector conductivity multiplication factor

of the six datasets. A description of the parameters is included in Table 5.

All data shown here is for their effects on the FOM, the DLOFC peak fuel temperature. The *magnitude* of the coefficients provides insight into the degree which a specific input parameter influences the output parameter values: zero values imply almost no link between the input and output uncertainty variations, values up to  $\sim 0.4$  are considered weak correlations, and values above  $\sim 0.7$  indicate strong correlations. The *sign* of the Kendall coefficient indicate a positive or negative relationship (e.g., an increase in decay heat will lead to an increase in fuel temperature). This information can be used to confirm the effect of known physical phenomena or to highlight the primary drivers behind the output uncertainty variations.

Apart from a change in order between input parameters 7 and 8, the Kendall rank correlation coefficients results shown Figures 14(a) and 14(b) are very similar. According to the SUSA analysis, the three primary drivers of uncertainty in the fuel temperature are the decay heat (index no. 3) and the reflector and pebble bed conductivity (no. 7 and no. 8). This finding is in agreement with the simple one-by-one parametric sensitivity study results performed previously for the PBMR 400 MW design with a different model and code [15], where these three factors were also identified as being responsible for the largest changes in the output fuel temperature. The dominant role played by the decay heat and graphite thermal conductivity can also be expected from the basic physical phenomena that determines the fuel temperature during a loss of cooling transient: the decay heat is the only remaining active heat source, and the thermal conductivity of the several hundred tons of graphite material is the dominant resistance on the heat flow path towards the final heat sink. It is also of interest to note that the FOM sensitivity to the decay heat multiplier is approximately three times higher than the sensitivity to the steady state reactor power, that is, a similar ratio when compared to their uncertainty variation magnitudes (2% versus 5.9%). (As indicated in Section 2.2, a roughly linear dependency exists between the decay heat and the long term steady state reactor power). The correlated nature of the decay and total power can be observed in the high *partial* Kendall correlation

coefficient of the for the decay heat parameter, presented in Figure 14(c).

The empirical correlation ratios presented in Figures 14(d) and 14(e) do not show a directional influence (all values are positive), but the three primary drivers can still be readily identified. This indicator is known to be more sensitive to the number of model calculations performed; when the data for the 100 LHS Uniform set shown in Figure 14(c) and the 200 LHS Normal set shown in Figure 14(d) are compared, it can be seen that the three primary parameters' amplitudes (3, 7, and 8) remained similar, but the values of all of the lesser contributors decreased for the 200 model calculations set. The need for a higher number of model runs to distinguish low-level contributions in sensitivity studies is also identified in the literature [3, 17], and should be kept in mind when a small number of model runs are used for sensitivity conclusions. The Wilks criteria on the validity of using a limited number of model runs only apply to uncertainty studies, and cannot be extended to sensitivity studies.

As a final example, the time dependent empirical correlation ratios for the 200 LHS Normal data set shown in Figure 15 illustrate the principle that the rank of the input parameters is not constant over time (e.g., compare the correlation ratios at 5 and 100 hours). The trends shown here highlights an often neglected feature of sensitivity studies: in time-dependent problems, various parameters can rise/fall in importance during the evolution of the transient, depending on the physical phenomena involved.

## 6. Conclusions

This report summarizes the results of an uncertainty and sensitivity quantification study performed with the GRS code SUSA, utilizing a typical high temperature reactor benchmark (the IAEA CRP-5 PBMR 400 MW Exercise 2) and the INL suite of codes PEBBED-THERMIX. The following steps were performed as part of the uncertainty and sensitivity analysis.

- (1) Eight PEBBED-THERMIX model input parameters were selected for inclusion in the uncertainty study: the total reactor power, inlet gas temperature, decay heat, and the specific heat capacity and thermal conductivity of the fuel, pebble bed, and reflector graphite.
- (2) The input parameters variations and probability density functions were specified, and a total of 800 PEBBED-THERMIX model calculations were performed, divided into 4 sets of 100 and 2 sets of 200 steady state and DLOFC transient calculations each.
- (3) The DLOFC peak fuel temperature was supplied to SUSA as model output parameters of interest. Using both the Simple Random and the Latin Hypercube Sampling techniques, the Wilks formulation was applied to the 6 datasets, and the 5% and 95% tolerance limits were determined with 95% confidence levels.

- (4) A SUSAs sensitivity study was performed to obtain correlation data between the input and output parameters, and to identify the primary contributors to the output data uncertainties.

It was found that the uncertainties in the decay heat, pebble bed, and reflector thermal conductivities were responsible for significant contributions to the propagated uncertainty in the DLOFC peak fuel temperature. No significant differences were observed between the results of SRS or LHS sampled datasets, and the same conclusion was made from a comparison between the results of sets that used uniform input parameter distributions as opposed to normal distributions. The 95%/95% two-sided tolerance intervals values of 1531°C and 1680°C represent an uncertainty band/spread of approximately 4.6% around the mean value of 1604°C for the peak fuel temperature during a DLOFC transient in the PBMR 400 MW design.

Possible future investigations in the HTGR uncertainty assessment program at INL include the following.

- (i) Clarify the approach on complex non-statistical uncertainties: bypass flows through the reflectors, including radial and axial power peaking factors, control rod worths, and so forth.
- (ii) The propagation of the uncertainties in the cross section data from the basic nuclear ENDF libraries to the coupled transient solutions represents a significant challenge. In this regard, it is currently planned to utilize the Generalized Perturbation Theory (GPT) and stochastic sampling (XSUSA) capabilities of the upcoming SCALE 6.2 release [25] to propagate the cross-section uncertainties through to a typical steam generator tube rupture scenario, as part of the new IAEA CRP on HTGR UAM [14].

## Acknowledgment

This work is supported by the U.S. Department of Energy, Assistant Secretary for the Office of Nuclear Energy, under DOE Idaho Operations Office Contract DE-AC07-05ID14517.

## References

- [1] 10 CFR 50.46, "Acceptance Criteria for Emergency Core Cooling Systems for Light Water Nuclear Power Reactors," Appendix K to 10 CFR Part 50: "ECCS Evaluation Models," *Code of Federal Regulations*, 1996.
- [2] K. Ivanov, M. Avramova, I. Kodeli et al., "Benchmark for Uncertainty Analysis in Modeling (UAM) for Design, Operation and Safety Analysis of LWRs: Volume I Version 1.0: Specification and Supporting Data for the Neutronics Cases (Phase I)," NEA/NSC/DOC(2007)23, 2007.
- [3] A. de Crécy, P. Bazin, H. Glaeser et al., "Uncertainty and sensitivity analysis of the LOFT L2-5 Test: results of the BEMUSE Programme," *Nuclear Engineering and Design*, vol. 238, no. 12, pp. 3561–3578, 2008.
- [4] B. M. Tyobeka, F. Reitsma, and K. Ivanov, "HTGR reactor physics, thermal-hydraulics and depletion uncertainty analysis: a proposed IAEA coordinated research project," in *Proceedings of the International Conference on Mathematics and Computational Methods Applied to Nuclear Science and Engineering (M&C '11)*, Rio de Janeiro, Brazil, May 2011.
- [5] H. Glaeser, "GRS method for uncertainty and sensitivity evaluation of code results and applications," *Science and Technology of Nuclear Installations*, vol. 2008, Article ID 798901, 7 pages, 2008.
- [6] W. Wisselquist, A. Vasiliev, and H. Ferroukhi, "Nuclear data uncertainty propagation in a lattice physics code using stochastic sampling," in *Proceedings of the International Conference on Advances in Reactor Physics (PHYSOR '12)*, Knoxville, Tenn, USA, 2012.
- [7] A. Yankov, M. Klein, M. A. Jessee et al., "Comparison of XSUSA and "Two Step" approaches for full-core uncertainty quantification," in *Proceedings of the International Conference on Advances in Reactor Physics (PHYSOR '12)*, Knoxville, Tenn, USA, April 2012.
- [8] G. Strydom and A. Epiney, "RELAP5-3D results for phase I, (Exercise 2) of the OECD/NEA MHTGR-350 MW benchmark," in *Proceedings of the International Congress on Advances in Nuclear Power Plants (ICAPP '12)*, Chicago, Ill, USA, June 2012.
- [9] A. B. Salah, S. Kliem, U. Rohde, F. D'Auria, and A. Petruzzi, "Uncertainty and sensitivity analyses of the Kozloduy pump trip test using coupled thermal-hydraulic 3D kinetics code," *Nuclear Engineering and Design*, vol. 236, no. 12, pp. 1240–1255, 2006.
- [10] B. M. Adams, W. J. Bohnhoff, K. R. Dalbey et al., "DAKOTA, a multilevel parallel object-oriented framework for design optimization, parameter estimation, uncertainty quantification, and sensitivity analysis: version 5.0 user's manual," Sandia Technical Report SAND 2010-2183, 2009.
- [11] F. D'Auria and W. Giannotti, "Development of code with capability of internal assessment of uncertainty," *Journal of Nuclear Technology*, vol. 131, no. 1, pp. 159–196, 2000.
- [12] S. S. Wilks, "Determination of sample sizes for setting tolerance limits," *Annals of Mathematical Statistics*, vol. 12, no. 1, pp. 91–96, 1941.
- [13] H. D. Gougar, A. M. Ougouag, W. K. Terry, and K. N. Ivanov, "Automated design and optimization of pebble-bed reactor cores," *Nuclear Science and Engineering*, vol. 165, no. 3, pp. 245–269, 2010.
- [14] B. M. Tyobeka and F. Reitsma, "Results of the IAEA CRP5—benchmark analysis related to the PBMR-400, PBMM, GT-MHR, HTR-10 and the ASTRA critical facility," in *Proceedings of the International Conference on the Physics of Reactors (PHYSOR '10)*, pp. 3204–3223, Pittsburgh, Pa, USA, May 2010.
- [15] G. Strydom, "TINTE uncertainty analysis of the maximum fuel temperature during a DLOFC event for the 400 MW pebble bed modular reactor," in *Proceedings of the International Congress on Advances in Nuclear Power Plants (ICAPP '04)*, pp. 284–293, Pittsburgh, Pa, USA, June 2004.
- [16] DIN 25485, "Decay Heat Power in Nuclear Fuels of High-Temperature Reactors with Spherical Fuel Elements," German National Standard, 1990.
- [17] J. C. Helton, J. D. Johnson, C. J. Sallaberry et al., "Survey of sampling-based methods for uncertainty and sensitivity analysis," *Reliability Engineering & System Safety*, vol. 91, no. 10–11, pp. 1175–1209, 2006.
- [18] J. Roy, I. M. Chakravarti, and R. G. Laha, *Handbook of Methods of Applied Statistics. Vol. 1*, John Wiley & Sons, 1967.

- [19] H. Lilliefors, "On the kolmogorov-smirnov test for normality with mean and variance unknown," *Journal of the American Statistical Association*, vol. 62, no. 318, pp. 399–402, 1967.
- [20] J. C. Helton and F. J. Davis, "Latin hypercube sampling and the propagation of uncertainty in analysis of complex systems," Report SAND 2001-0417, Sandia National Laboratories, 2002.
- [21] A. Hernandez-Solis, C. Demazière, C. Ekberg et al., "Statistical uncertainty analysis applied to the DRAGONv4 code lattice calculations and based on JENDL-4 covariance data," in *Proceedings of the International Conference on Advances in Reactor Physics (PHYSOR '12)*, Knoxville, Tenn, USA, April 2012.
- [22] R. S. Denning, T. Aldemir, and M. Nakayama, "The use of latin hypercube sampling for the efficient estimation of confidence intervals," in *Proceedings of the International Congress on Advances in Nuclear Power Plants (ICAPP '12)*, Chicago, Ill, USA, 2012.
- [23] J. C. Helton, F. J. Davis, and J. D. Johnson, "A comparison of uncertainty and sensitivity analysis results obtained with random and latin hypercube sampling," *Reliability Engineering & System Safety*, vol. 89, no. 3, pp. 305–330, 2005.
- [24] H. Glaeser, P. Bazin, J. Baccou et al., "BEMUSE Phase VI report: Status Report on the Area, Classification of the Methods, Conclusions and Recommendations," NEA/CSNI/R(2011)4, 2011.
- [25] B. T. Rearden, M. L. Williams, M. A. Jessee, D. E. Mueller, and D. A. Wiarda, "Sensitivity and uncertainty analysis capabilities and data in SCALE," *Nuclear Technology*, vol. 174, no. 2, pp. 236–288, 2011.

## Research Article

# A Two-Step Approach to Uncertainty Quantification of Core Simulators

**Artem Yankov,<sup>1</sup> Benjamin Collins,<sup>1</sup> Markus Klein,<sup>2</sup> Matthew A. Jessee,<sup>3</sup>  
Winfried Zwermann,<sup>2</sup> Kiril Velkov,<sup>2</sup> Andreas Pautz,<sup>2</sup> and Thomas Downar<sup>1</sup>**

<sup>1</sup>Department of Nuclear Engineering and Radiological Sciences, University of Michigan, 2355 Bonisteel Boulevard, Ann Arbor, MI 48109, USA

<sup>2</sup>Reactor Safety Research Division, Gesellschaft für Anlagen- und Reaktorsicherheit (GRS) mbH, Boltzmannstraße 14, 85748 Garching bei München, Germany

<sup>3</sup>Reactor and Nuclear Systems Division, Oak Ridge National Laboratory, P.O. Box 2008 MS6172, Oak Ridge, TN 37831, USA

Correspondence should be addressed to Artem Yankov, yankovai@umich.edu

Received 30 July 2012; Accepted 7 December 2012

Academic Editor: Kostadin Ivanov

Copyright © 2012 Artem Yankov et al. This is an open access article distributed under the Creative Commons Attribution License, which permits unrestricted use, distribution, and reproduction in any medium, provided the original work is properly cited.

For the multiple sources of error introduced into the standard computational regime for simulating reactor cores, rigorous uncertainty analysis methods are available primarily to quantify the effects of cross section uncertainties. Two methods for propagating cross section uncertainties through core simulators are the XSUSA statistical approach and the “two-step” method. The XSUSA approach, which is based on the SUSA code package, is fundamentally a stochastic sampling method. Alternatively, the two-step method utilizes generalized perturbation theory in the first step and stochastic sampling in the second step. The consistency of these two methods in quantifying uncertainties in the multiplication factor and in the core power distribution was examined in the framework of phase I-3 of the OECD Uncertainty Analysis in Modeling benchmark. With the Three Mile Island Unit 1 core as a base model for analysis, the XSUSA and two-step methods were applied with certain limitations, and the results were compared to those produced by other stochastic sampling-based codes. Based on the uncertainty analysis results, conclusions were drawn as to the method that is currently more viable for computing uncertainties in burnup and transient calculations.

## 1. Introduction

Computational modeling of nuclear reactor stability and performance has evolved into a multiphysics and multiscale regime. Various computer codes have been developed and optimized to model individual facets of reactor operation such as neutronics, thermal hydraulics, and kinetics. These codes are most often coupled to produce more realistic results. While it is crucial to produce best-estimate calculations for the design and safety analysis of nuclear reactors, it is equally important to obtain design margins by propagating uncertainty information through the entire computational process. The purpose of the OECD (Organization for Economic Cooperation and Development) Uncertainty Analysis in Modeling (UAM) benchmark is to produce a framework for the development of uncertainty analysis methodologies in reactor simulations [1]. Three phases comprise the

benchmark, with each phase building in scale on its predecessors. The first phase deals with uncertainties in neutronics calculations, the second phase deals with neutron kinetics, and the final phase requires the propagation of uncertainties through coupled neutronics/thermal-hydraulics simulations.

The neutronics phase of the UAM benchmark deals specifically with the propagation of input parameter uncertainties to uncertainties in output parameters on a full-core scale. In the established framework of full-core analyses, lattice homogenized few-group cross sections are used as inputs to core simulators. Core simulators utilize a number of approximations to the exact transport equation, effectively introducing uncertainties into output parameters. Geometrical uncertainties and numerical method simplifications can also be attributed to the introduction of modeling uncertainties. While it is important to propagate all known uncertainties when conducting a thorough uncertainty analysis,

the necessary methods to make this possible must still be developed. However, rigorous methods already have been developed to propagate cross section uncertainties from lattice transport solvers to core simulators. Consequently, few-group homogenized cross section errors are assumed for now to be the sole source of uncertainty in the subsequent analyses.

Two methods already exist for propagating cross section uncertainties through core simulators. The first method is commonly referred to as the stochastic sampling (Monte Carlo) method. The XSUSA (Cross Section Uncertainty and Sensitivity Analysis) code system is representative of this approach [2]. XSUSA was developed by GRS based on the SUSA code package [3]. An alternate approach, the two-step method, utilizes generalized perturbation theory in the first step and stochastic sampling in the second step [4, 5]. The purpose of this paper is to show consistency between these two methods in the framework of phase I-3 of the UAM benchmark. As defined in the UAM benchmark specifications, the Three Mile Island Unit 1 (TMI) core will be the focus of application for the XSUSA and two-step methods. The TMI core is chosen for analysis mainly because it has been the focus of past benchmark problems and is therefore of great familiarity in the nuclear engineering community [6].

The two-step method is motivated largely by the computationally expensive solution of the transport equation. In the stochastic sampling approach there is effectively a one-to-one mapping between the solutions of the transport equation and the set of homogenized cross section inputs for a core simulator. Alternatively, for practical problems the two-step method provides a means by which an unlimited number of core simulator inputs can be generated at the cost of relatively few transport-type solutions. The means mentioned above is a few-group covariance matrix whose elements are generated with linear perturbation theory. Hence, the quality of the core simulator inputs produced by the two-step method is limited by the extent to which linear perturbation theory can describe the system under study. Contrarily, stochastic sampling through the XSUSA approach produces core simulator random inputs whose distributions are not subject to linear approximations. This paper shows that the linear approximations used in the two-step method can be remarkably accurate.

## 2. Methodology

Both the stochastic and two-step methods actively use the modules in SCALE to propagate cross section uncertainties [7]. Also, both methods make strong use of SCALE's 44-group covariance library. The multigroup cross sections are assumed to follow a multivariate normal distribution and so expected values and a covariance matrix suffice to fully describe the distribution. In the XSUSA approach, all input parameters are varied simultaneously, and the number of required calculations to achieve a certain statistical accuracy in output parameters of interest is independent of the number of inputs [2]. The number of required runs can

be calculated by Wilks' formula, which gives the confidence level that the maximum code output will not exceed with some specified probability. Contrarily, the two-step method depends on the number of input parameters since each input requires a transport-like solution. The two different methodologies are summarized below.

*2.1. XSUSA Approach.* The covariance matrix between inputs plays a central role in stochastic sampling. Cross section uncertainties are correlated, and the degree of correlation can be described by a covariance matrix. Cross section uncertainties must be perturbed such that their correlation relations are always preserved. If  $\bar{X}$  is a vector of mean values whose covariance relations are defined by the matrix  $\bar{\Sigma}$ , then correlated random variables  $\bar{X}'$  can be generated by applying [8]

$$\bar{X}' = \bar{X} + \bar{A}^T \bar{Z}. \quad (1)$$

In (1) the operator  $\bar{A}^T$  is the upper right triangular matrix obtained by taking the Cholesky decomposition of the covariance matrix. Every covariance matrix is Hermitian and positive definite; thus, all covariance matrices have a Cholesky decomposition  $\bar{\Sigma} = \bar{A}^T \bar{A}$ . The vector  $\bar{Z}$  in (1) is a random normal vector. When  $\bar{A}^T$  multiplies  $\bar{Z}$ , linear combinations of the uncertainties are taken in accordance with their covariance relations, and so  $\bar{X}'$  is normally distributed with covariance  $\bar{\Sigma}$ .

Hence, to produce perturbed cross sections  $\bar{X}'$ , only the Cholesky decomposition of the cross section's covariance matrix is needed along with a random normal vector. In the XSUSA approach, ENDF/B-VII nuclear data in the SCALE 238-group structure are used. Spectral calculations are performed in BONAMI and CENTRM to produce a problem-specific cross section library, as seen in Figure 1. By use of SCALE's 44-group covariance library with the problem-specific library generated by the spectral calculations, the XSUSA code applies perturbations to create a set of  $N$  varied, problem-dependent cross section libraries. Specifically, the MEDUSA module samples the 44-group covariance library that is enlarged to accommodate all problem-specific nuclides and reactions. CLAROL-plus then takes the output from MEDUSA and creates a problem-specific multigroup library. The XSUSA code works to make sure varied data are physically consistent. This procedure does not include the implicit effects of uncertainties in self-shielding, but extensions are currently being made to include these effects [9].

Each set of  $N$  cross section libraries produced by XSUSA is passed to SCALE's lattice physics transport solver NEWT, which in turns produces  $N$  perturbed, homogenized, few-group cross section libraries. The perturbed few-group libraries are then used as input for core simulators such as PARCS [11] and QUABOX/CUBBOX [12]. Once all  $N$  libraries are processed by the core simulator, statistics can be taken on the output parameters of interest. As indicated in Figure 1, NEWT can be replaced by any of SCALE's

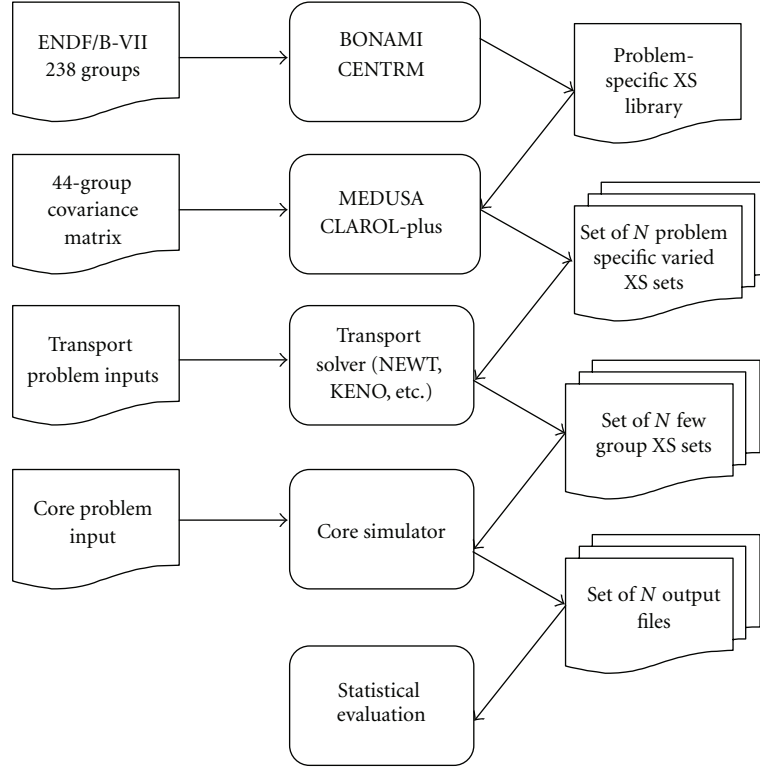


FIGURE 1: Flow diagram of the XSUSA approach starting from use of the ENDF/B-VII 238-group library and ending with a statistical evaluation of output parameters.

transport solvers. For example, XSDRN can be used for one-dimensional (1D) calculations and KENO for Monte Carlo reference solutions [2].

**2.2. Two-Step Method.** Unlike the XSUSA approach, the two-step method is only partly based on sampling techniques. In the first step it makes use of the generalized adjoint for the transport equation [13]. In the two-step method, problem-dependent self-shielded data are also generated before any perturbed cross sections are calculated, as seen in Figure 2. Using the problem-dependent cross sections, the TSUNAMI module is applied to calculate the forward transport, adjoint transport, and generalized adjoint transport solutions to the problem at hand. The SCALE module SAMS then uses the problem solutions to calculate sensitivity coefficients for responses of interest. A response  $R_{xG}$  for reaction type  $x$  in broad-group  $G$  is defined as a ratio of inner products with the forward neutron flux [10]:

$$R_{xG} = \frac{\langle H_1 \Phi \rangle}{\langle H_2 \Phi \rangle}. \quad (2)$$

The explicit sensitivity coefficient of the response  $R_{xG}$  with respect to some nuclear data parameter  $\sigma_{ng}$  in the transport equation is then given as [10]

$$\frac{\partial R_{xG}}{\partial \sigma_{ng}} = \frac{\langle \Phi (\partial H_1 / \partial \sigma_{ng}) \rangle}{\langle \Phi H_1 \rangle} - \frac{\langle \Phi (\partial H_2 / \partial \sigma_{ng}) \rangle}{\langle \Phi H_2 \rangle} + \left\langle \Gamma_{xG}^* \frac{\partial (L - \lambda P)}{\partial \sigma_{ng}} \Phi \right\rangle, \quad (3)$$

where  $\Phi$  is the solution of the forward transport equation,  $L$  is the migration and loss operator, and  $P$  is the production operator.

The generalized adjoint  $\Gamma_{xG}^*$  can be obtained by solving the generalized adjoint transport equation in [10]

$$(L^* - \lambda P^*) \Gamma_{xG}^* = \frac{1}{R_{xG}} \frac{dR_{xG}}{d\Phi}. \quad (4)$$

The solution of (4) requires the solution of the adjoint transport problem for each response. The pertinent responses of interest are the homogenized few-group cross sections needed for core simulators. Equations (3) and (4) above are used to compute explicit sensitivity coefficients. The TSUNAMI methodology incorporates implicit sensitivity effects arising from resonance self-shielding [10].

If the covariance matrix  $\bar{\bar{C}}_i$  of some input parameters is available along with the sensitivities  $\bar{\bar{S}}$  relating the change in outputs with respect to the change in input parameters, the “sandwich rule” can be applied to obtain a covariance matrix for the outputs  $\bar{\bar{C}}_o$ . The “sandwich rule” is expressed in [14]

$$\bar{\bar{C}}_o = \bar{\bar{S}} \bar{\bar{C}}_i \bar{\bar{S}}^T. \quad (5)$$

Consequently, since  $\bar{\bar{C}}_i$  is the SCALE 44-group covariance matrix, a covariance matrix for the few-group homogenized cross sections can be obtained. The SCALE module TSUNAMI-IP is used to generate a global covariance matrix relating the few-group cross sections in each assembly and

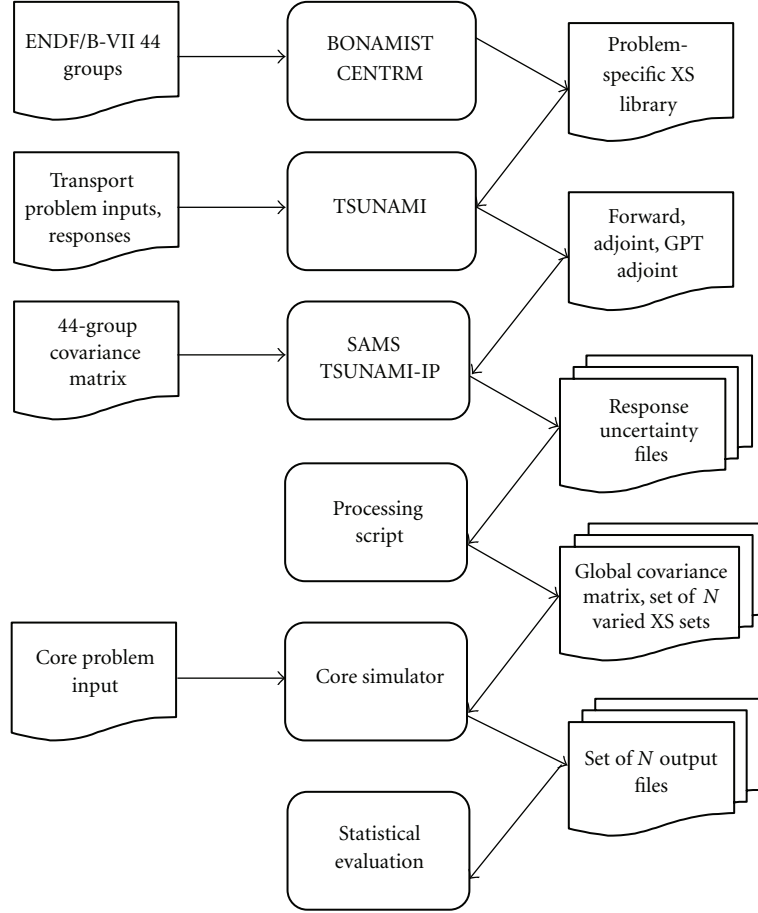


FIGURE 2: Flow diagram for the proposed two-step method, which mainly utilizes the generalized perturbation theory modules in SCALE [10].

reflector regions comprising a full-core problem. With (1), this global covariance matrix is sampled to produce  $N$  perturbed cross section libraries that can then be used as input for a core simulator. By applying the XSUSA and two-step methods to calculate uncertainties in output parameters of interest for the full-core TMI problem, it can be shown that the two different approaches produce consistent results.

### 3. Application

**3.1. Implementation.** The computational implementation of the two-step and XSUSA methods strays somewhat from their theoretical formulations. Specifically, modifications must be made since the generalized perturbation theory capabilities in SCALE are currently limited to only some of the responses required by core simulators. First, the TSUNAMI module currently cannot compute the uncertainty in the few-group homogenized transport cross section. However, uncertainties in the total and scatter cross sections can be calculated. To approximate perturbations to the transport cross section, is used the following:

$$\Sigma_{tr,G}^* = \Sigma_{t,G} - \bar{\mu}\Sigma_{s,G}. \quad (6)$$

The average cosine of the scattering angle  $\bar{\mu}$  is held constant while the total cross sections  $\Sigma_{t,G}$  and scatter cross sections  $\Sigma_{s,G}$  are perturbed to yield an effectively perturbed transport cross section  $\Sigma_{tr,G}^*$  that can be used as input to a core simulator. Normally a critical spectrum based on either the P1 or B1 approximation is utilized to compute few-group cross sections. However, the critical spectrum cannot be correctly accounted for in the TSUNAMI generalized perturbation theory methodology. Consequently, in the proceeding analysis the default B1 critical spectrum calculation in SCALE is disabled in favor of the simplified P1 formulation shown in (6). Similarly, TSUNAMI does not generate uncertainties for kappa, the average energy release per fission event. To calculate a perturbed kappa-fission cross section, the average value of kappa  $\bar{\kappa}$  is multiplied by a perturbed fission cross section  $\Sigma_{f,G}$  to obtain an effectively perturbed kappa-fission cross section  $\kappa\Sigma_{f,G}^*$  as shown in

$$\kappa\Sigma_{f,G}^* = \bar{\kappa}\Sigma_{f,G}. \quad (7)$$

A more subtle modification must be made when calculating the uncertainties in assembly discontinuity factors (ADFs). At the assembly level where reflective boundary conditions are used, TSUNAMI can approximate ADF uncertainties

very well by taking the ratio of the average flux of a thin surface at the assembly boundary to the assembly averaged flux [15]. A cell volume normalization factor is also needed to account for the size of the thin surface at the assembly boundary. While this approach is valid for an infinite system, TSUNAMI is currently not capable of accurately quantifying ADF uncertainties at reflector interfaces due to leakage effects. To calculate uncertainties in few-group ADFs along reflector interfaces, a method developed by Yankov et al. is used [15]. The method is based on the 1D adjoint diffusion approximation generally used to treat reflector interface ADFs, the neutron balance equation on a fuel assembly/reflector interface, and the “sandwich rule.”

The two-step method is presented algorithmically in Table 1. The majority of the algorithm consists of file manipulations. In the second step of the algorithm, it is important to check that the global covariance matrix produced by TSUNAMI-IP is positive definite. The global covariance matrix consists of examining the correlations among few-group cross sections between all assemblies in the core. Use of a global covariance matrix is essential when sampling cross sections for an entire core, since otherwise the similarity of the nuclide composition of different fuel assembly types is neglected. If the global covariance matrix is not used, the output parameter uncertainties can be greatly misrepresented. In most cases, the global covariance matrix produced by TSUNAMI-IP will only be nearly positive definite due to a lack of diagonal dominance. However, the matrix can be made more diagonally dominant by multiplying the matrix’s off-diagonal terms by  $1 - \epsilon$  for some very small value  $\epsilon$ .

Note that the XSUSA approach does not require any of these modifications since it is fundamentally a statistically based approach, whereas the two-step method uses a deterministic approach in the first step.

### 3.2. Results

**3.2.1. Pin-Cell Calculations.** Before the two-step and XSUSA methods are applied to a full core problem, it is prudent to perform a preliminary investigation on an easily tractable problem. Such a tractable problem consists of a single TMI pin-cell, as defined in the UAM benchmark [1]. Since the two methods of interest fundamentally work with covariances, the preliminary investigation will compare how the two-step and XSUSA methods can calculate variances and covariances for few-group parameters. Recall that SCALE/TSUNAMI, the underlying code system used in the two-step method, considers both the explicit and implicit contributions from cross sections. The XSUSA method only considers explicit effects for the same perturbations. Consequently, to produce a fair comparison the implicit sensitivity coefficient component is disabled in TSUNAMI. To this end, 1000 XSUSA samples of few-group scatter and fission cross sections are compared to those produced by the modified TSUNAMI code.

First, the standard deviations for the scatter and fission cross sections are compared in Figure 3, which depicts ratios

TABLE 1: Algorithm for applying the two-step method using SCALE and a core simulator.

(1)	For each assembly and reflector in the core, create a TSUNAMI-2D input file. In each input, responses should correspond to the few-group total, absorption, nu-fission, fission, Chi, and scatter cross sections. Responses for ADFs should also be specified. The TSUNAMI-2D input files can be executed in parallel.
(2)	From the “.sdf” sensitivity files in TSUNAMI-2D outputs, use TSUNAMI-IP to generate a global covariance matrix along with mean and standard deviations of the responses. Verify that the global covariance matrix is positive definite.
(3)	Sample the covariance matrix to produce $N$ perturbed cross section sets. Using (6) and (7), process the perturbed cross sections to obtain perturbed values for the transport and kappa-fission cross sections. Also, apply the method developed by Yankov et al. [15] to determine uncertainties in the reflector ADFs.
(4)	Using each set of perturbed cross sections, produce $N$ input files for the core simulator.
(5)	Execute the core simulator $N$ times using a different cross section set each time. These executions can be done in parallel.
(6)	Scanning the core simulator’s $N$ output files, extract relevant data. Perform a statistical analysis on the relevant output data.

of standard deviations produced by XSUSA and SCALE. In Figure 3, two different SCALE results are shown. The first result, labeled “GPT(explicit),” considers only the explicit sensitivity coefficients in SCALE. The second result, labeled “GPT(explicit, XSUSA),” not only considers the explicit sensitivity coefficients but also utilizes the same perturbation factors generated by the XSUSA simulations. For an in-depth discussion of how perturbation factors are used in the pertinent methodologies the interested reader is referred to [16]. Ideally, all ratios in Figure 3 would be identical unity in the case where the responses depend linearly on the uncertain parameters. However, since XSUSA is a statistical method, some variability is present in the results. Some variability can also result from nonlinear phenomena. When the same perturbation factors are used in SCALE and XSUSA, all points are well contained in the 95% confidence interval bounds. The same phenomenon can be observed when the generalized perturbation theory and statistically generated covariance matrices are compared in Figure 4.

In Figure 4 the correlation coefficients should ideally lay along the dotted line, representing a one-to-one relationship. Figure 4(b) has points concentrated more closely around the dotted line because identical perturbation factors are used in XSUSA and SCALE. All effects considered, the slight discrepancies visible in Figure 4(b) must be from nonlinear effects. The black lines bounding the points in Figure 4 represent the 95% confidence bounds for the correlation coefficients calculated with the Fisher transformation [17].

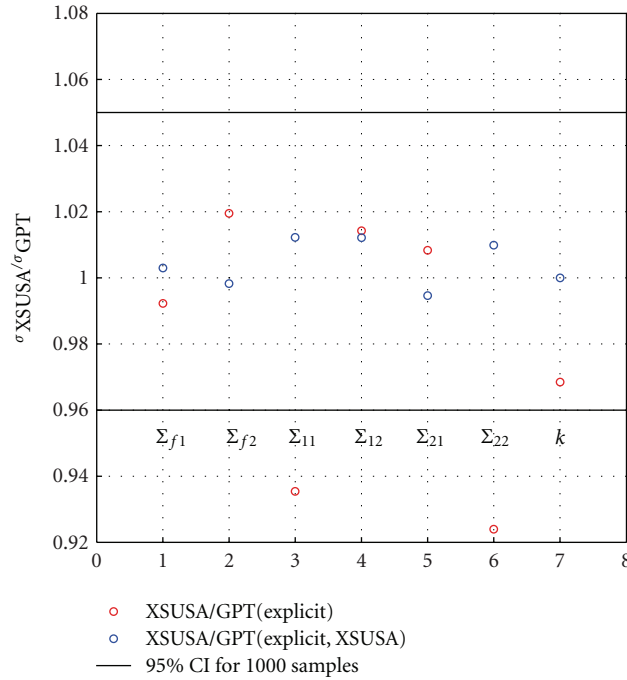


FIGURE 3: The ratio of the stochastic to generalized perturbation theory standard deviations of few-group cross sections. The independent axis represents various cross section indices.

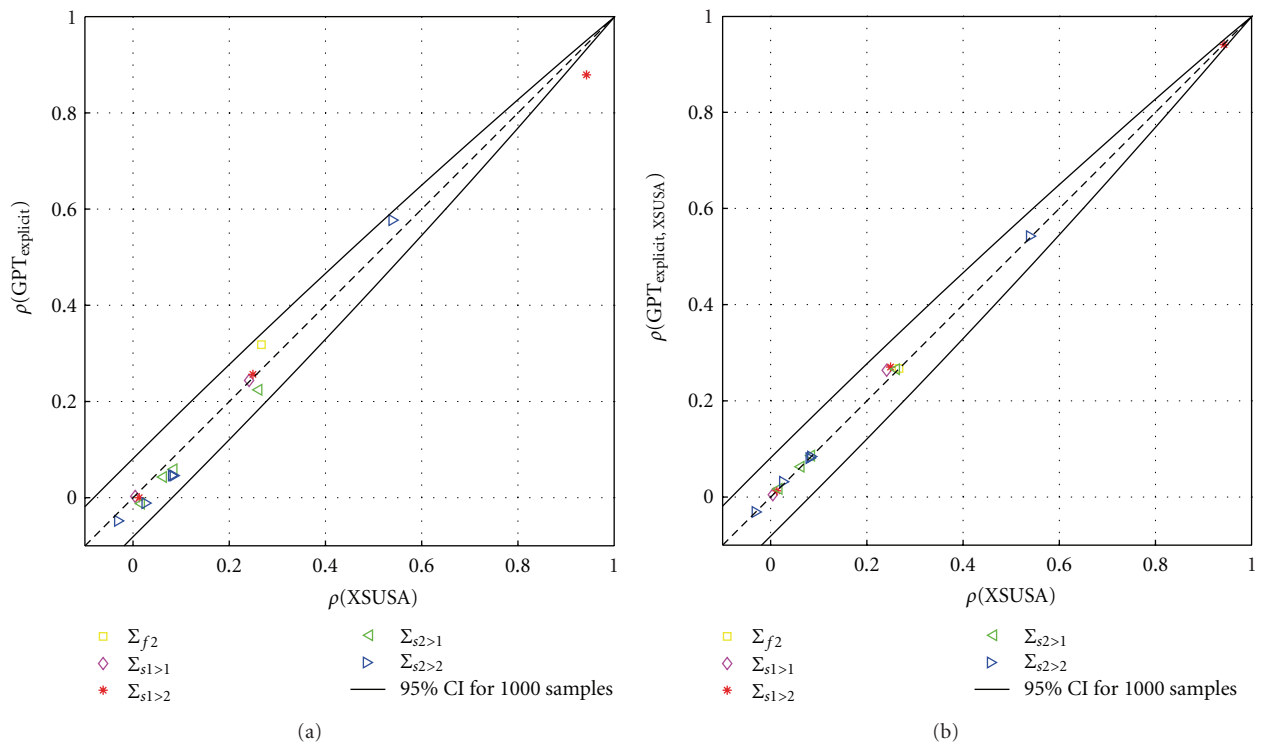


FIGURE 4: Correlation coefficients calculated by XSUSA compared to those calculated by SCALE. (a) Only the explicit effect is represented in the SCALE coefficients. (b) The explicit effect and the XSUSA perturbation factors are considered.

TABLE 2: Uncertainty in the effective multiplication factor from using the two-step and XSUSA methods with a sample size of 290.

	Two-step method	XSUSA method	Absolute difference (pcm)
$k$ -eff mean	1.30268	1.30330	62
$k$ -eff stand. deviation	0.00569	0.00564*	5
Relative SD %	0.43706	0.43272	

\*The 95% confidence interval is [0.00522, 0.00614].

TABLE 3: Uncertainty in the effective multiplication factor from using “one-step” schemes.

	XSUSA/KENO	TSUNAMI-3D	Absolute difference (pcm)
$k$ -eff mean	1.30294	1.30279	15
$k$ -eff stand. deviation	0.00608* <sup>1</sup>	0.00588* <sup>2</sup>	20
Relative SD %	0.46679	0.45120	

\*<sup>1</sup>The 95% confidence interval is [0.00563, 0.00661]. \*<sup>2</sup>The 95% confidence interval is [0.00544, 0.00639].

**3.2.2. Full-Core Calculations.** The TMI core under consideration consists of 11 different UO<sub>2</sub> assemblies and a reflector region placed in 1/8 symmetry. All control rods are ejected from the core, which is at hot zero power [1]. By use of the XSUSA and two-step methods, uncertainties are obtained for the core-wide multiplication factor and for the assembly-wise relative power distribution. For a two-group formulation, each assembly in the TMI core requires 11 perturbed cross sections. These are the transport, absorption, kappa-fission, and nu-fission cross sections along with a down-scatter cross section and two ADFs. The reflector region requires only 7 cross section inputs for a total of 128 perturbed cross sections per core simulation.

The core simulator utilized for the proceeding analysis is PARCS. The multigroup NEM nodal kernel is used to execute all 290 core simulations [11]. Initially 300 core simulations were proposed, but some of the cross section perturbations in the two-step method were too large, so PARCS was unable to produce a converged solution. The large number of core simulations ensures that the largest output values obtained will not be exceeded with a high probability by Wilks’ formula. The multiplication factor uncertainty results obtained with the XSUSA and two-step methods for the TMI core are summarized in Table 2. The table clearly shows that the XSUSA and two-step methods can consistently calculate uncertainties in the multiplication factor.

Both the “one-step” reference solutions and the two-step and XSUSA methods produced results that are well within statistical uncertainty of each other, as evidenced by comparing Tables 2 and 3. The agreement between the “one-step” reference solutions and between the two-step and XSUSA methods appears to be better than the overall agreement among all four calculation schemes.

The mean power distributions obtained from the XSUSA/PARCS and two-step methods are shown in Figure 5 along with XSUSA/KENO reference solutions. The values displayed in Figure 5 are relative power distributions such that the mean power in the core is unity. As expected, the mean power distributions predicted by the XSUSA and two-step methods are very similar, with the largest node-wise discrepancy being less than 1%. The relative standard deviation (%) in power for each node is shown in Figure 6.

Before looking at the numerical values of the uncertainty in the core power distribution calculated by the three methods in Figures 6 and 7, it is evident that the distribution of uncertainty is spread evenly in all the methods. Uncertainties with the highest magnitudes congregate around the center of the core. This is due to the radial heterogeneity of the core configuration [18]. The two-step method seems to attribute less uncertainty overall to each nodal power. Although the reasons for this observation are currently under investigation, the authors have noticed that the relative power distribution uncertainties are particularly sensitive to the way in which uncertainties are propagated to the transport cross section in the two-step method.

## 4. Conclusions

The core simulator output uncertainties for the TMI core obtained with the XSUSA and two-step methods indicate that both methods are consistent in general and are able to propagate nuclear data uncertainties to the core simulator. However, further investigation is needed to explain some of the discrepancies observed between the two methods, especially in the calculation of uncertainty in the relative power distribution. Since the TMI core used in this analysis is relatively homogeneous, the linear approximations employed by the two-step method are completely satisfactory. While the authors anticipate that the linear approximations will hold for more inhomogeneous cores, such as the MOX cores specified in the UAM benchmark [1], this matter should be examined in greater detail.

Despite some of the current limitations of the generalized perturbation theory implementations in SCALE, both uncertainty quantification methods yield an uncertainty of  $\Delta k = 0.5\%$  in the core simulator  $k$ -effective. Currently, the limitations of generalized perturbation theory as applied in the two-step method make the XSUSA approach a more robust choice for reactor uncertainty analysis. In order to perform a steady-state uncertainty analysis, methods should be developed in the current generalized perturbation theory framework in SCALE to capture all uncertainty within reach of the XSUSA approach. Methods should

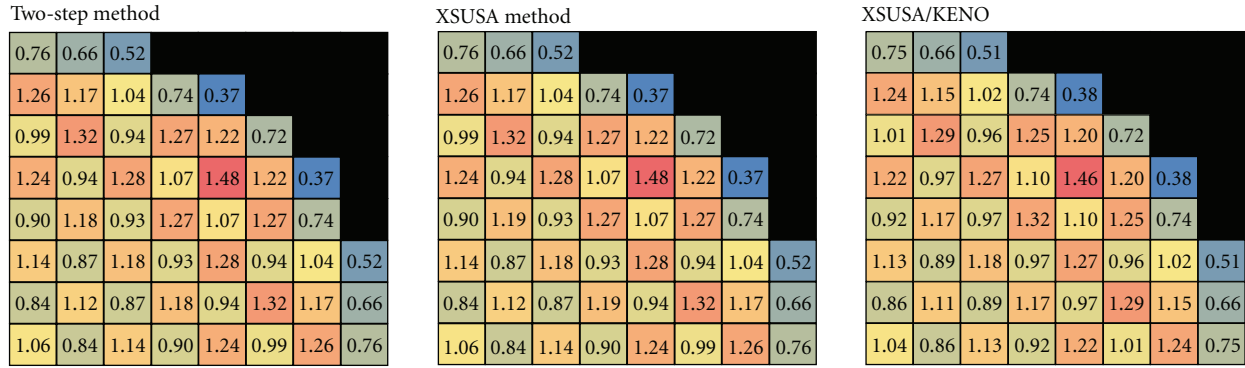


FIGURE 5: Mean power distribution calculated by the two-step and XSUSA methods along with the XSUSA/KENO reference. Values shown are calculated such that unity is the core average power. Quarter symmetry is displayed.

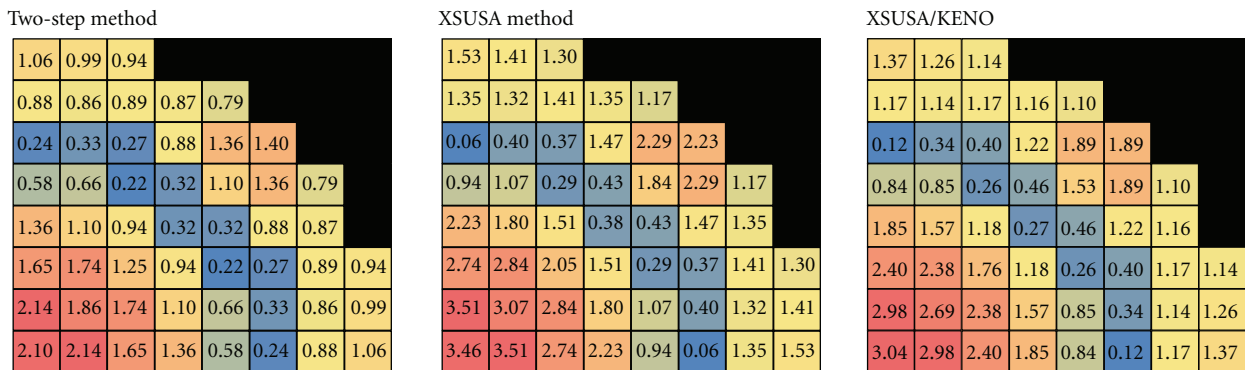


FIGURE 6: Relative standard deviation (%) calculated by the two-step and XSUSA methods along with the XSUSA/KENO reference. Uncertainties in assembly discontinuity factors are included. Quarter symmetry is displayed.

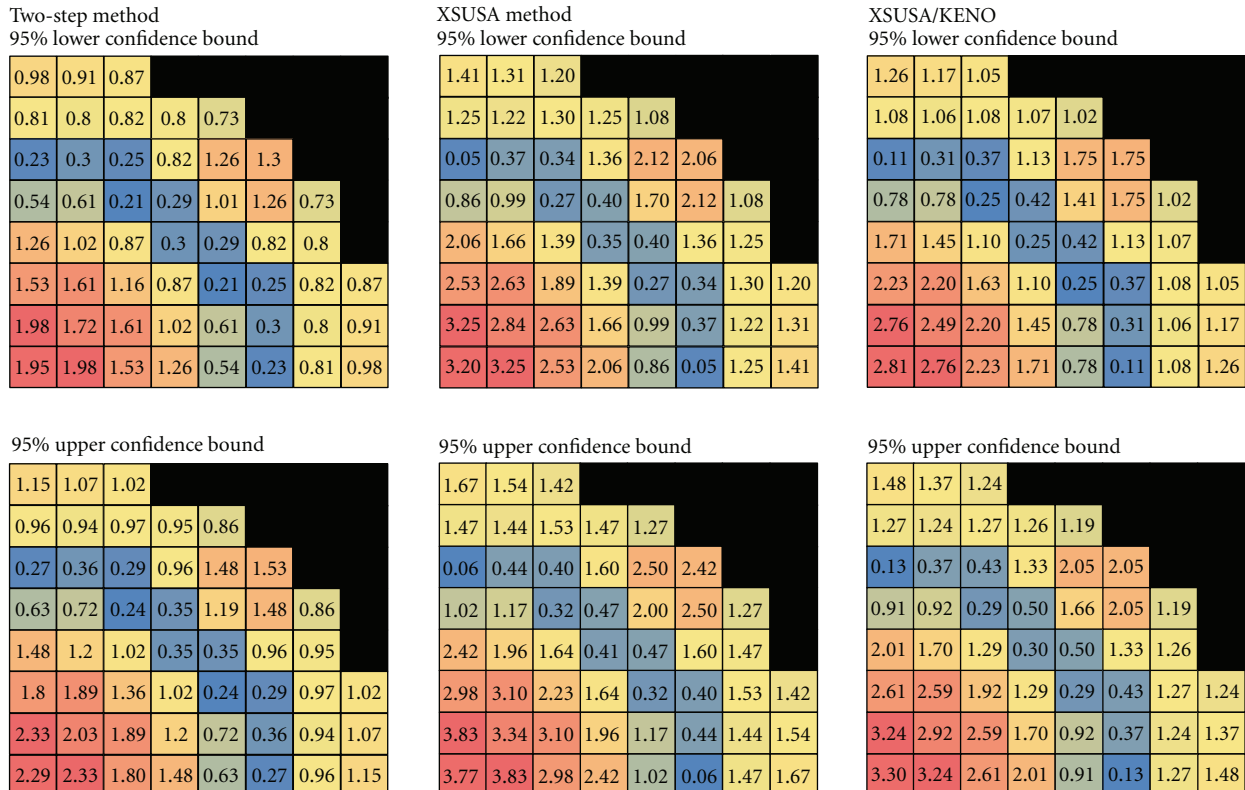


FIGURE 7: The 95% confidence bounds are shown for the relative standard deviations corresponding to Figure 6.

also be developed so that two-step-type methods can be applied to burnup and transient calculations, as defined in phases II-III of the UAM benchmark. The XSUSA approach already allows for such calculations, as evident from [16, 19].

In terms of efficiency, the XSUSA and two-step methods require similar computation times if parallel computing is employed. For the TMI core, 128 transport-like solutions on an assembly were required to obtain a global covariance matrix in TSUNAMI, one solution for each response. To obtain the desired statistical accuracy this covariance matrix was sampled around 300 times. Relatively speaking, sampling the covariance matrix and running the perturbed cross sections through a core simulator are free. Since no covariance matrix is used in the XSUSA approach, some 3600 full transport solutions on an assembly are needed to be able to execute 300 core simulations (11 assemblies plus 1 reflector, multiplied by 300 perturbed cross section sets). To summarize, for full-core problems the computational burden is much less when the two-step method is used. However, due to the nature of parallel processing the two-step and XSUSA methods can take the same amount of time. Overall, more work should be done with the two-step method to make it a viable tool for uncertainty quantification in core simulations. However, the results in this paper suggest that the two-step method can be made to be fully consistent with more versatile stochastic methods.

## Acknowledgments

This work was supported by the German Ministry of Economics and Technology and the US Nuclear Regulatory Commission. This paper has been authored by UT-Battelle LLC under Contract no. DE-AC05-00OR22725 with the U.S. Department of Energy. The United States Government retains and the publisher, by accepting the paper for publication, acknowledges that the United States Government retains a nonexclusive, paid-up, irrevocable, world-wide license to publish or reproduce the published form of this paper, or allow others to do so, for the United States Government purposes.

## References

- [1] K. Ivanov, M. Avramova, I. Kodeli, and E. Sartori, *Benchmark for Uncertainty Analysis in Modeling (UAM) for Design, Operation and Safety Analysis of LWRs*, Rep. NEA/NSC/DOC(2007) 23, Nuclear Energy Agency, 2nd edition, 2007.
- [2] M. Klein, L. Gallner, B. Krzykacz-Hausmann, A. Pautz, and W. Zwermann, "Influence of nuclear data uncertainties on reactor core calculations," *Kerntechnik*, vol. 76, no. 3, pp. 174–178, 2011.
- [3] B. Krzykacz, E. Hofer, and M. Kloos, "A software system for probabilistic uncertainty and sensitivity analysis of results from computer models," in *Proceedings of the International Conference on Probabilistic Safety Assessment and Management (PSAM '94)*, San Diego, Calif, USA, 1994.
- [4] M. Williams, M. A. Jessee, R. Ellis, and B. Rearden, "Sensitivity and uncertainty analysis for OECD UAM benchmark of peach bottom BWR," in *Proceedings of the 4th Uncertainty Analysis in Modelling Benchmark Meeting*, Pisa, Italy, April 2010.
- [5] A. Yankov, M. Klein, M. A. Jessee et al., "Comparison of XSUSA and "two-step" approaches for full-core uncertainty quantification," in *Proceedings of the International Conference on the Physics of Reactors (PHYSOR '12)*, Knoxville, Tenn, USA, April 2012.
- [6] K. Ivanov, T. M. Beam, A. J. Baratta, A. Irani, and N. Trikouros, "Pressurised water reactor Main Steam Line Break (MSLB) benchmark," Tech. Rep. NEA/NSC/DOC(99)8, Nuclear Energy Agency, 1999.
- [7] SCALE: A Comprehensive Modeling and Simulation Suite for Nuclear Safety Analysis and Design, ORNL/TM-2005/39, Version 6. 1, Radiation Safety Information Computational Center at Oak Ridge National Laboratory as CCC-785, Oak Ridge, Tenn, USA, 2011.
- [8] P. R. Bevington and K. Robinson, *Data Reduction and Error Analysis for the Physical Sciences*, McGraw-Hill, Boston, Mass, USA, 2003.
- [9] M. Williams, D. Wiarda, H. Smith et al., "Development of a statistical sampling method for uncertainty analysis with scale," in *Proceedings of the International Conference on the Physics of Reactors (PHYSOR '12)*, Knoxville, Tenn, USA, April 2012.
- [10] M. A. Jessee, M. L. Williams, and M. D. DeHart, "Development of generalized perturbation theory capability within the scale code package," in *Proceedings of the International Conference on Mathematics, Computational Methods, and Reactor Physics (M&C '09)*, Saratoga Springs, New York, NY, USA, May 2009.
- [11] T. Downar, Y. Xu, and V. Seker, "PARCSv3. 0 Theory Manual," UM-NERS-09-001, October 2009.
- [12] S. Langenbuch and K. Velkov, "Overview on the development and application of the coupled code system ATHLET—QUABBOX/CUBBOX," in *Proceedings of the Mathematics and Computation, Supercomputing, Reactor Physics and Nuclear and Biological Applications*, Avignon, France, September 2005.
- [13] M. Williams, "Perturbation theory for nuclear reactor analysis," in *CRC Handbook of Nuclear Reactor Calculations*, vol. 3, pp. 63–188, 1986.
- [14] M. A. Jessee, *Cross section adjustment techniques for BWR adaptive simulation [Dissertation]*, North Carolina State University, Raleigh, NC, USA, 2008.
- [15] A. Yankov, B. Collins, M. A. Jessee, and T. Downar, "A generalized adjoint approach for quantifying reflector assembly discontinuity factor uncertainties," in *Proceedings of the International Conference on the Physics of Reactors (PHYSOR '12)*, Knoxville, Tenn, USA, April 2012.
- [16] M. L. Williams, G. Ilas, M. A. Jessee et al., "A statistical sampling method for uncertainty analysis with SCALE and XSUSA," submitted to *Nuclear Technology*.
- [17] R. Fisher, "On the 'probable error' of a coefficient of correlation deduced from a small sample," *Metron*, vol. 1, pp. 3–32, 1921.
- [18] M. Klein, L. Gallner, B. Krzykacz-Hausmann, A. Pautz, K. Velkov, and W. Zwermann, "Interaction of loading pattern and nuclear data uncertainties in reactor core calculations," in *Proceedings of the International Conference on the Physics of Reactors (PHYSOR '12)*, Knoxville, Tenn, USA, April 2012.
- [19] I. Pasichnyk, M. Klein, K. Velkov, W. Zwermann, and A. Pautz, "Nuclear data uncertainties by the PWR MOX/UO2 core rod ejection benchmark," in *Proceedings of the International Conference on the Physics of Reactors (PHYSOR '12)*, Knoxville, Tenn, USA, April 2012.

## Research Article

# Computational Method for Global Sensitivity Analysis of Reactor Neutronic Parameters

**Bolade A. Adetula and Pavel M. Bokov**

Research and Development Division, The South African Nuclear Energy Corporation (Necsa), Building 1900, P.O. Box 582, Pretoria 0001, South Africa

Correspondence should be addressed to Bolade A. Adetula, adetulap@yahoo.com

Received 25 April 2012; Accepted 5 October 2012

Academic Editor: Kostadin Ivanov

Copyright © 2012 B. A. Adetula and P. M. Bokov. This is an open access article distributed under the Creative Commons Attribution License, which permits unrestricted use, distribution, and reproduction in any medium, provided the original work is properly cited.

The variance-based global sensitivity analysis technique is robust, has a wide range of applicability, and provides accurate sensitivity information for most models. However, it requires input variables to be statistically independent. A modification to this technique that allows one to deal with input variables that are blockwise correlated and normally distributed is presented. The focus of this study is the application of the modified global sensitivity analysis technique to calculations of reactor parameters that are dependent on groupwise neutron cross-sections. The main effort in this work is in establishing a method for a practical numerical calculation of the global sensitivity indices. The implementation of the method involves the calculation of multidimensional integrals, which can be prohibitively expensive to compute. Numerical techniques specifically suited to the evaluation of multidimensional integrals, namely, Monte Carlo and sparse grids methods, are used, and their efficiency is compared. The method is illustrated and tested on a two-group cross-section dependent problem. In all the cases considered, the results obtained with sparse grids achieved much better accuracy while using a significantly smaller number of samples. This aspect is addressed in a ministudy, and a preliminary explanation of the results obtained is given.

## 1. Introduction

The apportioning of uncertainty in the output of a model (numerical or otherwise) to different sources of uncertainty in the model input is known as *sensitivity analysis* [1], and the associated quantitative values are known as *sensitivity indices*. The sensitivity indices can be used to rank the input variables of the model, based on the influence they have on the output. It thus becomes possible to recognize the probabilistically insignificant/unessential input variables that exert little influence on the output. This allows for the reduction of the dimensionality of the problem by fixing the unessential input variables, whilst more experiments, computations, research, and so forth can be done to determine the essential input variables with a higher degree of accuracy.

The focus of this study will be on *global sensitivity analysis* (GSA), which explores the full phase space of input parameters, as opposed to *local sensitivity analysis* (LSA) methods that are usually based on derivatives and analyse

the behaviour of the model output around a chosen point. The implementation of GSA can be achieved by using either variance-[1–3] or entropy-[4, 5] based methods. In our study, we will use the Sobol's variance-based method [3]. This method is referred to as "variance-based" because within the framework of this approach, the uncertainty of the output is characterized by its (output) variance. The Sobol's method is robust, has a wide range of applicability, and, as stated in [6, 7], provides accurate sensitivity information for most models. However, the Sobol's method is defined for mutually independent input variables that are uniformly distributed. A modification of the method which allows one to deal with input variables that are blockwise correlated and normally distributed is presented in this work.

The modified method can then be applied to nuclear reactor calculations. Many reactor parameters of interest (such as the neutron multiplication factor, decay heat, reaction rates, etc.) are dependent on neutron cross-sections. These cross-sections are often described by only their first

two statistical moments and are assumed to be normally distributed [8]. The uncertainties associated with the cross-sections are propagated to the final result of the calculated reactor parameters, and the uncertainty in a calculated reactor parameter can be apportioned to the different sources of uncertainty in the neutron cross-sections.

In this paper, we will present the method of global sensitivity analysis that will address the previous limitations and take into account the previously mentioned assumptions with an emphasis on the numerical/calculational aspects in implementing the method. The rest of the paper is organised in the following way. Section 2 contains two major parts: in the beginning, we give theoretical background and some mathematical derivations for the method we present, and in the second part of the section, we discuss its practical numerical implementation. The theory description is supported by two appendices: Appendix A is used to summarize the definitions and properties of the functional ANOVA decomposition, and Appendix B provides explanations concerning the sparse grid integration method. In Section 3, we describe the particularities of our implementation of the proposed method and the problem we use to test and characterise the method, as well as the results obtained. Finally, Section 4 is used to present our conclusions.

## 2. Method

*2.1. Definitions and Assumptions.* Consider a problem in which some important reactor parameters, such as the neutron multiplication factor and the decay heat, depend on multigroup or few-group neutron cross-sections. We will use  $Y$  to denote the reactor parameter of interest and  $X_i$  ( $i = 1, 2, \dots, d$ ) to denote the cross-sections. The dependence of the parameter of interest on cross-sections can be written as a model

$$Y = f(X_1, X_2, \dots, X_d), \quad (1)$$

where  $X_i$  are called *inputs* and  $Y$  is called the *output* or *response*. Model (1) is generally nonlinear and often calculated numerically in practice.

The cross-sections can be gathered in a column vector  $\mathbf{X} = (X_1, X_2, \dots, X_d)^T$ , where the symbol “ $T$ ” denotes the operation of transposing a row to a column. If input  $\mathbf{X}$  is a random vector with a joint probability density function  $p(\mathbf{x}) = p(x_1, x_2, \dots, x_d)$ , then the response  $Y$  is a random variable with the expected value  $E[Y]$  and the variance  $\text{Var}[Y]$  defined as

$$\begin{aligned} E[f(\mathbf{x})] &= \int_{\mathbb{R}^d} f(\mathbf{x})p(\mathbf{x})d\mathbf{x}, \\ \text{Var}[f(\mathbf{x})] &= \int_{\mathbb{R}^d} (f(\mathbf{x}) - E[f(\mathbf{x})])^2 p(\mathbf{x})d\mathbf{x}, \end{aligned} \quad (2)$$

correspondingly. Note that we will use, as it is the rule in statistics, a capital letter to denote a random variable and a lowercase letter to denote its value (realizations).

In this work, we will assume that the cross-sections are random variables distributed according to the normal law

with known means and covariances. The multivariate normal distribution for the probability  $\text{Pr}[X_i < x_i : i = 1, \dots, d]$  is characterized by the probability density function [9]

$$p(\mathbf{x}) = \frac{1}{(2\pi)^{d/2} \det(\boldsymbol{\Sigma})^{1/2}} \exp\left[-\frac{1}{2}(\mathbf{x} - \boldsymbol{\mu})^T \boldsymbol{\Sigma}^{-1}(\mathbf{x} - \boldsymbol{\mu})\right], \quad (3)$$

where  $\mathbf{X}$  is the column vector of random variables,  $\boldsymbol{\mu} = E[\mathbf{X}]$  is the column vector of their expected values, and  $\boldsymbol{\Sigma} = E[(\mathbf{x} - \boldsymbol{\mu})(\mathbf{x} - \boldsymbol{\mu})^T]$  is the covariance matrix.

*2.1.1. Block-Correlated Random Variables.* Let us assume that the input vector  $\mathbf{X}$  can be partitioned into  $\Gamma$  subsets of variables, that is,  $\mathbf{X} = (\mathbf{X}_1, \mathbf{X}_2, \dots, \mathbf{X}_\Gamma)$ , and that random vectors  $\mathbf{X}_\alpha$  and  $\mathbf{X}_\beta$  from this partitioning are mutually independent for  $\alpha, \beta = 1, 2, \dots, \Gamma$ .

Using the definition of a covariance matrix, one can show [9] that in this case  $\boldsymbol{\Sigma}_{\alpha\beta} = \boldsymbol{\Sigma}_{\beta\alpha} = 0$  for  $\alpha \neq \beta$ . Hence, the covariance matrix becomes block diagonal, that is,  $\boldsymbol{\Sigma} = \text{diag}(\boldsymbol{\Sigma}_{11}, \boldsymbol{\Sigma}_{22}, \dots, \boldsymbol{\Sigma}_{\Gamma\Gamma})$ , where  $\boldsymbol{\Sigma}_{\alpha\alpha}$  is the covariance matrix of  $\mathbf{X}_\alpha$  ( $\alpha = 1, 2, \dots, \Gamma$ ). The inverse of a block diagonal matrix is another block diagonal matrix, composed of the inverse of each block, that is,  $\boldsymbol{\Sigma}^{-1} = \text{diag}(\boldsymbol{\Sigma}_{11}^{-1}, \boldsymbol{\Sigma}_{22}^{-1}, \dots, \boldsymbol{\Sigma}_{\Gamma\Gamma}^{-1})$ . Moreover, taking into account that for block matrices  $\det(\boldsymbol{\Sigma}) = \prod_{\alpha=1}^{\Gamma} \det(\boldsymbol{\Sigma}_{\alpha\alpha})$ , one can write the expression for the joint probability density function defined in (3) in a form that reflects the block independence of variables:

$$\begin{aligned} p(\mathbf{x}) &= \prod_{\alpha=1}^{\Gamma} \frac{1}{(2\pi)^{d_\alpha/2} \det(\boldsymbol{\Sigma}_{\alpha\alpha})^{1/2}} \\ &\quad \times \exp\left[-\frac{1}{2}(\mathbf{x}_\alpha - \boldsymbol{\mu}_\alpha)^T \boldsymbol{\Sigma}_{\alpha\alpha}^{-1}(\mathbf{x}_\alpha - \boldsymbol{\mu}_\alpha)\right], \end{aligned} \quad (4)$$

where  $p(\mathbf{x}_\alpha)$  is the joint probability density function of a subset  $\alpha$  and  $d_\alpha = \dim(\mathbf{x}_\alpha)$  is the number of variables in  $\mathbf{X}_\alpha$ .

*2.2. Global Sensitivity Analysis.* The *variance-based global sensitivity analysis* method aims to quantify the relative importance of each input parameter in the response variance. It involves the calculation of the *global sensitivity indices*, sometimes called *Sobol's sensitivity indices* [2, 10].

In order to describe the global sensitivity indices, let us introduce the following notations: let  $\{1, 2, \dots, d\}$  be the set of input variable indices and let  $u$  be its arbitrary subset. Hence,  $\mathbf{X}_u$  is a subset of variables whose indices are in  $u$ , whereas  $\mathbf{X}_{-u}$  are the complimentary variables, that is, variables with indices not in  $u$ . Notation  $|u|$  will be used for the cardinality of the set  $u$ . Variables  $X_i$  from non-overlapping sets  $u$  and  $-u$  constitute the input vector  $\mathbf{X} = (\mathbf{X}_u, \mathbf{X}_{-u})^T$ .

Let us consider a subset  $\mathbf{X}_u$  of input variables. Two types of sensitivity indices of the model response to the input random variables  $\mathbf{X}_u$  can be introduced:

- (i) the *main effect sensitivity index*  $S_{X_u}$ , which describes the fraction of variance of the output  $Y$  that is expected to be *removed* if the true values of variables  $\mathbf{X}_u$  become known.

- (ii) the *total sensitivity index*  $S_{X_u}^{\text{tot}}$ , which can be interpreted as the fraction of variance of the output  $Y$  that is expected to *remain* if the true values of variables  $X_{-u}$  become known.

In other words,  $S_{X_u}$  represents the effect due to  $X_u$  only, and  $S_{X_u}^{\text{tot}}$  represents the contribution to the variance of  $X_u$  with all the interactions of this variable with other variables.

The definition of sensitivity indices and their theoretical justification comes from functional ANOVA (analysis of variance). In Appendix A, we summarize formulae of the functional ANOVA decomposition, assuming that inputs are independent random variables with arbitrary continuous distributions.

Sobol [2, 3] introduced an alternative way of calculating sensitivity indices by sampling directly from  $f(\mathbf{x})$ , that is, without passing through the ANOVA decomposition. Sobol's alternative formulae are valid for uniformly distributed, independent random variables. Generalizing this result for continuous independent random variables with an arbitrary probability density function  $p(\mathbf{x}) = p(\mathbf{x}_1) \cdot \dots \cdot p(\mathbf{x}_d)$ , one can write:

$$f_{\emptyset} = \int_{\mathbb{R}^d} f(\mathbf{x})p(\mathbf{x})d\mathbf{x}, \quad D = \int_{\mathbb{R}^d} f^2(\mathbf{x})p(\mathbf{x})d\mathbf{x} - f_{\emptyset}^2, \quad (5)$$

$$D_{X_u} = \int_{\mathbb{R}^{2d-|u|}} f(\mathbf{x})f(\mathbf{x}_u, \mathbf{x}'_{-u})p(\mathbf{x})p(\mathbf{x}'_{-u})d\mathbf{x}d\mathbf{x}'_{-u} - f_{\emptyset}^2, \quad (6)$$

$$D_{X_u}^{\text{tot}} = \frac{1}{2} \int_{\mathbb{R}^{d+|u|}} [f(\mathbf{x}) - f(\mathbf{x}'_u, \mathbf{x}_{-u})]^2 p(\mathbf{x})p(\mathbf{x}'_u)d\mathbf{x}d\mathbf{x}'_u. \quad (7)$$

Here, the prime symbol over a variable (e.g., as in  $\mathbf{x}'_u$ ) means that this variable has to be sampled independently from the corresponding marginal distribution ( $p(\mathbf{x}'_u)$  in this case) of its unprimed analogue. Using the results from (5)–(7), the global sensitivity indices can be calculated as ratios:

$$S_{X_u}^{\text{tot}} = \frac{D_{X_u}^{\text{tot}}}{D}, \quad S_{X_u} = \frac{D_{X_u}}{D}. \quad (8)$$

Note that  $f_{\emptyset}$  and  $D$  correspond to the output mean and the output variance introduced in (2).

The independence condition for input variables can be relaxed. As discussed in [11], it is not necessary that *all* variables are mutually independent—this result holds when assuming independent blocks of input variables  $X_{\alpha}$  instead of single independent input variables  $X_i$ . Thus, if subsets of variables from  $X_u$  and  $X_{-u}$  are mutually independent, that is,  $p(\mathbf{x}) = p(\mathbf{x}_u)p(\mathbf{x}_{-u})$ , the sensitivity analysis formulas (6) and (7) are still applicable. Moreover, as one can see from (5), the formula for the output variance does not explicitly involve any particular subset of input variables. As a result, the variance of the output ( $D$ ) can be calculated with the method presented here even in the case when all input variables are correlated. Since the variance is used to characterise the uncertainty in the output due to the uncertainty of the input, the method from this paper can be used for uncertainty analysis disregarding whether normally distributed inputs are correlated or not.

As follows from the previous description, the evaluation of sensitivity indices requires the calculation of the integrals in (5)–(7), which can be written in the following general form:

$$I_{d_{\text{eff}}} [g] = \int_{\mathbb{R}^{d_{\text{eff}}}} g(\tilde{\mathbf{x}})p(\tilde{\mathbf{x}})d\tilde{\mathbf{x}}, \quad (9)$$

where  $I_{d_{\text{eff}}}[\cdot]$  is the integration operator,  $g(\tilde{\mathbf{x}})$  represents a function being integrated,  $d_{\text{eff}} = \dim(\tilde{\mathbf{x}})$  is the effective dimensionality of the integral, and  $p(\tilde{\mathbf{x}})$  is the joint probability density function of  $\tilde{\mathbf{x}}$ . For instance, in integral (6), function  $g(\tilde{\mathbf{x}})$  represents  $[f(\mathbf{x})f(\mathbf{x}_u, \mathbf{x}'_{-u})]$ ,  $\tilde{\mathbf{x}} = (\mathbf{x}, \mathbf{x}'_{-u}) = (\mathbf{x}_u, \mathbf{x}_{-u}, \mathbf{x}'_{-u})$ ,  $p(\tilde{\mathbf{x}}) = p(\mathbf{x})p(\mathbf{x}'_{-u})$ , and the effective dimensionality is  $d_{\text{eff}} = 2d - |u|$ .

**2.3. Standard Normal Law Representation.** Though the blockwise representation (4) of the joint probability density function (3) allows the exploiting of the independence of different subsets of variables, it gives no information about the practical way of a sensitivity index calculation. It is convenient to rewrite the expression in the so-called *standard* form in order to simplify future numerical evaluations of the global sensitivity indices.

Since covariance matrices are both symmetric and positive definite, for each  $\Sigma_{\alpha\alpha}$  there is a nonsingular matrix  $\mathbf{P}_{\alpha\alpha}$  such that  $\Sigma_{\alpha\alpha} = \mathbf{P}_{\alpha\alpha}\mathbf{P}_{\alpha\alpha}^T$  (Cholesky factorization). Consider the linear transformation  $\mathbf{z}_{\alpha} = \mathbf{P}_{\alpha\alpha}^{-1}(\mathbf{x}_{\alpha} - \boldsymbol{\mu}_{\alpha})$ . For any  $\alpha$ , it leads to

$$(\mathbf{x}_{\alpha} - \boldsymbol{\mu}_{\alpha})^T \Sigma_{\alpha\alpha}^{-1} (\mathbf{x}_{\alpha} - \boldsymbol{\mu}_{\alpha}) = \mathbf{z}_{\alpha}^T \mathbf{z}_{\alpha}, \quad (10)$$

and one can show that  $E[\mathbf{z}_{\alpha}] = 0$ ,  $\text{Cov}[\mathbf{z}_{\alpha}] = \mathbf{I}_{\alpha}$ , where  $\mathbf{I}_{\alpha} = \text{diag}(1, 1, \dots, 1)$  is the  $d_{\alpha} \times d_{\alpha}$  identity matrix. Since  $\sum_{\alpha=1}^{\Gamma} \mathbf{z}_{\alpha}^T \mathbf{z}_{\alpha} = \mathbf{z}^T \mathbf{z}$ , the joint probability density function can be written in the standard form:

$$p(\tilde{\mathbf{z}}) = \frac{1}{(2\pi)^{d_{\text{eff}}/2}} \exp\left(-\frac{1}{2}\tilde{\mathbf{z}}^T \tilde{\mathbf{z}}\right) = \frac{1}{(2\pi)^{d_{\text{eff}}/2}} \exp\left(-\frac{1}{2}\sum_{i=1}^{d_{\text{eff}}} z_i^2\right), \quad (11)$$

where  $p(\tilde{\mathbf{x}})d\tilde{\mathbf{x}} = p(\tilde{\mathbf{z}})d\tilde{\mathbf{z}}$ . New standard random variables  $Z_i$  ( $i = 1, 2, \dots, d$ ) have zero mean, standard deviations equal to one, and are not correlated, that is,  $Z_i \sim N(0, 1)$ .

Representation (11) can now be used for the calculation of sensitivity indices: variables  $Z_i$  can be sampled individually from  $N(0, 1)$  and the corresponding  $\tilde{\mathbf{x}}$ -points can be calculated as

$$\mathbf{x}_{\alpha}(\tilde{\mathbf{z}}) = \boldsymbol{\mu}_{\alpha} + \mathbf{P}_{\alpha\alpha}\mathbf{z}_{\alpha}, \quad (12)$$

where  $\alpha$  goes over all subsets of  $\tilde{\mathbf{X}}$ . Nevertheless, in order to simplify the sampling procedure, to allow the use of a single calculational path and make a wider range of numerical integration techniques suitable for solving the problem, we do one more transformation from the normally distributed variables to the uniformly distributed ones.

Consider the following coordinate-wise change of variable from  $z_i \in \mathbb{R}$  to  $s_i \in (0, 1)$ :

$$s_i(z_i) = \Phi(z_i), \quad (13)$$

where  $\Phi(\cdot)$  is the cumulative distribution function for the normal distribution. From the properties of  $\Phi(\cdot)$  follows  $\lim_{z_i \rightarrow -\infty} s_i(z_i) = 0$ ,  $\lim_{z_i \rightarrow +\infty} s_i(z_i) = 1$ ,

$$ds_i = \frac{1}{\sqrt{2\pi}} \exp\left(-\frac{1}{2}z_i^2\right) dz_i. \quad (14)$$

Applying this transformation coordinate-wise (i.e., for  $i = 1, 2, \dots, d_{\text{eff}}$ ) and introducing  $h(\tilde{\mathbf{s}}) = g(\tilde{\mathbf{x}}[\tilde{\mathbf{z}}(\tilde{\mathbf{s}})])$  give the representation of the integral (9) in the form

$$I_{d_{\text{eff}}}[g] = \int_{[0,1]^{d_{\text{eff}}}} h(\tilde{\mathbf{s}}) d\tilde{\mathbf{s}}. \quad (15)$$

Here,  $z_i(s_i) = \Phi^{-1}(s_i)$  for  $i = 1, 2, \dots, d_{\text{eff}}$ , where  $\Phi^{-1}(\cdot)$  is the inverse cumulative distribution function for the normal distribution, called the probit function, and  $\tilde{\mathbf{x}}(\tilde{\mathbf{z}})$  is defined by (12).

#### 2.4. Numerical Calculation of Sensitivity Indices

**2.4.1. Numerical Quadratures.** The integral in (15) can be approximated with a *quadrature* (sometimes called *cubature* in the literature), that can be written in the following general form:

$$I_{d_{\text{eff}}}[h(\tilde{\mathbf{s}})] \approx Q_{d_{\text{eff}}}^N[h(\tilde{\mathbf{s}})] = \sum_{n=1}^N w_n h(\tilde{\mathbf{s}}_n), \quad (16)$$

where  $w_n$  are method-dependent quadrature weights,  $h(\tilde{\mathbf{s}}_n)$  are samples of the integrand at method-dependent nodes  $\tilde{\mathbf{s}}_n \in [0, 1]^{d_{\text{eff}}}$ , and  $N$  is the number of samples.

The integral in (15) is multidimensional, and, therefore, special numerical techniques, that can cope with the curse of dimension, are required to calculate it. Monte Carlo (including quasi-Monte Carlo) and sparse grid integration methods are suitable for this task and will be considered in our paper. Later, we will briefly introduce these methods and discuss their implementation in our work.

**2.4.2. Monte Carlo and Quasi-Monte Carlo Quadratures.** In the case of the traditional Monte Carlo method, the integral is sampled on a set of  $d_{\text{eff}}$ -dimensional *pseudo-random* points  $\tilde{\mathbf{s}}_n$ , uniformly distributed in the unit hypercube  $[0, 1]^{d_{\text{eff}}}$ . In the case of quasi-Monte Carlo, so-called *low discrepancy sequences of quasirandom* points (also uniformly distributed in  $[0, 1]^{d_{\text{eff}}}$ ), are used for integration. For both traditional Monte Carlo and quasi-Monte Carlo, the weights  $w_n$  are point-independent and equal, that is,  $w_n = 1/N$ . The quasi-Monte Carlo quadratures have a higher asymptotic convergence rate and often outperform the traditional Monte Carlo quadrature in practical applications [12].

There is a strong similarity between traditional Monte Carlo and quasi-Monte Carlo quadratures except for the type of sampling points (pseudo-random or quasi-random) and the way of error estimation. The error estimation will be done in the same way for both quadratures (see the discussion later). Hence, in this paper, both the traditional Monte Carlo and the quasi-Monte Carlo quadratures will be referred to as Monte Carlo quadratures.

In this work, we follow Sobol's recommendations [3] on the implementation of the Monte Carlo quadratures for the calculation of sensitivity indices. In particular, sampling is done from hypercube  $[0, 1]^{2d}$  instead of  $[0, 1]^{d_{\text{eff}}}$  and, in order to improve the accuracy of the estimation in (15), the function  $f(\mathbf{x}) - c_0$  is evaluated instead of  $f(\mathbf{x})$  in (5)–(7), where  $c_0 \approx f_{\emptyset}$ .

Our estimation of the accuracy of the Monte Carlo quadratures is based on a so-called randomization procedure [13]. This procedure consists of calculating  $R$  independent estimates,  $\hat{I}_r^N$ , of integral (15). The approximation to integral (15) is then calculated as an average of independent estimates, that is:

$$\hat{I}^N = \frac{1}{R} \sum_{r=1}^R \hat{I}_r^N, \quad (17)$$

and the error of such an approximation is characterized by the sample standard deviation, defined as

$$\hat{\epsilon}_{RN} = \sqrt{\frac{1}{R(R-1)} \sum_{r=1}^R (\hat{I}_r^N - \hat{I}^N)^2}. \quad (18)$$

Each estimate  $\hat{I}_r^N$  is based on an independent sequence of  $N$  quasi- or pseudo-random points, where each new sequence of points is obtained from the initial one by a random modulo 1 shift [13].

**2.4.3. Sparse Grid Quadratures.** A sparse grid  $\mathcal{H}_{\ell, d_{\text{eff}}}$  is a set of  $d_{\text{eff}}$ -dimensional points, which is generated using *Smolyak construction* [14] and is based on a chosen sequence of the univariate quadrature formulas  $Q_l$ , where  $l \geq 0$  is the *accuracy level* of  $Q_l$  (see Appendix B for details). When applied to the integration of multivariate functions, the Smolyak construction is a multidimensional quadrature  $Q_{\ell, d_{\text{eff}}}$  based on a tensor product of one-dimensional quadratures  $Q_l$ , which are combined in a special way in order to optimize the quadrature convergence rate [15, 16]. The sequence of univariate quadrature formulae  $Q_l$  leads to a sequence of sparse grid quadratures with an increasing *sparse grid accuracy level*  $\ell \geq 0$ .

$Q_{\ell, d_{\text{eff}}}[h(\tilde{\mathbf{s}})]$  is a linear functional that depends on  $h(\tilde{\mathbf{s}})$  through function values at the set  $\mathcal{H}_{\ell, d_{\text{eff}}}$ , and the number of terms  $N$  in (16) is defined by its cardinality. The sparse grid points  $\tilde{\mathbf{s}}_n \in \mathcal{H}_{\ell, d_{\text{eff}}}$  and the quadrature weights  $w_n$  can be calculated using the procedure described in Appendix B.

If  $\mathcal{H}_{\ell, d_{\text{eff}}} \subset \mathcal{H}_{\ell+1, d_{\text{eff}}}$ , the quadrature is called *nested*. Nested quadratures permit the use of function values from previous levels, thus making integration less computationally expensive. Quadrature rules are said to be *open* when they do not include points on the boundary and *closed* otherwise. Points on the boundary (i.e.,  $s_i = 0$  or  $s_i = 1$  for  $i = 1, 2, \dots, d_{\text{eff}}$ ) represent a problem for the numerical integration in (9), as a transformation  $s_i \rightarrow z_i$  will lead to infinities in these points. Hence, only nested and strictly open sparse grid quadratures will be used in this work.

The sequence of sparse grid quadratures naturally leads to a formula for a practical estimation of the integration error

$$\hat{\epsilon}_\ell = |Q_{\ell, d_{\text{eff}}}[h(\tilde{\mathbf{s}})] - Q_{\ell-1, d_{\text{eff}}}[h(\tilde{\mathbf{s}})]|, \quad (19)$$

although this estimation is usually quite conservative.

Note that sparse grids are often defined on the hypercube  $s^* \in [-1, 1]^{d_{\text{eff}}}$ . In this case, they can easily be mapped to the unit hypercube  $[0, 1]^{d_{\text{eff}}}$  using the transformation of variables  $s_i = (s_i^* + 1)/2$ . When this mapping is performed, all sparse grid quadrature weights  $w_n$  have to be adjusted by a factor of  $2^{d_{\text{eff}}}$ .

**2.4.4. Inversion of the Standard Normal Cumulative Density Function.** According to the methodology discussed in the previous section, each sample vector  $\tilde{\mathbf{s}}_n$ , generated with either Monte Carlo or sparse grid techniques, requires transformation to the corresponding  $\tilde{\mathbf{z}}_n$  vector.

The traditional way to generate normally distributed points in conventional Monte Carlo is to sample from the uniform distribution and then to use the so-called Box-Muller transformation [17]. Unfortunately, it is not recommended [18] for use with quasi-Monte Carlo and is not suitable for use with sparse grids. An alternative way is to sample from the uniform distribution and then to use the inverse of the standard normal cumulative density function. It is recommended to use Moro's inversion algorithm [19], which is reported to be faster than the Box-Muller approach and has good accuracy for both the central region and the tails of the normal distribution [18].

In our work, Moro's algorithm is used for variable transformation  $\tilde{\mathbf{s}}_n \rightarrow \tilde{\mathbf{z}}_n$  ( $n = 1, 2, \dots, N$ ) coordinate-wise (i.e., for each  $s_{i,n}$ , where  $i = 1, 2, \dots, d_{\text{eff}}$ ) for both Monte Carlo and sparse grid samples.

**2.4.5. Algorithms for Calculation of Global Sensitivity Indices.** Algorithms 1 and 2 provide examples of how to calculate sensitivity indices based on a Monte Carlo quadrature and a sparse grid quadrature, respectively. Note that these algorithms are given for the sake of illustration and do not contain details about possible memory management or performance enhancements.

### 3. Results

**3.1. Test Problem Description.** The OECD LWR UAM (OECD: Organization for Economic Co-operation and Development; LWR: light water reactor; UAM: Uncertainty Analysis in Modelling) benchmark [8] seeks to determine the uncertainty in LWR system calculations at all stages of coupled reactor physics/thermal hydraulics calculations. The benchmark specification consists of three phases, where the first phase is the neutronic phase.

The neutronic phase involved obtaining multigroup microscopic cross-section libraries. These libraries would then be used to calculate few group macroscopic cross-sections, which are to be used in criticality (steady state) stand-alone calculations. One of the reactors that was chosen as a reference LWR for the benchmark was the Peach Bottom

TABLE 1: Assembly homogenized 2-group cross-sections [21].

Variable	Notation	Value, $\text{cm}^{-1}$
Fast capture	$\Sigma_c^1$	$5.336 \cdot 10^{-3}$
Thermal capture	$\Sigma_c^2$	$2.693 \cdot 10^{-2}$
Fast fission	$\Sigma_f^1$	$1.9124 \cdot 10^{-3}$
Thermal fission	$\Sigma_f^2$	$2.8438 \cdot 10^{-2}$
Fast neutron production	$\nu\Sigma_f^1$	$4.920 \cdot 10^{-3}$
Thermal neutron production	$\nu\Sigma_f^2$	$6.929 \cdot 10^{-2}$
Fast removal	$\Sigma_s^{1-2}$	$2.063 \cdot 10^{-2}$

TABLE 2: Test covariance matrix [21]. Values in bold correspond to Case A, in bold and non-italic correspond to Case B, and the full covariance matrix correspond to Case C.

	$\Sigma_c^1$	$\Sigma_c^2$	$\Sigma_f^1$	$\Sigma_f^2$	$\nu\Sigma_f^1$	$\nu\Sigma_f^2$	$\Sigma_s^{1-2}$
$\Sigma_c^1$	<b>1.21</b>	0.23	-0.63	-0.04	-0.57	-0.03	0.77
$\Sigma_c^2$	0.23	<b>0.54</b>	-0.09	-0.48	-0.07	-0.34	-0.01
$\Sigma_f^1$	-0.63	-0.09	<b>0.68</b>	0.11	0.87	0.08	-0.68
$\Sigma_f^2$	-0.04	-0.48	0.11	<b>0.32</b>	0.06	0.72	0.04
$\nu\Sigma_f^1$	-0.57	-0.07	0.87	0.06	<b>0.98</b>	0.12	-0.64
$\nu\Sigma_f^2$	-0.03	-0.34	0.08	0.72	0.12	<b>0.45</b>	0.04
$\Sigma_s^{1-2}$	0.77	-0.01	-0.68	0.04	-0.64	0.04	<b>1.11</b>

reactor. By energy collapsing and spatial homogenization of microscopic cross-section and covariance data [20], Williams et al. [21] obtained the 2-group homogenized neutron cross-section, with an energy boundary of 0.625 eV, and the corresponding covariance matrix for the Peach Bottom reactor fuel assembly. The neutron cross-sections are given in Table 1, they are assumed to be independent and normally distributed, and their mean values (given in the third column of Table 1) correspond to the vector  $\boldsymbol{\mu}$  used in our methodology. The covariance matrix is shown in Table 2, where the diagonal terms are the percentage relative standard deviation and the off-diagonal terms are the correlation coefficients.

The global sensitivity analysis methodology discussed in Section 2 was applied to nuclear reactor calculations. The reactor parameter of interest that was chosen for this study is the infinite neutron multiplication factor,  $k_\infty$ , and it was modelled as [22]

$$k_\infty = \frac{\nu\Sigma_f^1}{\Sigma_c^1 + \Sigma_f^1 + \Sigma_s^{1-2}} + \frac{\nu\Sigma_f^2\Sigma_s^{1-2}}{(\Sigma_c^2 + \Sigma_f^2)(\Sigma_c^1 + \Sigma_f^1 + \Sigma_s^{1-2})}, \quad (20)$$

where the traditional notation for macroscopic cross-sections is used (see Table 1). To illustrate our methodology, three cases were considered (all three cases are shown in Table 2): one with a diagonal covariance matrix, another one with a block-diagonal covariance matrix, and the last one with the full covariance matrix.

In the first case (hereafter referred to as Case A), it was assumed that the input parameters (cross-sections) are not correlated, and the covariance matrix consisted of only the diagonal entries, highlighted in bold, while all other elements of the matrix were set to zero.

In the second case (hereafter referred to as Case B), we assumed a test block-diagonal covariance matrix. The test

```

input:  $\mu_1, \dots, \mu_\Gamma, \Sigma_{11}, \dots, \Sigma_{\Gamma\Gamma}, u, R, N$ 
for  $\alpha = 1$  to  $\Gamma$  do
   $\mathbf{P}_{\alpha\alpha} \leftarrow$  Cholesky decomposition of  $\Sigma_{\alpha\alpha}$ 
   $\mathbf{P}'_{\alpha}, \mu'_{\alpha} \leftarrow \mathbf{P}_{\alpha}, \mu_{\alpha}$ 
end for
 $\tilde{\mathbf{P}} \leftarrow \text{diag}(\mathbf{P}_{11}, \dots, \mathbf{P}_{\Gamma\Gamma}, \mathbf{P}'_{11}, \dots, \mathbf{P}'_{\Gamma\Gamma})$ 
 $\tilde{\boldsymbol{\mu}} \leftarrow \text{vec}(\mu_1, \dots, \mu_\Gamma, \mu'_1, \dots, \mu'_\Gamma)$ 
 $d_{\text{eff}} \leftarrow \text{dim}(\tilde{\boldsymbol{\mu}})$ 
for  $n = 1$  to  $N$  do
  for  $r = 1$  to  $R$  do
     $\tilde{s}_n \leftarrow d_{\text{eff}}$ -dimensional quasi- or pseudo-random point
     $w_n \leftarrow 1/N$ 
     $\tilde{\mathbf{z}}_n \leftarrow \Phi^{-1}(\tilde{s}_n)$ 
     $\tilde{\mathbf{x}}_n \leftarrow \tilde{\boldsymbol{\mu}} + \tilde{\mathbf{P}}\tilde{\mathbf{z}}_n$ 
     $\mathbf{g}_n \leftarrow \mathbf{g}(\tilde{\mathbf{x}}_n)$ 
  end for
   $(f_{\emptyset}, D, D_{X_u}, D_{X_u}^{\text{tot}})_r \leftarrow \sum_{n=1}^N w_n \mathbf{g}_n$ 
end for
calculate  $S_{X_u}, S_{X_u}^{\text{tot}}, \hat{\epsilon}_{RN}$ 
return  $S_{X_u}, S_{X_u}^{\text{tot}}, \hat{\epsilon}_{RN}$ 

```

ALGORITHM 1: The calculation of sensitivity indices using Monte Carlo quadrature.

```

input:  $\mu_1, \dots, \mu_\Gamma, \Sigma_{11}, \dots, \Sigma_{\Gamma\Gamma}, u, \ell_{\text{max}}$ 
for  $\alpha = 1$  to  $\Gamma$  do
   $\mathbf{P}_{\alpha\alpha} \leftarrow$  Cholesky decomposition of  $\Sigma_{\alpha\alpha}$ 
   $\mathbf{P}'_{\alpha}, \mu'_{\alpha} \leftarrow \mathbf{P}_{\alpha}, \mu_{\alpha}$ 
end for
 $\tilde{\mathbf{P}} \leftarrow \text{diag}(\mathbf{P}_{11}, \dots, \mathbf{P}_{\Gamma\Gamma}, \mathbf{P}'_{11}, \dots, \mathbf{P}'_{\Gamma\Gamma})$ 
 $\tilde{\boldsymbol{\mu}} \leftarrow \text{vec}(\mu_1, \dots, \mu_\Gamma, \mu'_1, \dots, \mu'_\Gamma)$ 
 $d_{\text{eff}} \leftarrow \text{dim}(\tilde{\boldsymbol{\mu}})$ 
for  $\ell = 1$  to  $\ell_{\text{max}}$  do
  generate  $\mathcal{H}_{\ell, d_{\text{eff}}}$ 
   $N \leftarrow$  size of  $\mathcal{H}_{\ell, d_{\text{eff}}}$ 
  for  $n = 1$  to  $N$  do
     $\tilde{s}_n \leftarrow$  node from  $\mathcal{H}_{\ell, d_{\text{eff}}}$ 
     $w_n \leftarrow$  sparse grid weight
     $\tilde{\mathbf{z}}_n \leftarrow \Phi^{-1}(\tilde{s}_n)$ 
     $\tilde{\mathbf{x}}_n \leftarrow \tilde{\boldsymbol{\mu}} + \tilde{\mathbf{P}}\tilde{\mathbf{z}}_n$ 
     $\mathbf{g}_n \leftarrow \mathbf{g}(\tilde{\mathbf{x}}_n)$ 
  end for
   $(f_{\emptyset}, D, D_{X_u}, D_{X_u}^{\text{tot}})_\ell \leftarrow \sum_{n=1}^N w_n \mathbf{g}_n$ 
  calculate  $S_{X_u}, S_{X_u}^{\text{tot}}, \hat{\epsilon}_\ell$ 
  return  $S_{X_u}, S_{X_u}^{\text{tot}}, \hat{\epsilon}_\ell$ 
end for

```

ALGORITHM 2: The calculation of sensitivity indices using sparse grid quadrature.

matrix was artificially constructed based on the 2-group covariance matrix from [21] in such a way that the input variables can be partitioned into three mutually independent subsets  $\{\Sigma_c^1, \Sigma_c^2, \Sigma_f^1, \Sigma_f^2\}$ ,  $\{\nu\Sigma_f^1, \nu\Sigma_f^2\}$ , and  $\{\Sigma_s^{-2}\}$ , such that elements in the off-diagonal blocks are set to zero, that is, terms highlighted in *italic* are set to zero. It should be noted that the elements of the first subset correspond to those terms that contribute to the absorption cross-section. The elements of the second subset correspond to those terms that contribute to the production of neutrons, and the last subset

corresponds to the removal of neutrons from the fast group to the thermal group.

For the last case (hereafter referred to as Case C), it was assumed that all the input parameters (cross-sections) are correlated with one another, and the full covariance matrix was used, that is, all entries highlighted in **bold**, *italic*, and non-*italic*.

It should be emphasised that neither of the first two examples (Cases A and B) considered pretends to reflect physical reality, but both the cross-section values and the

TABLE 3: Estimated uncertainty of the infinite multiplication factor in terms of variance and standard deviation (given in parenthesis).

Case	Traditional Monte Carlo	Quasi-Monte Carlo	Sparse grid
A	$3.680 \cdot 10^{-5}$ (607 pcm)	$3.680 \cdot 10^{-5}$ (607 pcm)	$3.671 \cdot 10^{-5}$ (606 pcm)
B	$3.575 \cdot 10^{-5}$ (598 pcm)	$3.576 \cdot 10^{-5}$ (598 pcm)	$3.567 \cdot 10^{-5}$ (597 pcm)
C	$3.115 \cdot 10^{-5}$ (558 pcm)	$3.116 \cdot 10^{-5}$ (558 pcm)	$3.108 \cdot 10^{-5}$ (558 pcm)

elements of the test covariance matrix are of a plausible order of magnitude (close to the values given in [21]); hence, this example is representative and suitable for testing of our method. Therefore, the results and conclusions will be given in order to characterise the method presented and not the neutron multiplication properties of the Peach Bottom reactor.

**3.2. Method Implementation.** A Fortran 90 program was written to implement all the steps of the methodology outlined in Section 2. The program was subdivided into blocks of code, where each block had an input to be evaluated to give an expected output and corresponded to step(s) along the calculational path of the methodology. The testing, verification, and validation of the program were done for each block of code using test functions, for which the corresponding results could be evaluated analytically.

Pseudo-random points were generated using the Fortran intrinsic subroutine `random_number()`. In implementing quasi-Monte Carlo, a Sobol quasi-random number generator written by J. Burkardt [23] was used. Furthermore, a randomization procedure was used in estimating the integration error,  $\hat{\epsilon}_{RN}$ , for the Monte Carlo quadratures, by considering  $R = 100$  independent sequences with  $N = 10^6$  samples in each sequence.

The implementation of sparse grid quadratures was greatly facilitated by subroutines written by J. Burkardt [23]. Different open sparse grid quadrature rules such as Fejer, Gauss-Patterson, and Gauss-Legendre rules were applied (note that closed rules were also tested and, as expected, numerical problems for the boundary points were encountered). The Gauss-Legendre quadrature outperformed the other rules in terms of computational time needed to achieve a given accuracy for the cases considered, and its results will be reported up to a sparse grid level of  $\ell = 4$ . A conservative procedure defined by (19) was used in estimating the integration error  $\hat{\epsilon}_\ell$  for the sparse grid quadratures and is reported in this paper.

Variations were introduced into the neutron cross-sections by using a standardizing transformation as explained in (12), that is,  $\tilde{\mathbf{x}}(\tilde{\mathbf{z}}) = \tilde{\boldsymbol{\mu}} + \tilde{\mathbf{P}}\tilde{\mathbf{z}}$ , where  $\tilde{\mathbf{P}}$  is the extended Cholesky decomposed neutron cross-section covariance matrix, and  $\tilde{\mathbf{z}}$  is obtained by using Moro's inversion of samples required by each of the implemented quadratures. Finally, in order to improve the accuracy of the Monte Carlo estimation of integral (15), a variance reduction technique [3], which consists of sampling function  $\Delta f(\mathbf{x}) = [f(\mathbf{x}) - c_0]$  instead of  $f(\mathbf{x})$  in (5)–(7), where  $c_0 \approx f_\emptyset$ , was used.

**3.3. Computed Uncertainty and Sensitivity.** The uncertainty of multiplication factor  $k_\infty$ , computed in terms of variance  $D$ , are given in Table 3 for Cases A, B, and C. Though the output variance is the natural result of variance-based sensitivity analysis, the standard deviation is preferred in the literature because it allows an intuitive interpretation as the error bar for the value of the analysed parameter. The standard deviations are calculated as square root of variance,  $\sqrt{D}$ , and reported in Table 3 in parentheses for all cases and each quadrature. The uncertainty of the multiplication factor (expressed in relative units as  $100\% \times \delta k/k$ ), which we obtained in Case C, was 0.51% for each of the three quadratures, and this result is in good agreement with the value of 0.49% reported in [21].

The computed sensitivity indices for each of the variables (cross-sections) in Case A and for each subset in Case B are given in Table 4. No sensitivity analysis was performed for Case C, since any sensitivity indices computed with our method would be meaningless because all input parameters are correlated in this case.

Considering the results of Case A, the input variable with the greatest influence on the infinite neutron multiplication factor is the thermal neutron production,  $\nu\Sigma_f^2$ , and the input variable with the least influence is the fast neutron fission,  $\Sigma_f^1$ . This is similar to what we anticipated, given the fact that the infinite neutron multiplication factor is highly dependent on the number of neutrons produced in the system. Since the system being considered is thermal, the thermal neutron production should account for most of the neutrons produced, and the effect of fast neutron fission was not expected to be significant.

Considering the results of Case B, the subset  $\{\nu\Sigma_f^1, \nu\Sigma_f^2\}$ , which corresponds to the neutron production, had the greatest influence on the infinite neutron multiplication factor. The subset  $\{\Sigma_s^{1-2}\}$ , which corresponds to the fast neutron removal, was the least influential. It should be noted that the value of the sensitivity index for  $\{\Sigma_s^{1-2}\}$  is different in Cases A and B. This is because the off-diagonal terms of the covariance matrix influenced the results for  $\{\Sigma_s^{1-2}\}$ . In other words, due to the off-diagonal terms in the correlation matrix, Cases A and B define different problems.

**3.4. Error Analysis.** The results for Cases A and B, in Tables 3 and 4, were obtained by using a high number of samples with all three numerical quadratures ( $N = 10^6, R = 10^2$  in the case of Monte Carlo quadratures and  $\ell = 4, N = 56785$  in the case of sparse grid quadrature), and these results are taken as the reference. There seems to be very good agreement of the computed uncertainties and sensitivity indices between all three quadratures.

TABLE 4: Estimated sensitivities of the infinite multiplication factor to different cross-sections (Case A) or their subsets (Case B).

Case	Subset of cross-sections $\mathbf{X}_u$	Traditional Monte Carlo		Quasi-Monte Carlo		Sparse grid	
		$S_{\mathbf{X}_u}$	$S_{\mathbf{X}_u}^{\text{tot}}$	$S_{\mathbf{X}_u}$	$S_{\mathbf{X}_u}^{\text{tot}}$	$S_{\mathbf{X}_u}$	$S_{\mathbf{X}_u}^{\text{tot}}$
A	$\Sigma_c^1$	0.1766	0.1766	0.1766	0.1766	0.1766	0.1766
	$\Sigma_c^2$	0.1624	0.1626	0.1626	0.1626	0.1626	0.1626
	$\Sigma_f^1$	0.0071	0.0072	0.0072	0.0072	0.0072	0.0072
	$\Sigma_f^2$	0.0640	0.0641	0.0641	0.0641	0.0641	0.0641
	$\nu\Sigma_f^1$	0.0807	0.0808	0.0808	0.0808	0.0808	0.0808
	$\nu\Sigma_f^2$	0.4676	0.4678	0.4677	0.4677	0.4677	0.4677
	$\Sigma_s^{1-2}$	0.0409	0.0410	0.0410	0.0410	0.0410	0.0410
B	$\Sigma_c^1, \Sigma_c^2, \Sigma_f^1, \Sigma_f^2$	0.3453	0.3453	0.3453	0.3453	0.3453	0.3453
	$\nu\Sigma_f^1, \nu\Sigma_f^2$	0.6124	0.6126	0.6125	0.6125	0.6125	0.6125
	$\Sigma_s^{1-2}$	0.0420	0.0422	0.0422	0.0422	0.0421	0.0421

The accuracy obtained for the reference results is much better than the accuracy needed to draw practical conclusions concerning the contribution of uncertainties of different cross-sections. By this we mean that the accuracy of the sensitivity index estimation has to be, at least, sufficient to discriminate between the contribution of different inputs and should also be able to discriminate between  $S_{\mathbf{X}_u}^{\text{tot}}$  and  $S_{\mathbf{X}_u}$  for a given input  $\mathbf{X}_u$ .

Therefore, an error estimation study was done in order to determine the influence of the number of samples on the absolute and relative quadrature error of the computed sensitivity indices, where the relative quadrature error is given by

$$\hat{\delta} = \frac{\hat{\epsilon}(S_{\mathbf{X}_u}^{\text{tot}})}{S_{\mathbf{X}_u}^{\text{tot}}} \times 100 [\%], \quad (21)$$

where the absolute quadrature error  $\hat{\epsilon}$  is given by either (18) or (19). This study would help in determining the number of samples that is needed to get a good estimation of the sensitivity indices with the different numerical methods. For Monte Carlo methods, three different sample sizes were considered,  $N = 10^2$ ,  $N = 10^4$ , and  $N = 10^6$ . In all cases, the number of independent sequences  $R$  was taken as  $10^2$ . For the sparse grid, levels  $\ell = 1$  to  $\ell = 4$  were considered.

It was observed in both cases that the results obtained for  $S_{\mathbf{X}_u}^{\text{tot}}$  and  $S_{\mathbf{X}_u}$  are statistically similar for all subsets of the input variables, for all the three numerical methods that were used. This implies that the interaction effects can be neglected. It was also observed that the integration error for  $S_{\mathbf{X}_u}^{\text{tot}}$  was smaller than for  $S_{\mathbf{X}_u}$  in all the cases; hence, from now on, we will only consider  $S_{\mathbf{X}_u}^{\text{tot}}$ .

When considering Case A, it was observed that increasing  $N$  by a factor of 100 resulted, as expected, in a reduction of the integration error by a factor of approximately 10 for all the computed total sensitivity indices when using traditional Monte Carlo. The results for quasi-Monte Carlo showed that increasing  $N$  from  $10^2$  to  $10^4$ , and subsequently from  $10^4$  to  $10^6$ , resulted in a decrease of the integration error by a factor of about 30 and 40, respectively, for all the computed total sensitivity indices. For the sparse grid, a level change from

$\ell = 2$  to  $\ell = 3$  and from  $\ell = 3$  to  $\ell = 4$  both resulted in a decrease of the integration error by a factor of about 3.

The maximal absolute and relative errors for the total sensitivity indices computed with different number of samples are reported in Table 5 for Monte Carlo quadratures and Table 6 for sparse grid quadrature. These maximal absolute errors are obtained by taking the maximal absolute error of all the sensitivity indices for a given case, a given number of samples, and a given quadrature. The maximal relative error is obtained in the same way.

As one can see from Table 5, a relatively small number of samples ( $100 \times 100$ ) in the case of Monte Carlo gave fairly good accuracy (about 2%) in the estimation of the total sensitivity indices.

It should be noted that levels  $\ell = 0$  and  $\ell = 1$  for the sparse grid were not considered in the error estimation. This is because for level  $\ell = 0$ , the abscissa consists of only one point, and the variance is zero; hence, the total sensitivity index will be undefined. For the same reason, the application of (19) cannot give reasonable results for level  $\ell = 1$ . However, looking at Table 6, it can be seen that the maximal difference between the results obtained for levels  $\ell = 1$  and  $\ell = 2$  is smaller than  $2 \cdot 10^{-5}$ , and the maximum relative quadrature error obtained when moving from level  $\ell = 1$  to  $\ell = 2$  is smaller than  $3.8 \cdot 10^{-2}\%$ . Hence, this shows that for both cases, level  $\ell = 1$ , which contains only 29 points, is sufficient to estimate the total sensitivity indices with a very good accuracy.

The relatively small number of sparse grid points needed for an accurate estimation of the sensitivity indices as well as the absence of interactions between input variables (as discussed earlier) was unexpected. This result can potentially be explained in the following way: the uncertainty in cross-sections is so small that only the vicinity of the cross-section mean values contributes to the integrals used in the estimation of sensitivity indices. In this vicinity, the neutron multiplication factor, which is used as the example, can be approximated with a fairly linear function.

A small numerical experiment was done to clarify this aspect. The standard deviations given in Table 1 were initially multiplied by arbitrary factors between 1 and 10 and, in the second phase, by arbitrary factors between 1 and 20,

TABLE 5: Maximal error of Monte Carlo quadratures.

Case	Samples $N \times R$	Traditional Monte Carlo		Quasi-Monte Carlo	
		$\hat{\epsilon}_{RN}$	$\hat{\delta}, \%$	$\hat{\epsilon}_{RN}$	$\hat{\delta}, \%$
A	$10^2 \times 10^2$	$9.0 \cdot 10^{-3}$	2.2	$7.4 \cdot 10^{-3}$	1.6
	$10^4 \times 10^2$	$8.0 \cdot 10^{-4}$	$1.9 \cdot 10^{-1}$	$2.7 \cdot 10^{-4}$	$5.8 \cdot 10^{-2}$
	$10^6 \times 10^2$	$7.8 \cdot 10^{-5}$	$2.0 \cdot 10^{-2}$	$6.8 \cdot 10^{-6}$	$1.8 \cdot 10^{-3}$
B	$10^2 \times 10^2$	$1.2 \cdot 10^{-2}$	2.1	$9.8 \cdot 10^{-3}$	1.6
	$10^4 \times 10^2$	$1.1 \cdot 10^{-3}$	$1.9 \cdot 10^{-1}$	$3.5 \cdot 10^{-4}$	$5.8 \cdot 10^{-2}$
	$10^6 \times 10^2$	$9.1 \cdot 10^{-5}$	$2.0 \cdot 10^{-2}$	$1.2 \cdot 10^{-5}$	$1.9 \cdot 10^{-3}$

TABLE 6: Maximal error for the sparse grid quadrature.

$\ell$	$N$	Case A		Case B	
		$\hat{\epsilon}_\ell$	$\hat{\delta}, \%$	$\hat{\epsilon}_\ell$	$\hat{\delta}, \%$
1	29	N/A	N/A	N/A	N/A
2	477	$2.0 \cdot 10^{-5}$	$3.8 \cdot 10^{-2}$	$1.3 \cdot 10^{-5}$	$3.0 \cdot 10^{-2}$
3	5769	$6.4 \cdot 10^{-6}$	$1.3 \cdot 10^{-2}$	$4.3 \cdot 10^{-6}$	$1.0 \cdot 10^{-2}$
4	56785	$2.0 \cdot 10^{-6}$	$4.1 \cdot 10^{-3}$	$1.4 \cdot 10^{-6}$	$3.6 \cdot 10^{-3}$

and the sensitivity indices were recalculated. These factors were chosen to make the effect of a wider distribution more prominent without introducing a significant nonphysical effect due to negative cross-section values at the left tail of the distributions. It was observed that as the values of the standard deviations increase, interaction effects can be observed, that is,  $S_{X_u}^{\text{tot}}$  becomes statistically different from  $S_{X_u}$ . Furthermore, a larger number of points (higher levels) is needed to achieve the same accuracy as in the reference case. These results may be used to confirm our assumption on the nature of the good performance of the sparse grid quadrature. However, a proper study was done to confirm our conclusion, and the results are reported in [24].

## 4. Conclusions

In this paper, the global variance-based sensitivity and uncertainty analysis of reactor parameters dependent on few-group or multigroup neutron cross-sections was discussed. It was assumed that the cross-sections are normally distributed random variables, with known means and correlation matrices, which can be partitioned into statistically independent blocks of variables and that this partitioning allows one to formulate scientifically and practically sound sensitivity analysis problems. The theoretical and mathematical aspects of the calculation of the global sensitivity indices under the previous assumptions have been discussed. The problem of practical numerical calculations of the variance-based global sensitivity indices was addressed; namely, different options for numerical integration were considered. A consistent overall path for the calculation of sensitivity indices was proposed and described.

The method was successfully implemented in practice and was tested on a problem that involved two-group assembly homogenised cross-sections as input variables. The performance of different numerical integration techniques was tested on a reactor problem with arbitrary, but plausible, two-group cross-sections and covariance matrices. Different

implementations gave consistent results for the test problem under consideration. The implementation based on sparse grid quadrature demonstrated the best accuracy with as low as a few dozen samples.

This good performance of sparse grid integration was not expected and a special mini-study was performed with the purpose of explaining its origin as well as the absence of interactions in the obtained sensitivity indices. The results of this study confirmed our hypothesis that the observed results can be explained by the very small cross-section error. Nevertheless, this conclusion still has to be supported by a theoretical explanation.

From the methodological point of view, the method presented in the paper is applicable to problems with an arbitrary number of input variables. Nevertheless, one has to be cautious when dealing with multivariate problems in order to escape the curse of dimension. In this work, the applicability of our method to a few-group problem was demonstrated, but its applicability to multigroup reactor problems will be the topic of future studies.

## Appendices

### A. Functional ANOVA Decomposition for Independent Random Variables

Let  $p(x_1, x_2, \dots, x_d)$  be a joint probability density function of  $d$  random variables  $X_i$ :

$$P[X_1 \leq x_1, \dots, X_d \leq x_d] = \int_{-\infty}^{x_d} \cdots \int_{-\infty}^{x_1} p(x_1, x_2, \dots, x_d) dx_1 \cdots dx_d. \quad (\text{A.1})$$

Let  $f : \mathbb{R}^d \rightarrow \mathbb{R}$  be a square integrable function over  $\mathbf{x} = (x_1, \dots, x_d)$ . The expected value and the variance of the function  $f(\mathbf{x})$  with respect to the probability density function  $p(\mathbf{x})$  are defined as

$$\begin{aligned} E[f(\mathbf{x})] &= \int_{\mathbb{R}^d} f(\mathbf{x}) p(\mathbf{x}) d\mathbf{x}, \\ \text{Var}[f(\mathbf{x})] &= \int_{\mathbb{R}^d} (f(\mathbf{x}) - E[f(\mathbf{x})])^2 p(\mathbf{x}) d\mathbf{x}. \end{aligned} \quad (\text{A.2})$$

The *functional ANOVA decomposition* is a representation of the function  $f(\mathbf{x})$  as a sum of terms of increasing dimensionality:

$$f(\mathbf{x}) = \sum_u f_u(\mathbf{x}_u) = f_\emptyset + \sum_i f_i(x_i) + \sum_{i<j} f_{ij}(x_i, x_j) + \dots + f_{12\dots d}(x_1, x_2, \dots, x_d), \quad (\text{A.3})$$

where the sum is assumed over  $2^d$  subsets  $u \subseteq \{1, 2, \dots, d\}$  and  $f_u(\mathbf{x}_u)$  is a function that depends on  $\mathbf{x}$  only through  $x_i$  with  $i \in u$ . Here,  $\mathbf{x}_u$  is a subset of variables whose indices are in  $u$ , whereas  $\mathbf{x}_{-u}$  are the variables with indices not in  $u$ , and  $|u|$  is the cardinality of the set  $u$ .

According to Sobol's definition, for the representation given by (A.3) to be a functional ANOVA decomposition it has to satisfy the so-called *zero means* and *orthogonality* properties [2, 3]. Let random variables  $X_i$  ( $i = 1, 2, \dots, d$ ) be mutually independent with a joint probability density function  $p(\mathbf{x}) = p_1(x_1) p_2(x_2) \dots p_d(x_d)$ . Using an analogy with the case of uniformly distributed input variables, one can demonstrate that the functional ANOVA can be constructed by applying the following recurrent formula:

$$f_u(\mathbf{x}_u) = \int_{\mathbb{R}^{d-|u|}} \left( f(\mathbf{x}) - \sum_{v \subset u} f_v(\mathbf{x}_v) \right) p(\mathbf{x}_{-u}) d\mathbf{x}_{-u}. \quad (\text{A.4})$$

The constant mean term,  $f_\emptyset$ , is thus obtained by calculating  $f_\emptyset = \int_{\mathbb{R}^d} f(\mathbf{x}) p(\mathbf{x}) d\mathbf{x}$ , first order effects  $f_i(x_i)$  (where  $i = 1, \dots, d$ ) are obtained from  $f_i(x_i) = \int_{\mathbb{R}^{(d-1)}} (f(\mathbf{x}) - f_\emptyset) [p(\mathbf{x})/p(x_i)] d\mathbf{x}/dx_i$  and so on. For functions  $f_u(\mathbf{x}_u)$  obtained with recurrence (A.4), the zero means property becomes

$$\mathbb{E}[f_u(\mathbf{x}_u)] = \int_{\mathbb{R}^{|u|}} f_u(\mathbf{x}_u) p(\mathbf{x}_u) d\mathbf{x}_u = \int_{\mathbb{R}^d} f_u(\mathbf{x}_u) p(\mathbf{x}) d\mathbf{x} = 0. \quad (\text{A.5})$$

The orthogonality property holds in the weighted form

$$\int_{\mathbb{R}^d} f_u(\mathbf{x}_u) f_v(\mathbf{x}_v) p(\mathbf{x}) d\mathbf{x} = 0. \quad (\text{A.6})$$

Properties (A.5) and (A.6) are crucial for the functional ANOVA method because they lead to the variance decomposition formula:

$$\text{Var}[f(\mathbf{x})] = \sum_{u \subseteq \{1, 2, \dots, d\}} \text{Var}[f_u(\mathbf{x}_u)]. \quad (\text{A.7})$$

Let us assume that the function  $f(\mathbf{x})$  allows order-wise decomposition over subsets of variables (A.3). Applying the variance operator (A.2) to the left-hand side and right-hand side of (A.3) and using a standard statistical formula, we can write:

$$\text{Var}[f(\mathbf{x})] = \text{Var} \left[ \sum_u f_u(\mathbf{x}_u) \right] = \sum_u \text{Var}[f_u(\mathbf{x}_u)] + 2 \sum_{u, v \neq u} \text{Cov}[f_u(\mathbf{x}_u), f_v(\mathbf{x}_v)]. \quad (\text{A.8})$$

By definition,

$$\text{Cov}[f_u(\mathbf{x}_u), f_v(\mathbf{x}_v)] = \int_{\mathbb{R}^d} (f_u(\mathbf{x}_u) - \mathbb{E}[f_u(\mathbf{x}_u)]) (f_v(\mathbf{x}_v) - \mathbb{E}[f_v(\mathbf{x}_v)]) p(\mathbf{x}) d\mathbf{x}, \quad (\text{A.9})$$

and it can be observed from (A.9) that properties (A.5) and (A.6) lead to the zero-covariance condition  $\text{Cov}[f_u(\mathbf{x}_u), f_v(\mathbf{x}_v)] = 0$  for  $u \neq v$  and hence to the variance decomposition in the form of (A.7).

## B. Approximation of Multidimensional Integrals with Sparse Grid Quadratures

Let  $\varphi : \Omega \rightarrow \mathbb{R}$  be a continuous function of its arguments and with bounded mixed derivatives of order  $r$ :

$$\left\| \frac{\partial^{\|\mathbf{k}\|} \varphi(x_1, \dots, x_d)}{\partial x_1^{k_1} \dots \partial x_d^{k_d}} \right\|_{\infty} < \infty, \quad k_i \leq r, \quad (\text{B.1})$$

where  $\Omega = \Omega_1 \dots \Omega_d$ ,  $d$  is the dimensionality of the problem and  $\Omega_i \subset \mathbb{R}$  ( $i = 1, 2, \dots, d$ ) are bounded or unbounded intervals. We consider an approximation to the integral

$$I[\varphi(\mathbf{x})] = \int_{\Omega} \varphi(\mathbf{x}) \varrho(\mathbf{x}) d\mathbf{x}, \quad (\text{B.2})$$

where  $\mathbf{x} = (x_1, \dots, x_d)$ , with the tensor product form  $\varrho(x) = \varrho_1(x_1) \dots \varrho_d(x_d)$  of the weight function  $\varrho$ .

In order to construct a multidimensional sparse grid quadrature, let us consider a sequence of univariate quadrature formulas

$$Q_i[\psi(x_i)] = \sum_{j=1}^{m_i} w_{ji}^i \psi(x_{ji}^i), \quad (\text{B.3})$$

which approximate one-dimensional integrals

$$\int_{\Omega_i} \psi(x_i) \varrho_i(x_i) dx_i, \quad i = 1, 2, \dots, d. \quad (\text{B.4})$$

Here,  $\psi : \Omega_i \rightarrow \mathbb{R}$  is a continuous function of its argument,  $l_i \in \mathbb{Z}$ ,  $l_i \geq 0$  is the accuracy level of the quadrature formula,  $m_i$  is the number of abscissas (knots)  $x_{ji}^i$  of the quadrature, and  $w_{ji}^i$  is the corresponding weight. The index  $l_i$  is written explicitly over abscissas and weights in order to remind that they may change for different levels.  $\mathcal{H}_{l_i} = \{x_{ji}^i : 1 \leq j_i \leq m_i\}$  will be used to denote the set of knots of the one-dimensional quadrature formula.

In the sparse grid method, the integral (B.2) is approximated via the Smolyak formula [14, 15], defined for an accuracy level  $\ell \in \mathbb{Z}$  ( $\ell \geq 0$ ) of the sparse grid as follows:

$$Q_{\ell, d}[\varphi(\mathbf{x})] = \sum_{\ell - d + 1 \leq \|\mathbf{l}\|_1 \leq \ell} (-1)^{\ell - \|\mathbf{l}\|_1} \binom{d-1}{\ell - \|\mathbf{l}\|_1} \bigotimes_{i=1}^d Q_{l_i}[\varphi(\mathbf{x})], \quad (\text{B.5})$$

where  $\|\mathbf{l}\|_1 = \sum_{i=1}^d l_i$ , and the multi-index  $\mathbf{l} = (l_1, l_2, \dots, l_d) \in \mathbb{Z}^d$  contains the accuracy level of the one-dimensional quadrature (B.4) for each dimension. The tensor product  $\otimes$  in (B.5) can be calculated as

$$\bigotimes_{i=1}^d Q_{l_i}[\varphi(\mathbf{x})] = \sum_{j_1=1}^{m_{l_1}} \cdots \sum_{j_d=1}^{m_{l_d}} \varphi(x_{j_1}^{l_1}, \dots, x_{j_d}^{l_d}) \prod_{i=1}^d w_{j_i}^{l_i}, \quad (\text{B.6})$$

where the tensor product of quadrature weights  $w_{j_i}^{l_i}$  is replaced with the ordinary product, since they are real numbers. As one can see from the structure of (B.5) and (B.6), quadrature  $Q_{\ell,d}[\varphi(\mathbf{x})]$  is a linear functional that depends on  $\varphi$  through function values at a finite set of points. This set of points is called a “sparse grid” and is denoted by  $\mathcal{H}_{\ell,d}$ . A sparse grid is defined as the union

$$\mathcal{H}_{\ell,d} = \bigcup_{\ell-d+1 \leq \|\mathbf{l}\|_1 \leq \ell} (\mathcal{H}_{l_1} \times \cdots \times \mathcal{H}_{l_d}). \quad (\text{B.7})$$

For nested one-dimensional sets ( $\mathcal{H}_{l_i} \subset \mathcal{H}_{l_i+1}$ ), the corresponding sparse grids are also nested  $\mathcal{H}_{\ell,d} \subset \mathcal{H}_{\ell+1,d}$  and can be simplified, yielding

$$\mathcal{H}_{\ell,d} = \bigcup_{\|\mathbf{l}\|_1 = \ell} (\mathcal{H}_{l_1} \times \cdots \times \mathcal{H}_{l_d}). \quad (\text{B.8})$$

The integral (B.2) can now be approximated by the sum:

$$Q_{\ell,d}[\varphi(\mathbf{x})] = \sum_{\mathbf{x}_j^1 \in \mathcal{H}_{\ell,d}} w_j^1 \varphi(\mathbf{x}_j^1), \quad (\text{B.9})$$

where multidimensional knots  $\mathbf{x}_j^1 = (x_{j_1}^{l_1}, x_{j_2}^{l_2}, \dots, x_{j_d}^{l_d})$  can be constructed based on (B.7) and (B.8). The formulae for the quadrature weights  $w_j^1$  in (B.9) can be obtained in an analytical form only in a few particular cases; in all the other cases weights can be either precalculated or calculated online using (B.5) and (B.6).

## Acknowledgments

The authors would like to thank the South African National Research Foundation (NRF) for their financial support and Professor Kostadin N. Ivanov from Pennsylvania State University for his valuable suggestions.

## References

- [1] A. Saltelli, “Sensitivity analysis for importance assessment,” *Risk Analysis*, vol. 22, no. 3, pp. 579–590, 2002.
- [2] I. M. Sobol’, “Sensitivity estimates for nonlinear mathematical models,” *Mathematical Modelling and Computational Experiment*, vol. 1, pp. 407–414, 1993.
- [3] I. M. Sobol’, “Global sensitivity indices for nonlinear mathematical models and their Monte Carlo estimates,” *Mathematics and Computers in Simulation*, vol. 55, no. 1–3, pp. 271–280, 2001.
- [4] N. Lüdtke, S. Panzeri, M. Brown et al., “Information-theoretic sensitivity analysis: a general method for credit assignment in complex networks,” *Journal of the Royal Society Interface*, vol. 5, no. 19, pp. 223–235, 2008.
- [5] B. Aufer and B. Iooss, “Global sensitivity analysis based on entropy,” in *Safety, Reliability and Risk Analysis: Theory Methods and Applications*, S. Martorell, C. G. Soares, and J. Barnett, Eds., pp. 2107–2115, Taylor & Francis Group, London, UK, 2009.
- [6] U. Reuter and M. Liebscher, “Global sensitivity analysis in view of nonlinear structural behaviour,” in *German Conference Organized by DYNAmore GmbH, Anwenderforum, Bamberg, SC, USA, October 2008*.
- [7] B. Sudret, “Global sensitivity analysis using polynomial chaos expansions,” *Reliability Engineering and System Safety*, vol. 93, no. 7, pp. 964–979, 2008.
- [8] K. Ivanov, M. Avramova, I. Kodeli, and E. Sartori, “Benchmark for uncertainty analysis in modeling (UAM) for design, operation and safety analysis of LWRs,” NEA/NSC/DOC 23, OECD Nuclear Energy Agency, 2007.
- [9] R. A. Johnson and D. W. Wichern, *Applied Multivariate Statistical Analysis*, Pearson Prentice Hall, Upper Saddle River, NJ, USA, 6th edition, 2007.
- [10] A. Saltelli and I. M. Sobol’, “Sensitivity analysis for nonlinear mathematical models: numerical experience,” *Matematicheskoe Modelirovanie*, vol. 7, no. 11, pp. 16–28, 1995.
- [11] J. Jacques, C. Lavergne, and N. Devictor, “Sensitivity analysis in presence of model uncertainty and correlated inputs,” *Reliability Engineering and System Safety*, vol. 91, no. 10–11, pp. 1126–1134, 2006.
- [12] S. Kucherenko and N. Shah, “The importance of being Global. Application of Global sensitivity analysis in Monte Carlo option pricing,” *Wilmott Magazine*, vol. 4, pp. 2–10, 2007.
- [13] A. B. Owen, “Monte Carlo extension of Quasi-Monte Carlo,” in *Proceedings of the 30th Conference on Winter Simulation*, pp. 571–577, Washington, DC, USA, December 1998.
- [14] S. Smolyak, “Quadrature and interpolation formulas for tensor products of certain classes of functions,” *Doklady Akademii Nauk SSSR*, vol. 4, pp. 240–243, 1963.
- [15] E. Novak and K. Ritter, “High dimensional integration of smooth functions over cubes,” *Numerische Mathematik*, vol. 75, no. 1, pp. 79–97, 1996.
- [16] E. Novak, “Simple cubature formulas with high polynomial exactness,” *Constructive Approximation*, vol. 15, no. 4, pp. 499–522, 1999.
- [17] G. E. P. Box and M. E. Muller, “A note on the generation of random normal deviates,” *The Annals of Mathematical Statistics*, vol. 29, no. 2, pp. 610–611, 1958.
- [18] I. Krykova, *Evaluating of path-dependent securities with low discrepancy methods [M.S. thesis]*, Worcester Polytechnic Institute, 2003.
- [19] B. Moro, “The Full Monte,” *Risk*, vol. 8, no. 2, pp. 57–58, 1995.
- [20] B. T. Rearden, M. L. Williams, M. A. Jessee, D. E. Mueller, and D. A. Wiarda, “Sensitivity and uncertainty analysis capabilities and data in scale,” *Nuclear Technology*, vol. 174, no. 2, pp. 236–288, 2011.
- [21] M. Williams, M. Jessee, R. Ellis, and B. Rearden, “Sensitivity/uncertainty analysis for OECD UAM benchmark of peach bottom BWR,” in *Uncertainty Analysis and Modelling (UAM-4) Workshop*, Pisa, Italy, April 2010.
- [22] W. M. Stacey, *Nuclear Reactor Physics*, John Wiley & Sons, New York, NY, USA, 2001.
- [23] J. Burkardt, Source Codes in Fortran90, 2010, [http://people.sc.fsu.edu/~jburkardt/f\\_src/f\\_src.html](http://people.sc.fsu.edu/~jburkardt/f_src/f_src.html).
- [24] P. M. Bokov, “Asymptotic analysis for the variance-based global sensitivity indices,” *Science and Technology of Nuclear Installations*, vol. 2012, Article ID 253045, 8 pages, 2012.

## Research Article

# Sensitivity Studies for the Exercise I-1 of the OECD/UAM Benchmark

**E. Canuti,<sup>1</sup> A. Petruzzi,<sup>1</sup> F. D'Auria,<sup>1</sup> and T. Kozlowski<sup>2</sup>**

<sup>1</sup> San Piero a Grado Nuclear Research Group (GRNSPG), University of Pisa, Via Diotisalvi 2, 56122 Pisa, Italy

<sup>2</sup> Department of Nuclear, Plasma, and Radiological Engineering, University of Illinois, 216 Talbot Laboratory, MC-234, 104 South Wright Street, Urbana, IL 61801, USA

Correspondence should be addressed to E. Canuti, erika.canuti@gmail.com

Received 24 August 2012; Revised 30 October 2012; Accepted 31 October 2012

Academic Editor: Oscar Cabellos

Copyright © 2012 E. Canuti et al. This is an open access article distributed under the Creative Commons Attribution License, which permits unrestricted use, distribution, and reproduction in any medium, provided the original work is properly cited.

OECD/NEA has initiated an international Uncertainty Analysis in Modeling (UAM) benchmark focused on uncertainties in modeling of Light Water Reactor (LWR). The first step of uncertainty propagation is to perform sensitivity to the input data affected by the numerical errors and physical models. The objective of the present paper is to study the effect of the numerical discretization error and the manufacturing tolerances on fuel pin lattice integral parameters (multiplication factor and macroscopic cross-sections) through sensitivity calculations. The two-dimensional deterministic codes NEWT and HELIOS were selected for this work. The NEWT code was used for analysis of the TMI-1, PB-2, and Kozloduy-6 test cases; the TMI-1 test case was investigated using the HELIOS code. The work has been performed within the framework of UAM Exercise I-1 “Cell Physics.”

## 1. Introduction

OECD/NEA has initiated an international Uncertainty Analysis in Modeling (UAM) benchmark focused on propagation of uncertainties in the entire modeling chain of Light Water Reactor (LWR) in steady-state and transient conditions. The final objective is to benchmark uncertainty and sensitivity analysis methods in coupled multiphysics and multiscale LWR calculations.

The present paper is concerned only with cell and lattice physics. In reactor analysis, the lattice physics calculations are used to generate nodal (lattice-averaged) parameters, used for the full-core simulation. Similarly to other numerical simulations, the lattice-averaged parameters are affected by uncertainties. In lattice physics, these uncertainties can be divided into 3 types:

- (i) Multigroup cross sections uncertainties,
- (ii) Uncertainties associated with methods and modeling approximations used in lattice physics codes, and
- (iii) Fuel/assembly manufacturing tolerances.

The objective of the present paper is to study the effect of the last two uncertainty sources, within the framework of UAM Exercise I-1 “Cell Physics.” This exercise is focused on derivation of the multigroup microscopic cross-section libraries. Even if the intention for Exercise I-1 is to propagate the uncertainties in evaluated Nuclear Data Libraries—NDL—(microscopic point-wise cross sections) into multigroup microscopic cross-sections, here the NDL data have been used directly to perform lattice physics calculations (fuel pin lattices) in order to evaluate neutronics-related parameters.

For uncertainty propagation, the first step is to perform sensitivity to the input data affected by the errors or uncertainties. In this paper, the effect of numerical discretization errors and manufacturing tolerances on fuel pin lattice integral parameters (multiplication factor and cross-sections) has been analyzed through sensitivity calculations.

The two-dimensional deterministic codes NEWT and HELIOS were selected for this work. The NEWT code was used for analysis of the TMI-1, PB-2, and Kozloduy-6 test cases. Then, the TMI-1 test case was investigated using the

HELIOS code. Finally, a comparison has been made between the two lattice codes.

## 2. Codes Description

Two deterministic lattice codes have been used to perform the uncertainties studies: NEWT and HELIOS.

NEWT (New ESC-based Weighting Transport code) is a two-dimensional (2D) discrete-ordinates transport code developed at Oak Ridge National Laboratory [1]. It is based on the Extended Step Characteristic (ESC) approach for spatial discretization on an arbitrary mesh structure. This discretization scheme makes NEWT an extremely powerful and versatile tool for deterministic calculations in real-world nonorthogonal domains. The NEWT computer code has been developed to run within the SCALE package. Thus, NEWT uses AMPX-formatted cross-sections processed by other SCALE modules.

HELIOS is a generalized-geometry 2D lattice physics code developed by Studsvik-Scandpower [2]. HELIOS uses Current-Coupled Collision Probability (CCCP) method for its transport solution. The system to be calculated consists of heterogeneous space elements (e.g., pin-cell) that are coupled with each other and with the boundaries by interface currents, while the properties of each space element (i.e., its responses to sources and in-currents) are obtained from Collision Probability method (CP).

## 3. Model and Reference Simulation Parameters

The two-dimensional fuel pin-cell test problems representative of BWR PB-2, PWR TMI-1, and Kozloduy-6 VVER-1000 have been analyzed. The UAM specifications were used to define these three test problems, the details are shown in Figures 1, 2 and 3 for BWR, PWR, and VVER-1000 pin-cell, respectively [3].

In addition to the cell geometry, material compositions, and material temperatures, each code requires code-specific numerical parameters. Table 1 shows the numerical parameters used for the reference simulation of the three test cases.

## 4. Numerical Error and Sensitivity Calculation

The focus of the paper is on the numerical discretization error and the manufacturing tolerance sensitivities. The specific description of each type of calculation is described in the section below.

*4.1. Numerical Discretization Error.* The numerical discretization error was quantified for  $k_{\text{inf}}$  in the NEWT code. It was quantified for the two major numerical approximations used by NEWT code.

- (1) The spatial discretization of the cell grid: users can define a computational grid in which the NEWT ESC solution algorithm is applied. Convergence studies have been performed on  $k_{\text{inf}}$  value for the grid dimension from  $2 \times 2$  (base model) up to  $40 \times 40$  per cell.

TABLE 1: Reference simulation parameters.

Parameter	NEWT	HELIOS
Cross-sections library	ENDF/B-VII.0	HELIOS master library
Number of energy group	238	190
Grid structure	$2 \times 2$	$2 \times 2$
Number of sides per cylinder	12	—
Number of fuel pin azimuthal regions	—	4
Convergence Criteria		
Inner iterations	$10^{-4}$	$10^{-4}$
Outer iterations	$10^{-6}$	—
$k_{\text{inf}}$ value	$10^{-6}$	$10^{-6}$

- (2) The approximation of a circle with an equilateral polygon with a certain number of sides. The default number is 12. The influence of this approximation on the  $k_{\text{inf}}$  value has been evaluated for the number of sides from 8 to 28.

The study has been carried out for the three test cases in HZP condition only.

*4.2. Manufacturing Tolerance Sensitivities.* Sensitivity of lattice-averaged parameters to manufacturing tolerances has been studied using data provided by the UAM specifications for Phase I. For TMI-1 and PB-2 test cases, the manufacturing uncertainties are shown in Table 2. Normal distribution was assumed for each parameter Probability Density Function (PDF).

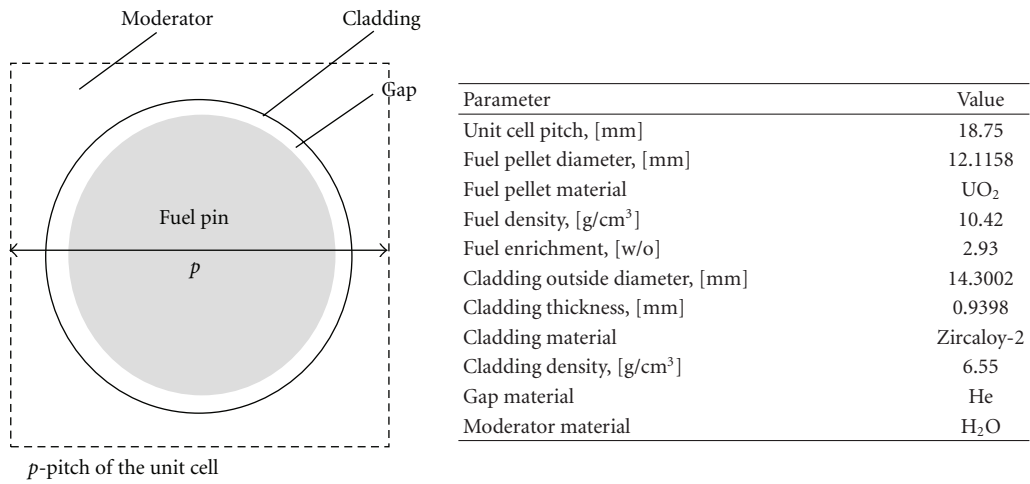
For VVER-1000 test case, the manufacturing tolerances are shown in Table 3. Uniform distribution was assumed for each parameter PDF.

It should be noted that these uncertainties were specified for the fuel assembly, but in this work they have been applied for the single pin-cell. The sensitivities have been performed by changing the listed parameters affected by manufacturing tolerances. For TMI-1 and PB-2 cases all the listed parameters have been increased by the quantity indicated in Table 2. For VVER-1000 case sensitivities have been performed using both the lower and the upper limits of the parameters listed in Table 3 (note that some limits correspond to the reference value). The sensitivities were calculated for the  $k_{\text{inf}}$  and the macroscopic 2 group cross-sections (absorption, fission, and scattering), in HZP and in HFP conditions.

It should be noted that in this work the term “sensitivity” has not been used in the usual way but as reactivity differences ( $\rho_2 - \rho_1$ ) due to a parameter variation.

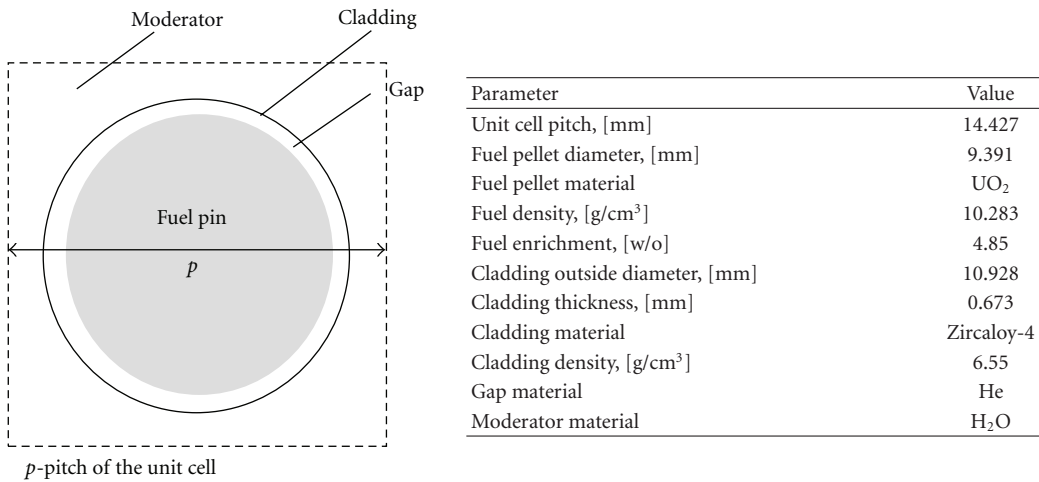
## 5. Results

*5.1. Criticality Results.* The reference (base case) results for the three test models are presented in this section. The lattice



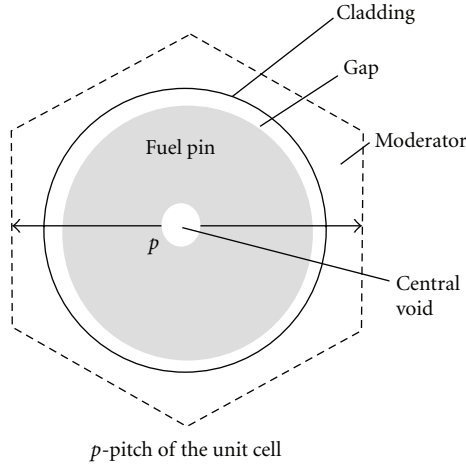
Parameter/reactor condition	HZP	HFP
Fuel temperature, [K]	552.833	900
Cladding temperature, [K]	552.833	600
Moderator (coolant) temperature, [K]	552.833	557
Moderator (coolant) density, [kg/m <sup>3</sup> ]	753.978	460.72
Reactor Power, [MWt]	3.293	3293
Void fraction (%)	—	40

FIGURE 1: Configuration of PB-2 BWR unit cell.



Parameter/reactor condition	HZP	HFP
Fuel temperature, [K]	551	900
Cladding temperature, [K]	551	600
Moderator (coolant) temperature, [K]	551	562
Moderator (coolant) density, [kg/m <sup>3</sup> ]	766	748.4
Reactor power, [MWt]	2.772	2772
Void fraction (%)	551	900

FIGURE 2: Configuration of TMI-1 PWR unit cell.



Parameter	Value
Unit cell pitch, [mm]	12.75
Fuel pellet diameter, [mm]	7.56
Fuel pellet material	UO <sub>2</sub>
Fuel density, [g/cm <sup>3</sup> ]	10.4
Fuel enrichment, [w/o]	3.3
Central void diameter, [mm]	1.4
Central void material	dry air
Cladding outside diameter, [mm]	9.1
Cladding thickness, [mm]	0.69
Cladding material	Zr + 1% Nb
Cladding density, [g/cm <sup>3</sup> ]	n/a
Gap material	He
Moderator material	H <sub>2</sub> O

Parameter/reactor condition	HZP	HFP
Fuel temperature, [K]	552.15	900
Cladding temperature, [K]	552.15	600
Moderator (coolant) temperature, [K]	552.15	560
Moderator (coolant) density, [kg/m <sup>3</sup> ]	767	752.5
Reactor Power, [MWt]	3.000	3000
Void fraction (%)	552.15	900

FIGURE 3: Configuration of Kozloduy-6 VVER-1000 unit cell.

TABLE 2: Manufacturing tolerances for TMI-1 test case.

Parameter	Reference value	Variation	
		TMI-1	PB-2
Fuel density	10.283 g/cm <sup>3</sup>	±0.17 g/cm <sup>3</sup>	±0.91% (= ± 0.095 g/cm <sup>3</sup> )
Fuel pellet diameter	9.391 mm	±0.013 mm	±0.013 mm
Gap thickness	0.0955 mm	±0.024 mm	—
Clad thickness	0.673 mm	±0.025 mm	±0.04 mm
<sup>235</sup> U concentration	4.85 w/o	±0.00224 w/o	—

$k_{\text{inf}}$  has been converted into reactivity using the following expression:

$$\rho = \frac{k_{\text{inf}} - 1}{k_{\text{inf}}}. \quad (1)$$

The results from HELIOS and NEWT are compared for TMI-1 pin-cell on Table 4. The  $k_{\text{inf}}$  value calculated by HELIOS is lower than the NEWT one, both for HZP (−550 pcm) and HFP (−840 pcm) conditions. These discrepancies can be due to the different cross-section libraries used by the two codes and the different energy group structures (Table 1).

The difference between HZP and HFP values is of about 1200 pcm in NEWT evaluations and 900 pcm in HELIOS ones. Criticality results for PB-2 and Kozloduy-6 test cases are provided in Tables 5 and 6.

## 5.2. Numerical Discretization Error

**5.2.1. Spatial Discretization Error.** One of the user-defined values is a computational grid in which the NEWT ESC solution algorithm is applied. Convergence study has been performed on  $k_{\text{inf}}$  value for the grid dimension from  $2 \times 2$  (base model) up to  $40 \times 40$  per cell. The finer discretization results in lower spatial discretization error, however it requires larger computational effort. Figure 4 shows the reactivity deviation (in pcm) from the asymptotic  $k_{\text{inf}}$  value (grid  $40 \times 40$ ) against the grid dimension for the three test cases.

For all the three test cases increasing the number of computational points the  $k_{\text{inf}}$  converges, but the convergence is faster for the Kozloduy-6 lattice. The  $k_{\text{inf}}$  convergence behavior is similar for the TMI-1 and the PB-2 lattice, but it differs from the Kozloduy one. Coarse grid overestimates the  $k_{\text{inf}}$  for BWR and PWR and underestimates the  $k_{\text{inf}}$  for the VVER. This is most likely because of the different types of lattice: PWR and BWR is a square lattice while the VVER is a hexagonal lattice.

TABLE 3: Manufacturing tolerances for Kozloduy-6 test case.

Parameter	Reference value	Lower limit	Upper limit
Inner hole diameter	1.4 mm	1.4 mm	1.7 mm
Fuel density	10.4 g/cm <sup>3</sup>	10.4 g/cm <sup>3</sup>	10.7 g/cm <sup>3</sup>
Fuel pellet diameter	7.56 mm	7.53 mm	7.56 mm
Clad inner diameter	7.72 mm	7.72 mm	7.78 mm
Clad outer diameter	9.1 mm	9.05 mm	9.15 mm
<sup>235</sup> U concentration	3.3 w/o	3.25 w/o	3.35 w/o

TABLE 4: TMI-1 fuel pin—NEWT and HELIOS results for reference model.

	HZP		HFP	
	NEWT	HELIOS	NEWT	HELIOS
$k_{inf}$	1.41481	1.42595	1.39138	1.40788
Reactivity $\rho$ (pcm)	29319	29871	28129	28971

TABLE 5: PB-2 fuel pin—NEWT results for reference model.

	HZP	HFP
	NEWT	NEWT
$k_{inf}$	1.33869	1.21906
Reactivity $\rho$ (pcm)	25300	17932

TABLE 6: Kozloduy-6 fuel pin—NEWT results for reference model.

	HZP	HFP
	NEWT	NEWT
$k_{inf}$	1.34311	1.32530
Reactivity $\rho$ (pcm)	25546	24546

It is important to note that the value corresponding to a  $2 \times 2$  grid is very far from the converged value, especially for BWR and PWR. In fact, grids lower than  $10 \times 10$  have numerical error larger than 100 pcm.

For subsequent calculations a  $3 \times 3$  computational grid has been chosen for BWR and PWR, taking into account both the accuracy of results and the computational time (that increases with the grid dimension). The reason for such coarse grid is that it is typically used for lattice calculations and recommended by the NEWT manual.  $6 \times 6$  grid has been chosen for VVER-1000.

**5.2.2. Circle Polygon Approximation Error.** Another important NEWT user-defined value is the approximation of a circle with an equilateral polygon with a certain number of sides. Convergence study has been performed on  $k_{inf}$  for the number of polygon sides from 8 to 28 (the default values are 12). Figure 5 shows the reactivity deviation (in pcm) from the asymptotic  $k_{inf}$  value (28 sides) against the number of polygon sides for the three test cases.

Nonmonotonic convergence is observed when varying the number of polygon sides, in particular for TMI-1 and PB-2 cases, while for Kozloduy-6 trend is much more monotonic. A possible reason for such behavior is that the

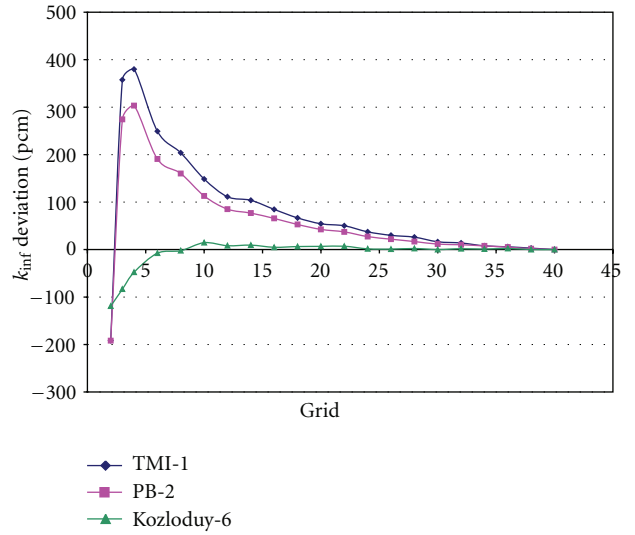


FIGURE 4: Grid influence on  $k_{inf}$ .

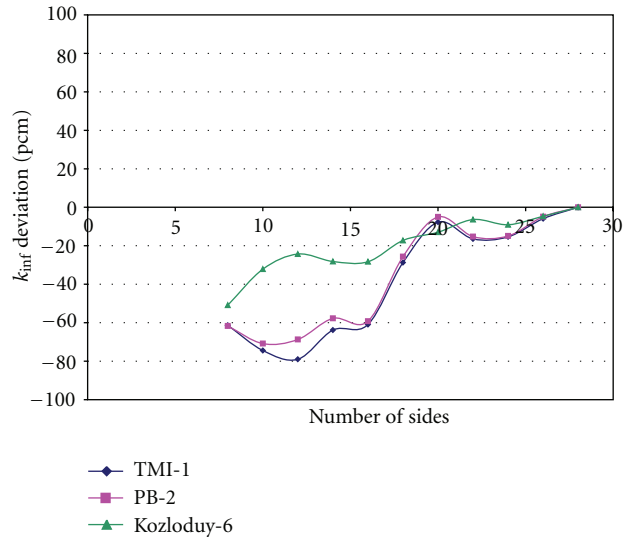
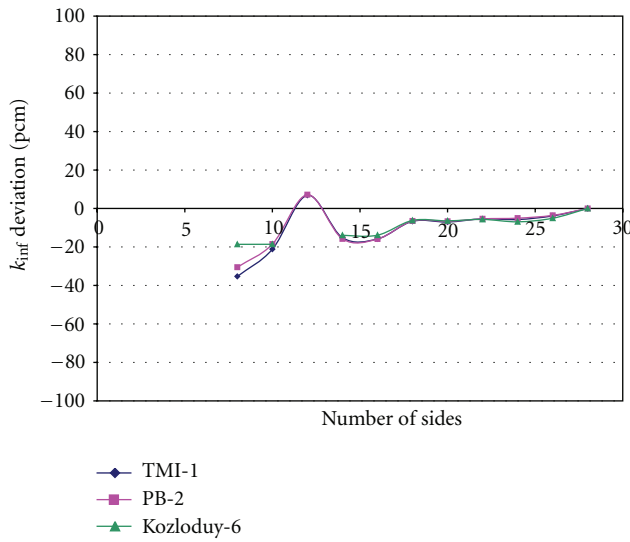


FIGURE 5: Number of polygon sides' influence on  $k_{inf}$  ( $3 \times 3$  grid).

use of the  $3 \times 3$  grid that is too coarse for a square lattice. Therefore, the same convergence study was performed using the finest grid ( $40 \times 40$ ), in order to eliminate the possible grid effect. The corresponding result is shown on Figure 6.

TABLE 7: Manufacturing sensitivities for TMI-1 and PB-2 test cases.

Parameter	Variation	TMI-1		Variation	PB-2	
		$\Delta\rho$ (pcm)			$\Delta\rho$ (pcm)	
		HZP	HFP		HZP	HFP
Fuel density	+0.17 g/cm <sup>3</sup>	-97	-104	+0.91%	-43	-95
Fuel pellet diameter	+0.013 mm	-19	-20	+0.013 mm	-12	-23
Gap thickness						
from outside	+0.024 mm	-84	-91	—	—	—
from inside	+0.024 mm	69	74	—	—	—
Clad thickness						
from outside	+0.025 mm	-104	-110	+0.04 mm	-129	-226
from inside	+0.025 mm	-16	-15	+0.04 mm	-23	-24
<sup>235</sup> U concentration	+0.00224 w/o	4	4	—	—	—

FIGURE 6: Number of polygon sides' influence on  $k_{inf}$  ( $40 \times 40$  grid).

With the  $40 \times 40$  grid all the test cases have the same asymptotic trend after the first fluctuation. The polygon approximation error is much lower on a finer mesh (compare Figures 5 and 6). It is interesting to note that this fluctuation appears for the default number of polygon sides (12). For the following calculations the default sides' number (12) will be always used.

An important effect is that the spatial discretization error (Figure 4) is opposite to the polygon approximation error (Figure 5). This demonstrates that relatively coarse spatial mesh and coarse polygon approximation can produce good criticality results due to fortunate cancellation of error.

**5.3. Manufacturing Tolerance Sensitivities.** Sensitivity of lattice-averaged parameters to manufacturing tolerances has been studied for the 3 test cases. For TMI-1 and PB-2 cases the sensitivities were calculated by increasing the parameters listed in Table 2. For VVER-1000 case the sensitivities were calculated using both the lower and the upper limits of the parameters listed in Table 3. The  $k_{inf}$  sensitivities were

TABLE 8: Manufacturing sensitivities for Kozloduy-6 test case.

Parameter	Variation	$\Delta\rho$ (pcm)	
		Kozloduy-6	
		HZP	HFP
Inner hole diameter			
Upper limit (0.17 cm)	+0.03 cm	80	87
Fuel density			
Upper limit (10.7 g/cm <sup>3</sup> )	+0.3 g/cm <sup>3</sup>	-151	-163
Fuel pellet diameter			
Lower limit (0.753 cm)	-0.003 cm	50	54
Clad inner diameter			
Upper limit (0.778 cm)	+0.006 cm	31	31
Clad outer diameter			
Upper limit (0.915 cm)	+0.005 cm	-135	-144
Lower limit (0.905 cm)	-0.005 cm	132	141
<sup>235</sup> U concentration			
Upper limit (3.35%)	-0.05 w/o	168	170
Lower limit (3.25%)	+0.05 w/o	-173	-175

TABLE 9: Manufacturing sensitivities on macroscopic cross-sections for TMI-1 fuel pin lattice.

Parameter	Variation	$\Delta\Sigma_a$ %	$\Delta\Sigma_f$ %	$\Delta\Sigma_s$ %
Fuel density	+0.17 g/cm <sup>3</sup>	1.16%	-1.22%	-1.16%
Fuel pellet diameter	+0.013 mm	0.22%	-0.24%	-0.22%
Gap thickness				
from outside	+0.024 mm	-0.08%	0.07%	0.08%
from inside	+0.024 mm	-0.81%	0.87%	0.81%
Clad thickness				
from outside	+0.025 mm	-0.10%	0.10%	0.10%
from inside	+0.025 mm	-0.02%	0.02%	0.02%
<sup>235</sup> U concentration	+0.00224 w/o	0.03%	-0.03%	-0.03%

calculated for the three cases at HZP and HFP conditions. The macroscopic 2 group cross-sections (absorption, fission, and scattering) sensitivities were calculated only for TMI-1 at HZP conditions.

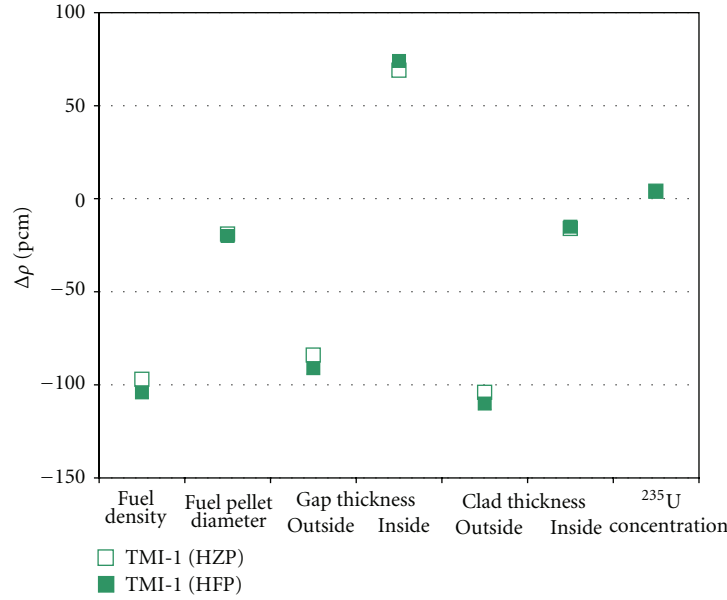


FIGURE 7: Manufacturing sensitivities for TMI-1 test case.

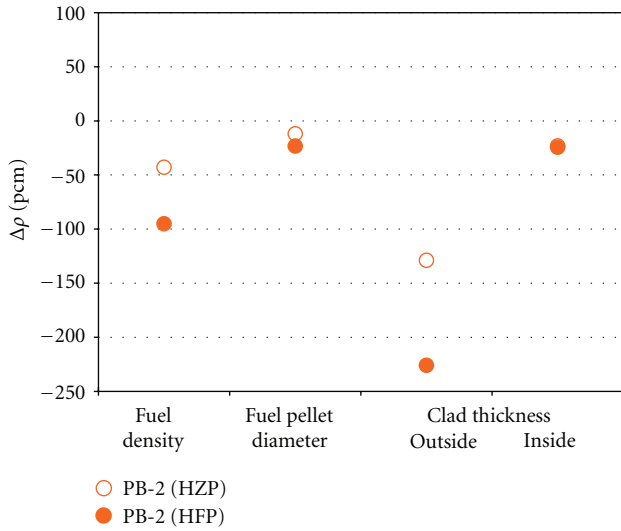


FIGURE 8: Manufacturing sensitivities for PB-2 test case.

Table 7 shows  $k_{inf}$  sensitivity due to the manufacturing tolerances for TMI-1 and PB-2 test cases at HWP and HFP conditions. The same results are shown graphically on Figures 7 and 8.

It should be noted that errors in gap and clad thickness can be considered in two ways.

- (1) The gap thickness can increase because the fuel pellet diameter decreases or the clad thickness decreases (increase of the internal clad diameter);
- (2) The clad thickness can increase because the gap thickness decrease (while outer clad diameter remains the same) or the outer clad diameter increases (while the inner clad diameter remains the same).

Each of the gap and clad thickness variations have been analyzed and are included in Table 7 and Figures 7 and 8.

The largest  $k_{inf}$  sensitivity (absolute values) for both the TMI-1 and PB-2 occur for the manufacturing tolerance of clad thickness (by changing the outer diameter) and fuel density. For all parameters HFP conditions sensitivities are larger (in magnitude) than HWP conditions, especially for the PB-2 test case. The highest  $k_{inf}$  sensitivity (absolute value) due to manufacturing tolerances are 110 pcm for TMI-1 and 226 pcm for PB-2. Further calculations show that  $\Delta k$  values change linearly with manufacturing tolerances for all the parameters considered.

Kozloduy-6  $k_{inf}$  sensitivities due to the manufacturing tolerances are shown on Table 8 and Figure 9. In this case the largest  $k_{inf}$  sensitivity occurs for manufacturing tolerance of fuel density and <sup>235</sup>U concentration. These variations have an absolute value of about 150–170 pcm.

The same sensitivity calculations have been performed using a 40 × 40 computational grid. It was observed that the  $k_{inf}$  sensitivities remain the same for all the test cases. Therefore, the spatial discretization has an effect on  $k_{inf}$  (see Figure 4), but it does not have an effect on  $k_{inf}$  sensitivity due to manufacturing tolerance.

Table 9 contains manufacturing sensitivities on macroscopic 1 group cross-sections ( $\Sigma$ ) for TMI-1 case in HWP conditions. The manufacturing tolerances have relatively small influence on macroscopic cross-sections. The highest variation is about 1.2% for the manufacturing tolerance of fuel density.

**5.4. Thermal Expansion Effect.** The geometric data used so far for our analysis corresponds to the atmospheric temperature, even for HFP calculations. At high temperatures, corresponding to the HFP conditions, both the fuel pellet and the clad undergo thermal expansion. To analyze

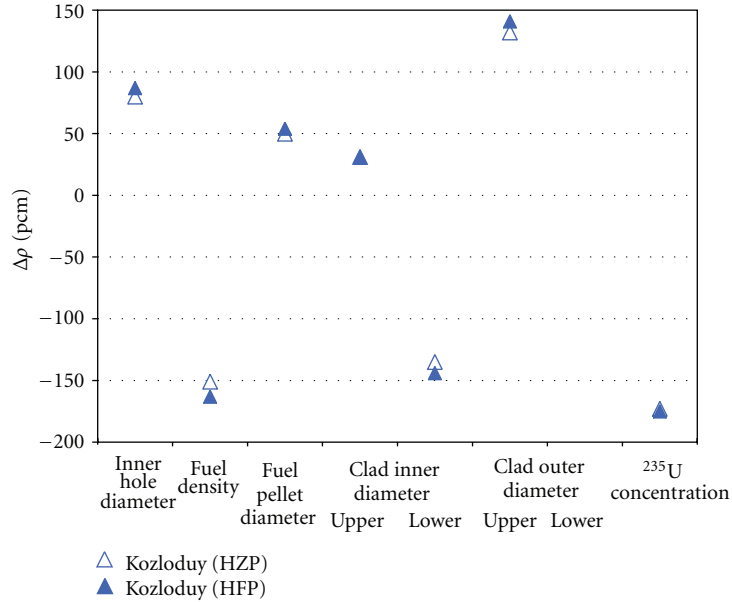


FIGURE 9: Manufacturing sensitivities for Kozloduy-6 test case.

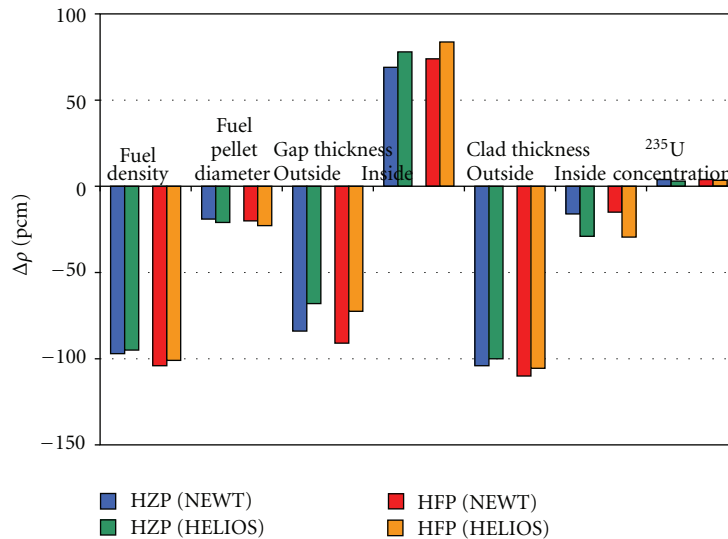


FIGURE 10: Comparison between HELIOS and NEWT sensitivities for TMI-1.

this effect, we calculated the actual fuel pellet diameter and clad dimensions following the thermal expansion (at HFP temperatures) [4] and recalculated the manufacturing tolerance sensitivities with these new geometric data at HFP conditions. This is to determine if the manufacturing tolerance sensitivities calculated with “cold” dimensions are consistent with the HFP dimensions.

The “hot” pin dimensions have been calculated using a thermal expansion coefficient for the fuel of  $17.5 \times 10^{-6}/\text{K}$  and a thermal expansion coefficient for the clad of  $6.1 \times 10^{-6}/\text{K}$ . In order to maintain consistent geometry, we verified that the fuel pellet diameter at HFP temperature plus its manufacturing tolerance remains smaller than the internal clad diameter.

After the calculation of “hot” pin dimension, the manufacturing tolerances sensitivities have been recalculated, at HFP conditions, as before (cf. Section 4.2).

The new results have been compared with the original sensitivities obtained with “cold” dimensions and they are shown in Table 10.

The reactivity sensitivities are the same as those calculated with the “cold” geometry.

*5.5. Comparison between NEWT and HELIOS Results for TMI-1.* The TMI-1 sensitivities have been recalculated with lattice code HELIOS and compared with the NEWT results. The results are summarized in Table 11 and shown graphically on Figure 10. Both codes predictions are consistent

TABLE 10: Manufacturing sensitivities for TMI-1 at HFP conditions considering thermal expansion.

Parameter	Variation	$\Delta\rho$ (pcm)	
		HFP	HFP with thermal expansion
Fuel density	+0.17 g/cm <sup>3</sup>	-104	-105
Fuel pellet diameter	+0.013 mm	-20	-20
Gap thickness			
from outside	+0.024 mm	-91	-92
from inside	+0.024 mm	74	74
Clad thickness			
from outside	+0.025 mm	-110	-111
from inside	+0.025 mm	-15	-15
<sup>235</sup> U concentration	+0.00224 w/o	4	4

TABLE 11: Comparison between HELIOS and NEWT sensitivities for TMI-1.

Parameter	Variation	$\Delta\rho$ (pcm)			
		NEWT		HELIOS	
		HZP	HFP	HZP	HFP
Fuel density	+0.17 g/cm <sup>3</sup>	-97	-104	-95	-101
Fuel pellet diameter	+0.013 mm	-19	-20	-21	-23
Gap thickness					
from outside	+0.024 mm	-84	-91	-68	-73
from inside	+0.024 mm	69	74	78	84
Clad thickness					
from outside	+0.025 mm	-104	-110	-100	-106
from inside	+0.025 mm	-16	-15	-29	-30
<sup>235</sup> U concentration	+0.00224 w/o	4	4	3	4

with each other. The highest discrepancy between the two is only 18 pcm. Therefore, even though the absolute value of reactivity differs by 100 s pcm (see Table 4), the sensitivities are practically the same.

## 6. Conclusions

This work has been carried out in the framework of UAM Exercise I-1 “Cell Physics.” Three test cases (TMI-1, PB-2, and Kozloduy-6) have been analyzed with the deterministic code NEWT. In addition, the TMI-1 fuel pin has also been modeled with the HELIOS code in order to compare the results of the two codes.

The infinite multiplication factor has been calculated for each of the lattice configuration. A significant discrepancy was found in the multiplication factor between NEWT and HELIOS for the TMI-1 case. The difference was about 600 pcm at HZP conditions and about 900 pcm at HFP conditions.

Sensitivity calculations have been performed in order to study the influence of numerical approximations and manufacturing tolerances on  $k_{\text{inf}}$ . The spatial discretization error was quantified for  $k_{\text{inf}}$  in the NEWT code and the

manufacturing sensitivities have been performed using data from UAM specifications for Phase I.

The following important conclusions related to the NEWT numerical approximation can be highlighted.

- (i) The spatial discretization error for  $k_{\text{inf}}$  shows an asymptotic convergence. The difference between the coarsest and the finest grid is about 300–400 pcm for TMI-1 and PB-2 test cases, and about 100 pcm for Kozloduy-6 test case.
- (ii) The spatial discretization error is very large with the default discretization ( $2 \times 2$  or  $3 \times 3$  grid), it is larger than any of the manufacturing sensitivities.
- (iii) The equilateral polygon approximation of a circle has relatively small influence on  $k_{\text{inf}}$ . Calculations performed with a coarse grid ( $3 \times 3$ ) show a fluctuating trend that becomes asymptotic on a finer grid ( $40 \times 40$ ).
- (iv) The spatial discretization error and circle polygon approximation error are in opposite direction, causing a fortunate cancelation of error.

The following important conclusions related to the manufacturing sensitivities can be highlighted.

- (i) Sensitivities change linearly with manufacturing tolerances for all the parameters considered.
- (ii) HFP sensitivities are larger than HZP ones, especially for PB-2 case.
- (iii) The manufacturing tolerance that has the largest influence on the  $k_{\text{inf}}$  is the outer clad diameter for TMI-1 and PB-2 test case and <sup>235</sup>U enrichment for Kozloduy-6 test case. The second most important parameter for all test cases is the fuel density.
- (iv) The influence of manufacturing tolerances on two group macroscopic cross-sections has been analyzed and maximum variation is about 1.2%.
- (v) Manufacturing tolerances sensitivities with “cold” and “hot” dimensions are the same.
- (vi) The spatial discretization has a significant effect on  $k_{\text{inf}}$ , but it does not have appreciable effect on manufacturing tolerance sensitivities.
- (vii)  $k_{\text{inf}}$  value is significantly different for HELIOS and NEWT, but the manufacturing tolerance sensitivities are almost the same.

The propagation of manufacturing tolerances for reactivity and few group nodal homogenized data at the fuel assembly level will be performed in the future.

## References

- [1] M. D. Dehart, “NEWT: a new transport algorithm for two-dimensional discrete ordinates analysis in non-orthogonal geometries,” ORNL/TM-2005/39, 2009.
- [2] Studsvik-Scandpower, *User Manual HELIOS*, 2009.

- [3] K. Ivanov, M. Avramova, I. Kodeli, and E. Sartori, “Benchmark for uncertainty analysis in modeling (UAM) for design, operation and safety analysis of LWRs—volume I: specification and support data for the neutronics cases (phase I),” NEA/NSC/DOC(2012), 2012.
- [4] F. A. Halden, H. C. Wohlers, and R. H. Reinhart, “Thermal expansion of uranium dioxide,” Final Report SRI/TDI-5722, 1959.

## Research Article

# Uncertainty and Sensitivity of Neutron Kinetic Parameters in the Dynamic Response of a PWR Rod Ejection Accident Coupled Simulation

C. Mesado,<sup>1</sup> A. Soler,<sup>1</sup> T. Barrachina,<sup>1</sup> R. Miró,<sup>1</sup> J. C. García-Díaz,<sup>2</sup>  
R. Macián-Juan,<sup>3</sup> and G. Verdú<sup>1</sup>

<sup>1</sup>Institute for the Industrial, Radiophysical and Environmental Safety (ISIRYM), Universitat Politècnica de València, 46022 Valencia, Spain

<sup>2</sup>Applied Statistics, Operations Research and Quality Department, Universitat Politècnica de València (UPV), Cami de Vera, s/n, 46022 Valencia, Spain

<sup>3</sup>Lehrstuhl für Nukleartechnik, Technische Universität München (TUM), Boltzmannstraße 15, 85747 Garching, Germany

Correspondence should be addressed to R. Miró, rmiro@iqn.upv.es

Received 21 August 2012; Revised 24 October 2012; Accepted 12 November 2012

Academic Editor: Oscar Cabellos

Copyright © 2012 C. Mesado et al. This is an open access article distributed under the Creative Commons Attribution License, which permits unrestricted use, distribution, and reproduction in any medium, provided the original work is properly cited.

In nuclear safety analysis, it is very important to be able to simulate the different transients that can occur in a nuclear power plant with a very high accuracy. Although the best estimate codes can simulate the transients and provide realistic system responses, the use of nonexact models, together with assumptions and estimations, is a source of uncertainties which must be properly evaluated. This paper describes a Rod Ejection Accident (REA) simulated using the coupled code RELAP5/PARCSv2.7 with a perturbation on the cross-sectional sets in order to determine the uncertainties in the macroscopic neutronic information. The procedure to perform the uncertainty and sensitivity (U&S) analysis is a sampling-based method which is easy to implement and allows different procedures for the sensitivity analyses despite its high computational time. DAKOTA-Jaguar software package is the selected toolkit for the U&S analysis presented in this paper. The size of the sampling is determined by applying the Wilks' formula for double tolerance limits with a 95% of uncertainty and with 95% of statistical confidence for the output variables. Each sample has a corresponding set of perturbations that will modify the cross-sectional sets used by PARCS. Finally, the intervals of tolerance of the output variables will be obtained by the use of nonparametric statistical methods.

## 1. Introduction

Being able to simulate accurately the different transients that can occur in a nuclear power plant is one of the main aims in nuclear safety analysis. Transient simulations involve both neutronic and thermalhydraulic calculations which are solved by different computer codes using best estimate models. Even though this approach provides more realistic responses than conservative codes, because of the reduction of the conservatism, the uncertainty in the code predictions of relevant safety system variable resulting from assumptions and code model estimates must be carefully evaluated. Uncertainties may stem from various sources, for example, lack of knowledge, approximate character of

physical models, uncertainty in model data, and so forth, and will be statistically propagated to code output parameters which have a probability density function and a range limit.

In order to obtain the uncertainties in the macroscopic neutronic information using a best estimate neutronics-thermalhydraulic coupled code, a Rod Ejection Accident (REA) has been simulated and the results are presented in this paper. The REA accident belongs to the reactivity-induced accidents (RIA) category and is part of the licensing basis accident analyses required for pressurized water reactors (PWR). The REA consists of a rod ejection due to the failure of its operating mechanism with the power evolution driven by a continuous reactivity insertion. The main factor limiting the consequences of the accident is

the Doppler reactivity effect. The physical description of the reactor response is based on the coupled neutronic-thermohydraulic code RELAP5/PARCSv2.7. Since a coupled code is used for the best estimate analysis, uncertainties from both aspects should be included and jointly propagated. CASMO4-SIMULATE3 provides the cross-section sets which are processed using the SIMTAB methodology developed at the Polytechnic University of Valencia (UPV) together with Iberdrola [1].

With the objective of providing a realistic environment for the development of the dynamic behaviour, monitoring and adjustment procedures, dynamic models for monitoring and control the output system have been developed.

## 2. Statistical Methodology

**2.1. Introduction.** It is possible to quantify the uncertainty by means of statistical measures. For instance, even when the exact values for a given code input are unknown, a range of possible values that it can take may be available. It is then possible to quantify uncertainty by considering the range, and a probability density function (PDF) that assigns a probability to the values inside the range. Sometimes, however, a third factor has to be considered [2], namely, the model uncertainty, that is, the difference between the real system and the result predicted by a set of approximations depending on the used model.

In this work, both the tolerance limits and the PDF distributions were an assumption. The real values of the tolerance limits for each kinetic parameter and its PDF distribution type will be known only after a validated uncertainty propagation methodology is applied to the whole process. This process, consisting in neutron kinetic parameters generation for coupled 3D neutronic-thermohydraulic, could be divided into three steps: (1) cell physics (derivation of the multigroup microscopic cross-section libraries and associated uncertainties), (2) lattice physics (derivation of the few-group macroscopic cross-section libraries and associated uncertainties), and (3) core physics (core steady-state and transient behavior with the associated uncertainties). Hence, this work is a general approach to the third step (core physics) on the assumption that the uncertainties corresponding to the first two steps are previously obtained.

Moreover, it is known that the fractions of delayed neutrons precursors (and their decay constants) play an important role in output variable variance. This influence depends on how far from prompt critical the insertion of reactivity is. Thus for small insertions of reactivity, delayed neutrons play an important role in the time evolution of the neutron flux, and so the uncertainty in  $\beta_i$  and  $\lambda_i$  will have a greater effect in the kinetic output variables. As the weight of the delayed neutrons decreases with the proximity to prompt criticality, the influence of  $\beta_i$  and  $\lambda_i$  also diminish as does the effect of their uncertainty.

In any case, the reason why the uncertainties in  $\beta_i$  and  $\lambda_i$  have not been included in this current study is the lack of available information. It is not expected, however, that maintaining these parameters unchanged will influence the

conclusions about the uncertainty and sensitivity results taking into consideration the uncertainties in the most important neutronic data considered in this work. The effects of the uncertainties on the kinetic parameters related to the precursors of delayed neutrons, however, will be taken into account in future studies.

The computer code plays the role as the used model and its associated uncertainty is calculated using the presented methodology. Figure 1 provides an easy explanation of the followed procedure (step 3).

The computer code is a deterministic function that transforms stochastic uncertain in its inputs and models,  $X_1$  to  $X_n$ , into stochastic uncertainty associated to its outputs  $Y$ .

The coupled code is represented by the function  $f$ , which calculated the output variables  $Y$ , as a function of input variables,  $X_i$ , whose uncertainties can be determined. With sensitivity analysis, the importance of each  $X_i$  regarding its influence on the uncertainty of  $Y$  can be calculated and hence a numerical value to that influence can be assigned.

To get a proper understanding on what is actually happening in the model, it is also important to perform a sensitivity analysis. This type of analysis reflects the variance of one response random variable when an input related random variable is perturbed. In this work, the sensitivity analysis performed is based on statistical measures of correlation between the input variables selected as sources of uncertainty and those output variables of interest. Two kinds of correlations can be used, those based on regression analysis, for example, Pearson Product Moment, and those based on nonparametric Rank correlation, for example, Spearman regression coefficients. Pearson correlation is most suitable for linear dependencies, whereas Spearman correlation can better quantify nonlinear and linear dependencies. For this work, Spearman correlation has been selected to carry out the sensitivity analysis. Additionally, full and partial correlations have been computed and analysed. Full correlations include the effects of all the input variables simultaneously, and partial correlations can eliminate the effects of the other variables for a given one. A threshold value of  $\pm 0.2$  is usually accepted as a threshold value below which an input variable is considered to have no significant influence on an output variable. In the paper, we have selected a value of  $\pm 0.16$  for this purpose.

It is important to point out that statistical sensitivity measures only quantify statistical relationships and do not offer quantitative values about the magnitude of the relationship which could be used to further compute linear uncertainties in the output variables of interest. For this, analytical or numerically obtained first-order derivatives must be computed,  $\partial \text{Output} / \partial \text{Input}$ , which is not always possible, especially for systems with nonlinear behaviour, for which second order and cross derivatives should be also included.

**2.2. Methodology Description.** This paper discusses a work based on previous studies [3]. The procedure followed to perform the uncertainty and sensitivity analysis is a sampling-based method. This method has been chosen because it is easy to implement, allows different procedures

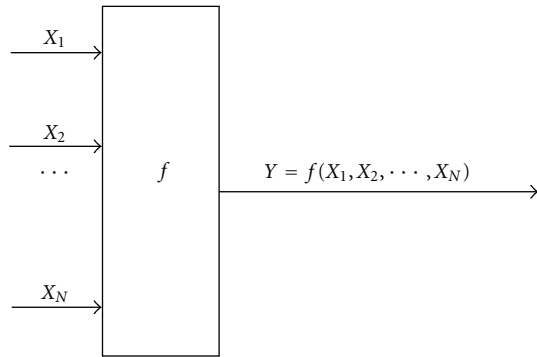


FIGURE 1: Model with input and output variables, extracted from [2].

for the sensitivity analyses [4], and is suitable for all computer codes. One of its main advantages is that the user does not need to know beforehand the importance of each input variable since the order of importance is provided by the sensitivity analysis afterwards. However, the main drawback of the sampling-based methods is the high computational cost. Another important feature of the methodology is that the accuracy of the obtained results is not dependent on the number of input parameters but among other factors, as the sample size or even the sampling procedure randomness. The latter condition ensures the randomness in the output variables.

The first step in the methodology is the characterization of the input variables uncertainty. As a starting point, the user must decide which input variables could be more relevant or sensitive for the output variables. As stated earlier, two factors are used in order to define the uncertainties related to the input variables: the intervals of possible values and the PDF associated. The uncertainty analysis with nonparametric methods can lead to range limits for  $Y$  in the form (*lower limit*, *upper limit*). These limits contain the real value of  $Y$  with a certain probability,  $p$ , and a prescribed level of confidence,  $\gamma$ . The lower and upper selected bounds for all input variables are  $(-0.003, +0.003)$ .

Regarding the selection of the distribution, if there is no information or knowledge in order to provide a PDF for a certain  $X_i$ , the uniform distribution is recommended since it assigns equal probability to each value within the sample space. However, depending on the phenomena modelled, the selection of the normal or even the log-normal distribution could be a better choice. In this paper, the chosen PDF distributions are uniform and normal which presents three different standard deviations, 0.1%, 0.5%, and 1%, respectively, both with mean value equals to 0. Once the distribution type is chosen, the sample has to be generated.

Computer codes, in general, do not accept intervals as  $X_i$ , but rather a unique numerical value for each  $X_i$ . Thus the methodology must provide a value for each  $X_i$  within each interval. There are several statistical techniques which could provide the desired values but two methods were selected in this work: Random and Latin Hypercube Lattice Sample (LHS), which is described in Section 2.4.

The second step involves performing the simulations a certain  $N$  number of times. This action is equivalent to obtain  $Y$  as a function of different sampled  $X$  (each time with a different sampled  $X$ ). An appropriate sample size value,  $N$ , is another important part of the methodology. This value depends on the desired uncertainty accuracy and is related with Wilks' formula which gives the minimum number of simulations and, hence, the number of input samples.

The Wilks' approach, also known as GRS's (Gesellschaft für Anlagen- und Reaktorsicherheit) method in nuclear safety field, is based on a pure statistical method [5]. The sample size, obtained by applying the Wilks' formula for double tolerance limits with a 95% of uncertainty and with 95% of statistical confidence for the output variables, is equal to 93 [6]. However, it has been recently published that the recommended minimum number of required code runs for the condition of 95/95 for 1st order two-sided approach are 146 [7], which is the code runs performed in this present work.

Each of the  $N$  simulations uses a different sampled  $X$  and leads to one different  $Y$ . In other words,  $N$  sets of  $X$  lead to  $N$  different output variables,  $Y$ . Furthermore,  $Y$  will be randomly provided due to the fact that  $X$  was randomly chosen. The PDFs of  $Y$  are sufficient to calculate the uncertainty in  $Y$ . However, the PDFs are not always easy to evaluate, thus, the only remaining alternative is to obtain as much information as possible about the PDFs properties together with the main parameters. One of the most used parameter is the quantile which comes from empirical PDFs and estimators.

The uncertainty of  $Y$ , for a certain uncertainty in  $X$ , can be easily calculated if  $Y$  is randomly sampled with a normal PDF. Provided those hypotheses, the tolerance intervals can be calculated with only two parameters: sample mean,  $m_y$ , and sample standard deviation,  $s_y$ . As stated earlier, the hypothesis of normal PDF for  $Y$  is not always easy to guarantee; however, there are some statistical tests that can be used to quantify how well the hypothesis of normality fits the sampled data. An important statistic test is the Rank correlation test for detecting linear relationship as well as nonlinear behaviour between  $X$  and  $Y$ . Examples of linear measures are the simple correlation coefficient (SCC), or Pearson's moment product, and the partial correlation coefficient (PCC). The most important advantage of the PCC is that it eliminates the linear influence of the remaining  $X_{j,j \neq i}$  on  $Y$ , leaving only the  $X_i$  whose sensitivity is being calculated. Both Rank correlations, simple and partial, will be described in Section 2.3.

**2.3. Simple or Partial Rank Correlation.** In order to deal with models which are not clearly linear, simple (SRCC) or partial rank correlation (PRC) coefficients can be used. To calculate these two correlations, the sample values of  $X_i$  and  $Y$ , whose relationship has to be determined, are separately "ranked"; that is, two separate and ordered lists (in decreasing or increasing order) are created, followed by the assignment of a rank or an integer number to each value.

If the two "unranked" original series of values are related monotonously, then the ordered series are linearly related.

This is true even if the relationship between the unordered series is not linear. Thus the absolute values of SRCC and PRCC will quantify the degree of relationship between the given  $X_i$  and  $Y_i$  of interest. The closer the values of these coefficients are to one, the more influence that  $X_i$  will have on  $Y$ . In sensitivity analysis, the most used test is the Spearman's coefficient. The critical values for the Spearman rank correlation coefficient are calculated by equation  $r_s = \pm z/\sqrt{n-1}$ , where  $n$  is the number of runs and  $z$  represents the point on the standard normal PDF. This point represents the probability,  $p$ , of observing a value greater than  $z$ , which is known as the upper critical value (quantile). For a confidence interval of 95%,  $z = 1.96$ .

**2.4. Latin Hypercube Lattice Sample.** For more than twenty years, the Latin Hypercube Lattice Sampling program has been successfully used to generate multivariate samples of statistical distributions. Its ability to use either Latin hypercube sampling or pure Monte Carlo sampling with both random and restricted pairing methods has made it an important part of uncertainty analyses in areas ranging from Probabilistic Risk Assessment (PRA) to complex simulation modelling.

Latin Hypercube Lattice Sampling (LHS) is a stratified random procedure that provides an efficient way of sampling variables from their distributions [4, 8, 9]. LHS is very popular for use with computationally demanding models because its efficient stratification properties allow for the extraction of a large amount of uncertainty and sensitivity information with a relatively small sample size. In fact, the main advantage of LHS respect Simple Random is that LHS gets a better dispersion sample points over the input domain space [10].

The LHS process consists of three steps: (1) the range of each input variable,  $X_i$ , is divided into  $n$  intervals with equal probability according to the associated PDF, (2) a random point is generated in each interval and for each input variable, and (3) one sample is generated with a random combination, without replacement, of the points randomly generated in step 2 (one point from each  $X_i$ ). Step 3 is repeated for the  $N$  required samples. Since one point is randomly generated in each interval, the domain input space is efficiently covered.

### 3. DAKOTA Methodology

It is well known that some design parameters have a high influence on the response whereas the influence of other parameters can be neglected. In order to optimize the design process, sensitivity analysis techniques and parameter study methods are performed. Both techniques and methods are used for identifying which parameters could be needed and which could be taken as constant parameters. In addition, in a postoptimization role, sensitivity information is useful in determining whether or not the response functions are robust with respect to small changes in the optimum design point [11].

TABLE 1: Input file information summary.

Sample size	146
Input model variables	7
Lower bound	-0.003
Upper bound	+0.003
Sampling method	Random/LHS
Variables distribution	Uniform/normal

DAKOTA software, which stands for Design Analysis Kit for Optimization and Terascale Applications, is the selected toolkit for the present sensitivity analysis study. DAKOTA provides a flexible interface between analysis codes and iterative systems analysis methods [11]. Besides, DAKOTA is a very powerful tool that allows performing uncertainty quantification with sampling and sensitivity/variance analysis as well as a variety of more applications. The features implemented in DAKOTA lead to improved designs and system performance in earlier stages which may reduce development time and cost.

JAGUAR, which stands for JAVa GUI for Applied Research, is a graphical wizard program which parses a DAKOTA input specification and serves as a graphical user interface (GUI) providing both graphical and text representations of the problem setup for DAKOTA studies afterwards [12]. Basically, JAGUAR is a friendly user interface that helps the user to introduce the data and calls DAKOTA for calculations.

For this specific uncertainty and sensitivity analysis, the studied input variables are the following seven neutronic parameters: diffusion coefficient which determines the leakage for thermal and fast group (*Diff1* and *Diff2*), scattering cross-section (*SigR*) which determines the moderation, absorption cross-section for both groups (*SigA1* and *SigA2*), and neutrons per fission multiplied by fission cross section which determines the rate of fission power release for both groups as well (*NuSigF1* and *NuSigF2*). The sample size and the selected sample methods and distributions were discussed previously. The described input file information is summarized in Table 1.

After setting up the input model file, the perturbation matrix file is generated. Both processes are part of the so-called *prerun* process in Jaguar. The size of the generated matrix is equal to the sample size multiply by the number of input model variables (i.e.,  $146 \times 7$ ) and each matrix element represents a perturbation parameter. The matrix file is used for modifying the cross-section sets by multiplying the 7 input model variables by the obtained perturbations. Each sample has a corresponding set of perturbations so it means that the number of simulations must be equal to the sample size. Even though, the REA analysis is performed by the coupled system RELAP5-PARCS, the cross-sectional sets with the uncertainty perturbations are only used by PARCS.

Once the 146 simulations, with the corresponding perturbations, are performed, nonparametric statistical methods are applied for studying the influence of the uncertainty on the macroscopic neutronic information (*postrun* process). Moreover, the selected output model variables for the

TABLE 2: Values of  $\beta_{\text{eff}}$  and ejected control rod reactivity worth.

Case	$\beta_{\text{eff}}$	Control rod reactivity worth (pcm/\$)	Coords./bank
ARI	0.0052775	1057.8/2.0043581	14-10/5

TABLE 3: Sequence of the events during the simulated transient.

Time	Event
0 s	Start of simulation
2.0 s	The control rod with maximum reactivity worth begins to withdraw
2.1 s	The control rod with maximum reactivity worth is fully extracted
500 s	End of simulation

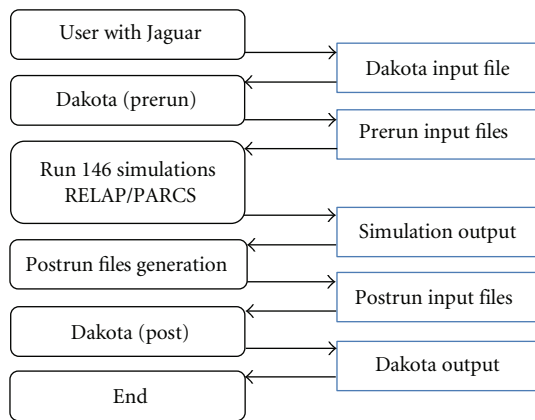


FIGURE 2: DAKOTA-Jaguar followed methodology.

uncertainty and sensitivity analysis are reactor power, total reactivity, and enthalpy. During the postrun process, the prerun input files generated by Jaguar and the perturbation matrix file are used. However, the matrix has to be modified by adding an extra column which includes the required information for the performed sensitivity analysis. Figure 2 summarizes the followed procedure using DAKOTA-Jaguar computer package.

The modification of the matrix is one of the main parts of the sensitivity analysis and it can be performed following two different approaches. The first one is based on maximum values so the extra column contains the maximum value for each output variable (power, enthalpy, or reactivity) for a given case. The second approach is based on the time step values and it has been repeated three times, one for each output variable. The extra column contains the desired output variable value for each time step for a given case. Furthermore, for this second approach, some interpolations may be required since not all the simulations have the same time steps.

This paper describes the two approaches and the sensitivity analysis performed based on them. Henceforth, the first approach will be named as scalar sensitivity analysis and the second approach as index-dependent sensitivity analysis.

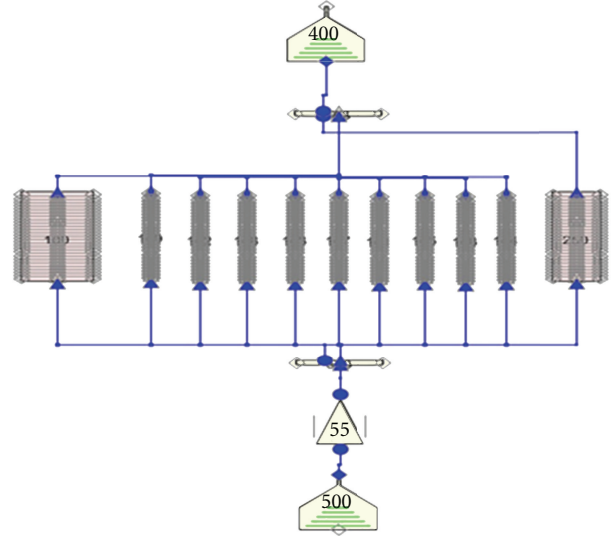


FIGURE 3: SNAP representation of the RELAP5 model.

## 4. Model Description

The reactor core contains 157 fuel elements. Each fuel element has 264 fuel rods, 24 guide tubes, and 1 tube for the instrumentation. Therefore, the core has been modelled with 157 thermalhydraulic flow channels, with a one-to-one correspondence with the fuel elements. The initial Hot zero power (HZP) steady-state conditions are: temperature equals to 565.58 K, initial density of 740.74 kg/m<sup>3</sup>, and a total inlet mass flow rate through the core of 13301 kg/s which is distributed among all the channels depending on the cross-sectional area. The transient is started by the ejection of a control rod with the maximum reactivity worth.

RELAP5 is the selected system code for modelling the 157 thermalhydraulic channels, which are connected with branches (*BRANCH*), and the by-pass which is modelled as an independent channel (see Figure 3). The inlet and the outlet boundary conditions are modelled as a time-dependent volume (*TMDPVOL*) and a time-dependent junction (*TMDPJUN*) respectively, as shown in Figure 3.

Radially, the core is divided into 21.504 cm × 21.504 cm cells (with a one-to-one correspondence between the cells and the fuel assemblies) plus a radial reflector. In total, there are 157 fuel assemblies plus 64 reflector assemblies. Axially, the core is divided into 26 layers (24 fuel layers plus top and bottom reflector) with a height of 15.24 cm each. The total active core height is 365.76 cm.

The neutronic nodal discretization consists of 157 × 24 active nodes. In addition, 13 different types of fuel elements (including one to represent the reflector), with 291 different neutronic compositions, are considered. The

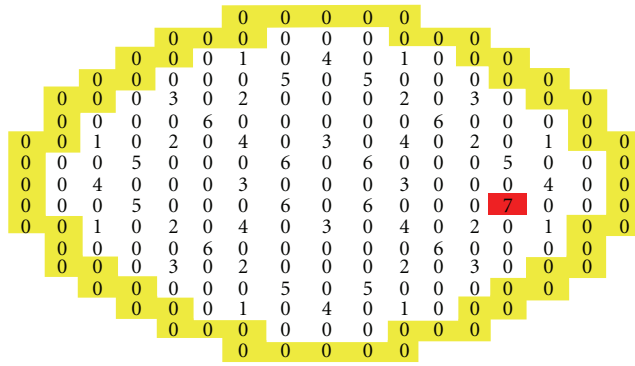


FIGURE 4: Control rod banks configuration.

neutronic model uses two prompt and six delayed neutron groups. Moreover, zero-flux at the outer reflector surface is considered as boundary conditions for the neutron diffusion equation and the decay heat model is activated.

The control rods are grouped in 6 banks which initially all are fully inserted. In a REA simulation, one of the main parameters that needs to be determined is the control rod with the maximum reactivity worth. Table 2 shows the coordinates and bank which correspond to the maximum reactivity worth control rod. Those results have been obtained using SIMULATE3.

As seen in Table 2, the control rod with the maximum reactivity worth corresponds to bank 5 at the location 14–10. It means that this is the selected rod for being ejected during the transient. Figure 4 represents the control rod banks and the ejected rod, the selected bank is renamed as bank 7.

The transient is started by the ejection of the rod 14–10 which is fully extracted in 0.1 s. The transient is simulated following the sequence of the events showed in Table 3.

## 5. Results

Recalling what was discussed previously, the sample size which guarantees double tolerance limits with a 95% of uncertainty and with 95% of statistical confidence for the output variables is equal to 146. The uncertainty and sensitivity analysis is performed assuming uniform distribution, on one hand, and normal distribution with three different deviations (0.1%, 0.5%, and 1%) on the other hand. Both cases have been simulated using Random and LHS sampling methods.

**5.1. Scalar Sensitivity Analysis.** Figures 5 and 6 represent the Partial rank correlation coefficients for the analysed case. From the point of view of the sensitivity analysis, the scalar sensitivity for the maximum power, enthalpy, and reactivity shows that the fast diffusion coefficient (1), the scattering cross-section (3), and both neutrons per fission multiplied by fission cross-section (6 and 7) have the highest influence on the uncertainties for all output variables. Moreover, the influence of absorption cross-sections and thermal diffusion coefficient could be neglected. Those extracted conclusions can be extended to all the cases performed.

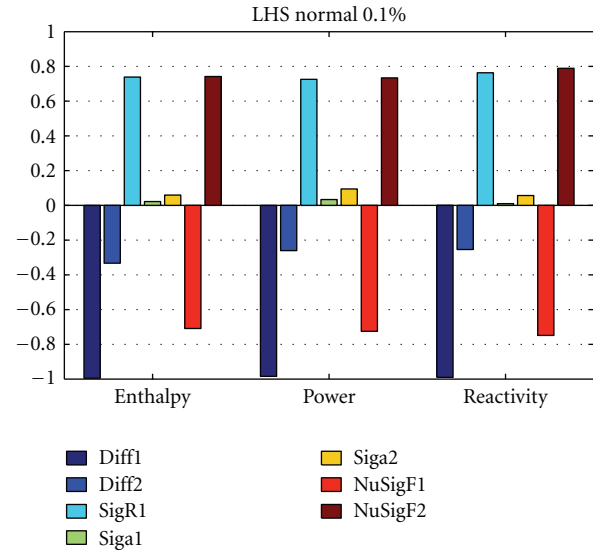


FIGURE 5: Partial rank correlation coefficient for maximum power, maximum enthalpy, and maximum reactivity for LHS normal 0.1% case (1: *Diff1*, 2: *Diff2*, 3: *SigR1*, 4: *SigA1*, 5: *SigA2*, 6: *NuSigF1*, 7: *NuSigF2*).

For simplicity, it has been only presented the comparison between the sampling methods for the normal PDF. In case of uniform PDF, the results are similar to normal PDF but with partial rank correlation slightly increased, that is, all output parameters are more sensitive with respect to input variables uncertainty. In next figures, it is seen that the fast absorption cross-section (*SigA1*) is positive for LHS method (Figure 5) and negative for the random method (Figure 6). Considering the sample size used (146) and the proximity of the mentioned cross-section, the sign change could be due to statistical fluctuations.

Figure 7 shows the scalar sensitivity analysis for the scattering cross-section (*SigR1*). It is shown that the use of the Uniform PDF to quantify the uncertainty of the input variables increases the sensitivity of a given output variable with respect to a specific input variable. The partial correlation coefficient statistically quantifies the influence of one variable, removing the effect of the rest, and, in this case, Figure 7 shows that assigning equal probability to the range of uncertainty of the variable (uniform distribution) increases the correlation coefficient, since the sampling results in a wider variation across the range compare to a normal PDF. Thus, Figure 7 shows that when normal PDF with LHS is used, the influence of the scattering cross-section is almost constant despite of the dispersion on the normal PDF, since the sampling variation tends to be concentrated around the mean of the normal distribution. Conversely, for Random sampling method, it is shown an increasing trend with the increase of the perturbation deviation. The same trends can be seen on other cross-sectional parameters.

**5.2. Index-Dependent Sensitivity Analysis.** The index-dependent sensitivity analysis for normal PDF and the two sampling methods are presented in this subsection. For the

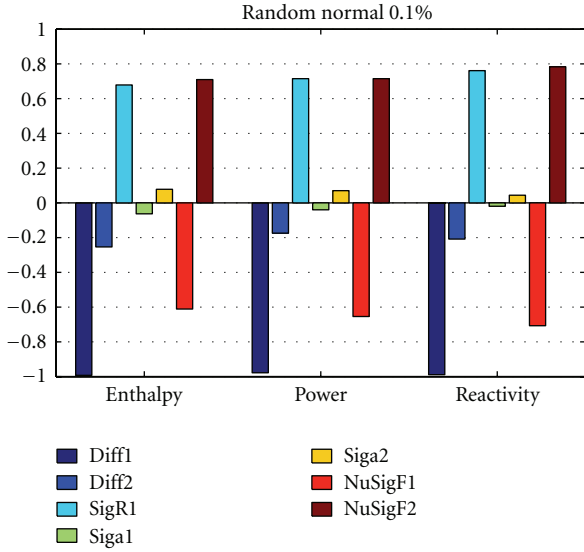


FIGURE 6: Partial rank correlation coefficient for maximum power, maximum enthalpy, and maximum reactivity for random normal 0.1% case (1: *Diff1*, 2: *Diff2*, 3: *SigR1*, 4: *SigA*, 5: *SigA2*, 6: *NuSigF1*, 7: *NuSigF2*).

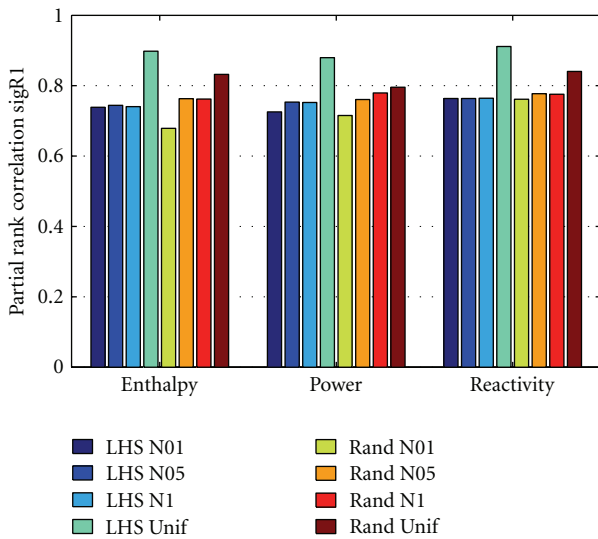


FIGURE 7: Scalar sensitivity of the scattering cross-section for all simulated cases.

particular case in which the number of runs is equal to 146, critical values for Spearman’s coefficient are  $r_s = \pm 0.16$ ; whether the correlation exceeds these values, then the parameter is influential.

First the results of Partial rank correlation coefficient (PRCC) for the output variable Power are presented. As shown in Figures 8 and 9, the most sensitive parameter is the fast diffusion coefficient (*Diff1*) with mostly a strong positive influence on the power. This is followed by the fast fission (*NuSigF1*), the scattering (*SigR1*), and the thermal fission (*NuSigF2*) cross-section, all of them with a similar absolute influence. The difference lies on the positive influence of

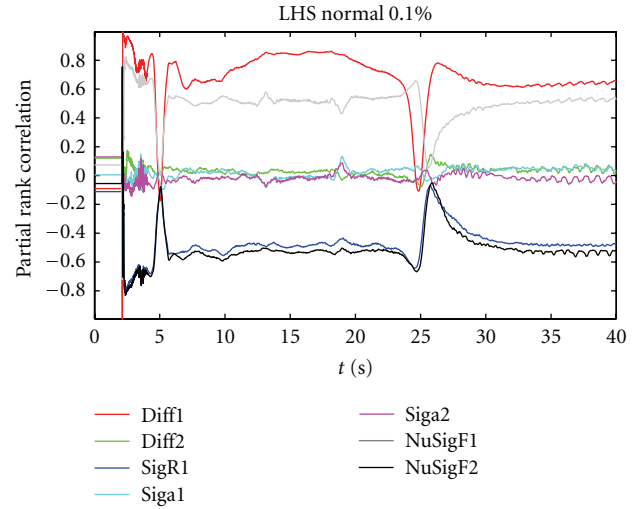


FIGURE 8: Partial rank correlation coefficient for LHS normal 0.1%, output variable : Power.

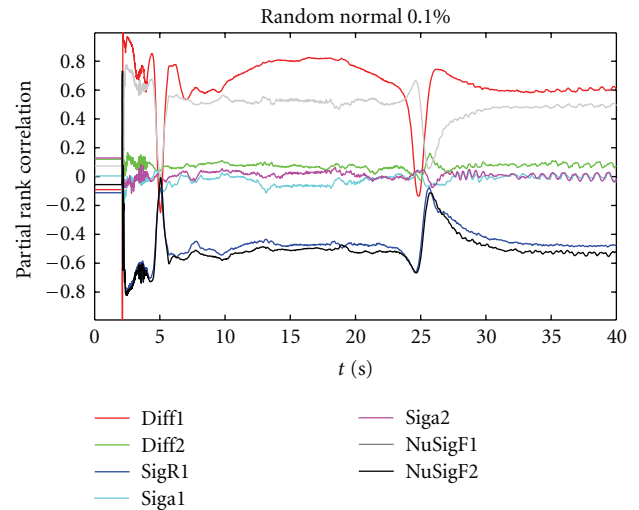


FIGURE 9: Partial rank correlation coefficient random normal 0.1%, output variable : power.

*NuSigF1* on the power and negative influence of the other two cross-sections.

As seen, there are changes in the sensitivities of these four neutronic parameters once the insertion of positive reactivity has occurred. Also, the sensitivities change slightly to reach stability when the rods have already been extracted leading to their final value, corresponding to the sensitivity of those values for the reached steady state. All these results and conclusions can be extended to the random sampling normal distribution with 0.1% deviation case as seen in Figure 9. The results for the uniform distribution are similar for those obtained for the normal PDF with 0.1% deviation.

Figure 10 shows the results for normal distribution with 0.5% deviation and LHS sample method. The most sensitive parameters remain unchanged. Furthermore, the values are smoother than in the 0.1% standard deviation case. The

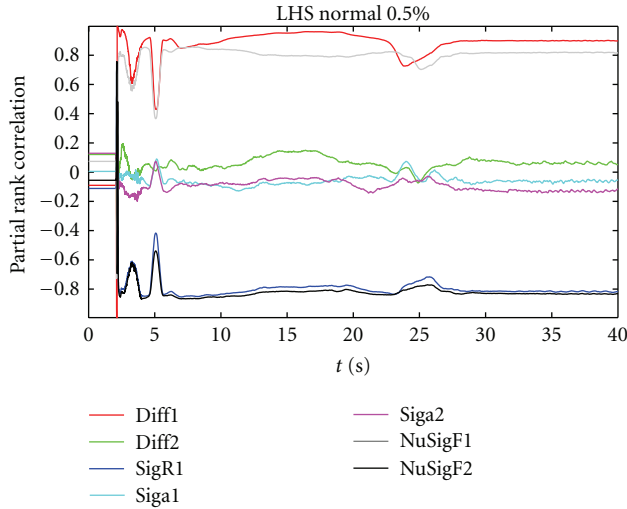


FIGURE 10: Partial Rank Correlation Coefficient LHS Normal 0.5%, output variable : Power.

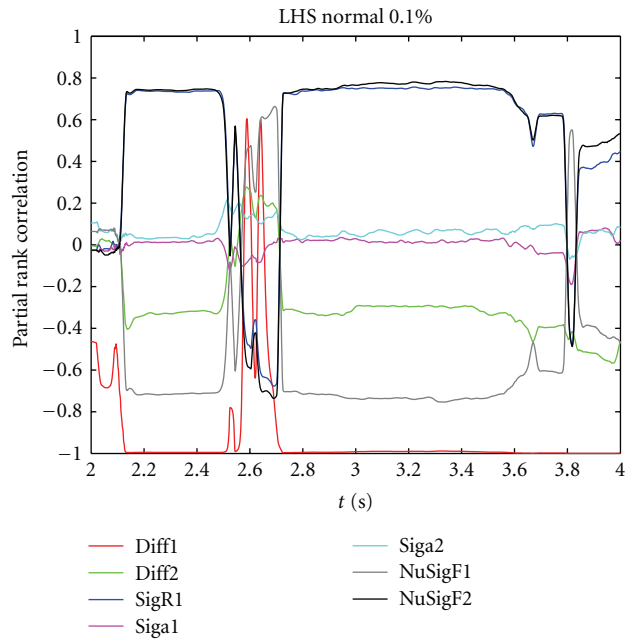


FIGURE 11: Partial rank correlation coefficient LHS normal 0.1%, output variable : enthalpy.

results for the 1% deviation cases are not shown in this paper because of their similarity to the 0.5% deviation results.

In Figure 11, results of PRC coefficient for the output variable enthalpy are presented. Since these results have few abrupt changes, and for the sake of simplicity, a zoom in time axis has been performed. The extracted conclusions are similar to those obtained for the power. The most sensitive parameters are as shown for the power case. Increasing the deviation, the results are smoother. Using uniform distribution, the input parameters become more sensitive.

In Figure 12, results of PRC coefficient for the output variable reactivity are presented. Again, the same conclusions

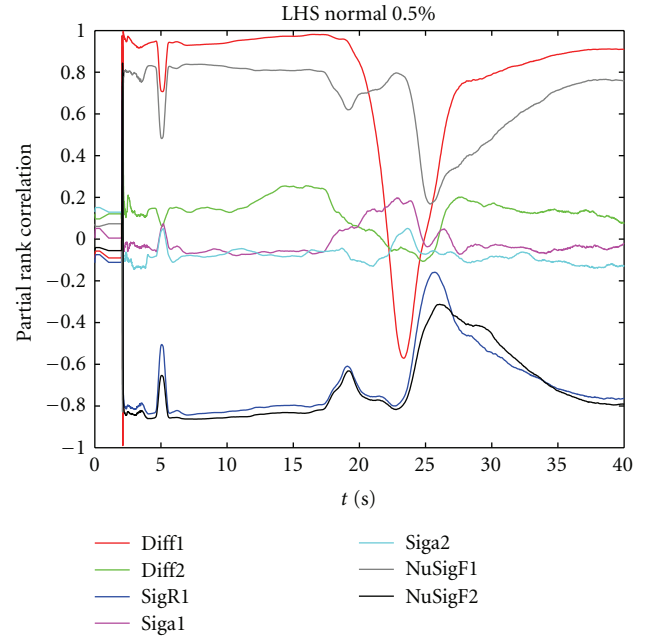


FIGURE 12: Partial rank correlation coefficient LHS normal 0.5%, output variable : reactivity.

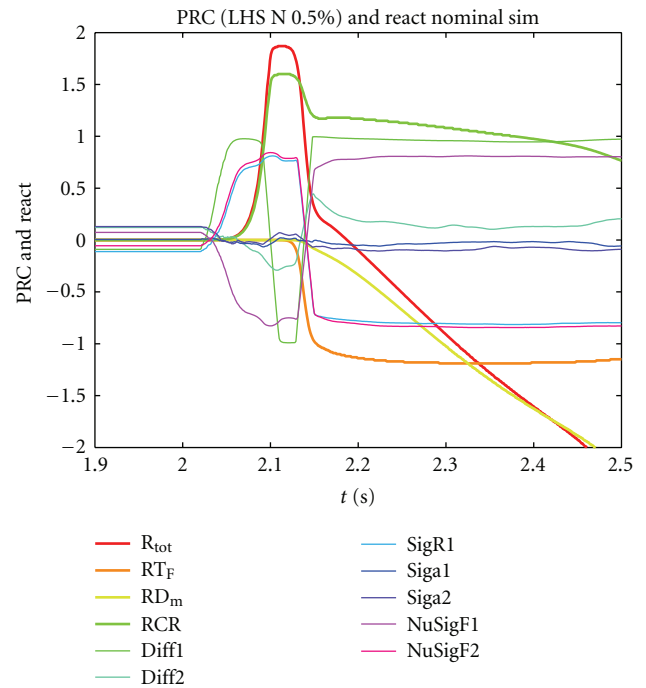


FIGURE 13: PRC coefficient related to the reactivity and the reactivities.

can be withdrawn, and the most sensitive parameters have the same sign as in the power case.

A final comment is needed with respect to the PRC coefficient variations. All output variables show an abrupt variation in PRC values at time 2 and around 25 seconds. As expected, the variation at time 2 s is due to the rod

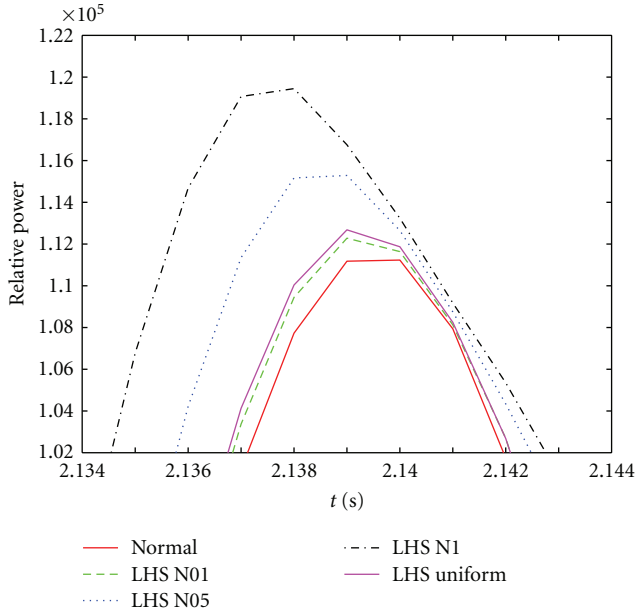


FIGURE 14: Power upper tolerance limit (UTL) for LHS sampling method.

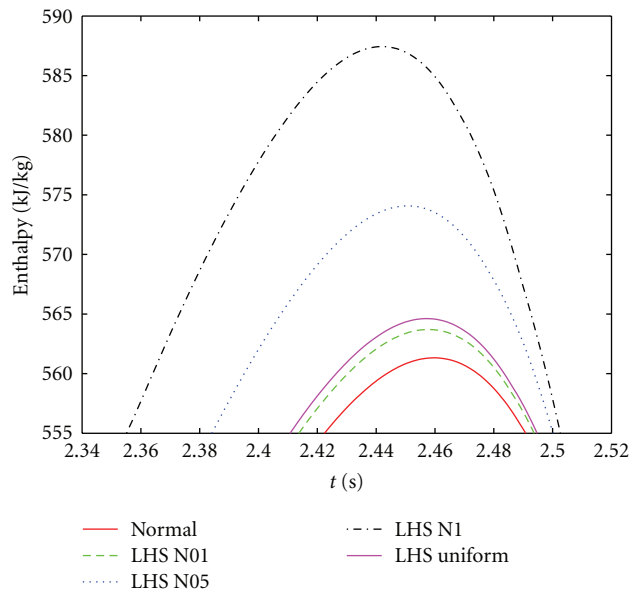


FIGURE 15: Enthalpy upper tolerance limit (UTL) for LHS sampling method.

ejection, this variation expands its effect until time 6 s, and then a plateau is reached. The variation at time 25 s could be explained as follows: the PRC is a relative magnitude, so when all input variables are almost constant, a small variation in a thermalhydraulic or neutronic variable could produce an important relative change in the PRC.

The effect of the rod ejection and the reactivity variation are explained in Figure 13. This figure depicts the total reactivity and its decomposed contributions (Doppler, moderator density and control rod reactivities). As expected,

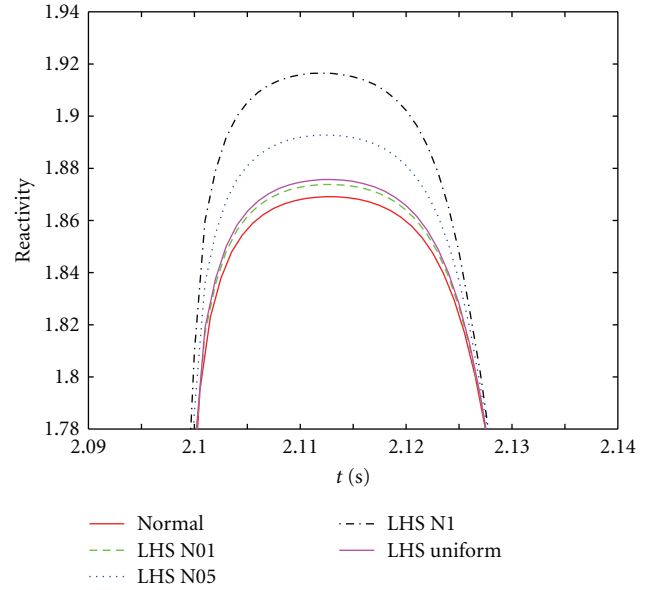


FIGURE 16: Reactivity upper tolerance limit (UTL) for LHS sampling method.

the rod ejection at time 2 seconds implies a fast positive reactivity insertion which is immediately compensated by the Doppler effect (broadening of absorption cross-sections) and a decrease in the moderator (liquid and gas) density. Following the rod ejection, the moderator density reactivity contributes the most to the total reactivity (as negative reactivity).

Figure 13 also shows the PRC coefficient related to the reactivity and the reactivities themselves. It can be seen that fast diffusion coefficient gains influence just after the rod ejection (2 s) and before the insertion of positive reactivity (2.1 s). This phenomenon is due to the loss of the neutron isotropic distribution inside the reactor. Fast diffusion factor maintains its importance (in absolute value). The reason for the change of the fast diffusion sign is the alteration in neutron production due to moderator density and fuel temperature variation (power increase and Doppler effect).

When Doppler reactivity becomes important (2.15 s), absorption parameters increase their influences and fission parameters have opposite tendency. This effect could be explained as follows: the power increases as a consequence of the rod ejection, then the fuel and moderator temperature rise. This is followed by a reduction in moderator density, hence, moderation, and the multiplication factor decrease.

**5.3. Uncertainty Analysis.** From the point of view of the uncertainty analysis, the results demonstrate that deviations about 0.1% have the smallest influence on the output variables of interest as expected. Figure 14 shows that both LHS and random samplings with normal distribution of 0.1% standard deviation reach a similar peak power at the approximate same time. As a result of the increasing of the uncertainty, there is a slight rise in the maximum output value. However, there is a spread in the time at which the

peak power (and enthalpy and reactivity, see Figures 15 and 16) occurs. Moreover, the intervals of tolerance are greater in normal than in Uniform distributions, so the use of normal PDF provides more conservative results than uniform PDF.

Finally, similar conclusions can be extracted for the uncertainty in power, enthalpy, and reactivity for Random sampling method.

## 6. Concluding Remarks

This paper has described a Rod Ejection Accident (REA) simulated using the coupled code RELAP5/PARCSv2.7 with a perturbation on the cross-sectional sets in order to determine the response of the computational system to uncertainties in the macroscopic neutronic information.

For all cases, the most influential uncertainties obtained by the scalar sensitivity analysis were the fast diffusion coefficient (1) with a positive influence on power, the scattering cross section (3) and both fission cross-sections (6 and 7) with mixed positive/negative influence. The absorption cross-sections together with the thermal diffusion coefficient could be neglected regarding the influence for the selected output variables. Therefore, the performed sensitivity analyses have shown that the influence of the uncertainties is not dependent on the selected sampling method.

The index-dependent sensitivity analysis showed the same influence for the different neutronic parameters. Moreover, there were sign changes in the most important neutronic parameters which are produced once the insertion of negative reactivity has been occurred. However, in all cases the tendency is to reach a steady-state condition for “long” time simulations. Regarding the sampling methods used, there were no significant differences. Furthermore, deviations greater than 0.1% showed smoother behavior; however, perturbations with standard deviations greater than 1% could lead to a run failure due to the high heat flux generation and consequently properties can be overpassed in steam tables.

## Conflict of Interests

The authors of this paper have no conflict of interests to declare.

## Acknowledgments

This work has been partially supported by the Spanish Ministerio de Educación y Ciencia under Project ENE2008-02669, the Generalitat Valenciana under Project ACOMP/2009/058, and the Universitat Politècnica de València under Project PAID-05-09-4285.

## References

- [1] O. Roselló, *Desarrollo de una metodología de generación de secciones eficaces para la simplificación del núcleo de reactores de agua ligera y aplicación en códigos acoplados neutrónicos termohidráulicos [Ph.D. thesis]*, Universitat Politècnica de València, 2004.
- [2] V. Kreinovich and S. A. Ferson, “A new Cauchy-based black-box technique for uncertainty in risk analysis,” *Reliability Engineering and System Safety*, vol. 85, no. 1–3, pp. 267–279, 2004.
- [3] J. Juanas, R. Macián, F. Áncel, T. Barrachina, R. Miró, and G. Verdú, “Uncertainty and sensitivity analysis in the neutronic parameters generation for BWR and PWR coupled thermalhydraulic-neutronic simulations,” in *International Conference on Nuclear Energy for New Europe*, Portorož, Slovenia, September 2010.
- [4] J. C. Helton and F. J. Davis, “Latin hypercube sampling and the propagation of uncertainty in analyses of complex systems,” *Reliability Engineering and System Safety*, vol. 81, no. 1, pp. 23–69, 2003.
- [5] H. G. Glaeser, “Uncertainty evaluation of thermal-hydraulic code results,” in *Proceedings of the International Meeting on Best Estimate Methods in Nuclear Installation Safety Analysis (BE '00)*, Washington, DC, USA, November 2000.
- [6] S. S. Wilks, *Mathematical Statistics*, John Wiley & Sons, 1962.
- [7] S. Hong, Oh, and Kim, “Generic application of Wilks tolerance limits evaluation approach to nuclear safety,” in *OECD/CSNI Workshop on Best Estimate Methods and Uncertainty Evaluations*, Barcelona, Spain, 2011 November.
- [8] R. L. Iman and W. J. Conover, “A distribution-free approach to inducing rank correlation among input variables,” *Communications in Statistics B*, vol. 11, no. 3, pp. 311–334, 1982.
- [9] M. D. McKay, R. J. Beckman, and W. J. Conover, “A comparison of three methods for selecting values of input variables in the analysis of output from a computer code,” *Technometrics*, vol. 21, no. 2, pp. 239–245, 1979.
- [10] A User’s Guide to Sandia’s Latin Hypercube Sampling Software: LHS UNIX Library/Stand-alone Version.
- [11] DAKOTA, A Multilevel Parallel Object-Oriented Framework for Design Optimization, Parameter Estimation, Uncertainty Quantification, and Sensitivity Analysis. Version 5.2 User’s Manual.
- [12] DAKOTA Jaguar 2.1 User’s Manual.

## Research Article

# Perturbation-Theory-Based Sensitivity and Uncertainty Analysis with CASMO-4

**Maria Pusa**

*VTT Technical Research Centre of Finland, P.O. Box 1000, VTT 02044, Finland*

Correspondence should be addressed to Maria Pusa, maria.pusa@vtt.fi

Received 25 June 2012; Accepted 5 October 2012

Academic Editor: Kostadin Ivanov

Copyright © 2012 Maria Pusa. This is an open access article distributed under the Creative Commons Attribution License, which permits unrestricted use, distribution, and reproduction in any medium, provided the original work is properly cited.

The topic of this paper is the development of sensitivity and uncertainty analysis capability to the reactor physics code CASMO-4 in the context of the UAM (Uncertainty Analysis in Best-Estimate Modelling for Design, Operation, and Safety Analysis of LWRs) benchmark. The sensitivity analysis implementation is based on generalized perturbation theory, which enables computing the sensitivity profiles of reaction rate ratios efficiently by solving one generalized adjoint system for each response. Both the theoretical background and the practical guidelines for modifying a deterministic transport code to compute the generalized adjoint solutions and sensitivity coefficients are reviewed. The implementation to CASMO-4 is described in detail. The developed uncertainty analysis methodology is deterministic, meaning that the uncertainties are computed based on the sensitivity profiles and covariance matrices for the uncertain nuclear data parameters. The main conclusions related to the approach used for creating a covariance library compatible with the cross-section libraries of CASMO-4 are presented. Numerical results are given for a lattice physics test problem representing a BWR, and the results are compared to the TSUNAMI-2D sequence in SCALE 6.1.

## 1. Introduction

The topic of this paper is the development of sensitivity and uncertainty analysis capability to the reactor physics code CASMO-4 [1] in the context of the UAM (Uncertainty Analysis in Best-Estimate Modelling for Design, Operation and Safety Analysis of LWRs) benchmark [2]. At VTT, CASMO-4 is the standard tool for lattice physics calculations, and therefore it was a natural choice as the development platform for a sensitivity and uncertainty calculation system for the pin cell and fuel assembly exercises in the benchmark.

Sensitivities with respect to uncertain parameters can be computed efficiently by utilizing the adjoint system of the criticality equation. The propagated parameter uncertainty can then be calculated deterministically by the Sandwich rule by combining the sensitivity profiles with the covariance matrices of the parameters. As a first step, classical perturbation theory (CPT) was implemented to CASMO-4 to enable the computation of critical eigenvalue sensitivities with respect to nuclear data parameters. In this context, a methodology was devised for processing the covariance matrices from SCALE 6 [3] to become compatible with the

cross-section libraries of CASMO-4 to enable uncertainty analysis. This work has been reported in detail in [4]. Recently, generalized perturbation theory (GPT) has been added to the code as a new feature. This enables performing sensitivity analysis for responses that can be presented as reaction rate ratios. In this framework, one generalized adjoint system needs to be solved for each response, after which the response sensitivity profiles for all parameters of interest can be computed in an efficient manner.

This paper is organized as follows. Section 2 reviews the theoretical background for sensitivity and uncertainty analysis based on generalized perturbation theory, and Section 3 focuses on the implementation to CASMO-4. In Section 3.1, the computation of generalized adjoint solutions is considered and practical guidelines are presented for modifying a deterministic transport code to solve the adjoint problems needed in sensitivity analysis. Section 3.2 concerns the computation of sensitivity and uncertainty profiles. Finally, in Section 4, numerical results are presented for a lattice physics test problem representing a BWR, and they are compared to the TSUNAMI-2D sequence in SCALE 6.1.

## 2. Theoretical Background

The purpose of sensitivity analysis is to study how sensitive a mathematical model is to perturbations in its uncertain parameters. The target of uncertainty analysis is to estimate how the uncertainty in these parameters is propagated to a response dependent on the mathematical model under consideration. In this work the mathematical model is the neutron transport eigenvalue problem, which can be written in operator form as

$$\mathbf{A}\Phi = \frac{1}{k}\mathbf{B}\Phi, \quad (1)$$

where  $\Phi \in H_\Phi$  is the neutron flux,  $H_\Phi$  is a Hilbert space, and  $k$  is the multiplication factor. The uncertain parameters consist of nuclear data parameters and they are denoted by the vector  $\sigma \in E_\sigma$ . It should be noted that both the continuous-energy criticality equation and the various systems derived from it in numerical computations can be written in the form of (1).

*2.1. Sensitivity Analysis.* The object of local sensitivity analysis is to determine how the response  $R$  depends on the uncertain parameters in the vicinity of their best-estimate values. In this work, the responses under consideration include homogenized assembly parameters and the multiplication factor, whereas the uncertain parameters are neutron cross-sections. When considering the continuous-energy eigenvalue problem, the cross-sections are functions of energy and location, and the appropriate derivative is the functional directional derivative called the Gâteaux variation [5]. It follows that the sensitivity of  $R$  with respect to the perturbation  $\mathbf{h} = [\delta\Phi, \delta\sigma] \in D = H_\Phi \times E_\sigma$  at the point  $\hat{\mathbf{e}} = [\hat{\Phi}, \hat{\sigma}] \in D$  may be defined as

$$\delta R(\hat{\mathbf{e}}; \mathbf{h}) = \lim_{t \rightarrow 0} \frac{R(\hat{\mathbf{e}} + t\mathbf{h}) - R(\hat{\mathbf{e}})}{t}. \quad (2)$$

When the parameters  $\sigma$  are perturbed, also the solution  $\Phi$  is affected and therefore the computation of the sensitivity  $\delta R(\hat{\mathbf{e}}; \mathbf{h})$  requires that the perturbation  $\delta\Phi$  is known. In principle,  $\delta\Phi$  can be computed to first order from the following *forward sensitivity system*:

$$\begin{aligned} \delta \mathbf{A}(\hat{\mathbf{e}}; \mathbf{h}) &= -\frac{1}{k^2} \delta k(\hat{\mathbf{e}}; \mathbf{h}) \mathbf{B}\Phi + \frac{1}{k} \delta \mathbf{B}(\hat{\mathbf{e}}; \mathbf{h}) \\ \Leftrightarrow \mathbf{A}'_\sigma(\hat{\mathbf{e}}) \delta \sigma + \mathbf{A}(\hat{\mathbf{e}}) \delta \Phi &= -\frac{1}{k^2} \delta k(\hat{\mathbf{e}}; \mathbf{h}) \mathbf{B}\Phi \\ &\quad + \frac{1}{k} \mathbf{B}'_\sigma(\hat{\mathbf{e}}) \delta \sigma + \frac{1}{k} \mathbf{B}(\hat{\mathbf{e}}) \delta \Phi, \end{aligned} \quad (3)$$

which can be derived by taking the Gâteaux variation of system (1) with respect to a perturbation  $\mathbf{h}$  on both sides. However, when computing several sensitivities, this approach would require the repetitive solving of (3).

Fortunately, the sensitivities can be computed more efficiently by exploiting the adjoint of (1), which is defined as the system that satisfies the following relation: (In some

cases the adjoint relation needs to be written in the form  $\langle \mathbf{A}\Phi + (1/k)\mathbf{B}\Phi, \Psi \rangle = \langle \Phi, \mathbf{A}^*\Psi + (1/k)\mathbf{B}^*\Psi \rangle + [\mathbf{P}(\Psi, \Phi)]_{\mathbf{x} \in \partial\Omega}$ , where  $[\mathbf{P}(\Psi, \Phi)]_{\mathbf{x} \in \partial\Omega}$  is a bilinear form associated with the system. We will only consider cases where it is straightforward to force this term to vanish.)

$$\left\langle \mathbf{A}\Phi - \frac{1}{k}\mathbf{B}\Phi, \Psi \right\rangle = \left\langle \Phi, \mathbf{A}^*\Psi - \frac{1}{k}\mathbf{B}^*\Psi \right\rangle, \quad (4)$$

where the brackets  $\langle \cdot, \cdot \rangle$  denote an inner product. When considering the continuous-energy criticality equation, it is customary to employ the  $L^2$  inner product [6, 7]. The solution to the adjoint problem

$$\left( \mathbf{A}^* - \frac{1}{k}\mathbf{B}^* \right) \Psi = 0 \quad (5)$$

is called the *fundamental adjoint*. Physically, the solution to this system can be interpreted to represent the average contribution, that is, importance of a neutron to the multiplication factor. Interestingly, the adjoint system of (5) can be derived solely based on this physical interpretation [8]. Like the neutron flux, the fundamental adjoint has an arbitrary normalization, and the concept of importance should be understood in relative terms. Therefore, the value  $\Psi(\mathbf{r}, \Omega, E)$  represents the importance of a neutron located at the point  $[\mathbf{r}, \Omega, E]$  compared to the importance of neutrons elsewhere in the phase space [9]. Based on this physical reasoning, it can be deduced that the fundamental adjoint must always be nonnegative.

By utilizing (4) and (5), it is straightforward to obtain the following expression for the relative sensitivity of the multiplication factor with respect to a perturbation  $\delta\sigma$  (For derivation, see for example, [4, 10]):

$$\frac{\delta k(\hat{\mathbf{e}}; \mathbf{h})}{k} = -\frac{\langle (\mathbf{A}'_\sigma(\hat{\mathbf{e}}) - (1/k)\mathbf{B}'_\sigma(\hat{\mathbf{e}})) \delta \sigma, \Psi \rangle}{\langle (1/k)\mathbf{B}\Phi, \Psi \rangle}. \quad (6)$$

This equation is known in reactor physics as *classical perturbation theory*. In addition, the adjoint system can be utilized in the sensitivity analysis of the eigenvalue problem for other responses fulfilling the following properties. Firstly, the response  $R$  must be Fréchet-differentiable with respect to  $\Phi$ , in which case we can write

$$\delta R(\hat{\mathbf{e}}; \mathbf{h}) = R'_\sigma(\hat{\mathbf{e}}) \delta \sigma + \langle \nabla_\Phi R(\hat{\mathbf{e}}), \delta \Phi \rangle_\Phi. \quad (7)$$

In addition, the response's Fréchet derivative  $\nabla_\Phi R$  (also called gradient) must be orthogonal to the forward solution

$$\langle \nabla_\Phi R, \Phi \rangle = 0. \quad (8)$$

When these assumptions are fulfilled, the *generalized adjoint* corresponding to the response  $R$  can be defined as the solution to the following inhomogeneous system:

$$\left( \mathbf{A}^* + \frac{1}{k}\mathbf{B}^* \right) \Gamma = \frac{\nabla_\Phi R}{R}. \quad (9)$$

Notice that in the previous equation the eigenvalue  $k$  is fixed to correspond to the solution of (1) and therefore the operator  $\mathbf{A}^* + (1/k)\mathbf{B}^*$  is singular, which necessitates (8) in

order for the solution  $\Gamma$  to exist. Also, when a solution  $\Gamma_0$  to (9) exists, there exists an infinite amount of solutions of the form

$$\Gamma = \Gamma_0 + a\Psi, \quad a \in \mathbb{R}. \quad (10)$$

In this case, it is possible to choose a solution that is orthogonal to the (forward) fission source. This particular solution can be written as

$$\begin{aligned} \Gamma_p &= \Gamma_0 - \frac{\langle \Gamma_0, \mathbf{B}\Phi \rangle}{\langle \Psi, \mathbf{B}\Phi \rangle} \Psi \\ &= \Gamma_0 - \frac{\langle \mathbf{B}^* \Gamma_0, \Phi \rangle}{\langle \mathbf{B}^* \Psi, \Phi \rangle} \Psi. \end{aligned} \quad (11)$$

We can now derive a practical expression for the response sensitivity with respect to a perturbation  $\delta\sigma$ :

$$\begin{aligned} \frac{\delta R(\hat{\mathbf{e}}, \mathbf{h})}{R} &= \frac{R'_\sigma(\hat{\mathbf{e}})\delta\sigma}{R} + \left\langle \frac{\nabla_\Phi R(\hat{\mathbf{e}})}{R}, \delta\Phi \right\rangle_\Phi \\ &\stackrel{(9)}{=} \frac{R'_\sigma(\hat{\mathbf{e}})\delta\sigma}{R} + \left\langle \left( \mathbf{A}^* + \frac{1}{k} \mathbf{B}^* \right) \Gamma, \delta\Phi \right\rangle_\Phi \\ &\stackrel{(4)}{=} \frac{R'_\sigma(\hat{\mathbf{e}})\delta\sigma}{R} + \left\langle \Gamma, \left( \mathbf{A} + \frac{1}{k} \mathbf{B} \right) \delta\Phi \right\rangle_\Phi \\ &\stackrel{(3)}{=} \frac{R'_\sigma(\hat{\mathbf{e}})\delta\sigma}{R} - \left\langle \Gamma, \left( \mathbf{A}'_\sigma(\hat{\mathbf{e}}) - \frac{1}{k} \mathbf{B}'_\sigma(\hat{\mathbf{e}}) \right) \delta\sigma \right\rangle_\Phi \\ &\quad - \frac{\delta k(\hat{\mathbf{e}}; \mathbf{h})}{k^2} \langle \Gamma, \mathbf{B}\Phi \rangle_\Phi \\ &= \frac{R'_\sigma(\hat{\mathbf{e}})\delta\sigma}{R} - \left\langle \Gamma_p, \left( \mathbf{A}'_\sigma(\hat{\mathbf{e}}) - \frac{1}{k} \mathbf{B}'_\sigma(\hat{\mathbf{e}}) \right) \delta\sigma \right\rangle_\Phi. \end{aligned} \quad (12)$$

This framework is often referred to as *generalized perturbation theory* when the response  $R$  is of the form:

$$R(\mathbf{e}) = \frac{\langle \Phi, \Sigma_1 \rangle}{\langle \Phi, \Sigma_2 \rangle}. \quad (13)$$

In this case, it is straightforward to show that (8) is satisfied and that  $R$  is Fréchet-differentiable, the relative gradient being

$$\frac{\nabla_\Phi R}{R} = \frac{\Sigma_1}{\langle \Phi, \Sigma_1 \rangle} - \frac{\Sigma_2}{\langle \Phi, \Sigma_2 \rangle}. \quad (14)$$

The generalized adjoint  $\Gamma(\mathbf{r}, \Omega, E)$  can be physically interpreted as the average contribution of an additional neutron at the phase space point  $[\mathbf{r}, \Omega, E]$  to the response under consideration. The generalized adjoint is normalized according to the value of the response. It should also be noticed that since an additional neutron may also reduce the value of the response, generalized adjoints can also have negative values. The gradient of the response may also be negative in some parts of the phase space.

In practice, the eigenvalue problem and the corresponding adjoint equations are solved numerically, which gives rise to some complications in the perturbation theory

formalism. Ideally, the discretizations should be performed in a consistent manner so that the respective adjoint relations are satisfied at all stages of the computation [5]. However, this is usually infeasible in reactor physics calculations, and therefore it is customary to take the eigenvalue problem discretized with respect to energy and direction as the starting point for sensitivity analysis. This issue is discussed in more detail in [4].

**2.2. Uncertainty Analysis.** The uncertainty of the uncertain parameters  $\sigma$  should be understood in terms of the Bayesian probability interpretation. In this framework, probability is defined as a subjective measure that characterizes the plausibility of various hypotheses. When estimating parameters, all knowledge about a parameter  $\sigma_j$  is assumed to be incorporated into its marginal probability distribution  $p(\sigma_j)$ . This distribution is defined so that the integral  $\int_a^b p(\sigma_j) d\sigma_j$  corresponds to the (Bayesian) probability that the value of  $\sigma_j$  belongs to the interval  $[a, b]$ . The distribution  $p(\sigma)$  can then be used to form an estimate for the parameters and their associated uncertainties. Usually, the mean value or the mode is chosen as the estimate for the parameters, whereas the covariance matrix of the distribution is chosen as the descriptive statistic for the uncertainty.

In the Bayesian formalism, the outcome of the uncertainty analysis should ideally be the full posterior distribution  $p(\mathbf{R})$ . However, determining  $p(\mathbf{R})$  analytically is usually extremely challenging and the distribution can only be estimated pointwise based on a simulation. In deterministic uncertainty analysis, the objective is not to form the entire distribution  $p(\mathbf{R})$ , but to compute an estimate for the covariance matrix  $\text{Cov}[\mathbf{R}]$  by linearizing the response  $\mathbf{R} \approx \mathbf{S}\sigma$ . Here  $\mathbf{S} \in \mathbb{R}^{J \times K}$  is the response vector sensitivity matrix,  $J$  is the number of responses, and  $K$  is the number of uncertain parameters. After linearizing the response, the covariance matrix can be computed simply using the identity

$$\text{Cov}[\mathbf{R}] \approx \text{Cov}[\mathbf{S}\sigma] = \mathbf{S} \text{Cov}[\sigma] \mathbf{S}^T, \quad (15)$$

known as the first-order uncertainty propagation formula or the *Sandwich rule*.

### 3. Implementation

**3.1. Computation of Generalized Adjoint Fluxes.** This section reviews the guidelines for modifying a deterministic transport solver to compute the adjoint solutions needed in generalized perturbation theory and describes the methodology used in the implementation to CASMO-4. As mentioned previously, the description on the implementation of classical perturbation theory to CASMO-4 has been recently published in [4], and therefore, in this paper, the emphasis is placed on the GPT-specific features.

As explained in Section 2.1, it is customary to take the energy- and direction-discretized system as the starting point for perturbation theory. In CASMO-4, the multigroup criticality equation is solved by the method of characteristics

assuming isotropic scattering. Therefore, the following system of equations may be taken as the forward problem:

$$\begin{aligned} & \mathbf{\Omega}_m \cdot \nabla \Phi^g(\mathbf{r}, \mathbf{\Omega}_m) + \Sigma^g \Phi^g(\mathbf{r}, \mathbf{\Omega}_m) \\ &= \frac{1}{4\pi} \sum_{h=1}^G \Sigma_s^{h-g} \phi^h(\mathbf{r}) + \frac{\chi_g}{4\pi k} \sum_{h=1}^G \bar{\nu} \Sigma_f^h \phi^h(\mathbf{r}), \quad (16) \\ & g = 1, \dots, G. \end{aligned}$$

In (16) the scalar flux is approximated by the quadrature formula

$$\phi^h(\mathbf{r}) = \sum_{m=1}^M \omega_m \Phi^h(\mathbf{r}, \mathbf{\Omega}_m). \quad (17)$$

In order to simulate an infinite lattice, the boundary conditions are often assumed to be reflective, that is,

$$\Phi(\mathbf{r}, \mathbf{\Omega}_m, E) = \Phi(\mathbf{r}, \mathbf{\Omega}'_m, E), \quad \mathbf{r} \in \Gamma, \mathbf{\Omega}_m \cdot \mathbf{n} < 0, \quad (18)$$

where  $\mathbf{\Omega}_m = \mathbf{\Omega}'_m - 2(\mathbf{n} \cdot \mathbf{\Omega}'_m)\mathbf{n}$  is the reflection direction. The inner product corresponding to this discretization can be defined in a consistent manner as

$$\langle \Phi, \Psi \rangle = \sum_{g=1}^G \sum_{m=1}^M \omega_m \int_D d^3\mathbf{r} \Phi^g(\mathbf{r}, \mathbf{\Omega}_m) \Psi^g(\mathbf{r}, \mathbf{\Omega}_m). \quad (19)$$

The adjoint system can now be written

$$\begin{aligned} & -\mathbf{\Omega}_m \cdot \nabla \Psi^g(\mathbf{r}, \mathbf{\Omega}_m) + \Sigma^g \Psi^g(\mathbf{r}, \mathbf{\Omega}_m) \\ &= \frac{1}{4\pi} \sum_{h=1}^G \Sigma_s^{g-h} \psi^h(\mathbf{r}) + \frac{\bar{\nu} \Sigma_f^g}{4\pi k} \sum_{h=1}^G \chi_h \psi^h(\mathbf{r}), \quad g = 1, \dots, G, \quad (20) \end{aligned}$$

with the boundary conditions

$$\Psi(\mathbf{r}, \mathbf{\Omega}_m, E) = \Psi(\mathbf{r}, \mathbf{\Omega}'_m, E), \quad \mathbf{r} \in \Gamma, \mathbf{\Omega}_m \cdot \mathbf{n} > 0. \quad (21)$$

It is straightforward to check that the systems (16) and (20) with their respective boundary conditions satisfy (4) with respect to the inner product defined by (19).

The generalized adjoint problem for a response of the form of (13) can now be written

$$\begin{aligned} & -\mathbf{\Omega}_m \cdot \nabla \Gamma^g(\mathbf{r}, \mathbf{\Omega}_m) + \Sigma^g \Gamma^g(\mathbf{r}, \mathbf{\Omega}_m) \\ &= \frac{1}{4\pi} \sum_{h=1}^G \Sigma_s^{g-h} \gamma^h(\mathbf{r}) + \frac{\bar{\nu} \Sigma_f^g}{4\pi k} \sum_{h=1}^G \chi_h \gamma^h(\mathbf{r}) \\ &+ \frac{\Sigma_1^g(\mathbf{r})}{\langle \Phi, \Sigma_1 \rangle} - \frac{\Sigma_2^g(\mathbf{r})}{\langle \Phi, \Sigma_2 \rangle}, \quad g = 1, \dots, G, \quad (22) \end{aligned}$$

where the generalized adjoint of the scalar flux has been denoted by  $\gamma^h(\mathbf{r})$ . As explained in Section 2.1, this system may have an infinite number of solutions, of which we wish to solve the one that satisfies

$$\langle \mathbf{B}^* \Gamma_p, \Phi \rangle = 0. \quad (23)$$

In deterministic transport solvers, the iteration for fixed source calculations is generally of the form

$$\mathbf{A} \Phi^{n+1} = \mathbf{B} \Phi^n + \mathbf{S}, \quad (24)$$

where  $\mathbf{S}$  is an external source. This iteration scheme with a fixed eigenvalue is also well suited for solving the generalized adjoint problem of (22), in which case the iteration takes the form

$$\mathbf{A}^* \Gamma^{n+1} = \frac{1}{k} \mathbf{B}^* \Gamma^n + \frac{\nabla \Phi R}{R}. \quad (25)$$

During the iteration, however, the convergence to the particular solution that is orthogonal to the fission source must be ensured. It is straightforward to show that if the initial guess for the generalized adjoint flux satisfies (23), this orthogonality property is preserved during the iteration. Firstly,

$$\begin{aligned} \langle \mathbf{A}^* \Gamma^{n+1}, \Phi \rangle &\stackrel{(25)}{=} \frac{1}{k} \langle \mathbf{B}^* \Gamma^n, \Phi \rangle + \left\langle \frac{\nabla \Phi R}{R}, \Phi \right\rangle \\ &\stackrel{(8)}{=} \frac{1}{k} \langle \mathbf{B}^* \Gamma^n, \Phi \rangle. \end{aligned} \quad (26)$$

On the other hand,

$$\begin{aligned} \langle \mathbf{A}^* \Gamma^{n+1}, \Phi \rangle &= \langle \Gamma^{n+1}, \mathbf{A} \Phi \rangle \stackrel{(1)}{=} \frac{1}{k} \langle \Gamma^{n+1}, \mathbf{B} \Phi \rangle \\ &= \frac{1}{k} \langle \mathbf{B}^* \Gamma^{n+1}, \Phi \rangle. \end{aligned} \quad (27)$$

Therefore, for each iteration  $n$ ,

$$\langle \mathbf{B}^* \Gamma^{n+1}, \Phi \rangle = \langle \mathbf{B}^* \Gamma^n, \Phi \rangle, \quad (28)$$

from which the result follows. In practice, however, due to round-off errors and the unavoidable inconsistencies in formulating the discretizations and adjoint relations, a refinement of the iteration scheme is necessary to guarantee that (23) remains satisfied [11]. A suitable procedure is to force the orthogonality of the solution with each outer iteration. In this case, in accordance with (11), the iteration takes the form

$$\mathbf{A}^* \Gamma^{n+1} = \frac{1}{k} \mathbf{B}^* \left( \Gamma^n - \frac{\langle \mathbf{B}^* \Gamma^n, \Phi \rangle}{\langle \mathbf{B}^* \Psi, \Phi \rangle} \Psi \right) + \frac{\nabla \Phi R}{R}. \quad (29)$$

Notice that this iteration scheme requires that the forward solution and the fundamental adjoint solution have been previously computed and that they are accessible during the iteration.

By comparing (29) with the forward problem of (16), it can be seen that if the forward system had an external source, the systems would be of the same form with the exception that the adjoint system is solved in the opposite direction. Therefore, if the transport solver does not rely on the assumption of the nonnegativity of the flux or the sources, relatively few modifications are needed to transform the solver to also compute the generalized adjoint functions. For example, the method of characteristics, used in CASMO-4, does not require that the solution or the sources are non-negative. In this case, the following operations need to be performed *before* the adjoint calculation [10].

- (1) Transpose the scattering matrix.
- (2) Interchange the vectors  $\bar{\nu}\sigma_f$  and  $\chi$ .
- (3) Invert the group indices for all variables as follows:  
 $G \leftrightarrow 1, (G-1) \leftrightarrow 2, \dots$

After these operations, the transport solver can be used to compute the fundamental adjoint solution. Notice also that these operations automatically convert the forward boundary conditions to the adjoint boundary conditions. When solving a generalized adjoint problem, the following changes need to be additionally implemented *within* the (forward) transport solver.

- (1) Add the response gradient  $\nabla_{\Phi} R/R$  to the variable for an external source.
- (2) Modify the fission source  $F_g$  to the form

$$F_g = \frac{\lambda_g}{4\pi k} \sum_{h=1}^G \bar{\nu} \Sigma_f^h \left( \phi^h(\mathbf{r}) - \frac{\langle \mathbf{B}\Phi, \Phi_F \rangle}{\langle \mathbf{B}\Psi, \Phi_F \rangle} \Psi^g \right), \quad (30)$$

where  $\Phi_F$  denotes the forward solution of (16) and  $\Psi$  the adjoint solution of (20).

The multigroup solution  $\Phi$  given by the solver must then be interpreted so that, for example,  $\Phi^g(\mathbf{r}, \Omega)$  corresponds to  $\Gamma^{G+1-g}(\mathbf{r}, -\Omega)$ . Notice that if the transport solver is based on a numerical scheme that relies on the nonnegativity of the flux or the sources, some additional modifications are necessary in addition to the ones described above. For further details, see for example, [11].

**3.2. Computation of Sensitivity and Uncertainty Profiles.** After obtaining the adjoint solutions, the sensitivities with respect to the multigroup nuclear data parameters can be computed according to (6) and (12). Notice that even after the multigroup approximation, these parameters are still spatial functions and therefore the derivatives in the equations refer to functional derivatives. The inner product in the sensitivity expressions can be discretized as

$$\langle \Phi, \Psi \rangle \approx \sum_{i=1}^I \sum_{g=1}^G \sum_{m=1}^M \omega_m V_i \bar{\Phi}^{g,i,m} \bar{\Psi}^{g,i,m}, \quad (31)$$

where  $i$  denotes the mesh index and  $\bar{\Phi}^{g,i,m}$  and  $\bar{\Psi}^{g,i,m}$  denote the average fluxes.

In order to compute the uncertainties using the Sandwich rule, the sensitivities and covariance matrices need to be formed with respect to the same parameters using the same energy group structure. In the SCALE 6 covariance library [3], the available covariance matrices are given in a 40-group structure for the parameters listed in Table 1. Most of these covariance matrices are nuclide specific. It should be emphasized that there is no covariance data for the group-to-group transfer cross-sections.

Multigroup covariance matrices can in principle be transformed to another multigroup structure by simple mathematical techniques. The applicability of this approach depends on the differences between the group structures.

TABLE 1: Parameters for which there exists covariance data in the SCALE library.

Parameter	MT number
$\sigma_t$	1
$\sigma_e$	2
$\sigma_i$	4
$\sigma_{n,2n}$	16
$\sigma_f$	18
$\sigma_\gamma$	102
$\sigma_{n,p}$	103
$\sigma_{n,d}$	104
$\sigma_{n,t}$	105
$\sigma_{n,He}$	106
$\sigma_{n,\alpha}$	107
$\bar{\nu}$	456
$\chi$	1018

In particular, the widths of the energy groups should not dramatically change. In this work, the code Angelo 2.3 [12] was used to transform the matrices to the energy group structure used in the sensitivity calculations with CASMO-4. The transformation procedure used in the code is based on flat-flux approximation, where the resampled values on the new grid are computed as lethargy overlap weighted averages. For further details, see [13]. When modifying the energy group structure of fission spectrum covariance matrices, further correction procedures are necessary in order to guarantee that the covariance matrices are in accordance with the normalization condition  $\sum_g \chi^g = 1$  [14]. The correction can also be applied to the fission spectrum sensitivities in which case the sensitivities are called *constrained* [14]. This was the approach chosen in this work.

In order to utilize the covariance data given for the parameters in Table 1, sensitivity profiles should be computed with respect to the same parameters. However, many lattice physics codes such as CASMO, HELIOS [15], WIMS [16], and DRAGON [17] employ nuclear data libraries that do not contain cross-section data for the individual capture and scattering reactions, but only for the total capture and scattering cross-section. There are generally three different approaches to overcome this difficulty. The most natural approach is perhaps to add the missing cross-sections to the code, either by creating a new cross-section library or by modifying the cross-sections inside the code [18]. Another option, suitable for deterministic analysis, is not to use problem-dependent cross-sections in the sensitivity analysis. In this case, the sensitivity coefficients can be computed outside the code based on the forward and adjoint fluxes and any set of cross-sections. This was the idea, for example, behind connecting DRAGON with the sensitivity and uncertainty analysis code SUS3D after a generalized adjoint mode was implemented to DRAGON [19]. The third option is to form the covariance matrices corresponding to the total capture and scattering cross-sections [4]. This is the approach that was chosen in this work.

Since the relationships between the total and individual capture and scattering reactions are linear, the covariance matrices corresponding to the total capture and scattering reactions can be computed with the Sandwich rule without introducing any approximation. The method used for combining the covariance matrices has been recently described in detail in [4]. Therefore, only the most important conclusions related to the methodology are repeated here.

Firstly, in the context of the capture reactions, the results are expected to be fully consistent with the case where the sensitivities are computed with respect to the individual capture reactions. In the case of the scattering reactions, however, the sensitivity profiles with respect to the individual and the total scattering cross-sections cannot be defined in a consistent manner and this affects the uncertainty results. In this context, it should be emphasized that the treatment of the covariance matrices involves no approximations and the inconsistency is solely related to the computation of the sensitivities. As mentioned previously, there is no cross-section data for the transfer cross-sections  $\sigma_x^{h-g,j}$  but only for  $\sigma_x^{g,j} = \sum_{h=1}^G \sigma_x^{g-h,j}$ , where  $x$  refers to a scattering reaction (e.g., elastic, inelastic) and  $j$  is the nuclide index. Therefore, in order to use the scattering covariance data, the sensitivity profiles should be computed with respect to  $\sigma_x^{g,j}$ . Because of the scattering source term in (16), however, the derivative with respect to  $\sigma_x^{g,j}$  is not mathematically well defined without additional constraints. Typically it is assumed that the probabilities of transfers to various groups are fixed, that is,

$$\sigma_x^{g-h,j} = \sigma_x^{g,j} p_x^{g-h,j}, \quad (32)$$

where  $p_x^{g-h}$  is the proportion of neutrons scattered from energy group  $g$  to energy group  $h$ , which is assumed to remain fixed even if the scattering cross-section  $\sigma_x^{g,j}$  is perturbed [20]. Based on this assumption, the scattering source in (16) can be written as

$$S^g = \frac{1}{4\pi} \sum_{h=1}^G \sum_s^{h-g} \phi^h = \frac{1}{4\pi} \sum_x \sum_j N^j \sum_{h=1}^G \sigma_x^{h,j} p_x^{h-g} \phi^h, \quad (33)$$

where the summations over  $x$  include all scattering reactions. After this assumption, the derivative with respect to  $\sigma_x^{g,j}$  is well defined and can be computed as usual. It is straightforward to show that this approach corresponds to computing the sensitivity coefficients with respect to the transfer cross-sections  $\sigma_x^{g-h,j}$  and summing them over  $h$ .

However, the sensitivity with respect to the total scattering cross-section  $\sigma_s^j = \sum_x \sigma_x^j$  is not well defined if the constraint (32) is enforced. In order to define this sensitivity, fixed transfer rates must be assumed for the total scattering cross-section. Also, computing the total scattering sensitivity as the sum of the individual scattering sensitivities implicitly enforces this constraint. Since the two assumptions required to compute the individual and total scattering sensitivities are inconsistent, the chain rule of derivation does not apply to them, and, for example, although  $\sigma_s^{g,j} = \sigma_e^{g,j} + \sigma_i^{g,j}$  holds,  $dR/d\sigma_e^{g,j} \neq (dR/d\sigma_s^{g,j})(d\sigma_s^{g,j}/d\sigma_e^{g,j})$ .

## 4. Numerical Results for PB-2 Lattice Physics Exercise

The calculation framework was applied to the BWR test case from the UAM benchmark lattice physics Exercise 1.2 considering a single fuel assembly with reflective boundary conditions [2], and the results were compared against the TSUNAMI-2D sequence in SCALE 6.1 [21]. The test problem represents Peach Bottom 2 (PB-2) under hot zero power conditions. Two-group homogenized cross-sections have been considered as responses in the GPT framework.

The outline of the CASMO-4 calculations is presented in Figure 1. The calculations were carried out using the cross-section library E60200 that contains 70 energy groups and is based on ENDF/B-VI data [22]. The covariance data were taken from the SCALE 6 library ZZ-SCALE6.0/COVA-44G [3] according to the guidelines of the benchmark. The library is based on evaluations from various sources (including ENDF/B-VII, ENDF/B-VI, JENDL-3.1) and approximate covariance data. The covariances in the library are given in relative terms, and therefore the library is intended to be used with all cross-section libraries including the ones that are inconsistent with the evaluations. While this is not strictly correct, it is considered to be acceptable due to the scarcity of comprehensive covariance data among other reasons [23].

The list of the nuclides present in these test cases can be found in the benchmark specification [2]. Apart from the isotopes of chromium and iron, all available covariance data in the library was included in the uncertainty computations. The reason for excluding these isotopes is that the employed cross-section library E60200 does not contain isotope-specific cross-sections for these materials but only cross-sections for natural chromium and iron.

The covariance matrices from ZZ-SCALE6.0/COVA-44G were processed for compatibility with CASMO-4. The sensitivity profiles in CASMO-4 were computed using the 40-group structure option that was the closest match to the amount of groups in the covariance data and, as mentioned in Section 3.2, the code Angelo 2.3 [12] was used to process the covariance matrices to this energy group structure. Next, the nuclear data processing code NJOY [24] was used to transform the 40-group covariance files to the BOXR format. Auxiliary FORTRAN programs were written for combining the covariance matrices according to the principles described in Section 3.2.

The TSUNAMI-2D calculations were performed using the ENDF/B-VI-based cross-section library V6-238 containing 238 energy groups. The module CENTRM was used for self-shielding. Implicit sensitivity analysis [9] was omitted in the TSUNAMI calculations in order to facilitate the comparison of the results given by CASMO-4 and TSUNAMI-2D.

*4.1. Results Based on Classical Perturbation Theory.* A summary of the results based on classical perturbation theory for the multiplication factor is presented in Table 2. The relative difference between the multiplication factors computed with CASMO-4 and TSUNAMI-2D is 52 pcm in both forward and adjoint cases. For the total uncertainty, the

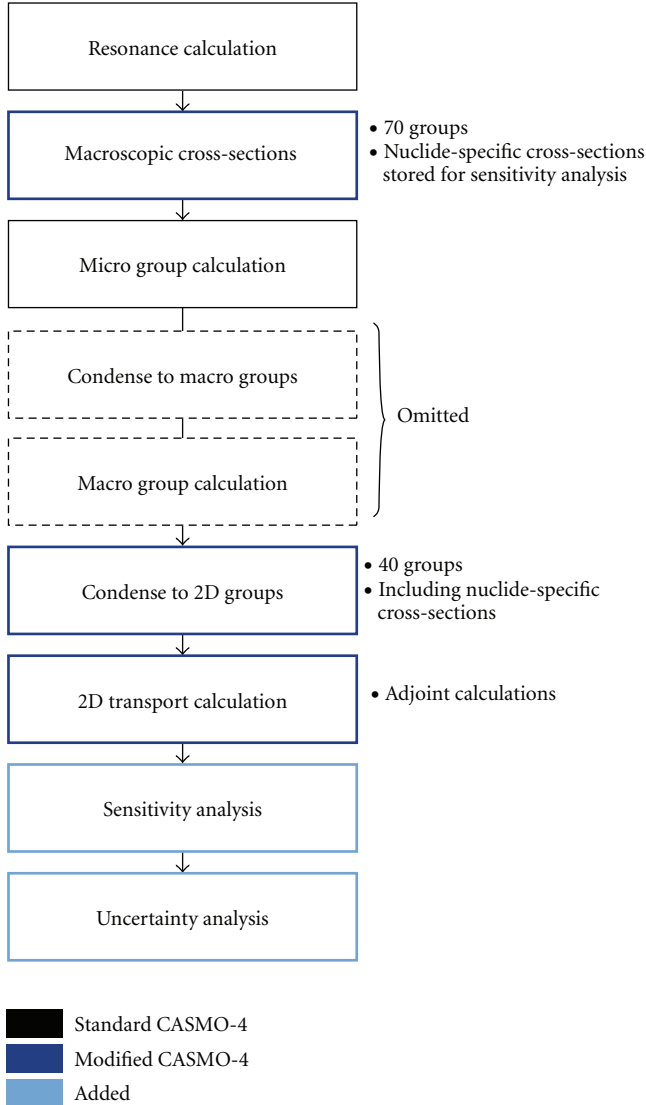


FIGURE 1: Outline of the CASMO-4 calculations.

values given by CASMO-4 and TSUNAMI-2D are also very consistent. Table 3 shows the five most significant sources of uncertainty together with the corresponding energy- and region-integrated sensitivity coefficients. As can be seen from this table, both the sensitivity and the uncertainty results are in good accordance. The greatest difference occurs for the capture cross-section of  $^{238}\text{U}$ , for which CASMO-4 yields a greater sensitivity. This appears to originate from the differences in the cross-section libraries. In particular, the cross-section library E60200 used in the CASMO-4 calculation has not been reduced in terms of the  $^{238}\text{U}$  resonance integral, which is known to be overestimated in the ENDF/B-VI data [22].

Figure 2 shows the volume-averaged forward flux and the volume-averaged fundamental adjoint  $\bar{\Psi}$  corresponding to this test case. As explained in Section 2.1, the value  $\bar{\Psi}^g$  represents the average importance of neutrons in the energy group  $g$  to the multiplication factor in comparison to neutrons

TABLE 2: Summary of the results for the multiplication factor.

Code	Forward $k$	Adjoint $k$	Rel. uncertainty, $\Delta k/k$ (%)
CASMO-4	1.10548	1.10546	0.508
TSUNAMI-2d	1.10490	1.10490	0.506

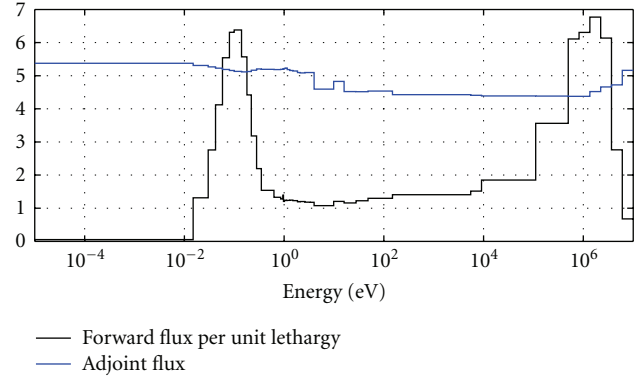


FIGURE 2: Volume-averaged forward flux and fundamental adjoint flux.

in other energy groups. The plot can be interpreted from this point of view. For example, it can easily be seen from the figure how the  $^{238}\text{U}$  capture cross-section resonances reduce the importance of neutrons in the corresponding energy groups. This phenomenon is particularly clear in the energy group  $E_{14} = [4.00\text{ eV}, 9.88\text{ eV}]$ , where the multigroup capture cross-section attains its maximum value. It can also be clearly distinguished from the plot how the adjoint function has a higher value in the energy groups corresponding to the peaks in the fission cross-section of  $^{235}\text{U}$ . To further demonstrate this, Figure 3 shows a plot of the problem-dependent  $^{235}\text{U}$  fission and  $^{238}\text{U}$  capture cross-sections in the same 40-group structure. The increase in the adjoint values in the highest energy groups corresponds mainly to the increase in the value of  $\bar{\nu}$  at these energies.

Figure 4 shows the multiplication factor sensitivity profiles for the parameters, whose integrated sensitivity coefficients have the greatest absolute values, excluding the sensitivity profile with respect to the fission spectrum of  $^{235}\text{U}$ , which was constrained in the computation. As can be seen from the figure, the multiplication factor is the most sensitive to the fission parameters of  $^{235}\text{U}$ , the capture cross-section of  $^{238}\text{U}$ , and the scattering cross-section of  $^1\text{H}$ . The positive sensitivity to the capture of  $^{238}\text{U}$  in the highest energy group follows from the fact that in CASMO-4 the  $(n, 2n)$  reaction cross-section has been included in the capture cross-section with a negative sign in this group. It is instructive to compare the sensitivity profiles with the forward and adjoint fluxes plotted in Figure 2. Notice that the peaks in the sensitivity profiles of  $^{235}\text{U}$  coincide with the thermal peak of the neutron flux, where most of the fissions occur. In general, perturbing a nuclear parameter has a greater impact on the results in the energy groups, where the flux is higher. On the contrary, the values of the fundamental adjoint represent the *average* importance

TABLE 3: The five most significant sources of uncertainty for the multiplication factor and the corresponding energy- and region-integrated relative sensitivity coefficients.

Nuclide	Parameter pair	Sensitivity		Contribution to $\Delta k/k$ (%)	
		CASMO	TSUNAMI	CASMO	TSUNAMI
$^{238}\text{U}$	$\sigma_c, \sigma_c$	$-2.434 \times 10^{-1}$	$-2.143 \times 10^{-1}$	$3.198 \times 10^{-1}$	$2.902 \times 10^{-1}$
$^{235}\text{U}$	$\bar{\nu}, \bar{\nu}$	$9.160 \times 10^{-1}$	$9.370 \times 10^{-1}$	$2.720 \times 10^{-1}$	$2.773 \times 10^{-1}$
$^{235}\text{U}$	$\sigma_c, \sigma_c$	$-1.027 \times 10^{-1}$	$-1.025 \times 10^{-1}$	$1.454 \times 10^{-1}$	$1.422 \times 10^{-1}$
$^{235}\text{U}$	$\sigma_f, \sigma_f$	$4.038 \times 10^{-1}$	$4.212 \times 10^{-1}$	$1.372 \times 10^{-1}$	$1.409 \times 10^{-1}$
$^{235}\text{U}$	$\sigma_f, \sigma_c$	$4.038 \times 10^{-1}$	$4.212 \times 10^{-1}$	$1.238 \times 10^{-1}$	$1.245 \times 10^{-1}$
		$-1.027 \times 10^{-1}$	$-1.025 \times 10^{-1}$		

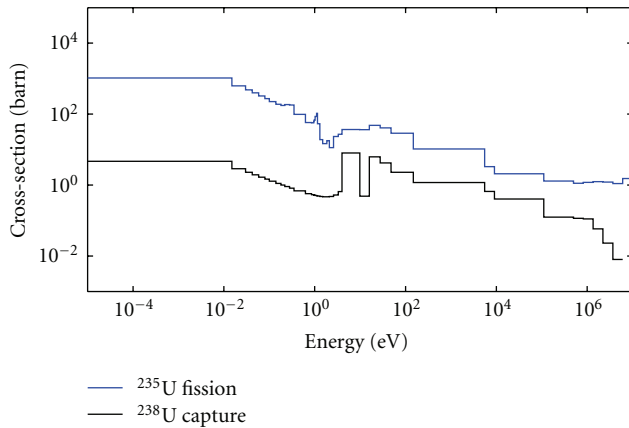


FIGURE 3: Self-shielded multigroup cross-sections corresponding to the test problem.

of neutrons in different energy groups. In particular, the lowest energy group has the highest importance, but this is not manifested in the sensitivity profiles, as the flux is very close to zero in this group. The negative sensitivities to the scattering reaction of  $^1\text{H}$  in the four lowest energy groups can be attributed to the fact that in these groups upscattering is more likely than downscattering. Therefore, neutrons are scattered to energy groups with a lower importance. The same reasoning applies to the scattering sensitivity of  $^1\text{H}$  in the highest energy groups, where neutrons are scattered downwards and the values of the adjoint function decrease rapidly with energy.

#### 4.2. Results Based on Generalized Perturbation Theory.

Table 4 presents the values and the total uncertainties of the homogenized two-group cross-sections that were considered as responses in the GPT-based sensitivity and uncertainty analysis. In computing the responses, the thermal cut-off was set at 0.625 eV. It can be seen from the table that all total uncertainty values are in good agreement with the thermal responses, whereas for the fast responses the uncertainties given by TSUNAMI-2D are consistently greater.

Tables 5 and 6 show more detailed sensitivity and uncertainty results for the two-group homogenized production cross-sections  $\nu\Sigma_{f,1}$  and  $\nu\Sigma_{f,2}$ . As can be seen from Table 6, in the case of  $\nu\Sigma_{f,1}$ , the difference in the total uncertainty

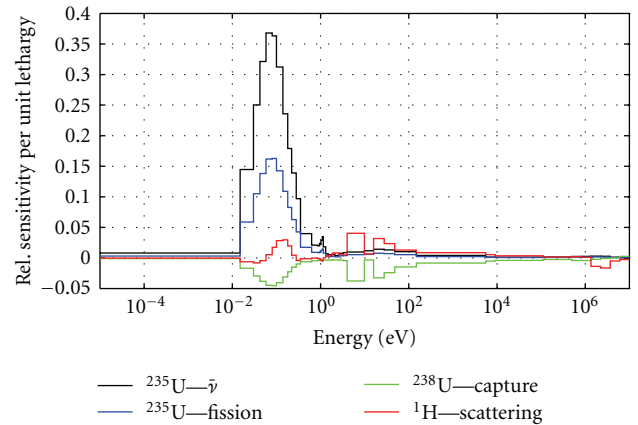


FIGURE 4: Multiplication factor sensitivity profiles.

values given by CASMO-4 and TSUNAMI-2D is attributable to the scattering of  $^{238}\text{U}$ , for which TSUNAMI-2D yields a significantly greater uncertainty value, although the total scattering sensitivity coefficients given by both codes are very close. As explained in Section 3.2, the sensitivity with respect to the total scattering cross-section can only be defined if the group-to-group transfer probabilities are assumed to be fixed for the total scattering. Also, defining the total scattering sensitivity as the sum of the individual scattering sensitivities implicitly enforces this assumption. However, in the TSUNAMI-2D computation, the total scattering uncertainty is computed based on the individual scattering sensitivities, which rely on the assumption of fixed transfer rates for each scattering reaction. The difference in the total scattering uncertainties is hence explained by incompatible constraints in the two uncertainty calculations. This phenomenon is more evident for the fast group responses since they are more sensitive to the inelastic scattering of  $^{238}\text{U}$ .

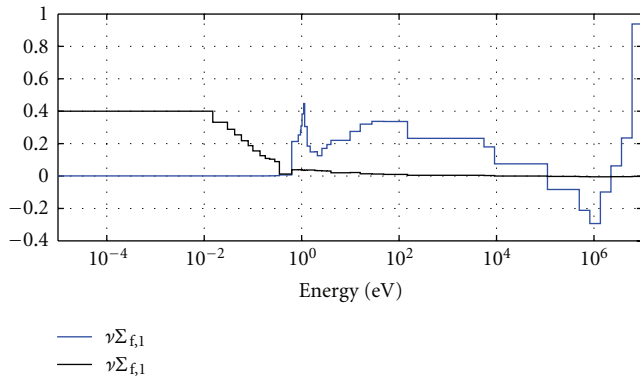
Figure 5 shows the volume-averaged generalized adjoint solutions for the responses  $\nu\Sigma_{f,1}$  and  $\nu\Sigma_{f,2}$ , denoted by  $\bar{\Gamma}_{f,1}$  and  $\bar{\Gamma}_{f,2}$ , respectively. As previously explained, the adjoint values in each energy group can be interpreted to represent the average importance of neutrons in that group to the response under consideration. Therefore, it is not surprising that thermal neutrons are more important to the response  $\nu\Sigma_{f,2}$ , whereas fast neutrons are more important to the response  $\nu\Sigma_{f,1}$ . The positive values of  $\bar{\Gamma}_{f,2}$  in the fast groups result

TABLE 4: Values and uncertainties of the responses considered in the GPT framework.

Response $R$	Value		Relative uncertainty $\Delta R/R$ (%)	
	CASMO	TSUNAMI	CASMO	TSUNAMI
$\nu\Sigma_{f,1}$	$4.976 \times 10^{-3}$	$4.951 \times 10^{-3}$	$8.399 \times 10^{-1}$	$9.754 \times 10^{-1}$
$\nu\Sigma_{f,2}$	$6.922 \times 10^{-2}$	$6.938 \times 10^{-2}$	$4.490 \times 10^{-1}$	$4.478 \times 10^{-1}$
$\Sigma_{c,1}$	$5.348 \times 10^{-3}$	$5.380 \times 10^{-3}$	$1.098 \times 10^0$	$1.168 \times 10^0$
$\Sigma_{c,2}$	$2.653 \times 10^{-2}$	$2.672 \times 10^{-2}$	$5.066 \times 10^{-1}$	$5.040 \times 10^{-1}$
$\Sigma_{f,1}$	$1.935 \times 10^{-3}$	$1.927 \times 10^{-3}$	$5.563 \times 10^{-1}$	$6.820 \times 10^{-1}$
$\Sigma_{f,2}$	$2.841 \times 10^{-2}$	$2.847 \times 10^{-2}$	$3.244 \times 10^{-1}$	$3.226 \times 10^{-1}$

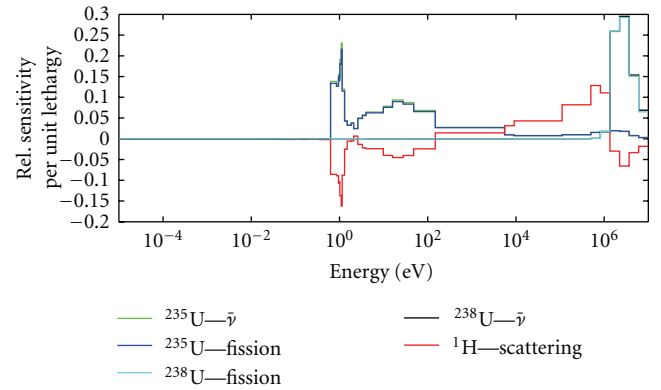
TABLE 5: The five most significant sources of uncertainty for the response  $\nu\Sigma_{f,2}$  and the corresponding energy- and region-integrated relative sensitivity coefficients.

Nuclide	Param. pair	Sensitivity		Contribution to $\Delta R/R$ (%)	
		CASMO	TSUNAMI	CASMO	TSUNAMI
$^{235}\text{U}$	$\bar{\nu}, \bar{\nu}$	$9.996 \times 10^{-1}$	$9.998 \times 10^{-1}$	$3.105 \times 10^{-1}$	$3.106 \times 10^{-1}$
$^{235}\text{U}$	$\sigma_f, \sigma_f$	$7.985 \times 10^{-1}$	$7.941 \times 10^{-1}$	$2.893 \times 10^{-1}$	$2.869 \times 10^{-1}$
$^{235}\text{U}$	$\sigma_f, \sigma_c$	$7.985 \times 10^{-1}$	$7.941 \times 10^{-1}$	$1.134 \times 10^{-1}$	$1.139 \times 10^{-1}$
		$-3.599 \times 10^{-2}$	$-3.667 \times 10^{-2}$		
$^{238}\text{U}$	$\sigma_c, \sigma_c$	$-4.406 \times 10^{-2}$	$-4.255 \times 10^{-2}$	$7.257 \times 10^{-2}$	$7.222 \times 10^{-2}$
$^{235}\text{U}$	$\sigma_c, \sigma_c$	$-3.599 \times 10^{-2}$	$-3.667 \times 10^{-2}$	$5.613 \times 10^{-2}$	$5.672 \times 10^{-2}$

FIGURE 5: Volume-averaged generalized adjoints corresponding to the responses  $\nu\Sigma_{f,1}$  and  $\nu\Sigma_{f,2}$ .

from the downscattering of neutrons. Notice that  $\bar{\Gamma}_{f,1}$  also has a small positive value in the first thermal group, which corresponds to the possibility of upscattering. For the most part, both adjoint fluxes qualitatively follow the fission cross-section of  $^{235}\text{U}$  plotted in Figure 3. In the highest energy groups, the values of  $\bar{\Gamma}_{f,1}$  increase rapidly due to the increase in the values of  $\bar{\nu}$ . The negative values of  $\bar{\Gamma}_{f,1}$  between 0.111 MeV and 2.231 MeV signify that additional neutrons in those energy groups would on average contribute more to the denominator  $\langle \Phi, \mathbf{1} \rangle_1$  than to the numerator  $\langle \Phi, \nu\Sigma_f \rangle_1$ . This in accordance with the fact that fission is unlikely to occur in this energy region.

Figure 6 shows the sensitivity profiles of  $\nu\Sigma_{f,1}$  with respect to the parameters, whose integrated sensitivity coefficients have the greatest absolute values. As can be anticipated, the response is the most sensitive to the fission parameters of  $^{235}\text{U}$  and  $^{238}\text{U}$  and in addition to the scattering of  $^1\text{H}$ . It

FIGURE 6: Sensitivity profiles of the response  $\nu\Sigma_{f,1}$ .

is interesting to compare these profiles with the plot of the generalized adjoint  $\bar{\Gamma}_{f,1}$  in Figure 5. The sensitivity to the scattering of  $^1\text{H}$  has the smallest values in the groups with the highest importance, as this reaction transfers neutrons to energy groups with a lower importance. Since fast neutrons mostly scatter downwards, the scattering sensitivity has positive values in the groups between 149 eV and 1.35 MeV, where the importance decreases with increasing energy. This trend is reversed at 1.35 MeV, where the importance of the energy groups begins to increase with energy, mainly due to the increase in the values of  $\bar{\nu}$  at these energies.

The sensitivity profiles corresponding to the response  $\nu\Sigma_{f,2}$  are plotted in Figure 7. It is noteworthy that the profiles qualitatively resemble the respective profiles of the multiplication factor in the thermal region, whereas they quickly fall to nearly zero in the fast region. From the perspective of the GPT framework, it is again enlightening

TABLE 6: The five most significant sources of uncertainty for the response  $\nu\Sigma_{f,1}$  and the corresponding energy- and region-integrated relative sensitivity coefficients. The sensitivity coefficients with respect to the parameter  $\chi$  have been constrained.

Nuclide	Param. pair	Sensitivity		Contribution to $\Delta R/R$ (%)	
		CASMO	TSUNAMI	CASMO	TSUNAMI
$^{235}\text{U}$	$\chi, \chi$	$4.657 \times 10^{-9}$	$-2.757 \times 10^{-10}$	$5.934 \times 10^{-1}$	$6.150 \times 10^{-1}$
$^{238}\text{U}$	$\bar{\nu}, \bar{\nu}$	$3.975 \times 10^{-1}$	$3.879 \times 10^{-1}$	$4.623 \times 10^{-1}$	$4.544 \times 10^{-1}$
$^{238}\text{U}$	$\sigma_f, \sigma_f$	$3.931 \times 10^{-1}$	$3.834 \times 10^{-1}$	$2.084 \times 10^{-1}$	$1.994 \times 10^{-1}$
$^{238}\text{U}$	$\sigma_s, \sigma_s$	$-2.743 \times 10^{-2}$	$-2.718 \times 10^{-2}$	$2.015 \times 10^{-1}$	$5.148 \times 10^{-1}$
$^{235}\text{U}$	$\sigma_f, \sigma_f$	$5.826 \times 10^{-1}$	$5.866 \times 10^{-1}$	$1.588 \times 10^{-1}$	$1.466 \times 10^{-1}$

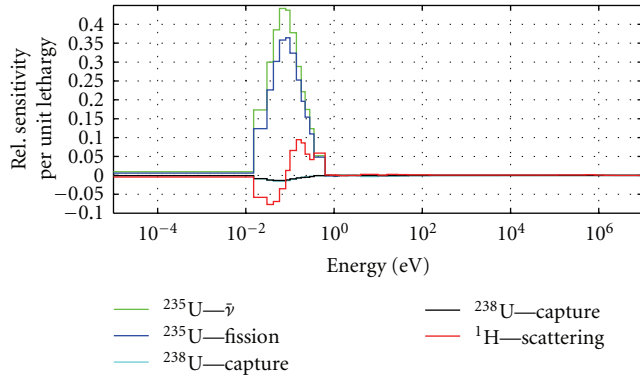


FIGURE 7: Sensitivity profiles of the response  $\nu\Sigma_{f,2}$ .

to compare the sensitivity plots with the adjoint function  $\bar{\Gamma}_{f,2}$  plotted in Figure 5 and the flux  $\bar{\Phi}$  shown in Figure 2. In the case of this response, the average importance of neutrons increases steadily with decreasing energy. Therefore, it is reasonable that the scattering sensitivities are again negative in the groups where upscattering is more likely than down-scattering. Also, the sensitivities peak in the energy region coinciding with the thermal peak of the forward flux.

## 5. Summary and Conclusions

Sensitivity and uncertainty analysis capability has been developed to the reactor physics code CASMO-4 in the context of the UAM benchmark. Sensitivities with respect to nuclear data parameters can be computed efficiently by utilizing the adjoint system of the criticality equation. The propagated nuclear data uncertainty can then be calculated deterministically by the Sandwich rule.

Initially, classical perturbation theory was implemented to the code, which enabled sensitivity analysis of the critical eigenvalue. In this context, covariance matrices from scale 6 were transformed to become compatible with CASMO-4, and the resulting covariance library was connected with the code. Since the cross-section libraries of CASMO-4 do not contain data for the individual capture and scattering reactions, the covariance matrices of the individual sub-reactions were combined in the covariance library. This work has been reported in detail in [4], and the main conclusions related to the methodology were summarized in this paper. In particular, the sensitivities with respect to total scattering

and individual scattering cross-sections cannot be defined in a consistent manner, which leads to some systematic differences in the uncertainty results.

Recently, generalized perturbation theory was added to the code as a new feature, which enables performing sensitivity analysis for responses that can be represented as reaction rate ratios. For each response, the computation of sensitivity profiles with respect to all parameters of interest requires solving one generalized adjoint system. The mathematical background as well as the physical interpretation of the generalized adjoint solutions were reviewed, and practical guidelines were given for modifying a deterministic transport code to solve the generalized adjoint systems needed in sensitivity analysis. The theory for computing the sensitivity profiles was presented both from the perspective of function space analysis and numerical computations.

Numerical results were presented for a lattice physics test problem representing a BWR in hot zero power conditions, and they were compared to the results given by the TSUNAMI-2D sequence in SCALE 6.1. Two-group homogenized cross-sections were considered as responses in the generalized perturbation theory framework. The results were in very good agreement with the thermal responses, whereas in the case of fast responses, the uncertainties given by TSUNAMI-2D were consistently greater. Detailed sensitivity and uncertainty results were presented and analyzed for the homogenized fast and thermal production cross-sections. The differences in the uncertainty results for the fast responses were explained by the incompatible constraints used in computing the scattering uncertainties.

In the future, the work will continue by extending the GPT framework to other responses in addition to two-group homogenized cross-sections with the eventual goal of modifying CASMO-4 to provide uncertainty estimates for all homogenized assembly data, which can then be propagated to coupled neutronics/thermal hydraulics calculations.

## Acknowledgment

This work was funded through the Finnish National Research Programme on Nuclear Power Plant Safety 2011–2014, SAFIR2014.

## References

- [1] J. Rhodes and M. Edenius, *CASMO-4, A Fuel Assembly Burnup Program, Users Manual*, 2001.

- [2] K. Ivanov, M. Avramova, I. Kodeli, and E. Sartori, "Benchmark for uncertainty analysis in modeling (UAM) for design, operation, and safety analysis of LWRs," NEA/NSC/DOC(2007) 23, 2007.
- [3] ZZ-SCALE6.0/COVA44G, "A 44-group cross section covariance matrix library retrieved from the scale-6.0 package," NEA Data Bank Code Package USCD1236/03, 2011.
- [4] M. Pusa, "Incorporating sensitivity and uncertainty analysis to a lattice physics code with application to CASMO-4," *Annals of Nuclear Energy*, vol. 40, no. 1, pp. 153–162, 2012.
- [5] D. G. Cacuci, *Sensitivity and Uncertainty Analysis*, vol. 1, Chapman & Hall/CRC, Boca Raton, Fla, USA, 2003.
- [6] B. G. Carlson and K. D. Lathrop, "Transport theory—the method of discrete ordinates," in *Computing Methods in Reactor Physics*, H. Greenspan, C. N. Kelber, and D. Okrent, Eds., Gordon and Breach Science Publishers, New York, NY, USA, 1968.
- [7] E. E. Lewis and J. W. F. Miller, *Computational Methods of Neutron Transport*, John Wiley & Sons, New York, NY, USA, 1984.
- [8] J. Lewins, *Importance: The Adjoint Function*, Pergamon Press, Oxford, UK, 1965.
- [9] M. L. Williams, B. L. Broadhead, and C. V. Parks, "Eigenvalue sensitivity theory for resonance-shielded cross sections," *Nuclear Science and Engineering*, vol. 138, no. 2, pp. 177–191, 2001.
- [10] M. L. Williams, "Perturbation theory for nuclear reactor analysis," in *CRC Handbook of Nuclear Reactors Calculations*, Y. Ronen, Ed., vol. 3, CRC Press, Boca Raton, Fla, USA, 1986.
- [11] R. L. Childs, "Generalized perturbation theory using two-dimensional, discrete ordinates transport theory," Tech. Rep. ORNL/CSD/TM-127, Oak Ridge National Laboratory, Oak Ridge, Tenn, USA, 1980.
- [12] I. Kodeli, "Manual for ANGELO2 and LAMBDA codes," NEA-1798/03 Package, 2010.
- [13] I. Kodeli and E. Sartori, "Neutron cross-section covariance data in multigroup form and procedure for interpolation to users' group structures for uncertainty analysis applications," in *Proceedings of the PHYSOR International Conference on the Physics of Reactors: Operation, Design and Computation*, Marseille, France, 1990.
- [14] I. Kodeli, M. Ishikawa, and G. Aliberti, "Evaluation of fission spectra uncertainty and their propagation," in *OECD/NEA WPEC Subgroup 26 Final Report: Uncertainty and Target Accuracy Assessment for Innovative Systems Using Recent Covariance Data Evaluations*, C. Appendix, Ed., OECD, Paris, France, 2008.
- [15] "HELIOS Methods," Studsvik Scanpower, 2000.
- [16] WIMS9A, "NEW FEATURES, A Guide to the New Features of WIMS Version 9A," Serco Assurance, <http://www.sercoassurance.com/answers/>, 2005.
- [17] G. Marleau, A. Hébert, and R. Roy, "A User Guide For Dragon Version 4," IGE294, <http://www.polymtl.ca/nucleaire/DRAGON/>, 2009.
- [18] W. Wieselquist, A. Vasiliev, and H. Ferroukhi, *Nuclear Data Uncertainty Propagation in a Lattice Physics Code Using Stochastic Sampling*, ANS Physics of Reactors (PHYSOR 2012): Advances of Reactor Physics, Knoxville, Tenn, USA, 2012.
- [19] A. Bidaud, G. Marleau, and E. Noblat, "Nuclear data uncertainty analysis using the coupling of DRAGON with SUS3D," in *Proceedings of the International Conference on Mathematics, Computational Methods & Reactor Physics (M&C '09)*, May 2009.
- [20] C. R. Weisbin, J. H. Marable, J. L. Lucius et al., "Application of FORSS sensitivity and uncertainty methodology to fast reactor benchmark analysis," Tech. Rep. ORNL/TM-5563, 1976.
- [21] "SCALE: a modular code system for performing standardized computer analyses for licensing evaluation," Tech. Rep. ORNL/TM-2005/39, Radiation Safety Information Computational Center at Oak Ridge National Laboratory as CCC-725, Oak Ridge, Tenn, USA, 2009, Version 6, Vols. I–III.
- [22] J. Rhodes, *JEF 2.2 and ENDF/B-VI 70 Group Neutron Data Libraries*, Studsvik, Nykoping, Sweden, 2005.
- [23] M. L. Williams, D. Wiarda, G. Arbanas, and B. L. Broadhead, "Scale nuclear data covariance library," in *SCALE: A Modular Code System for Performing Standardized Computer Analyses for Licensing Evaluation, Version 5*, ORNL/TM-2005/39, Oak Ridge National Library/U.S. Nuclear Regulatory Commission, Oak Ridge, Tenn, USA, 20052009.
- [24] R. E. MacFarlane and D. W. Muir, "The NJOY Nuclear Data Processing System, Version 91," Manual LA-12740-M, Los Alamos National Laboratory, Los Alamos, NM, USA, 1994.

## Research Article

# Uncertainty Propagation Analysis for PWR Burnup Pin-Cell Benchmark by Monte Carlo Code McCARD

Ho Jin Park,<sup>1</sup> Hyung Jin Shim,<sup>2</sup> and Chang Hyo Kim<sup>2</sup>

<sup>1</sup> Reactor Core Design Division, Advanced Reactor Development Institute, Korea Atomic Energy Research Institute, 989-111 Daedeok-Daero, Yuseong-gu, Daejeon 305-353, Republic of Korea

<sup>2</sup> Department of Nuclear Engineering, Seoul National University, 1 Gwanak-ro, Gwanak-gu, Seoul 151-744, Republic of Korea

Correspondence should be addressed to Hyung Jin Shim, shimhj@snu.ac.kr

Received 31 July 2012; Accepted 9 October 2012

Academic Editor: Oscar Cabellos

Copyright © 2012 Ho Jin Park et al. This is an open access article distributed under the Creative Commons Attribution License, which permits unrestricted use, distribution, and reproduction in any medium, provided the original work is properly cited.

In the Monte Carlo (MC) burnup analyses, the uncertainty of a tally estimate at a burnup step may be induced from four sources: the statistical uncertainty caused by a finite number of simulations, the nuclear covariance data, uncertainties of number densities, and cross-correlations between the nuclear data and the number densities. In this paper, the uncertainties of  $k_{\text{inf}}$ , reaction rates, and number densities for a PWR pin-cell benchmark problem are quantified by an uncertainty propagation formulation in the MC burnup calculations. The required sensitivities of tallied parameters to the microscopic cross-sections and the number densities are estimated by the MC differential operator sampling method accompanied by the fission source perturbation. The uncertainty propagation analyses are conducted with two nuclear covariance data—ENDF/B-VII.1 and SCALE6.1/COVA libraries—and the numerical results are compared with each other.

## 1. Introduction

Monte Carlo (MC) burnup analysis codes [1–5] have been successfully applied for the neutronics design and analysis of advanced nuclear systems with increasing computing power. Since Takeda et al. [6] first proposed a formulation to evaluate the uncertainty propagation of number densities in the MC burnup analysis using the sensitivities of the burnup matrix to cross-sections and number densities, several studies [7–11] on the uncertainty propagation of MC burnup analysis followed with different uncertainty quantification formulations.

The uncertainty quantification of a nuclear parameter, such as  $k_{\text{eff}}$ , reaction rates, and number densities, in the MC burnup analysis is currently conducted by two different approaches: the sensitivity and uncertainty (S/U) analysis [12] and the direct stochastic sampling methods. In the S/U analysis, the output uncertainty is quantified from its sensitivities to input parameters by the error propagation formulations. It provides explicit sensitivities but may suffer from low-order approximations. Park et al. [9] have established an uncertainty propagation formulation

based on the S/U analysis in the depletion calculations and demonstrated its usefulness in terms of an incineration analysis of a transuranic fuel assembly by using the Seoul National University MC code, McCARD [4].

The direct stochastic sampling methods can produce output distributions from a number of MC calculations each with different input data set sampled. This approach is easy to implement by running existing MC neutronics analysis codes with different input data sets but at the expense of high computational costs. This approach includes the XSUSA/SCALE [10] and TMC/SERPENT [11] methods. García-Herranz et al. [8] have developed an MC hybrid method combining MC spectrum and burnup calculations to reduce the computation time in the direct stochastic sampling approach.

In this paper, we perform the McCARD uncertainty propagation analysis for a PWR burnup pin-cell benchmark, one of the OECD benchmarks for uncertainty analysis modeling (UAM) for design, operation, and safety analysis of LWRs [13]. The uncertainty propagation of tallied parameters due to the statistical, microscopic cross-section, and number density uncertainties is calculated from their

TABLE 1: Comparison of  $k$  uncertainties due to the covariance of  $^{235}\text{U}$  and  $^{238}\text{U}$  from ENDF/B-VII.1 and SCALE6.1/COVA.

Covariance data		ENDF/B-VII.1 44G Cov.	SCALE6.1/ COVA-44G
RSD due to $^{235}\text{U}$ (%)	$\nu, \nu$	0.604	0.264
	$(n, \gamma), (n, \gamma)$	0.216	0.211
	$(n, \gamma), (n, \text{fis})$	0.075	0.076
	$(n, \text{fis}), (n, \text{fis})$	0.081	0.075
	$(n, n'), (n, n')$	0.001	0.002
RSD due to $^{238}\text{U}$ (%)	$\nu, \nu$	0.071	0.070
	$(n, \gamma), (n, \gamma)$	0.294	0.263
	$(n, \text{fis}), (n, \text{fis})$	0.016	0.015
	$(n, n'), (n, n')$	0.104	0.105
Total		0.729	0.463

TABLE 2:  $k_{\text{inf}}$ 's and their uncertainties versus pin burnup with ENDF/B-VII.1 and SCALE6.1/COVA covariance data.

Burnup (MWd/kgU)	$k_{\text{inf}}$	RSD (%)	
		ENDF/B-VII.1 44G Cov.	SCALE6.1/ COVA-44G
0.00	1.41701	0.731	0.469
0.10	1.39073	0.729	0.475
0.20	1.38327	0.726	0.465
0.50	1.36993	0.718	0.462
1.00	1.35687	0.714	0.455
2.00	1.34292	0.697	0.455
4.00	1.31499	0.666	0.446
6.00	1.28805	0.637	0.444
8.00	1.26320	0.608	0.448
10.00	1.23924	0.588	0.452
12.00	1.21683	0.569	0.464
14.00	1.19584	0.557	0.465
16.00	1.17646	0.532	0.478
18.00	1.15745	0.517	0.488
20.00	1.13972	0.499	0.492
30.00	1.05605	0.449	0.530
40.00	0.98051	0.397	0.579
50.00	0.91289	0.403	0.633
60.00	0.85671	0.411	0.682

sensitivities estimated by the MC perturbation techniques [14, 15] in the continuous-energy MC calculations. The numerical results with ENDF/B-VII.1 covariance data are compared with those from the SCALE6.1/COVA covariance libraries.

## 2. McCARD Uncertainty Propagation Methodology

The MC depletion calculations consist of the successive MC transport analyses with updating the material compositions. Microscopic reaction rates are estimated at every beginning

of a burnup step by the MC transport calculations. They are then used to solve the depletion equation to update isotopic number densities at the end of the burnup step. Thus, the uncertainties of the MC estimates on reaction rates due to the statistical and nuclear data and number density uncertainties cause those of the updated number densities. With the progress of the stepwise MC burnup calculations, the MC reaction rate uncertainties of a burnup step propagate to the number density uncertainties of the burnup step and to those of the following burnup steps. Figure 1 shows the uncertainty propagation mechanism in the MC burnup analysis. In the figure,  $N$ ,  $x$ ,  $r$ , and  $Q$  denote the number density, microscopic cross-section, microscopic reaction rate, and tally, respectively.  $n$ ,  $m$ ,  $i$ ,  $\alpha$ , and  $g$  are the indices of burnup step, region, nuclide, reaction type, and neutron energy, respectively. From the figure, one can see that the S/U analyses need be performed to quantify the uncertainty of  $Q$  in the MC transport calculations and the number density uncertainties in the depletion calculations.

In the McCARD uncertainty propagation formulation [9], the variance of  $Q$ ,  $\sigma^2[Q]$ , is estimated by

$$\sigma^2[Q] = \sigma_S^2[Q] + \sigma_{\text{NN}}^2[Q] + \sigma_{\text{XX}}^2[Q] + 2\sigma_{\text{NX}}^2[Q], \quad (1)$$

$$\sigma_{\text{NN}}^2[Q] = \sum_{m,i} \sum_{m',i'} \text{cov}[N_{m,i}^n, N_{m',i'}^n] \left( \frac{\partial Q}{\partial N_{m,i}^n} \right) \left( \frac{\partial Q}{\partial N_{m',i'}^n} \right),$$

$$\sigma_{\text{XX}}^2[Q] = \sum_{i,\alpha} \sum_{i',\alpha',g'} \text{cov}[x_{\alpha,g'}^i, x_{\alpha',g'}^{i'}] \left( \frac{\partial Q}{\partial x_{\alpha,g'}^i} \right) \left( \frac{\partial Q}{\partial x_{\alpha',g'}^{i'}} \right), \quad (2)$$

$$\sigma_{\text{NX}}^2[Q] = \sum_{m,i} \sum_{m',i',\alpha',g'} \text{cov}[N_{m,i}^n, x_{\alpha',g'}^{i'}] \left( \frac{\partial Q}{\partial N_{m,i}^n} \right) \left( \frac{\partial Q}{\partial x_{\alpha',g'}^{i'}} \right).$$

$\sigma_S^2$  denotes the statistical variance. It can be estimated by the sample variance or real variance estimation methods [16–18].

In the McCARD uncertainty propagation analysis, the partial derivatives in (2) are approximated as

$$\frac{\partial Q}{\partial X} \cong \frac{Q(\bar{X} + \sigma[X]) - Q(\bar{X})}{\sigma[X]} = \frac{\delta Q(X)}{\sigma[X]}, \quad (3)$$

where  $X$  denotes  $N$  or  $x$ . In the McCARD procedure,  $\delta Q(X)$  in (3) are estimated by the differential operator sampling method [14] accompanied by the fission source perturbation [15].

TABLE 3: RSDs (%) of one-group reaction rates with ENDF/B-VII.1 and SCALE6.1/COVA covariance data.

Cov. data	Burnup (MWd/kgU)	$^{235}\text{U}$ ( $n, \gamma$ )	$^{235}\text{U}$ ( $n, \text{fis}$ )	$^{238}\text{U}$ ( $n, \gamma$ )	$^{238}\text{U}$ ( $n, \text{fis}$ )
ENDF/B-VII.1	0	1.35	0.53	0.94	3.97
	10	1.45	0.69	0.87	3.97
	20	1.55	0.88	0.83	3.85
	30	1.62	1.06	0.79	3.88
	40	1.73	1.28	0.76	3.79
	50	1.79	1.43	0.67	3.80
	60	1.88	1.60	0.70	3.71
SCALE 6.1/COVA-44G	0	1.38	0.51	0.82	3.77
	10	1.46	0.61	0.81	3.89
	20	1.55	0.79	0.75	3.85
	30	1.58	0.90	0.73	3.77
	40	1.63	1.04	0.68	3.83
	50	1.69	1.18	0.64	3.81
	60	1.75	1.29	0.66	3.79

TABLE 4: RSDs (%) of number densities with ENDF/B-VII.1 and SCALE6.1/COVA covariance data.

Cov. data	Bunrup or time	$^{235}\text{U}$	$^{239}\text{Pu}$	$^{240}\text{Pu}$	$^{241}\text{Pu}$	$^{242}\text{Pu}$
ENDF/B-VII.1	0 MWd/kgU	0.00	0.00	0.00	0.00	0.00
	10 MWd/kgU	0.14	0.99	1.37	1.38	2.72
	30 MWd/kgU	0.58	1.47	1.78	1.31	2.47
	50 MWd/kgU	1.33	1.95	2.22	1.77	2.51
	Shutdown	1.95	2.16	2.47	2.06	2.60
	1 year cooling	1.95	2.13	2.47	2.16	2.60
	100 years cooling	1.95	2.13	2.34	2.06	2.60
SCALE 6.1/COVA-44G	0 MWd/kgU	0.00	0.00	0.00	0.00	0.00
	10 MWd/kgU	0.09	0.80	1.17	1.16	1.57
	30 MWd/kgU	0.43	1.11	1.46	0.97	0.42
	50 MWd/kgU	1.04	1.43	1.80	1.25	0.17
	Shutdown	1.53	1.58	2.00	1.47	0.23
	1 year cooling	1.53	1.56	1.99	1.54	0.23
	100 years cooling	1.52	1.56	1.90	1.47	0.23

In exactly the same way as above for the variance of  $Q$ , the variance of the number density in the depletion calculations can be written by

$$\sigma^2[N_{m,i}^{n+1}] = \sigma_{\text{NN}}^2[N_{m,i}^{n+1}] + \sigma_{\text{RR}}^2[N_{m,i}^{n+1}] + 2\sigma_{\text{NR}}^2[N_{m,i}^{n+1}], \quad (4)$$

$$\sigma_{\text{NN}}^2[N_{m,i}^{n+1}] = \sum_{i'} \sum_{i''} \text{cov}[N_{m,i'}^n, N_{m,i''}^n] \left( \frac{\partial N_{m,i}^{n+1}}{\partial N_{m,i'}^n} \right) \left( \frac{\partial N_{m,i}^{n+1}}{\partial N_{m,i''}^n} \right),$$

$$\sigma_{\text{RR}}^2[N_{m,i}^{n+1}] = \sum_{j,\alpha} \sum_{j',\alpha'} \text{cov}[r_{m,j,\alpha}^n, r_{m,j',\alpha'}^n] \left( \frac{\partial N_{m,i}^{n+1}}{\partial r_{m,j,\alpha}^n} \right) \left( \frac{\partial N_{m,i}^{n+1}}{\partial r_{m,j',\alpha'}^n} \right),$$

$$\sigma_{\text{NR}}^2[N_{m,i}^{n+1}] = \sum_{i'} \sum_{j,\alpha} \text{cov}[N_{m,i'}^n, r_{m,j,\alpha}^n] \left( \frac{\partial N_{m,i}^{n+1}}{\partial N_{m,i'}^n} \right) \left( \frac{\partial N_{m,i}^{n+1}}{\partial r_{m,j,\alpha}^n} \right). \quad (5)$$

In McCARD, the partial derivatives in (5) are approximated in the same way as (3) and obtained by the direct subtractions. The detailed algorithms are described in [9].

### 3. UAM PWR Pin-Cell Burnup Benchmark

The PWR burnup pin-cell benchmark problem in Phase I of the OECD LWR UAM benchmarks [13] is designed to address the uncertainties in the depletion calculation due to the basic nuclear data as well as the impact of processing of nuclear and covariance data. The benchmark represents the burnup uncertainty propagation analysis for a typical fuel rod from the TMI-1 PWR,  $15 \times 15$  assembly with 4.85 w/o enrichment. Its final burnup is 61.28 GWd/MTU with the specific power of 33.58 kW/kgU.

The McCARD analyses are conducted with the continuous-energy cross-section libraries processed by NJOY [19] from the ENDF/B-VII.1 neutron libraries. The cross-section covariance data are taken from the ENDF/B-VII.1 and SCALE6.1/COVA-44G. The 44-group covariance data from the ENDF/B-VII.1 covariance libraries are generated by the ERRORR module in the NJOY code.

For the fresh burnup state of the TMI-1 pin-cell problem, the  $k$  uncertainty due to the cross-section covariance data

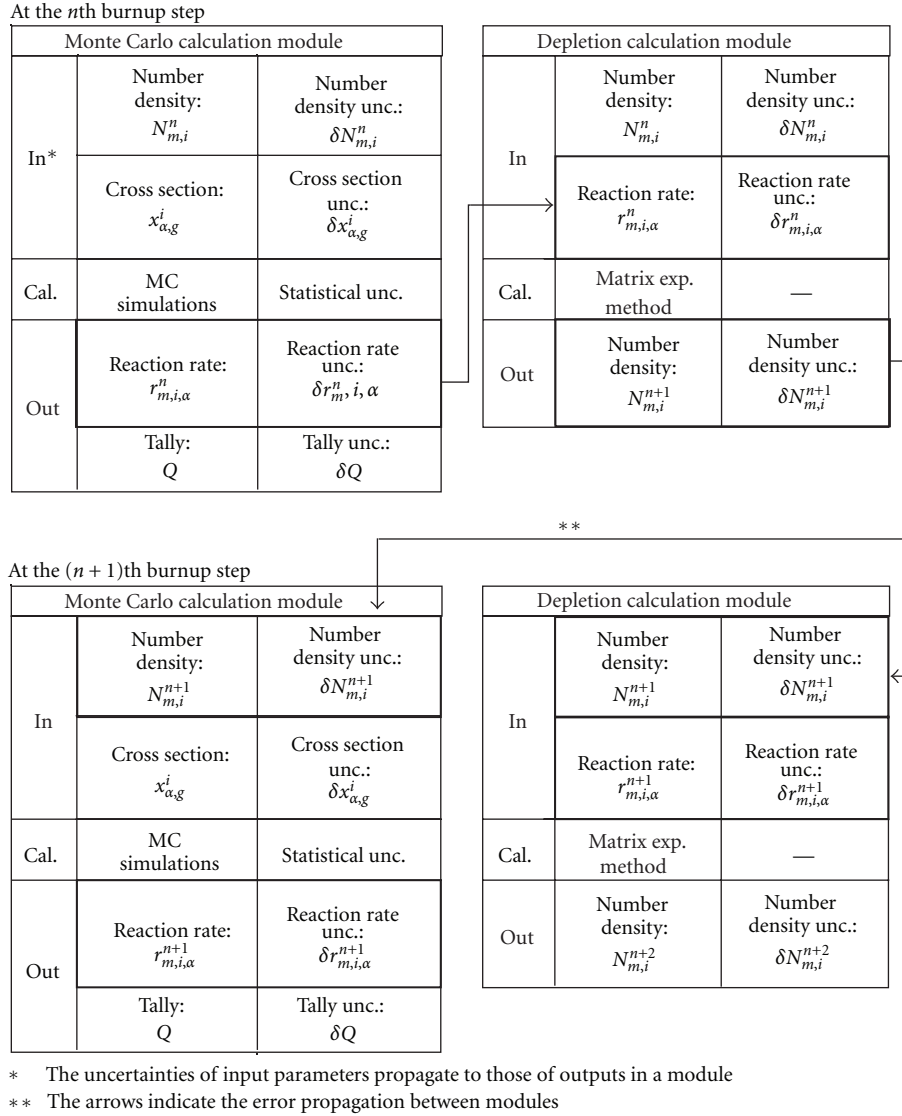


FIGURE 1: Uncertainty propagation in the MC burnup analysis.

is investigated by using McCARD. The  $k$  uncertainty can be estimated by (1) ignoring  $\sigma_S^2$ ,  $\sigma_{NN}^2$ , and  $\sigma_{NX}^2$ . The McCARD eigenvalue calculations are performed on 1000 active cycles with 10,000 histories per cycle. In the MC perturbation calculations, the perturbed fission source distribution is assumed to converge after 10 cycles.

Table 1 shows the contributions of  $^{235}\text{U}$  and  $^{238}\text{U}$  cross-section uncertainties to the relative standard deviation (RSD) of  $k_{\text{inf}}$ ,  $\sigma_{XX}[k_{\text{inf}}]$ , by reaction type and the covariance data. From Table 1, it is noted that the  $k$  uncertainty from the ENDF/B-VII.1 covariance data is 57% bigger than that from the SCALE6 covariance data and that contribution of the  $\nu$  uncertainties of  $^{235}\text{U}$  is a dominating factor to the  $k$  uncertainty.

The MC burnup uncertainty propagation analyses are conducted by using the covariance data of 10 isotopes— $^{235}\text{U}$ ,  $^{238}\text{U}$ ,  $^{239}\text{Pu}$ ,  $^{240}\text{Pu}$ ,  $^{241}\text{Pu}$ ,  $^{242}\text{Pu}$ ,  $^{241}\text{Am}$ ,  $^{242\text{m}}\text{Am}$ ,  $^{243}\text{Am}$ , and

$^{244}\text{Cm}$ . The McCARD eigenvalue calculations are performed on 100 active cycles with 10,000 histories per cycle. Table 2 shows the RSD of  $k_{\text{inf}}$  as a function of the burnup steps for the two cases using the ENDF/B-VII.1 and SCALE6.1/COVA-44G covariance data. From the figures, one can observe that the  $k$  uncertainties from the ENDF/B-VII.1 covariance data are decreasing, while those from SCALE6.1/COVA-44G are increasing, with the advancing burnup steps from 8 MWd/kgU. Figures 2 and 3 show the contributions of  $\sigma_S$ ,  $\sigma_{NN}$ , and  $\sigma_{XX}$  to the  $k$  uncertainties from the ENDF/B-VII.1 and SCALE6.1/COVA-44G covariance data, respectively.

Table 3 shows the RSD of one group reaction rates versus pin burnup for the cases using the ENDF/B-VII.1 and SCALE6.1/COVA-44G covariance data. From the table, we can observe that there are no great differences between the reaction rate uncertainties estimated from the ENDF/B-VII.1 and SCALE6.1/COVA-44G covariance data. Table 4 shows

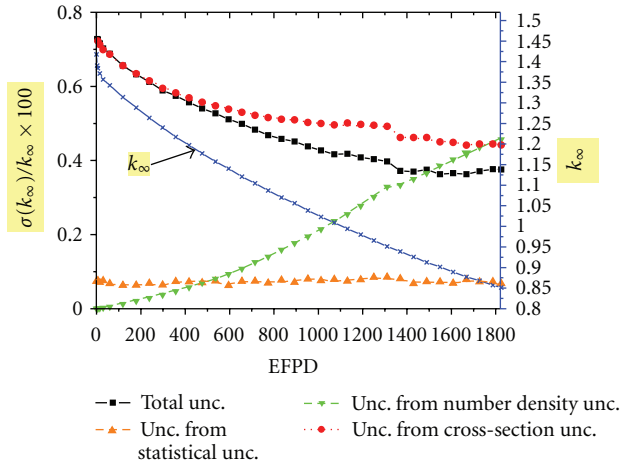


FIGURE 2:  $k_{inf}$  and  $\sigma[k_{inf}]$  versus pin burnup with ENDF/B-VII.1 covariance data.

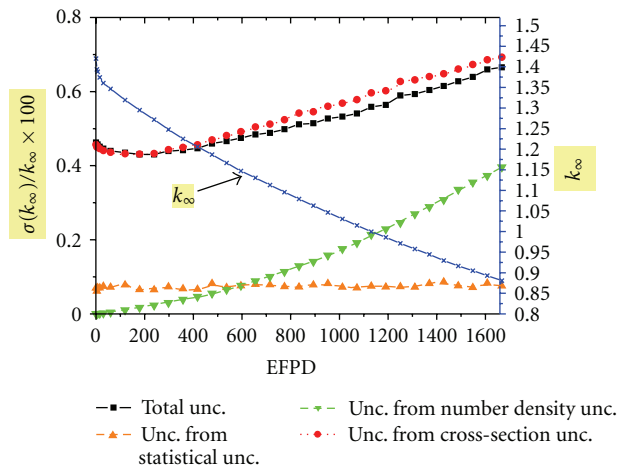


FIGURE 3:  $k_{inf}$  and  $\sigma[k_{inf}]$  versus pin burnup with SCALE6.1/COVA-43G covariance data.

RSDs of number densities estimated from the two covariance data as a function of, and the cooling time after, irradiation period.

#### 4. Conclusion

The McCARD uncertainty propagation analyses with different covariance data files have been performed for the TMI-1 burnup pin-cell problem in Phase I of the OECD LWR UAM benchmarks. The numerical results show that the uncertainty behavior over burnup strongly depends on the nuclear covariance data.

#### Acknowledgment

This work was performed through the contract with Korea Institute of Nuclear Safety as part of its research project “Development of Licensing Technologies for Very High Temperature Reactor” which is funded by Ministry of Education and Science of Korea.

#### References

- [1] D. L. Poston and H. R. Trelle, “User’s manual, version 2.0 for MONTEBURNS version 1.0,” LA-UR-99-4999, Los Alamos National Laboratory, 1999.
- [2] J. S. Hendricks, G. W. McKinney, L. S. Waters, T. L. Roberts, H. W. Egdorf, J. P. Finch et al., “MCNPX, Version 2.5.E,” LAUR-04-0569, Los Alamos National Laboratory, 2004.
- [3] K. Okumura, T. Mori, M. Nakagawa, and K. Kaneko, “Validation of a continuous-energy Monte Carlo burn-up code MVP-BURN and its application to analysis of post irradiation experiment,” *Journal of Nuclear Science and Technology*, vol. 37, no. 2, pp. 128–138, 2000.
- [4] H. J. Shim, B. S. Han, J. S. Jung, H. J. Park, and C. H. Kim, “McCARD: monte carlo code for advanced reactor design and analysis,” *Nuclear Engineering and Technology*, vol. 44, no. 2, pp. 161–176, 2012.
- [5] J. Leppänen, “PSG2/serpent—a continuous-energy monte carlo reactor physics burnup calculation code,” VTT Technical Research Centre of Finland, 2008, <http://montecarlo.vtt.fi/>.
- [6] T. Takeda, N. Hirokawa, and T. Noda, “Estimation of error propagation in Monte-Carlo burnup calculations,” *Journal of Nuclear Science and Technology*, vol. 36, no. 9, pp. 738–745, 1999.
- [7] M. Tohjoh, T. Endo, M. Watanabe, and A. Yamamoto, “Effect of error propagation of nuclide number densities on Monte Carlo burn-up calculations,” *Annals of Nuclear Energy*, vol. 33, no. 17-18, pp. 1424–1436, 2006.
- [8] N. García-Herranz, O. Cabellos, J. Sanz, J. Juan, and J. C. Kuipjer, “Propagation of statistical and nuclear data uncertainties in Monte Carlo burn-up calculations,” *Annals of Nuclear Energy*, vol. 35, no. 4, pp. 714–730, 2008.
- [9] H. J. Park, H. J. Shim, and C. H. Kim, “Uncertainty propagation in monte carlo depletion analysis,” *Nuclear Science and Engineering*, vol. 167, no. 3, pp. 196–208, 2011.
- [10] W. Zwermann, L. Gallner, M. Klein, B. Krzykacz-Hausmann, A. Pautz, and K. Velkov, “XSUSA solution for the PWR Pin-cell burnup benchmark,” in *Proceedings of the 6th Workshop on OECD Benchmark for Uncertainty Analysis in Best-Estimate Modeling for Design, Operation and Safety Analysis of LWRs (UAM-6)*, Karlsruhe, Germany, May 2012.
- [11] D. Rochmann and C. M. Sciolla, “Total Monte Carlo applied to Phase I-1: Burn-up Calculation,” in *Proceedings of the 6th Workshop on OECD Benchmark for Uncertainty Analysis in Best-Estimate Modeling for Design, Operation and Safety Analysis of LWRs (UAM-6)*, Karlsruhe, Germany, May 2012.
- [12] D. G. Cacuci, *Sensitivity and Uncertainty Analysis, Volume I: Theory*, Chapman & Hall/CRC, 2003.
- [13] K. Ivanov, M. Avramova, S. Kamerow et al., “Benchmark for uncertainty analysis in modeling (UAM) for design, operation and safety analysis of LWRs, volume I: specification and support data for the neutronics cases (Phase I),” NEA/NSC/DOC, Nuclear Energy Agency, 2012.
- [14] H. Rief, “Generalized Monte Carlo perturbation algorithms for correlated sampling and a second-order Taylor series approach,” *Annals of Nuclear Energy*, vol. 11, no. 9, pp. 455–476, 1984.
- [15] Y. Nagaya and T. Mori, “Impact of perturbed fission source on the effective multiplication factor in Monte Carlo perturbation calculations,” *Journal of Nuclear Science and Technology*, vol. 42, no. 5, pp. 428–441, 2005.
- [16] E. M. Gelbard and R. Prael, “Computation of standard deviations in Eigenvalue calculations,” *Progress in Nuclear Energy*, vol. 24, no. 1–3, pp. 237–241, 1990.

- [17] T. Ueki, T. Mori, and M. Nakagawa, "Error estimations and their biases in Monte Carlo eigenvalue calculations," *Nuclear Science and Engineering*, vol. 125, no. 1, pp. 1–11, 1997.
- [18] H. J. Shim and C. H. Kim, "Real variance estimation using an intercycle fission source correlation for Monte Carlo eigenvalue calculations," *Nuclear Science and Engineering*, vol. 162, no. 1, pp. 98–108, 2009.
- [19] R. E. MacFarlane and D. W. Muir, "NJOY99.0 code system for producing pointwise and multigroup neutron and photon cross sections from ENDF/B data," PSR-480/NJOY99.0, Los Alamos National Laboratory, 2000.

## Research Article

# Asymptotic Analysis for the Variance-Based Global Sensitivity Indices

**Pavel M. Bokov**

*Research and Development Division, The South African Nuclear Energy Corporation (Necsa), Building 1900, P.O. Box 582, Pretoria 0001, South Africa*

Correspondence should be addressed to Pavel M. Bokov, pavel.bokov@necsa.co.za

Received 24 April 2012; Accepted 8 August 2012

Academic Editor: Carlo Parisi

Copyright © 2012 Pavel M. Bokov. This is an open access article distributed under the Creative Commons Attribution License, which permits unrestricted use, distribution, and reproduction in any medium, provided the original work is properly cited.

We discuss the estimation of the uncertainty and sensitivity parameters for a model response under the assumption that the input variables are normally distributed and block-wise correlated with the covariance matrix, which is small in some norm. These conditions may arise when considering the impact of the group-wise neutron cross-sections' uncertainties on the uncertainty of some reactor parameters such as the neutron multiplication factor. The variance-based global sensitivity analysis, considered in our work, involves the calculation of multidimensional integrals. When the input uncertainties are small, the values of these integrals can be estimated using an asymptotic analysis method called the Laplace approximation. The asymptotic formulas for the output variance and for the global sensitivity indices have been obtained using the Laplace approximation method. It is demonstrated that the asymptotic formula for uncertainty propagation matches the uncertainty propagation formula being used in the local sensitivity analysis. The applicability of the obtained asymptotic approximations was successfully demonstrated on a test problem with realistic cross-section and covariance matrix values.

## 1. Introduction

Uncertainty analysis (UA) is a mathematical tool that allows one to quantify the uncertainty of the model output as a result of the uncertainty in the model input. If the input consists of more than one variable, another mathematical tool, sensitivity analysis (SA), may be used to quantify the contribution of each parameter to the output uncertainty. SA and UA methods can be gathered in two broad families: local sensitivity analysis (LSA) and global sensitivity analysis (GSA).

LSA methods allow one to analyze the behavior of the model output in the vicinity of a chosen point. They are usually efficient in computer time but may be inadequate for nonlinear models. GSA methods allow one to explore the full-phase space of input parameters and to take the nonlinearity of the model into account. GSA methods are generally more computationally intensive than LSA methods. The major difference between these two approaches can be summarized with the following quote from Sobol' [1]: "Global sensitivity indices should be regarded as a tool for studying the mathematical model rather than its specified

solution." A detailed discussion on SA methods can be found in [1–3]. The overview of SA as applied in the nuclear reactor calculation field is given in [4] and the references therein.

In this paper we will concentrate our attention on the so-called variance-based GSA. Amongst different GSA methods, the variance-based methods are the methods of preference because they are well established, robust and model-independent. On the other hand, despite the attractiveness of the variance-based GSA, UA, and SA for nuclear reactor problems are traditionally based on the LSA methods and rarely on GSA methods. The reason why the variance-based GSA method was not widely applied is that there are a few obstacles in the way of their implementation in reactor calculations. The first obstacle is the correlation between input parameters, that makes the variance-based GSA in its traditional formulation meaningless. This limitation may appear, for example, when considering multigroup neutron cross-sections as input parameters, which may have correlations between cross-sections from different energy groups. The partial remedy for this problem was proposed by Jacques et al. [5], who remarked that the variance-based

GSA is still applicable to the mutually independent subsets of input variables. Another, more radical solution, is to abandon the variance-based GSA and to use, for instance, entropy-based GSA [6, 7]. Entropy-based GSA methods can be used for correlated inputs, but they are not as well-established as variance-based ones, are algorithmically more complex and computationally more expensive. The second obstacle is the potential impracticality (and even intractability) when the number of input parameters is big. This problem appears because GSA methods involve the calculation of multidimensional integrals and is traditionally circumvented by applying the integration methods suitable for multidimensional problems, such as Monte Carlo [1, 8] or sparse grid [9, 10] quadratures. These quadratures are often applied in conjunction with model reduction methods [11–13], which are often based on the functional ANOVA (analysis of variance) decomposition [8, 14]. When applied in the field of nuclear reactor calculations, UA and SA methods have an additional limitation: the model value is often the result of an expensive calculation and this limits the number of samples available for the analysis.

Nevertheless, there are some indications that a large number of samples may not be needed for practical applications. Adetula and Bokov [15, 16] described a numerical method for the calculation of global sensitivity parameters for multigroup cross-section dependent problems with block-wise correlated inputs. The method was illustrated using a test two-group problem that involved realistic cross-section data. Various integration techniques were used and one of them, sparse grid quadrature, has demonstrated a surprisingly good accuracy with a small number of sample points. Moreover, it was observed that the interaction between inputs is negligible. Hence, it was concluded that the model is virtually additive and can be approximated with low-order polynomials. This result was explained with the following hypothesis: the uncertainty in cross-sections is so small that only the vicinity of the cross-section mean values contributes to the integrals used in the estimation of sensitivity indices. In this vicinity the neutron multiplication factor can be approximated with a fairly linear function. This hypothesis was tested and confirmed empirically (see [15, 16] for detail), but none theoretical support has been provided.

The present work aims to fill this gap and to provide a theoretical explanation and a quantitative description of this phenomenon. The idea behind this hypothesis is rather simple and may be illustrated with the sketch given in Figure 1 for a one-dimensional case. Consider a model represented with a smooth function  $f(x)$ , where the input variable  $x$  is normally distributed with a mean  $\mu$  and a standard deviation  $\sigma$ . Let us assume that it is necessary to evaluate the integral in the following form:

$$I = \int_{-\infty}^{+\infty} f(x)p(x)dx, \quad (1)$$

where  $p(x)$  is the probability density function for  $x$ . As one can observe in Figure 1, only the interval under the Gaussian (which is of the order of a few  $\sigma$ ) effectively contributes to the integral. In the limit, when  $\sigma \rightarrow 0$ , that corresponds to the case  $\sigma = \sigma_0$ , the probability distribution becomes the

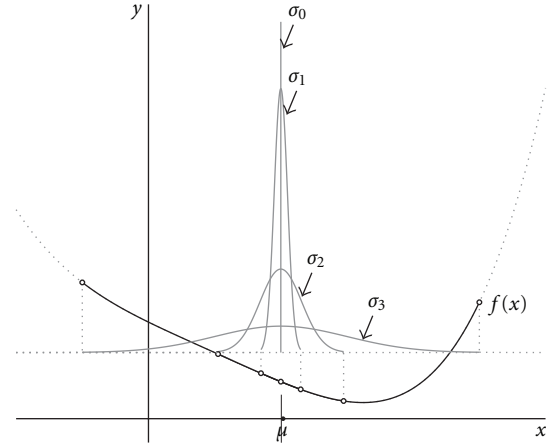


FIGURE 1: Effective vicinities of the cross-section mean, which contribute to the integral, for the standard deviations  $\sigma_3 > \sigma_2 > \sigma_1 > \sigma_0 = 0$ . Dots on the curve  $y = f(x)$  represent the boundaries of the corresponding effective intervals on which integrand is essentially not zero.

delta function and the contribution of the function to the integral is point-wise, that is,  $I = f(\mu)$ . When  $\sigma$  is small enough, as in the case  $\sigma = \sigma_1$ , the part of the function  $f(x)$ , contributing to the integral, is almost linear. Finally, if the the Gaussian spans wider intervals, then the nonlinearity of  $f(x)$  becomes progressively more prominent (see cases for  $\sigma = \sigma_2$  and  $\sigma = \sigma_3$ ). A similar behavior can be observed in the multi-dimensional case. The qualitative description of this behavior in a one- and multidimensional case can be given using a method known as the Laplace approximation through the asymptotic approximation of the involved integral.

In this work we intend to apply the Laplace method for the calculation of the output variance and sensitivity indices as they are defined in GSA. The application of the Laplace approximation in a one-dimensional case is relatively straightforward, while in a multidimensional case it may become cumbersome, this is why we limit our approximation with the first nonvanishing term in the approximation. Nevertheless, as we will demonstrate below, this approximation is sufficient to explain the results as obtained in [15, 16].

The rest of the paper is organized in the following way. Section 2 provides necessary definitions followed by a derivation of the asymptotic approximation. Section 3 is used to discuss the asymptotic approximation. Section 4 contains the description and analysis of the test problem. Finally, Section 5 is used to present our conclusions.

## 2. Asymptotic Approximation of Sensitivity Indices

**2.1. Variance-Based Global Sensitivity Analysis.** Let  $\mathcal{X} = \{X_1, X_2, \dots, X_d\}$  be a set of continuous random variables,  $\mathcal{X}_u$  be its arbitrary subset and  $\mathcal{X}_v$  be a subset of complimentary variables, that is,  $\mathcal{X} = \mathcal{X}_u \cup \mathcal{X}_v$ . The random variables can be gathered into the corresponding column vectors:  $\mathbf{X}_u$ ,  $\mathbf{X}_v$ , and  $\mathbf{X} = (\mathbf{X}_u, \mathbf{X}_v)$ . Following the arguments given

in [5, 15, 16], we assume that random variables from  $\mathcal{X}_u$  and  $\mathcal{X}_v$  are mutually statistically independent, hence their joint probability function is the product of the marginal probability density functions:

$$p(\mathbf{x}) = p(\mathbf{x}_u)p(\mathbf{x}_v). \quad (2)$$

Note that we will use, as is the rule in statistics, a capital letter (e.g.,  $X_i$ ) to denote a random variable and the corresponding lowercase letter ( $x_i$ ) to denote its value (realizations). Let us assume that the random variables  $X_i$  ( $i = 1, 2, \dots, d$ ) are distributed according to the normal law with known means and covariances. The multivariate normal distribution is characterized by the probability density function [17]

$$p(\mathbf{x}) = \frac{1}{(2\pi)^{d/2} \det(\boldsymbol{\Sigma})^{1/2}} \exp\left[-\frac{1}{2}(\mathbf{x} - \boldsymbol{\mu})^T \boldsymbol{\Sigma}^{-1}(\mathbf{x} - \boldsymbol{\mu})\right], \quad (3)$$

where  $\mathbf{X}$  is the column vector of the input random variables,  $\boldsymbol{\mu} = E[\mathbf{X}]$  is the column vector of their expected values,  $\boldsymbol{\Sigma} = E[(\mathbf{x} - \boldsymbol{\mu})(\mathbf{x} - \boldsymbol{\mu})^T]$  is the covariance matrix and  $E$  denotes the mathematical expectation and the symbol “ $T$ ” denotes the operation of transposing a row to a column.

Consider a model

$$Y = f(X_1, X_2, \dots, X_d) = f(\mathbf{X}), \quad (4)$$

where the function  $f : \mathbb{R}^d \rightarrow \mathbb{R}$  is generally nonlinear and may result from numerical calculations.  $X_i$  are called inputs and  $Y$  is called the output or response. The response  $Y = f(\mathbf{X})$  is a random variable itself, with the expected value  $f_{\mathcal{O}} = E[f(\mathbf{X})]$  and the variance  $D = E[(f(\mathbf{X}) - f_{\mathcal{O}})^2]$ . The variance of the output,  $D$ , can be used to characterize the uncertainty in the response due to the uncertainty in the input, or in other words, the uncertainty propagation. Note that  $D$  can be calculated, regardless of whether the normally distributed inputs are correlated or not. Sensitivity indices characterize the contribution of a subset  $\mathcal{X}_u$  (and, correspondingly, vector  $\mathbf{X}_u$ ) to the response variance and they are meaningful only if subset  $\mathcal{X}_u$  and its complementary subset  $\mathcal{X}_v$  are statistically independent. Two types of global sensitivity indices, with respect to a subset  $\mathcal{X}_u$ , can be introduced:

- (1)  $S_{\mathbf{X}_u}$ , which is called the main sensitivity index (MSI) and it represents the effect due to  $\mathbf{X}_u$  only;
- (2)  $S_{\mathbf{X}_u}^{\text{tot}}$ , which is called the total sensitivity index (TSI) and it represents the contribution to the variance of  $\mathbf{X}_u$  along with all the interactions of this variable with other variables.

The global sensitivity indices can be calculated using the ratios [1, 8]

$$S_{\mathbf{X}_u}^{\text{tot}} = \frac{D_{\mathbf{X}_u}^{\text{tot}}}{D}, \quad S_{\mathbf{X}_u} = \frac{D_{\mathbf{X}_u}}{D}, \quad (5)$$

where parameters  $D$ ,  $D_{\mathbf{X}_u}$ , and  $D_{\mathbf{X}_u}^{\text{tot}}$  can be calculated through the following multidimensional integrals [12, 15, 16]:

$$f_{\mathcal{O}} = \int_{\mathbb{R}^d} f(\mathbf{x})p(\mathbf{x})d\mathbf{x}, \quad (6)$$

$$D = \int_{\mathbb{R}^d} f^2(\mathbf{x})p(\mathbf{x})d\mathbf{x} - f_{\mathcal{O}}^2, \quad (7)$$

$$D_{\mathbf{X}_u} = \int_{\mathbb{R}^{2d - \dim(\mathbf{X}_u)}} f(\mathbf{x})f(\mathbf{x}_u, \mathbf{x}'_v)p(\mathbf{x})p(\mathbf{x}'_v)d\mathbf{x}d\mathbf{x}'_v - f_{\mathcal{O}}^2, \quad (8)$$

$$D_{\mathbf{X}_u}^{\text{tot}} = \frac{1}{2} \int_{\mathbb{R}^{d + \dim(\mathbf{X}_u)}} [f(\mathbf{x}) - f(\mathbf{x}'_u, \mathbf{x}_v)]^2 p(\mathbf{x})p(\mathbf{x}'_u)d\mathbf{x}d\mathbf{x}'_u, \quad (9)$$

which are a generalization of the classical formulas given by Sobol' [1, 8]. Here the prime symbol over a variable (e.g., as in  $\mathbf{x}'_u$ ) means that this variable has to be sampled independently from the corresponding marginal distribution ( $p(\mathbf{x}'_u)$  in this case) of its unprimed analogue and  $\dim(\cdot)$  is the number of elements in a vector, that is, the dimensionality of the vector. Calculation of the sensitivity indices requires the calculation of integrals (6)–(9), which can be written in the following general form:

$$E[g] = \int_{\mathbb{R}^{d_{\text{eff}}}} g(\tilde{\mathbf{x}})p(\tilde{\mathbf{x}})d\tilde{\mathbf{x}}, \quad (10)$$

where the integration operator  $E[\cdot]$  denotes the mathematical expectation with respect to extended random variables  $\tilde{\mathbf{X}}$ ,  $g(\tilde{\mathbf{x}})$  represents a function being integrated and  $d_{\text{eff}} = \dim(\tilde{\mathbf{X}})$  is the effective dimensionality of the integral. For instance, in integral (8) function  $g(\tilde{\mathbf{x}})$  represents  $[f(\mathbf{x})f(\mathbf{x}_u, \mathbf{x}'_v)]$ ,  $\tilde{\mathbf{x}}$  represents  $(\mathbf{x}_u, \mathbf{x}_v, \mathbf{x}'_v)$ , and the effective dimensionality is  $d_{\text{eff}} = 2d - \dim(\mathbf{X}_u)$ . Similarly, in the integral (6) function  $g(\tilde{\mathbf{x}})$  represents  $f(\mathbf{x})$ ,  $\tilde{\mathbf{x}} = \mathbf{x}$  and  $d_{\text{eff}} = d$ .

*2.2. Laplace Approximation of Integrals.* In the limit when elements of the covariance matrix are small in some norm, one can use for the calculation of integrals (6)–(9) the asymptotic analysis technique known as the Laplace approximation. The Laplace approximation is an approximation to integrals in the following form:

$$I(\lambda) = \int_{\Omega} h(\mathbf{x}) \exp[\lambda R(\mathbf{x})] d\mathbf{x}, \quad (11)$$

as  $\lambda \rightarrow \infty$  with  $\lambda > 0$ . Here  $\Omega$  is a measurable subset of  $\mathbb{R}^d$  and  $R(\mathbf{x})$  is a real-valued function of  $\mathbf{x}$ . When applying the Laplace approximation formula, it is assumed that  $R(\mathbf{x})$  is an infinity differentiable function with its maximum value at a single point  $\mathbf{x}_0$  in the interior of  $\Omega$  (see [18] for details) and  $h(\mathbf{x})$  is a sufficiently smooth function of its argument.

Integrals in the form (10), used for the calculation of sensitivity indices, fulfill the above requirements for the applicability of the Laplace approximation formula if one considers  $\mathbf{x}_0 = \boldsymbol{\mu}$  and assumes that elements of the covariance matrix  $\boldsymbol{\Sigma}$  are small. Let us assume that the covariance matrix  $\boldsymbol{\Sigma}$  is small in some norm, that is, in the limit  $\|\boldsymbol{\Sigma}\| \rightarrow 0$ . For the sake of the asymptotic analysis, let us introduce the big

parameter  $\lambda$  as the inverse absolute value of the determinant of the covariance matrix

$$\lambda = |\det(\boldsymbol{\Sigma})|^{-1}. \quad (12)$$

We will assume that the covariance matrix is strictly positive definite, hence the absolute value sign in (12) may be omitted. Factoring out the coefficient  $\lambda$  allows us to introduce the normalized covariance matrix

$$\mathbf{C} = \Sigma |\det(\boldsymbol{\Sigma})|^{-1} = \lambda \boldsymbol{\Sigma}. \quad (13)$$

Taking into account that  $\det(\mathbf{C}) = \det(\lambda \boldsymbol{\Sigma}) = \lambda^d \det(\boldsymbol{\Sigma})$ , the probability density function (3) can be written in a form suitable for the Laplace approximation:

$$p(\mathbf{x}) = \frac{1}{|\det(\mathbf{C})|^{1/2}} \left( \frac{\lambda}{2\pi} \right)^{d/2} \exp \left[ -\lambda \frac{1}{2} (\mathbf{x} - \boldsymbol{\mu})^T \mathbf{C}^{-1} (\mathbf{x} - \boldsymbol{\mu}) \right]. \quad (14)$$

The covariance matrix  $\boldsymbol{\Sigma}$  is real-valued, symmetric, and positively definite, hence matrix  $\mathbf{C}$  allows the Cholesky factorization:

$$\mathbf{C} = \mathbf{L} \mathbf{L}^T, \quad (15)$$

where  $\mathbf{L}$  is a lower triangular matrix with strictly positive diagonal entries. The exponent in the joint probability density function can then be transformed in the following way:

$$\lambda \frac{1}{2} (\mathbf{x} - \boldsymbol{\mu})^T \mathbf{C}^{-1} (\mathbf{x} - \boldsymbol{\mu}) = \lambda \frac{1}{2} \mathbf{z}^T \mathbf{z}, \quad (16)$$

where new random variables  $Z_i$  ( $i = 1, \dots, d$ ) are introduced by the linear transformation  $\mathbf{z} = \mathbf{L}^{-1}(\mathbf{x} - \boldsymbol{\mu})$ . The initial variables  $\mathbf{X}$  can be obtained via the inverse linear transformation

$$\mathbf{x} = \mathbf{L} \mathbf{z} + \boldsymbol{\mu}. \quad (17)$$

Changing variables  $\mathbf{x} \rightarrow \mathbf{z}$  by using the linear transformation (17) in the integral (10) and taking into account that the Jacobian matrix for this transformation is

$$\frac{\partial \mathbf{x}}{\partial \mathbf{z}} = \frac{\partial (x_1, \dots, x_d)}{\partial (z_1, \dots, z_d)} = \mathbf{L} \quad (18)$$

gives for the integral (10):

$$E[g] = |\det(\mathbf{L})| \int_{\mathbb{R}^d} g(\mathbf{L} \mathbf{z} + \boldsymbol{\mu}) p(\mathbf{L} \mathbf{z} + \boldsymbol{\mu}) d\mathbf{z}. \quad (19)$$

Taking into account that  $|\det(\mathbf{C})| = |\det(\mathbf{L} \mathbf{L}^T)| = |\det(\mathbf{L})|^2$  and substituting the explicit formula for  $p(\mathbf{x}[\mathbf{z}])$  after the change of variables, one obtains

$$E[g] = \left( \frac{\lambda}{2\pi} \right)^{d/2} \int_{\mathbb{R}^d} g(\mathbf{L} \mathbf{z} + \boldsymbol{\mu}) \exp \left[ -\frac{1}{2} \lambda \mathbf{z}^T \mathbf{z} \right] d\mathbf{z}. \quad (20)$$

The Laplace approximation formula for (11) can be found, for example, in [18]. Applying this formula to integral (20) leads, after a few simplifications, to the asymptotic series:

$$E[g] \sim \sum_{m=0}^{\infty} c_m \lambda^{-m}, \quad (21)$$

where

$$c_m = \frac{1}{2^m} \times \sum_{p_1 + \dots + p_d = 2m (p_k \text{ all even})} \frac{\partial^{2m}}{\partial z_1^{p_1} \dots \partial z_d^{p_d}} g(\mathbf{L} \mathbf{z} + \boldsymbol{\mu}) \Big|_{\mathbf{z}=0} \times \prod_{k=1}^d \frac{1}{(p_k/2)!}. \quad (22)$$

If the expansion is truncated at  $m = 0$ , the obtained formula is usually referred to as the Laplace approximation with  $c_0 = g(\boldsymbol{\mu})$ . For many applications this is sufficient, but not for ours: as will be shown below, the first nontrivial term in the asymptotic expansion for integrals (6)–(9) is linear with respect to  $(\lambda^{-1})$ . Therefore, we retain the first two terms in the asymptotic expansion:

$$E[g] = g(\boldsymbol{\mu}) + \frac{1}{2\lambda} \sum_{k=1}^d \frac{\partial^2}{\partial z_k^2} g(\mathbf{L} \mathbf{z} + \boldsymbol{\mu}) \Big|_{\mathbf{z}=0} + O(\lambda^{-2}). \quad (23)$$

By introducing the  $d$ -dimensional gradient and the Laplace operators, defined as:

$$\nabla_{\mathbf{z}} = \left( \frac{\partial}{\partial z_1}, \dots, \frac{\partial}{\partial z_d} \right)^T, \quad \nabla_{\mathbf{z}}^2 = \sum_{k=1}^d \frac{\partial^2}{\partial z_k^2}, \quad (24)$$

respectively, one can write (23) in a compact form:

$$E[g] = g(\boldsymbol{\mu}) + \frac{1}{2\lambda} \nabla_{\mathbf{z}}^2 g(\mathbf{L} \mathbf{z} + \boldsymbol{\mu}) \Big|_{\mathbf{z}=0} + O(\lambda^{-2}). \quad (25)$$

The subscript next to the nabla operator (e.g.,  $\mathbf{z}$  next to  $\nabla_{\mathbf{z}}$ ) will be used to indicate explicitly the variables with respect to which partial derivatives are taken. Asymptotic formulas (23)–(25) can now be applied for the estimation of the integrals (6)–(9) used in the calculation of sensitivity indices.

### 2.3. Calculation of Sensitivity Indices

**2.3.1. Variance.** In order to calculate parameter  $D$ , given by (7), one can use the well-known statistical formula for the variance:

$$D = E[f^2(\mathbf{x})] - (E[f(\mathbf{x})])^2, \quad (26)$$

where  $f_{\mathcal{O}} = E[f(\mathbf{x})]$  is substituted. As one can see from (26) two integrations are needed: for  $f(\mathbf{x})$  and  $f^2(\mathbf{x})$ . We will approximate these integrals independently to the second order, that is,  $O(\lambda^{-2})$ . The application of the approximation formula (25) to the first term in (26) yields

$$\begin{aligned} E[f^2(\mathbf{x})] &= f^2(\boldsymbol{\mu}) + \frac{1}{2\lambda} \nabla_{\mathbf{z}}^2 f^2(\mathbf{L} \mathbf{z} + \boldsymbol{\mu}) \Big|_{\mathbf{z}=0} + O(\lambda^{-2}) \\ &= f^2(\boldsymbol{\mu}) + \frac{1}{\lambda} [\nabla_{\mathbf{z}} f(\mathbf{L} \mathbf{z} + \boldsymbol{\mu}) \cdot \nabla_{\mathbf{z}} f(\mathbf{L} \mathbf{z} + \boldsymbol{\mu}) \\ &\quad + f(\boldsymbol{\mu}) \nabla_{\mathbf{z}}^2 f(\mathbf{L} \mathbf{z} + \boldsymbol{\mu})] \Big|_{\mathbf{z}=0} \\ &\quad + O(\lambda^{-2}). \end{aligned} \quad (27)$$

Note, that the vector algebra formula

$$\nabla^2(\varphi\psi) = \nabla \cdot \nabla(\varphi\psi) = 2(\nabla\varphi) \cdot (\nabla\psi) + \psi\nabla^2\varphi + \varphi\nabla^2\psi \quad (28)$$

for the Laplacian of the product of two scalar fields,  $\varphi$  and  $\psi$  was used in the above derivation.

The approximation formula for  $f_{\mathcal{O}}$  can be obtained by a simple substitution of  $f(\mathbf{x})$  instead of  $g(\mathbf{x})$  into (25), that is,

$$f_{\mathcal{O}} = E[f(\mathbf{x})] = f(\boldsymbol{\mu}) + \frac{1}{2\lambda} \nabla_z^2 f(\mathbf{Lz} + \boldsymbol{\mu}) \Big|_{z=0} + O(\lambda^{-2}). \quad (29)$$

Keeping the terms up to the second order with respect to  $\lambda^{-1}$  in the asymptotic approximation of  $f_{\mathcal{O}}^2$  gives

$$f_{\mathcal{O}}^2 = (E[f(\mathbf{x})])^2 = f^2(\boldsymbol{\mu}) + f(\boldsymbol{\mu}) \frac{1}{\lambda} \nabla_z^2 f(\mathbf{Lz} + \boldsymbol{\mu}) \Big|_{z=0} + O(\lambda^{-2}). \quad (30)$$

For the sake of the derivation in the next section, let us rewrite (30) in a different form:

$$f_{\mathcal{O}}^2 = (E[f(\mathbf{x})])^2 = f^2(\boldsymbol{\mu}) + f(\boldsymbol{\mu}) \text{tr}(\boldsymbol{\Sigma}\mathbf{H}) + O(\lambda^{-2}), \quad (31)$$

where  $\text{tr}(\cdot)$  denotes the trace of a matrix and  $\mathbf{H}$  is the Hessian matrix for the function  $f(\mathbf{x})$  at a point  $\mathbf{x} = \boldsymbol{\mu}$  with the matrix elements defined as

$$\mathbf{H}_{ij} = \frac{\partial^2 f(\mathbf{x})}{\partial \mathbf{x}_i \partial \mathbf{x}_j} \Big|_{\mathbf{x}=\boldsymbol{\mu}} \quad \text{for } i, j = 1, 2, \dots, d. \quad (32)$$

After substitution of (27) and (30) into (26), one obtains the asymptotic approximation to the variance of  $f$ :

$$D = \frac{1}{\lambda} \nabla_z f(\mathbf{Lz} + \boldsymbol{\mu}) \cdot \nabla_z f(\mathbf{Lz} + \boldsymbol{\mu}) \Big|_{z=0} + O(\lambda^{-2}). \quad (33)$$

Returning back to the initial variables  $\mathbf{X}$  and taking into account that the gradient operator transforms as

$$\nabla_z f(\mathbf{Lz} + \boldsymbol{\mu}) = \mathbf{L}^T \nabla_{\mathbf{x}} f(\mathbf{x}), \quad (34)$$

where  $\nabla_{\mathbf{x}} f(\mathbf{x})$  is the gradient of  $f$  with respect to the ‘‘initial’’ variables  $X_i$  (where  $i = 1, 2, \dots, d$ ), (33) becomes

$$D = \frac{1}{\lambda} \nabla_{\tilde{\mathbf{x}}}^T f(\mathbf{x}) \mathbf{L} \mathbf{L}^T \nabla_{\mathbf{x}} f(\mathbf{x}) \Big|_{\mathbf{x}=\boldsymbol{\mu}} + O(\lambda^{-2}). \quad (35)$$

Furthermore, taking into account properties (13) and (15), one obtains:

$$D = \nabla_{\tilde{\mathbf{x}}}^T f(\mathbf{x}) \boldsymbol{\Sigma} \nabla_{\mathbf{x}} f(\mathbf{x}) \Big|_{\mathbf{x}=\boldsymbol{\mu}} + O(\lambda^{-2}). \quad (36)$$

Finally, by introducing the sensitivity vector  $\mathbf{s} = \nabla_{\mathbf{x}} f(\mathbf{x}) \Big|_{\mathbf{x}=\boldsymbol{\mu}}$  the asymptotic formula for  $D$  can be written as:

$$D = \mathbf{s}^T \boldsymbol{\Sigma} \mathbf{s} + O(\lambda^{-2}). \quad (37)$$

2.3.2. *Numerator in the Formula for MSI.* Formula (8) contains the integrand, which depends on variables from  $\mathcal{X}_u$ ,  $\mathcal{X}_v$ , and  $\mathcal{X}'_v$ . Let us introduce the extended vector of input variables:

$$\tilde{\mathbf{X}} = \begin{bmatrix} \mathbf{X}_u \\ \mathbf{X}_v \\ \mathbf{X}'_v \end{bmatrix}. \quad (38)$$

Note that the tilde symbol will be used for extended variables. By the assumptions discussed previously  $\mathbf{X}_u$ ,  $\mathbf{X}_v$ , and  $\mathbf{X}'_v$  are statistically independent, hence  $p(\tilde{\mathbf{x}}) = p(\mathbf{x}_u)p(\mathbf{x}_v)p(\mathbf{x}'_v)$ . Therefore, the random vector  $\tilde{\mathbf{X}}$  has the mean  $\tilde{\boldsymbol{\mu}}$  and the covariance matrix  $\tilde{\boldsymbol{\Sigma}}$ , which can be written in the following block form:

$$\tilde{\boldsymbol{\mu}} = \begin{bmatrix} \boldsymbol{\mu}_u \\ \boldsymbol{\mu}_v \\ \boldsymbol{\mu}'_v \end{bmatrix}, \quad \tilde{\boldsymbol{\Sigma}} = \begin{bmatrix} \boldsymbol{\Sigma}_{uu} & \mathbf{0} & \mathbf{0} \\ \mathbf{0} & \boldsymbol{\Sigma}_{vv} & \mathbf{0} \\ \mathbf{0} & \mathbf{0} & \boldsymbol{\Sigma}_{v'v'} \end{bmatrix}. \quad (39)$$

Let us introduce auxiliary functions:  $\varphi(\tilde{\mathbf{x}}) \equiv f(\mathbf{x}_u, \mathbf{x}_v)$  and  $\psi(\tilde{\mathbf{x}}) \equiv f(\mathbf{x}_u, \mathbf{x}'_v)$  for convenience. Applying formula (28) to  $g(\tilde{\mathbf{x}}) \equiv \varphi(\tilde{\mathbf{x}})\psi(\tilde{\mathbf{x}})$  and following the path used in the previous section, one obtains the asymptotic approximation of the first term in (8):

$$\begin{aligned} E[\varphi(\tilde{\mathbf{x}})\psi(\tilde{\mathbf{x}})] &= \varphi(\tilde{\mathbf{x}})\psi(\tilde{\mathbf{x}}) \Big|_{\tilde{\mathbf{x}}=\tilde{\boldsymbol{\mu}}} + \nabla_{\tilde{\mathbf{x}}}^T \varphi(\tilde{\mathbf{x}}) \tilde{\boldsymbol{\Sigma}} \nabla_{\tilde{\mathbf{x}}} \psi(\tilde{\mathbf{x}}) \Big|_{\tilde{\mathbf{x}}=\tilde{\boldsymbol{\mu}}} \\ &+ \frac{1}{2} \left[ \varphi(\tilde{\mathbf{x}}) \text{tr}(\tilde{\boldsymbol{\Sigma}}\tilde{\mathbf{H}}) + \psi(\tilde{\mathbf{x}}) \text{tr}(\tilde{\boldsymbol{\Sigma}}\tilde{\mathbf{H}}') \right] \Big|_{\tilde{\mathbf{x}}=\tilde{\boldsymbol{\mu}}} \\ &+ O(\lambda^{-2}), \end{aligned} \quad (40)$$

where  $\tilde{\mathbf{H}}$  and  $\tilde{\mathbf{H}}'$  are the Hessian matrices for  $\varphi(\tilde{\mathbf{x}})$  and  $\psi(\tilde{\mathbf{x}})$ , respectively, at  $\tilde{\mathbf{x}} = \tilde{\boldsymbol{\mu}}$ . As follows from the definitions of functions  $\varphi(\tilde{\mathbf{x}})$  and  $\psi(\tilde{\mathbf{x}})$ , these matrices have the following block structure:

$$\tilde{\mathbf{H}} = \begin{bmatrix} \mathbf{H}_{uu} & \mathbf{H}_{uv} & \mathbf{0} \\ \mathbf{H}_{vu} & \mathbf{H}_{vv} & \mathbf{0} \\ \mathbf{0} & \mathbf{0} & \mathbf{0} \end{bmatrix}, \quad \tilde{\mathbf{H}}' = \begin{bmatrix} \mathbf{H}_{uu} & \mathbf{0} & \mathbf{H}_{uv} \\ \mathbf{0} & \mathbf{0} & \mathbf{0} \\ \mathbf{H}_{vu} & \mathbf{0} & \mathbf{H}_{vv} \end{bmatrix}, \quad (41)$$

where the blocks are formally defined as

$$\begin{aligned} \mathbf{H}_{uu} &= \frac{\partial^2 f(\mathbf{x})}{\partial \mathbf{x}_u \partial \mathbf{x}_u}, & \mathbf{H}_{vv} &= \frac{\partial^2 f(\mathbf{x})}{\partial \mathbf{x}_v \partial \mathbf{x}_v}, \\ \mathbf{H}_{uv} &= \mathbf{H}_{vu} = \frac{\partial^2 f(\mathbf{x})}{\partial \mathbf{x}_v \partial \mathbf{x}_u}. \end{aligned} \quad (42)$$

Similarly, gradients  $\nabla_{\tilde{\mathbf{x}}} \varphi(\tilde{\mathbf{x}}) \Big|_{\tilde{\mathbf{x}}=\tilde{\boldsymbol{\mu}}}$  and  $\nabla_{\tilde{\mathbf{x}}} \psi(\tilde{\mathbf{x}}) \Big|_{\tilde{\mathbf{x}}=\tilde{\boldsymbol{\mu}}}$  have the following matrix structure:

$$\nabla_{\tilde{\mathbf{x}}} \varphi(\tilde{\mathbf{x}}) \Big|_{\tilde{\mathbf{x}}=\tilde{\boldsymbol{\mu}}} = \begin{bmatrix} \mathbf{s}_u \\ \mathbf{s}_v \\ \mathbf{0} \end{bmatrix}, \quad \nabla_{\tilde{\mathbf{x}}} \psi(\tilde{\mathbf{x}}) \Big|_{\tilde{\mathbf{x}}=\tilde{\boldsymbol{\mu}}} = \begin{bmatrix} \mathbf{s}_u \\ \mathbf{0} \\ \mathbf{s}_v \end{bmatrix}, \quad (43)$$

where  $\mathbf{s}_u = \nabla_{\mathbf{x}_u} f(\mathbf{x}) \Big|_{\mathbf{x}=\boldsymbol{\mu}}$  and  $\mathbf{s}_v = \nabla_{\mathbf{x}_v} f(\mathbf{x}) \Big|_{\mathbf{x}=\boldsymbol{\mu}}$  are sensitivity vectors with respect to  $\mathbf{X}_u$  and  $\mathbf{X}_v$ . Taking into account (41) and (43), the trace operators in (40) can be modified

in the following way:  $\text{tr}(\tilde{\Sigma}\tilde{\mathbf{H}}) = \text{tr}(\tilde{\Sigma}\tilde{\mathbf{H}}') = \text{tr}(\Sigma_{uu}\mathbf{H}_{uu}) + \text{tr}(\Sigma_{vv}\mathbf{H}_{vv}) = \text{tr}(\Sigma\mathbf{H})$ . From the definitions of  $\varphi(\tilde{\mathbf{x}})$  and  $\psi(\tilde{\mathbf{x}})$  it follows that  $\varphi(\tilde{\boldsymbol{\mu}}) = \psi(\tilde{\boldsymbol{\mu}}) = f(\boldsymbol{\mu})$ , hence (43) becomes

$$E[\varphi(\tilde{\mathbf{x}})\psi(\tilde{\mathbf{x}})] = f^2(\boldsymbol{\mu}) + \mathbf{s}_u^T \Sigma_{uu} \mathbf{s}_u + f(\boldsymbol{\mu}) \text{tr}(\Sigma\mathbf{H}) + O(\lambda^{-2}). \quad (44)$$

After subtracting (31) from (44) one obtains the following approximation for the factor  $D_{X_u}$  in the formula for the Main Sensitivity Index:

$$D_{X_u} = \mathbf{s}_u^T \Sigma_{uu} \mathbf{s}_u + O(\lambda^{-2}). \quad (45)$$

**2.3.3. Numerator in the Formula for TSI.** The calculation of  $D_{X_u}^{\text{tot}}$  requires the calculation of integral (9). In this section let us introduce the extended variable vector as the column vector

$$\tilde{\mathbf{X}} = \begin{bmatrix} \mathbf{X}_u \\ \mathbf{X}_v \\ \mathbf{X}'_u \end{bmatrix}. \quad (46)$$

Vector  $\tilde{\mathbf{X}}$  has the mean and covariance matrix that have the following block representation:

$$\tilde{\boldsymbol{\mu}} = \begin{bmatrix} \boldsymbol{\mu}_u \\ \boldsymbol{\mu}_v \\ \boldsymbol{\mu}'_u \end{bmatrix}, \quad \tilde{\Sigma} = \begin{bmatrix} \Sigma_{uu} & \mathbf{0} & \mathbf{0} \\ \mathbf{0} & \Sigma_{vv} & \mathbf{0} \\ \mathbf{0} & \mathbf{0} & \Sigma_{uu} \end{bmatrix}. \quad (47)$$

Introducing, for convenience, the auxiliary functions:  $\varphi(\tilde{\mathbf{x}}) \equiv f(\mathbf{x}_u, \mathbf{x}_v)$ ,  $\chi(\tilde{\mathbf{x}}) \equiv f(\mathbf{x}'_u, \mathbf{x}_v)$  and  $\omega(\tilde{\mathbf{x}}) \equiv \varphi(\tilde{\mathbf{x}}) - \chi(\tilde{\mathbf{x}})$ , one can write function  $g(\tilde{\mathbf{x}})$  in (10) as

$$g(\tilde{\mathbf{x}}) = \frac{1}{2} \omega^2(\tilde{\mathbf{x}}). \quad (48)$$

The Laplace approximation for  $D_{X_u}^{\text{tot}} = E[g(\tilde{\mathbf{x}})]$  can be obtained by substituting function (48) into formula (25), which gives:

$$D_{X_u}^{\text{tot}} = \frac{1}{2} \omega^2(\tilde{\mathbf{x}})|_{\tilde{\mathbf{x}}=\tilde{\boldsymbol{\mu}}} + \frac{1}{4\lambda} \nabla_{\tilde{\mathbf{z}}}^2 \omega^2(\tilde{\mathbf{L}}\tilde{\mathbf{z}} + \tilde{\boldsymbol{\mu}})|_{\tilde{\mathbf{z}}=\mathbf{0}} + O(\lambda^{-2}). \quad (49)$$

From the definition of functions  $\varphi(\tilde{\mathbf{x}})$  and  $\chi(\tilde{\mathbf{x}})$  it follows that  $\omega(\tilde{\boldsymbol{\mu}}) = \mathbf{0}$  and the first term in (49) vanishes. The second term can be transformed in the following way:

$$\begin{aligned} D_{X_u}^{\text{tot}} &= \frac{1}{4\lambda} \nabla_{\tilde{\mathbf{z}}}^2 \omega^2(\tilde{\mathbf{L}}\tilde{\mathbf{z}} + \tilde{\boldsymbol{\mu}})|_{\tilde{\mathbf{z}}=\mathbf{0}} + O(\lambda^{-2}) \\ &= \frac{1}{2\lambda} \left[ \nabla_{\tilde{\mathbf{z}}} \omega(\tilde{\mathbf{L}}\tilde{\mathbf{z}} + \tilde{\boldsymbol{\mu}}) \cdot \nabla_{\tilde{\mathbf{z}}} \omega(\tilde{\mathbf{L}}\tilde{\mathbf{z}} + \tilde{\boldsymbol{\mu}}) \right. \\ &\quad \left. + \omega(\tilde{\boldsymbol{\mu}}) \cdot \nabla_{\tilde{\mathbf{z}}}^2 \omega(\tilde{\mathbf{L}}\tilde{\mathbf{z}} + \tilde{\boldsymbol{\mu}}) \right]|_{\tilde{\mathbf{z}}=\mathbf{0}} \\ &\quad + O(\lambda^{-2}) \\ &= \frac{1}{2} \nabla_{\tilde{\mathbf{x}}}^T \omega(\tilde{\mathbf{x}}) \tilde{\Sigma} \nabla_{\tilde{\mathbf{x}}} \omega(\tilde{\mathbf{x}})|_{\tilde{\mathbf{x}}=\tilde{\boldsymbol{\mu}}} + O(\lambda^{-2}). \end{aligned} \quad (50)$$

Taking into account the structure of the extended covariance matrix, given by (47), and the structure of the gradients in (50), given by

$$\nabla_{\tilde{\mathbf{x}}} \omega(\tilde{\mathbf{x}})|_{\tilde{\mathbf{x}}=\tilde{\boldsymbol{\mu}}} = \begin{bmatrix} -\mathbf{s}_u \\ \mathbf{0} \\ -\mathbf{s}_u \end{bmatrix}, \quad (51)$$

one obtains the following formula:

$$D_{X_u}^{\text{tot}} = \mathbf{s}_u^T \Sigma_{uu} \mathbf{s}_u + O(\lambda^{-2}). \quad (52)$$

#### 2.3.4. Asymptotic Formulas for the Global Sensitivity Indices.

In the previous sections we have obtained approximation formulas for the integrals involved in the calculation of the global sensitivity indices. As we have demonstrated, these integrals can be approximated with the asymptotic series  $\sum_{m=1}^{\infty} c_m \lambda^{-m}$ , where the coefficients  $c_m$  depend on the derivatives of the model function with respect to input variables. Based on this result, the asymptotic formula for the sensitivity indices,  $S_{X_u}$  and  $S_{X_u}^{\text{tot}}$  can be written as a ratio:

$$\frac{\sum_{n=1}^{\infty} a_n \lambda^{-n}}{\sum_{k=1}^{\infty} b_k \lambda^{-k}} = \frac{a_1}{b_1} + \frac{(a_2 b_1 - a_1 b_2)}{b_1^2} \lambda^{-1} + O(\lambda^{-2}). \quad (53)$$

The first two terms of the Maclaurin series with respect to the small parameter  $\lambda^{-1}$  are written explicitly on the right-hand side of (53). Hence the first nontrivial term in the approximation of the sensitivity indices is the ratio of the first nonvanishing term in the integral approximations obtained above. Thus, the approximation for MSI can be obtained by dividing (45) by (37):

$$S_{X_u} = \frac{\mathbf{s}_u^T \Sigma_{uu} \mathbf{s}_u}{\mathbf{s}^T \Sigma \mathbf{s}} + O(\lambda^{-1}). \quad (54)$$

Similarly, the approximation for the TSI is

$$S_{X_u}^{\text{tot}} = \frac{\mathbf{s}_u^T \Sigma_{uu} \mathbf{s}_u}{\mathbf{s}^T \Sigma \mathbf{s}} + O(\lambda^{-1}). \quad (55)$$

### 3. Discussion

Formula (37) relates the input uncertainties, given by the covariance matrix  $\Sigma$ , to the output uncertainty, characterized by the variance  $D$  and, hence, describes the propagation of error. Contrary to what one would expect from (23), the approximation formula (36) involves first-order partial derivatives of  $f(\mathbf{x})$  and not zeroth and second-order derivatives.

As one can see, the structure of the first nonvanishing term in this expression corresponds to the famous sandwich formula for error propagation used in the derivative-based LSA [3, 4]. Note, that in this work sensitivity vector components are defined as  $s_i = (\partial f(\mathbf{x})/\partial x_i)_{\mathbf{x}=\boldsymbol{\mu}}$ , whereas in literature dimensionless sensitivity coefficients  $s_i = (\mu_i/f(\boldsymbol{\mu}))(\partial f(\mathbf{x})/\partial x_i)_{\mathbf{x}=\boldsymbol{\mu}}$  are often used.

Formulas (45) and (52) have the same sandwich structure as (37), but contains only the sensitivities and uncertainties with respect to the input variables  $\mathbf{X}_u$ . Moreover, factor

$D_{\mathbf{x}_u}$  matches factor  $D_{\mathbf{x}_u}^{\text{tot}}$  under conditions used in the approximation and the corresponding sensitivity indices coincide. As a result, sensitivity indices given by (54) and (55) do not differ in the first nonvanishing term in the approximation. The difference between  $S_{\mathbf{x}_u}$  and  $S_{\mathbf{x}_u}^{\text{tot}}$  may be of the order  $O(\lambda^{-1})$ . Formulas (54) and (55) involve, besides elements of the covariance matrix, only gradients of the model function, which are proportional to the coefficients of the linear expansion of the model at  $\mathbf{x} = \boldsymbol{\mu}$ . This indicates that, in the considered limit, the model is approximately linear. As a consequence, interactions are negligible and  $S_{\mathbf{x}_u}$  coincides with  $S_{\mathbf{x}_u}$  that is reflected by results (54) and (55).

The remaining question of this analysis is the criterion for the applicability of the asymptotic results. We could not derive this criterion directly for the sensitivity indices. The indirect indication can be obtained by using (27):

$$f^2(\boldsymbol{\mu}) \gg \mathbf{s}^T \boldsymbol{\Sigma} \mathbf{s} + f(\boldsymbol{\mu}) \text{tr}(\boldsymbol{\Sigma} \mathbf{H}), \quad (56)$$

by taking into account that the calculation of the sensitivity index involves the calculation of integrals for  $f^2(\mathbf{x})$ .

#### 4. Example

Adetula and Bokov [15, 16] discussed a test problem, where the model  $f : \mathbb{R}^7 \rightarrow \mathbb{R}$  represents the two-group infinite multiplication factor described by the analytical formula [19]:

$$f(X_1, \dots, X_7) = \frac{X_5}{X_1 + X_3 + X_7} + \frac{X_6 X_7}{(X_2 + X_4)(X_1 + X_3 + X_7)}, \quad (57)$$

where variables  $X_i$  with  $i = 1, 2, \dots, 7$  represent the following macroscopic cross-sections:  $X_1$  is the fast capture,  $X_2$  is the thermal capture,  $X_3$  is the fast fission,  $X_4$  is the thermal fission,  $X_5$  is the fast neutron production,  $X_6$  is the thermal neutron production, and  $X_7$  is the fast removal. The mean values of the cross-sections and covariance matrix used were based on the data given in [20]:

$$\begin{aligned} \boldsymbol{\mu} &= 10^{-2} \\ &\times [0.5336 \ 2.693 \ 0.19124 \ 2.8438 \ 0.4920 \ 6.929 \ 2.063]^T, \\ \boldsymbol{\Sigma} &= 10^{-8} \\ &\times \begin{bmatrix} 0.42 & 0.22 & -0.05 & -0.02 & 0 & 0 & 0 \\ 0.22 & 2.14 & -0.02 & -0.65 & 0 & 0 & 0 \\ -0.05 & -0.02 & 0.02 & 0.01 & 0 & 0 & 0 \\ -0.02 & -0.65 & 0.01 & 0.84 & 0 & 0 & 0 \\ 0 & 0 & 0 & 0 & 0.23 & 0.18 & 0 \\ 0 & 0 & 0 & 0 & 0.18 & 9.64 & 0 \\ 0 & 0 & 0 & 0 & 0 & 0 & 5.28 \end{bmatrix}, \end{aligned} \quad (58)$$

where the cross-sections are given in  $\text{cm}^{-1}$  and the variances are given in  $\text{cm}^{-2}$ . The test covariance matrix has three uncorrelated blocks, corresponding to subsets:  $\{X_1, X_2, X_3, X_4\}$ ,  $\{X_4, X_5\}$ , and  $\{X_7\}$ , for which the calculation of sensitivity indices is not meaningless.

Values of the global sensitivity indices, which are calculated using the asymptotic formulas obtained in our work and the values as reported in [15, 16] are presented in Table 1. The output uncertainty, characterized by the variance ( $D$ ) or the standard deviation ( $\sqrt{D}$ ) calculated with these two methods are also given in Table 1. The values taken from [15, 16] were calculated with the sparse grid quadrature, as it has been found to be the most accurate amongst all the applied quadratures. (Other quadratures were Monte Carlo and quasi-Monte Carlo. Values obtained with all three quadratures were in a good agreement, this indicates that the quadratures have converged and the result obtained may be taken as the reference.) As one can see from Table 1, the results for sensitivity indices and uncertainties are in good agreement and differ for only one case in the fourth significant digit for sensitivity indices and in the third significant digit for the variance. It is worth mentioning that this discrepancy is still within the error of numerical integration as reported in [15, 16]. Results given in Table 1 confirm the validity of the asymptotic approximation for the considered test problem. Similar results have been obtained for the second case, as discussed in [15, 16], namely the case of the diagonal covariance matrix. These results also confirm the correctness of the hypothesis given in [15, 16] and discussed in earlier in Section 1 of this paper.

#### 5. Conclusions

The problem of calculating the uncertainty and sensitivity parameters in the framework of the variance-based Global Sensitivity Analysis was addressed. It was assumed that the input variables are normally distributed and block-wise correlated. Under the additional assumption that the covariance matrix is small in some norm, the Laplace approximation technique was applied and the asymptotic approximation of the output variance and the global sensitivity indices was obtained.

Our results demonstrate that the first nontrivial term in the asymptotic expansion of the output uncertainty (variance) has the so-called sandwich structure well known from the local sensitivity analysis, that is, it depends linearly on the covariance matrix and quadratically on the partial derivatives of the outputs with respect to the inputs. The dependence of uncertainty on the partial derivatives means that, under the above assumptions, the model can be considered to be approximately linear, and, as a consequence, the interaction (but not correlation) between inputs is negligible. The above conclusion is supported by the asymptotic approximation obtained for sensitivity indices: the expression for the main sensitivity indices coincides with the expression for the total sensitivity indices, thus indicating that interactions between input variables can be neglected.

A test problem with realistic values of multigroup cross-sections and their covariances was considered. The values of the global sensitivity indices calculated via asymptotic formula were found to be in good agreement with the values calculated from the exact formulas using numerical integration. This demonstrates that the results obtained may not only be of academic interest but of practical interest

TABLE 1: Sensitivity indices and output uncertainty (both dimensionless) as calculated with the asymptotic formula and multidimensional quadrature.

Parameter	Asymptotic approximation	Sparse grid integration [15, 16]
Sensitivity index for $\{X_1, X_2, X_3, X_4\}$	0.3453	0.3453
Sensitivity index for $\{X_5, X_6\}$	0.6126	0.6125
Sensitivity index for $\{X_7\}$	0.0421	0.0421
Variance $D$	$3.575 \cdot 10^{-5}$	$3.567 \cdot 10^{-5}$
Standard deviation $\sqrt{D}$	598 pcm	597 pcm

as well. The theoretical and numerical results obtained in this work indicate that, from the point of view of numerical calculations, the sparse-grid integration-based method for the uncertainty propagation can be an alternative to the perturbation/derivative methods used in the local sensitivity analysis. Moreover, the results for the uncertainty obtained by these two methods are interchangeable in the limit of small cross-section errors.

## Acknowledgments

The author is grateful to Dr. Djordje I. Tomašević for inspiring this study and for pointing out an error in the initial paper. The author is also thankful to the South African National Research Foundation (NRF) for the financial support.

## References

- [1] I. M. Sobol', "Global sensitivity indices for nonlinear mathematical models and their Monte Carlo estimates," *Mathematics and Computers in Simulation*, vol. 55, no. 1–3, pp. 271–280, 2001.
- [2] A. Saltelli and I. M. Sobol', "Sensitivity analysis for nonlinear mathematical models: numerical experience," *Matematicheskoe Modelirovanie*, vol. 7, no. 11, pp. 16–28, 1995.
- [3] A. Saltelli, S. Tarantola, F. Campolongo, and M. Ratto, *Sensitivity Analysis in Practice: A Guide to Assessing Scientific Models*, John Wiley & Sons, 2004.
- [4] D. G. Cacuci, M. Ionescu-Bujor, and I. M. Navon, *Sensitivity and Uncertainty Analysis: Applications To Large-Scale Systems*, CRC Press, 2005.
- [5] J. Jacques, C. Lavergne, and N. Devictor, "Sensitivity analysis in presence of model uncertainty and correlated inputs," *Reliability Engineering and System Safety*, vol. 91, no. 10–11, pp. 1126–1134, 2006.
- [6] N. Lüdtke, S. Panzeri, M. Brown et al., "Information-theoretic sensitivity analysis: a general method for credit assignment in complex networks," *Journal of the Royal Society Interface*, vol. 5, no. 19, pp. 223–235, 2008.
- [7] B. Iooss and M. Ribatet, "Global sensitivity analysis of computer models with functional inputs," *Reliability Engineering and System Safety*, vol. 94, no. 7, pp. 1194–1204, 2009.
- [8] I. M. Sobol', "Sensitivity estimates for nonlinear mathematical models," *Mathematical Modeling and Computational Experiment*, vol. 1, pp. 407–414, 1993.
- [9] E. Novak and K. Ritter, "High dimensional integration of smooth functions over cubes," *Numerische Mathematik*, vol. 75, no. 1, pp. 79–97, 1996.
- [10] E. Novak and K. Ritter, "The curse of dimension and a universal method for numerical integration," in *Multivariate Approximation and Splines*, vol. 125 of *International Series of Numerical Mathematics*, p. 177, Birkhäuser, 1998.
- [11] Ch. Lemieux and A. B. Owen, "Quasi-regression and the relative importance of the ANOVA components of a function," in *Monte Carlo and Quasi-Monte Carlo Methods, 2000*, pp. 331–344, Springer, 2002.
- [12] W. Chen, R. Jin, and A. Sudjianto, "Analytical variance-based global sensitivity analysis in simulation-based design under uncertainty," *Journal of Mechanical Design*, vol. 127, no. 5, pp. 875–886, 2005.
- [13] N. H. Kim, H. Wang, and N. V. Queipo, "Adaptive reduction of random variables using global sensitivity in reliability-based optimisation," *International Journal of Reliability and Safety*, vol. 1, pp. 102–119, 2006.
- [14] A. B. Owen, "Orthogonal arrays for computer experiments, integration and visualization," *Statistica Sinica*, vol. 2, pp. 439–452, 1992.
- [15] B. A. Adetula and P. M. Bokov, "Computational method for global sensitivity analysis of reactor neutronic parameters," submitted to *Science and Technology of Nuclear Installations*, special issue on *Uncertainty Analysis in Reactor Physics Modelling*.
- [16] B. A. Adetula and P. M. Bokov, "Method for calculation of global sensitivity indices for few-group cross-section-dependent problems," in *Proceedings of the International Conference on Mathematics and Computational Methods Applied to Nuclear Science and Engineering (MC '11)*, Rio de Janeiro, Brazil, May 2011.
- [17] R. A. Johnson and D. W. Wichern, *Applied Multivariate Statistical Analysis*, Prentice Hall, Englewood Cliffs, NJ, USA, 1998.
- [18] P. D. Miller, *Applied Asymptotic Analysis*, American Mathematical Society, 2006.
- [19] W. M. Stacey, *Nuclear Reactor Physics*, Wiley-Interscience, 2nd edition, 2007.
- [20] M. Williams, M. Jessee, R. Ellis, and B. Rearden, "Sensitivity/uncertainty analysis for OECD UAM benchmark of peach bottom BWR," in *Proceedings of the Uncertainty Analysis and Modelling Workshop (UAM '04)*, Pisa, Italy, April 2010.